Seismic wave propagation, attenuation and scattering in porous media across various scales

By

Khemraj Shukla

Master of Science in Physics
Banaras Hindu University
Varanasi, India
2005

Submitted to the Faculty of the
Graduate College of the
Oklahoma State University
in partial fulfillment of
the requirements for
the Degree of
Doctor of Philosophy
December, 2019

Seismic wave propagation, attenuation and scattering in porous media across various scales

Dissertation Approved:

Prof. Priyank Jaiswal

Dissertation Adviser

Prof. Jack C. Pashin

Prof. Todd Halihan

Prof. Yanqiu Wang

ACKNOWLEDGEMENTS

I would like to take this opportunity to express my sincere thanks to my advisor, Professor Priyank Jaiswal, for his unconditional support, patience and his believes in me regarding this work. Out of many, the most admired quality of his was pushing me to reaching out the experts in wave physics and computational mathematics around the world, which ultimately shaped up my PhD work at to an exceptional level. I would also like to thank Professor Jan S. Hesthaven of EPFL, Switzerland for his supports during my one year stay at EPFL, Switzerland. I express my sincere gratitude to Prof. Hesthaven for introducing me nodal discontinuous Galerkin finite element method and its implementation from a bottom up approach. The work presented in Chapter 3 of this thesis was carried out under the luminary guidance of Prof. Hesthaven. I also express my sincere thanks to Dr. José M. Carcione, Director of Research, INOGS Italy, for his continuous and tireless support through out my PhD and his time and efforts to provide me the hospitality during my various visits to Italy. Dr. Carcione introduced me with various concepts of wave propagation in porous medium saturated with single and multi-phase fluids. Dr. Carcione contributions made me successful in writing the three papers with him as a coauthor and leading to three chapters (Chapter 2, Chapter 3 and Chapter 6) of this thesis. I also thank you my committee members Prof. Yanqiu Wang, Prof. Jack Pashin and Prof. Todd Halihan for various helps and supports during my PhD work.

I also would like to thank Prof. Maarten V. de Hoop and Prof. Jesse Chan of Computational and Applied Mathematics (CAAM) department at Rice University, for his all

*Acknowledgements reflect the views of the author and are not endorsed by committee members or Oklahoma State University.

all supports and guidance during my three years of stay at the Rice University. I express my sincere thanks to Prof. Jesse Chan for his priceless time to explain me weight-adjusted discontinuous Galerkin method from analysis and algorithmic point of view along with various concepts of numerical analysis and scientific computing. The work with Prof. Chan and Prof. de Hoop resulted into two research paper and also contributed thesis's two chapters (Chapter 4 and Chapter 5).

I would also thank my mentors in my internships at Halliburton/Landmark, Colorado (Dr. Andreas Rueger), Hewlett Packard, California (Dr. Harumi Kuno) and BP, Houston (Dr. Elizabeth L'heureux and Dr. Xin wang) for their support and guidance during my projects at those organizations. I would like to thank Dr. Dhananjay Kumar and my friend Madhav Vyas, Geophysicists at BP, for his help in explaining the various concepts of computational geophysics. I also extend my sincere thanks to my friend Sundeep Sharma for his presence in an around my commitment to the thesis and his contribution to my PhD work is un-parallel and could not be constrained by the words.

I also would like to thank Mrs. Delphine Vieira and Mrs. Miranda Joyce for doing everything to make my stay smooth at EPFL and Rice University. I also express my sincere gratitude to my friends and office mates Babak Maboudi and Allan Nielsen at EPFL for various technical discussions. I also extend my thanks to my office mates Vitaly Katnelson, Peter Caday, Chirstopher Wong, Ruichao Ye and Teemu Saksala for various helps, especially clearing my doubts in abstract mathematics.

Finally, I would like to thank my family especially my brother, *Sh. Kamlesh Kumar*, for supporting me everyway possible, starting from my decision of going for a PhD. Last but not least, I dedicate this thesis to *Soma Roy* for her untiring support and sacrifices during the course of this journey, starting from motivating me to pursue a PhD.

*Acknowledgements reflect the views of the author and are not endorsed by committee members or Oklahoma State University.

Name: Khemraj Shukla

Date of Degree: December, 2019

Title of Study: Seismic wave propagation, attenuation and scattering in porous media across various scales

Major Field: Geology

Abstract:

The theory of poroelasticity describes the mechanics of fluid saturated deformable porous solids. Poroelastic theory accurately model the seismic wave propagation in oil and gas reservoirs with an extension to other porous medium e.g. living bones and soft tissues. The poroelastic theory also incorporates the attenuation of energy caused by the relative motion between solid and fluid excited by a point source perturbation.

First and foremost, this thesis presents a comprehensive description of seismic attenuation in a viscoacoustic medium by using a fractional derivative approach. Representation of attenuation by using a fractional derivative avoids the solution of augmented system represented by memory process i.e. convolution. In this thesis, a highly accurate time integration scheme, known as rapid expansion method, with a spectral accuracy is implemented to solve the viscoacoustic wave equation.

Next, this thesis describes the implementation of a high-order weight-adjusted discontinuous Galerkin (WADG) scheme for the numerical solution of two and three-dimensional (3D) wave propagation problems in anisotropic porous media. The use of a penalty-based numerical flux avoids the diagonalization of Jacobian matrices into polarized wave constituents necessary when solving element-wise Riemann problems.

Additionally, a system of hyperbolic partial differential equations describing Biot's poroelastic wave equation for quasi-static Poisseulle and potential flow is also introduced. To incorporate effects from micro-heterogeneities due to pores, we have used the Johnson-Koplik-Dashen (JKD) model of dynamic permeability, which also account for frequency-dependent viscous dissipation caused by wave-induced pore fluids.

Next, this thesis uses a model to quantify capillary effects on velocity and attenuation. Studies that have attempted to extend Biot's poroelasticity to include capillary effects found changes in fast P-wave velocity of up to 5 % between the sonic and ultrasonic frequency ranges.

TABLE OF CONTENTS

List of Figures

List of Tables

Chapter I

Introduction

In Acoustics, we have sometimes to consider the incidence of aerial waves upon porous bodies, in whose interstices some sort of aerial continuity is preserved...

John William Strutt (Lord Rayleigh)

1.1 Motivations

The work on physics of the wave propagation in the porous media was originally motivated by the work of Dr. José M. Carcione [3] on pseudo-spectral modeling of 2D poroelastic wave equation in an homogeneous media. The work by Carcione [3] discussed the effect of anisotropy on phase velocity and attenuation of a plane wave propagating in a porous media. A rigorous study dealing with physics and mathematics of wave propagation in 3D anisotropic porous media was completely lacking in the study presented by Carcione [3]. additionally, the numerically solution of wave propagation in porous media presented by Carcione [3] was carried out by using a low-order numerical scheme with an accuracy of 2^{nd} order in time and 4^{th} order in space ($[\mathcal{O}(2,4)]$). This scheme was based on pseudo-spectral method with spatial discretization based on the structured grid. The low-order scheme is proned to numerical dissipation [6] and also structure grid based discretization lacks the adaptivity to irregular domain geometry such as sea-floor surfaces, geological discontinuity and undulated topography.

Consequent upon the study carried by Carcione [3], numerical scheme and computational modeling presented int this work was motivated by the work of Professor Lucas

Wilcox [7] on modeling of wave propagation in coupled acoustic-elastic media using nodal discontinuous Galerkin finite element method. Nodal discontinuous Galerkin method is a high order accurate numerical scheme based on unstructured meshes, which discretize the the irregular geometry of computational domain accurately. Numerical scheme presented by The study carried out by [7] does not extend to anisotropic media naturally as the numerical flux used is dependent on the eigenecomposition of the Jacobian matrices of the isotropic wave equation and does not extend to generic medium. In this study, a method to obtain the generic numerical scheme for an anisotropic medium is well derived and implemented for the poroelastic wave equation.

A porous medium is made of solid matrix (skeleton of frame) and pervaded by an interconnected network of pores filled with a single or multiphase fluid. Unlike the acoustic and elastic medium, the wave propagation in porous medium is a complex and rich phenomena. A first complete dynamic poroelastic model was proposed by Biot [8, 9, 10], wherein poroelastic theory was proposed a a homogenized model of solid porous media containing the fluids with an ability to move through the pore network. Though the Biot developed this model to model the fluid-saturated rocks and soils but it has been also rigorously used in underwater acoustics [11, 12] and modeling the wave propgation in *in vivo* bone [13].

Biot theory of poroelasticity predicts three types of wave; fast P wave, similar to elastic P wave in which there is no relative displacement between solid and fluid: S wave similar to elastic shear wave and slow P wave resulted due to large relative displacement between solid and fluid. The energy of these waves are dependent on the viscosity of the fluid, which affects slow P wave more than fast P and S waves.

1.2 Previous work on computational dynamic poroelasticity

The first theory of poroelasticity was proposed by Darcy [14] where he measured the flow of water in sand. Terzaghi [15] first brought the idea of porous medium by proposing the concept of effective stress for quasi-static deformation of fluid saturate soils. Subsequently, Biot [16] first proposed general theory of quasi-static poroelasticity and then expanded it to dynamic poroelasticity, also known as Biot's theory, providing a general description of mechanical behavior of poroelastic medium [8, 9, 10]. Since the advent of the Biot's theory, various numerical methods have been used to solve the poroelastic wave equations. A detailed

review on the computational dynamic proelasticity is carried out by Carcione et al. [17]. The first study on computational porelasticity was carried by Garg [18] in 1D and using a finite difference method. Afterwards various finite difference methods and pseudospectral methods have been used to solve the poroelastic wave equations [19, 20, 21, 22]. The first implementation of pseudo-speactram method to solve the anisotropic porous media was carried out by [3]. To solve the poroelastic wave equation, the implementation of finite element, boundary element and spectral element method (in time and frequency domain) are carried out by Santos and Oreña [23], Attenborough et al. [24], Morency et al. [5] and [25], respectively. The first implementation of finite volume based method is carried out by Naumovich [26] by using a staggered grid approach. Naumovich [26] solved the isotropic poroelastic wave equation in 3D using the rectilinear grids. Recently, Lemoine et al. [27, 28] solved the poroelastic wave equation in orthotropic poroelastic media using a finite volume method. In high-order regime de la Puente et al. has solved the 3D poroelastic wave equation in time domain [4] using a local time-space discontinuous Galerkin (dG) method. Recently, Dupuy [29] has also solved the 2D isotropic poroelastic wave equation in frequency domain using a dG method. Additionally, various indirect methods were also used to solve in inverse problem in the poroelastic medium, e.g. Buchanan and Gilbert [30] used the method of numerical integration of contour integral to estimated the poroelastcic parameter in a cancellous bone.

1.3 Contribution of this work

This work primarily solves the problem of wave propagation in the anisotropic porous medium using the nodal discontinuous Galerkin finite element method in two and three dimensions. The system are solved for frequency range varying from sonic (kHz) to ultrasonic (MHz) ranges. These methods are of high-order accuracy and are applied to complicated domain geometry. To incorporate the interface conditions a penalty flux, analogous Riemann solver, is derived which gives the same accuracy as any Riemann solver. The implementation of penalty flux resulted in a very efficient numerical scheme and unlike Riemann solver can be extended to anisotropic and heterogeneous media naturally. To address the effect of micro-heterogeneities, prominent at very high frequency simulation, a weight-adjusted mass matrix method is derived. The weight -adjusted mass matrix is implement very efficiently

for a memory constrained computing architecture e.g. Graphic Processing Unit (GPU). To the author's knowledge this is the first use of nodal DG method to solve the poroelastic for unstructured meshes (tetrahedral in this work) wave equation by using a penalty flux. The accuracy of the solution was carried out in details by comparing it with existing results

In this work we also extended the physics of wave propagation for a porous media saturated with multiphase phase fluid. This system is solved numerically using a pseudo-spectral method to quantify the effect of the capillary pressure on seismic velocities. Additionally, this work is kicked of by studying the attenuation of wave energy in viscoelastic media using a fractional Laplacian operator, which is solved by using a a very efficient rapid-expansion-method (REM).

In addition, several novel ideas were developed while studying the wave propagation in porous media such as

1. A detailed derivation of well-posedness of poroelastic system is carried out by using a charecterstic based approach.

2. Numerical stiffness due to presence of slow P wave is handled by implementing operator splitting and unified numerical scheme. The deterioration in accuracy of the scheme due to operator splitting was circumvented using the unified scheme by implementing a more conservative criteria of time-steps depending the order of numerical scheme.

3. A broad-band system is derived to unify the low and high frequency Biot system using a frequency dependent permeability.

4. A detailed numerical study of dependence of seismic velocity on capillary pressure is carried out and validated by various experimental results available.

1.4 Outline of the chapters

The contents of this thesis work is organized as follows: Chapter 2 describes the seismic attenuation in a a viscoelastic medium using fractional Laplacian, obtained by approximating the relaxation of the medium with a time-dependent Kjartansson's model [31]. Unlike the conventional relaxation model e.g. Zener or Burger's models [32], the model proposed here does not result in an augmented system of relaxation variables. To solve the system

numerically, we introduced a highly accurate and efficient method of rapid-expansion-method (REM) for numerical integration and pseudo-spectral method for fractional Laplacian. We showed the accuracy method by comparing the numerical solution with analytical solution and efficiency of the method was shown by computing the solution for large model containing a gas chimney.

Chapter 3 describes the formulation of governing partial differential equations in conservation form for a two-dimension anisotropic poroelastic medium. The wellposedness of the system was proved by constructing a simultaneous symmetrizer and subsequently, proving that rate of energy of system is bounded. This system was solved numerically using a nodal discontinuous Galerkin finite element method with domain discretized by using the triangles. The interface condition or (natural boundary conditions) is implemented using a Lax-Friedrich flux. The stiffness of the system was handled by using a first-order operator splitting method.

Chapter 4 describes the formulation of a symmetric governing partial differential equations in conservation form for a three-dimension anisotropic poroelastic medium. The implementation of Lax-Friedrich as discussed in Chapter 3 requires computation of medium velocity for each element, which is a computationally demanding. Additionally, the Lax-Friedrich method is dissipative in nature. To overcome the drawbacks of Lax-Friedrich flux, the numerical solution of 3D anisotropic poroelasticity was computed by deriving an energy-stable a penalty flux. The penalty flux implements the interface condition (natural boundary conditions) by penalizing a central flux. In this chapter, a method weight-adjusted mass matrix was derived for poroelastic system to handle the micro-heterogeneities of sub-element level. The stiffness of the system is addressed using 2^{nd} order operator splitting approach and also incorporated implicitly using a unified numerical scheme. Various computational experiment such as convergence and stability of the scheme, validation against exiting solutions and computation of solutions for various real-case scenarios are performed. The solution for a very large reservoir models with undulated topography, discretized with tetrahedral elements, are performed by implementing the scheme on a heterogeneous computing platform, formed by CPU and GPUs.

Chapter 5 describes the formulation of poroelastic wave equation applicable for entire frequency range (Hz - MHz). Studies presented in chapters 3 and 4 deal with the poroelsticity,

which is applicable for low frequency regime defined by dominance of viscous forces over the inertial forces. In this chapter a system of poroelasticity is presented by substituting the static permeability with frequency dependent permeability also known as Johnson-Koplik-Dashen model of permeability. The model obtained in this chapter is called as **brad-band Biot's** system. The Numerical scheme presented in the chapter 4 is also used to solve the braod-band Biot's system. Various computation experiments including the convergence and stability of the numerical scheme is performed.

Chapter 6 describes the poroelasticity for an isotropic porous medium saturated with two-phase fluids, wetting and non-wetting. The model describing this effect is presented in conservation form and solved numerically using a pseudo-spectral and 4^{th} order Runge-Kutta scheme to compute the spatial and time derivatives, respectively. A detailed study on the effects of capillary pressure on seismic velocities and attenuation is presented. Various computational experiments in different frequency regimes for various values capillary pressures are performed and studied.

Chapter 7 concludes the works in presented in the chapters 2-5 with an outline on future line of works.

Chapter II

Modeling the wave propagation in viscoacoustic media: An efficient spectral approach in time and space domain

2.1 Abstract

We present an efficient and accurate modeling approach for wave propagation in anelastic media, based on a fractional spatial differential operator. The problem is solved with the Fourier pseudo-spectral method in the spatial domain and the REM (rapid expansion method) in the time domain, which, unlike the finite-difference and pseudo-spectral methods, offers spectral accuracy. To show the accuracy of the scheme, an analytical solution in a homogeneous anelastic medium is computed and compared with the numerical solution. We present an example of wave propagation at a reservoir scale and show the efficiency of the algorithm against the conventional finite-difference scheme. The new method, being spectral in the time and space simultaneously, offers a highly accurate and efficient solution for wave propagation in attenuating media.

Keywords— Fractional derivative, attenuation, wave propagation, spectral methods

2.2 Introduction

Seismic modeling is essential for various seismic processing steps, which spans from seismic imaging to reservoir characterization. In the entire range of applications, seismic modeling must follow two important criteria, accurate physics and numerical accuracy. It has been very common to solve the second-order scalar wave equation using a finite-difference approximation in the time

and spatial domains for seismic imaging [33, 34, 35, 36] and inversion problem [37]. In these studies, the authors did not consider to incorporate the attenuative nature of the medium, which accounts for the anelastic effect present in the subsurface.

[38, 39] have modeled the attenuation effect on wave propagation by using memory variables. The wave propagation results in an augmented system of partial differential equations defining the evolution of these variables. On the other hand, [40] have solved the acoustic wave equation in the frequency domain incorporating the effects of attenuation, but this approach results into a computationally intensive process as it is required to solve a Helmholtz equation for each frequency.

In another approach, [41] used the theory of [31] to solve the scalar acoustic wave equation with the constraint of constant-Q at all frequencies. The effect of Q is incorporated in the form of a fractional power of the time derivative of the stress variable (σ). Fractional time-derivative of stress variable σ at time t depends on all previous value of σ. This is the memory property of fractional derivative, describing the attenuation. Carcione et al. [41] have solved the integral form of the fractional time-derivative [42] by using the Grünwald-Letinkov and a central-difference approximations with first and second order accuracy, respectively. The consistency, stability and convergence of the scheme is discussed in detail in [43]. The approach adopted in [41] is accurate in producing the desired effect but it is computationally intensive and constrained by the order of the accuracy.

To avoid the memory requirements of the fractional time operators, [44] introduced the fractional Fourier pseudo-spectral method to compute Laplacian derivatives of non-integer order. This approach implies anelastic attenuation and velocity dispersion when implemented in wave equations. Following this methodology, Carcione and co-workers simulated constant-Q wave propagation in a series of papers (e.g., [45, 46]). In these works, authors use second-order finite-difference scheme in time to solve the time derivatives. Here, we solve the time evolution with the spectral rapid expansion method (REM) [47], so that the solution is fully spectral, in the time and space domains, thus improving the accuracy and the computer efficiency.

2.3 Constant-Q medium

The constant-Q model [31] is based on a creep function of the form $t^{2\gamma}$, where t is time and $\gamma \ll 1$. Kjartansson model is completely described by two parameters, namely the phase velocity at a reference frequency and Q. Thus, it is much simpler than any constant-Q model, such as, for instance, the Kelvin-Voigt and Zener models [38, 39, 48] and mainly used in its frequency domain form. The relaxation function $\psi(t)$ for constants-Q model is given by [31]

$$\psi(t) = \frac{M_0}{\Gamma(1-2\gamma)} \left(\frac{t}{t_0}\right)^{-\gamma} H(t) \ , \tag{2.1}$$

where M_0 is a reference bulk modulus, Γ is the Euler Gamma function, t_0 is a reference time, γ is a non-dimensional parameter and $H(t)$ is the Heaviside function.

To derive the wave equation and its analytical solution in lossy media it is essential to have the complex modulus $M(\omega)$ for relaxation function given in equation (2.1). Following [32, p. 72], $M(\omega)$ can be expressed as

$$M(\omega) = \mathcal{F}\left[\partial_t \psi(\omega)\right] \ , \tag{2.2}$$

where $\mathcal{F}$ represent the Fourier transform and ∂_t the time derivative.
The modulus, $M(\omega)$ is given by [31]

$$M(\omega) = M_0 \left(\frac{\mathrm{i}\omega}{\omega_0}\right)^{2\gamma}, \quad \gamma = \frac{2}{\pi} \arctan \frac{1}{Q} \tag{2.3}$$

where $\omega_0 = 1/t_0$ is reference frequency, $\mathrm{i} = \sqrt{-1}$, and the reference modulus M_0 is expressed as

$$M_0 = \rho c^2 \cos^2 \left(\frac{1}{2} \arctan \frac{1}{Q}\right) \ , \tag{2.4}$$

where ρ and c are the mass density and phase velocity, respectively [32, p. 100].

In lossy media, the stress variable (σ) is related to the time history of the strain (ϵ) via a convolution operator,

$$\sigma(\mathbf{x}, t) = \psi(t) * \partial_t \epsilon(\mathbf{x}, t) \ , \tag{2.5}$$

where the symbol "$*$" denotes time convolution. The frequency-domain representation of equation (2.5) is

$$\mathcal{F}\left[\sigma(\mathbf{x}, \omega)\right] = M(\omega) \mathcal{F}\left[\epsilon(\mathbf{x}, \omega)\right] \ . \tag{2.6}$$

Combining equations (2.5), (2.6) and Newton's second law of motion, [32, p. 101] derived the wave

equation in a lossy medium as

$$\partial_t^\beta \sigma(\mathbf{x},t) = \rho\left(\frac{M_0}{\rho}\right)\omega_0^{2-\beta}\nabla_\rho\sigma(\mathbf{x},t)\ , \tag{2.7}$$

where $\nabla_\rho = \partial_x\left(\frac{1}{\rho}\partial_x\sigma\right) + \partial_z\left(\frac{1}{\rho}\partial_z\sigma\right)$ and $\beta = 2-2\gamma$.

Equation (2.7) has a fractional power in the time derivative term, which imposes a problem while computing the numerical solution because it requires to store the solution at all the previous time steps to compute the solution at the current time step [49, 41, 50]. To circumvent this computational issue, [44] proposed an anelastic wave equation for constant-Q, equivalent to equation (2.7), but with spatial fractional derivatives. The acoustic wave equation for uniform-density medium is given by [44],

$$\partial_t^2\sigma(\mathbf{x},t) = \omega_0^{2-2\beta}c^{2\beta}(\partial_x^2+\partial_z^2)^\beta\sigma(\mathbf{x},t) + f(x,z,t), \tag{2.8}$$

where $f(x,z,t)$ is the forcing function and β $(1 \le \beta \le 2)$ defines the extent of attenuation in the medium.

The equivalence between equation (2.7) and equation (2.8) can be easily proven by performing the dispersion analysis of a plane wave [44]. The constant $Q-$model shown by equation (2.8) provides the liberty of choosing the Q value in a direct way, unlike the models presented by [38, 39, 48], where Q values are computed by relaxation times of the material.

2.4 Numerical Scheme

2.4.1 Computation of Fractional Laplacian

To compute spatial derivatives with a fractional power in equation (2.8), a generalized form of pseudo-spectral method is used [51, 44] and expressed as

$$(\partial_x^2+\partial_z^2)^\beta\sigma(\mathbf{x},t) = \mathrm{FFT2D}^{-1}\left[(-1)^\beta(k_x^2+k_z^2)^\beta\mathrm{FFT2D}\left(\sigma(\mathbf{x},t)\right)\right], \tag{2.9}$$

where FFT2D($2\mathrm{D}^{-1}$) are forward (inverse) Fourier operator and $\mathbf{k}$ (k_x,k_z) is wavenumber vector.

In the present study, we have used direct-grid pseudo-spectral method to compute the spatial derivatives, which is a reasonable choice as equation (2.8) is scalar in nature. Unlike any finite-difference scheme, the pseudo-spectral method provides the optimal spatial accuracy for a given grid size, which substantially reduces the numerical errors such as grid dispersion. In addition

to the pseudo-spectral method, spectral finite element method (SPECFEM) can also be used. The SPECFEM will provide better accuracy for complex geometries, but it comes with an aided computational complexity. Finally, the finite volume method (FVM) is also successfully used to compute the spatial-derivative with integer power [52], but extension of this method to compute the spatial operator with fractional power is not trivial. The FVM, being a low order method, is also constrained by its accuracy.

The implementation of direct-grid method for the heterogeneous form of equation (2.8) will produce the Nyquist error due to FFT operators being global in nature. To circumvent the Nyquist error in numerical solution, [53] proposed staggered-grid pseudo-spectral method to compute the spatial derivatives. In staggered-grid pseudo-spectral method, the spatial derivatives are computed at half-grid points using the even-based Fourier transform.

2.4.2 Computation of time derivative

The spatial derivative in equations (2.8) is computed by using the pseudospectral method, which provides very high accuracy and reduces numerical artifacts, resulting due to grid dispersion [54, 55]. The high order accuracy of the pseudo-spectral method causes the total accuracy of the numerical scheme (in the time and the space domain) to be dependent on the accuracy of the time integration scheme. To achieve the high accuracy of the numerical scheme in the space and time domain simultaneously, it is essential to increase the accuracy of the time integration scheme.

It is not obvious to achieve the high order accuracy in computation of the time derivative and thus, the accuracy is confined to 2^{nd} order (using the finite-difference scheme), while modeling the acoustic [36, 33, 56] and the viscoacoustic [44] wave propagation. In these studies, second-order finite-difference approximations were used for time operator, but a high-accuracy and high-order approximations, such as 4^{th} order finite-difference scheme and pseudo-spectral schemes, are used for spatial operators. These approximation of time derivative operator can introduce the numerical error, resulting into the distortion of the shape of the wavelet and grid dispersion, especially, while using the 4^{th} order finite-difference spatial operator. To avoid these numerical errors, a small time step (Δt) must be taken, which in turn reduces the efficiency of the numerical scheme. Thus, combination of pseudo-spectral method (for the spatial derivative) and low-order finite-difference method (for the time derivatives) becomes slow while performing large-scale and high-frequency seismic modeling. Further, various improvements through the finite-difference scheme were proposed to alleviate the accuracy of time-derivative operator [34, 57, 58] but these schemes are based on the trade-off between efficiency and accuracy.

[59] proposed the rapid expansion method (REM) to compute the time integration more accurately and efficiently. Based on the work of [60], wherein a Chebyshev approximation for time marching is used, [59] incorporated Chebyshev approximation of cosine operator (appears in the solution of wave equation) in REM. To achieve the computational efficiency from one-step REM proposed by [59], [47] exploited the recursive property of Chebyshev polynomials and proved the efficiency and accuracy of seismic modeling. Following [47], we will derive the REM for equation (2.8). Fourier transform of equation (2.8) can be written as

$$\frac{\partial^2 \hat{\sigma}(k_x, k_z, t)}{\partial t^2} = -\left(\omega_0^{2-2\beta} c^{2\beta} (-1)^{\beta-1} \left(k_x^2 + k_z^2\right)^{\beta}\right) \hat{\sigma}(k_x, k_z, t), \tag{2.10}$$

where $\hat{\sigma}(k_x, k_z, t) = \mathrm{FFT2D}(\sigma(x, z, t))$.

Using the correspondence principle [32, p. 145–146], the solution of equation (2.10) can be written as [47, 61]

$$\sigma(t + \Delta t) = -\sigma(t - \Delta t) + 2\cos(\phi \Delta t)\sigma(t), \tag{2.11}$$

where $\phi^2 = \omega_0^{2-2\beta} c^{2\beta} (-1)^{\beta-1} \left(k_x^2 + k_z^2\right)^{\beta}$.
In order to derive an efficient numerical scheme, it is required that ϕ^2 can be written as summations of multiplication of functions of x $[f(x)]$ and wave vector k $[h(k)]$. Thus ϕ^2 is expressed as

$$\phi^2 = \sum_j f_j(\vec{x}) h_j(\vec{k}). \tag{2.12}$$

Equation (2.12) ensures that $\phi^2 \sigma = \sum_j f_j(\vec{x}) \mathrm{FFT}^{-1}(h_j(\vec{k}) \mathrm{FFT}(\sigma))$ and is satisfied by equation (2.10). Thus, our ultimate objective is to expedite the computation of cosine term in equation (2.8).

The cosine function in equation (2.11) can be expressed as [59]

$$\cos(\phi \Delta t) = \sum_{k=0}^{M} C_{2k} J_{2k}(R \Delta t) L_{2k}\left(\frac{i\phi}{R}\right) \ , \tag{2.13}$$

where C_{2k} are expansion coefficients with $C_0 = 1$, $C_{2k} = 2$ for $k > 0$. J_{2k} represents the Bessel's function of order $2k$ and $L_{2k}(z)$ are modified Chebyshev polynomials. R is the parameters defining the criteria for truncating the summation in equation (2.13). In addition to this, R also conditions the L_{2k} in such a way that arguments of L_{2k} falls in $[-1, 1]$, which is a strict requirement for

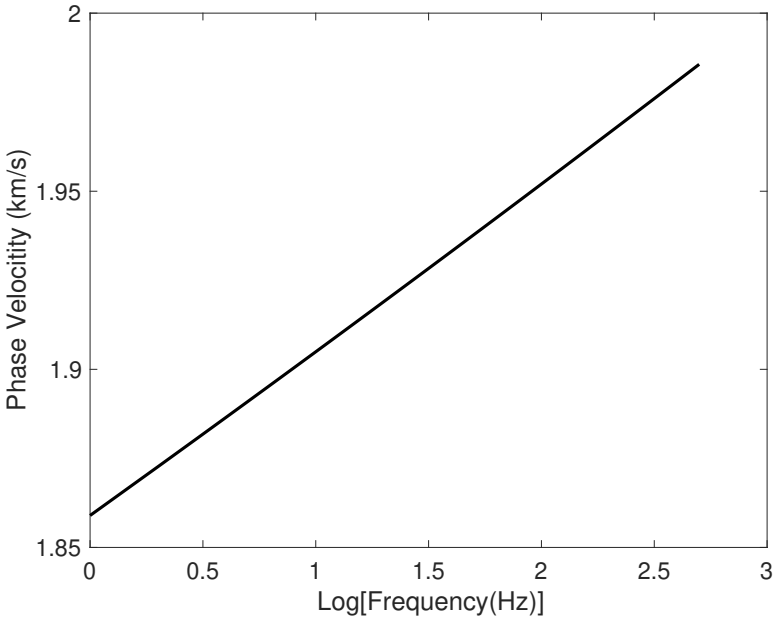

(a)

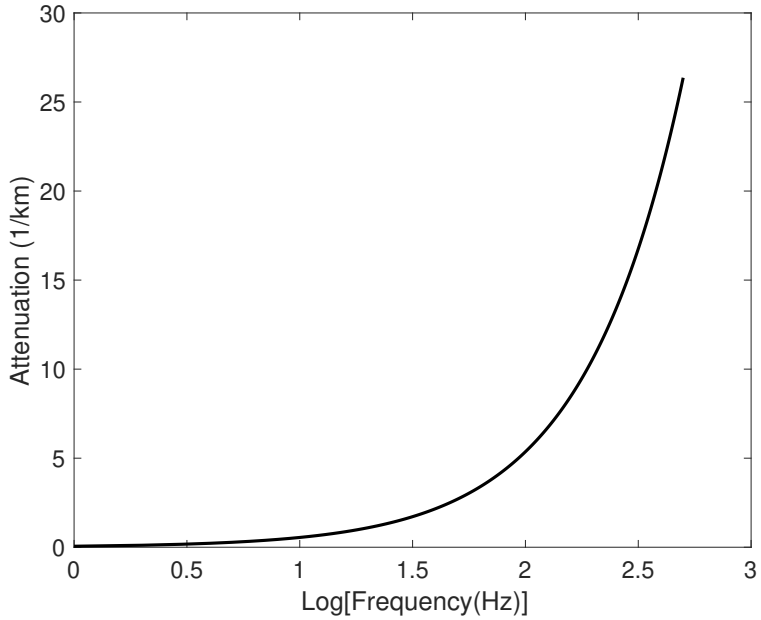

(b)

Figure 2.1: (a) Phase velocity and (b) attenuation factor corresponding to $Q = 30$.

computation of Chebyshev polynomials. R is equal to the maximum eigenvalue of operator ϕ and

given as

$$R = \omega_0^{1-\beta} c_{max}^{\beta} (-1)^{(\beta-1)/2} \sqrt{\left[\left(\frac{\pi}{\Delta x} \right)^2 + \left(\frac{\pi}{\Delta z} \right)^2 \right]^{\beta}}, \tag{2.14}$$

where c_{max} is maximum velocity and Δx and Δz are spatial grid size. R evaluated from equation (2.14) is complex thus, an absolute value of R is to be considered during numerical implementation.

The sum in equation (2.13) converges exponentially for $M > \Delta t R$ [62], also presented in A.1. Though, we are free to choose any value of Δt but selection of Δt will decide the number of terms required to converge the summation in equation (2.13). Since cosine is an even function so equation (2.13) contains only even polynomials and thus, recursive property of Chebyshev polynomials can be used to compute the $L_{2k}(z)$ efficiently. The $L_{2k}(z)$ can be written as

$$L_{k+2}(z) = 2(1 + 2z^2) L_k(z) - L_{k-2}(z). \tag{2.15}$$

Solution of equation (2.15) can be computed recursively with base conditions of $L_0(z) = 1$ and $L_2(z) = 1 + 2z^2$. The sequence of Chebyshev polynomials need to be computed at each time step of wave propagation.

2.5 Results

We consider $c = 2$ km/s and $\omega_0 = 2000$ Hz, representing the medium at an unrelaxed frequency. The unrelaxed frequency is defined by the frequency at which phase velocity achieves the maximum value. Alternatively, this can be also described by the fact that unrelaxed frequency corresponds to the maximum value of relaxation function [32, pp. 90-91]. Figure 2.1 shows the phase velocity and attenuation versus frequency computed for equation (2.8). The dispersion is significant, with a velocity of 1.92 km/s at 15 Hz. Expressions for the phase velocity and the attenuation are given in A.3. In subsequent simulations the reference frequency $\omega_0 = 2000$ Hz is considered, to produce the desired effect of attenuation on wave propagation.

Figure 2.2 shows two snapshots at 500 ms, computed for $Q = 5$ (Figure 2.2a) and $Q = 200$ (Figure 2.2b). The simulation is based on a 200×200 mesh, with square grid of size 10 m. The velocity of the medium, $c = 2$ km/s is assumed. Equation (2.8) is solved, using the pseudo-spectral method to compute the spatial derivative, whereas the time stepping is performed using REM. A 2D point source (with a cylindrical spreading), multiplication of the Dirac function in space and the Ricker wavelet with a dominant frequency of 15 Hz in time, is used as the forcing function $[f(x, z, t)]$.

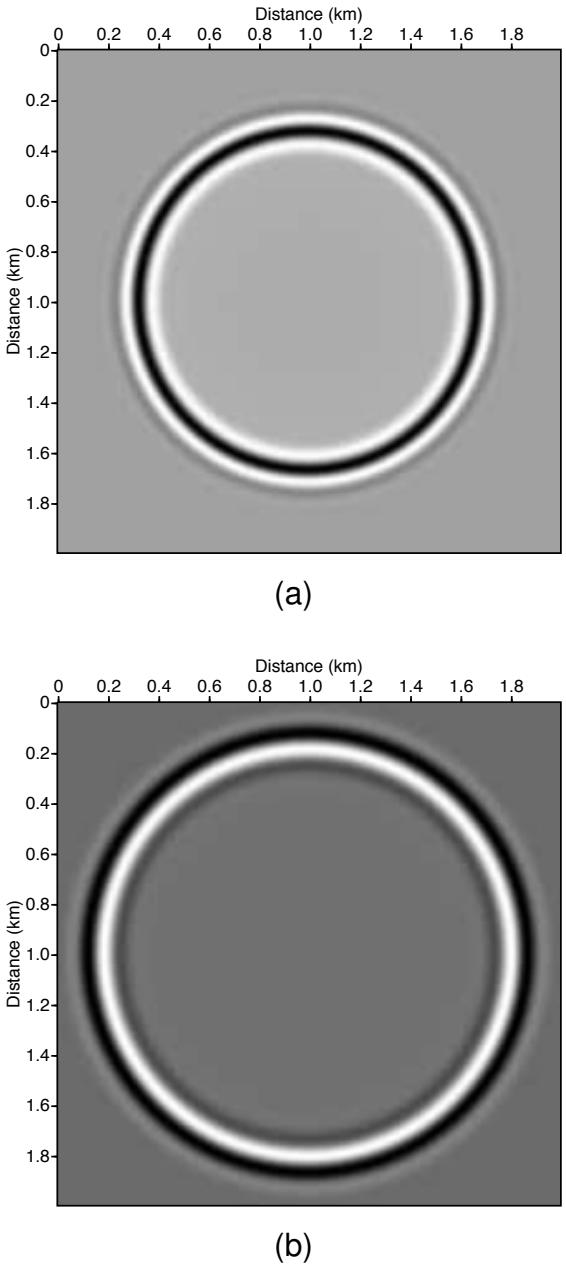

Figure 2.2: Snapshots computed at 500 ms using rapid expansion method for (a) $Q = 5$ (b) $Q = 200$.

As postulated, the wavefront of the lossy case (Figure 2.2a) travels slower than the waverfront of the quasi-elastic case (close to 2 km/s), shown in the Figure 2.2b.

Figure 2.3 represents the numerical simulation of equation (2.8), demonstrating the effect of spatially varying Q on wave propagation. Simulation parameters (except Q) are same as those used in while generating the Figure 2.2. Figure 2.3 clearly reflects the effect of Q on velocity and

amplitude of the wave field. Wavefronts for $Q = 10,\ 20,$ and 30 travel slower than those in the quasi-elastic (almost no attenuation) case ($Q = 200$).

To prove the accuracy of the presented numerical scheme, we computed and compared the analytical and numerical solutions of equation (2.8). An analytical solution of the equation (2.8) is derived by adopting the approach of [50] and shown in A.2. To compute the analytical and numerical solution, we use following forcing function,

$$f(t) = \left(a - \frac{1}{2}\right)\exp(-a), \quad a = \left[\frac{\pi(t - t_s)}{t_p}\right], \tag{2.16}$$

where t_p is period of wave and $t_s = 1.4t_p$ represents delay in source. To compute the analytical solution, a frequency domain representation of equation(2.16) is required, which is expressed as

$$F(\omega) = \left(\frac{t_p}{\sqrt{\pi}}\right)\bar{a}\exp(-\bar{a} - \mathrm{i}\omega t_s), \quad \bar{a} = \left(\frac{\omega}{\omega_p}\right)^2, \quad \omega_p = \frac{2\pi}{t_p}. \tag{2.17}$$

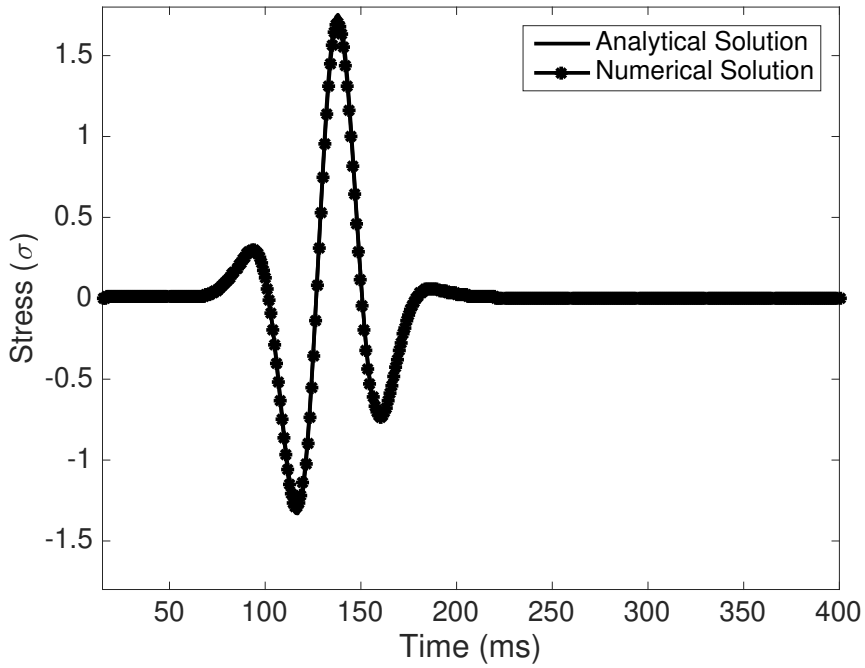

Figure 2.3: A comparison between the analytical (solid line) and numerical (dots) solutions computed at $Q = 5$. The stress field (σ) is computed at an offset of 60 m.

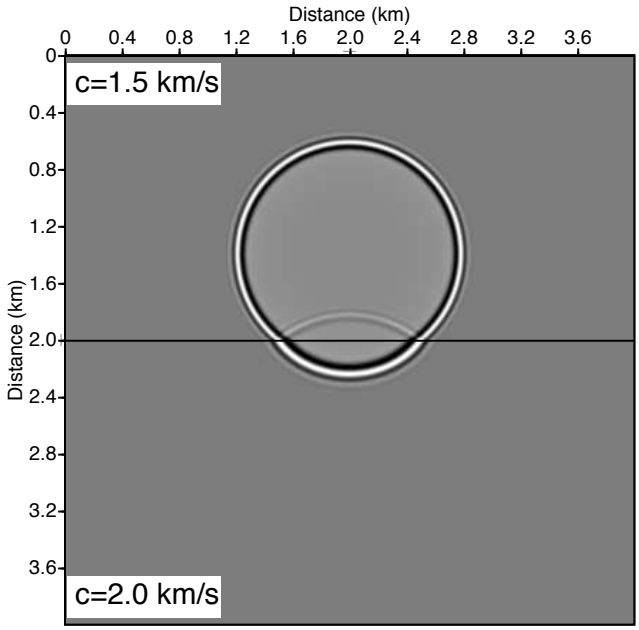

(a)

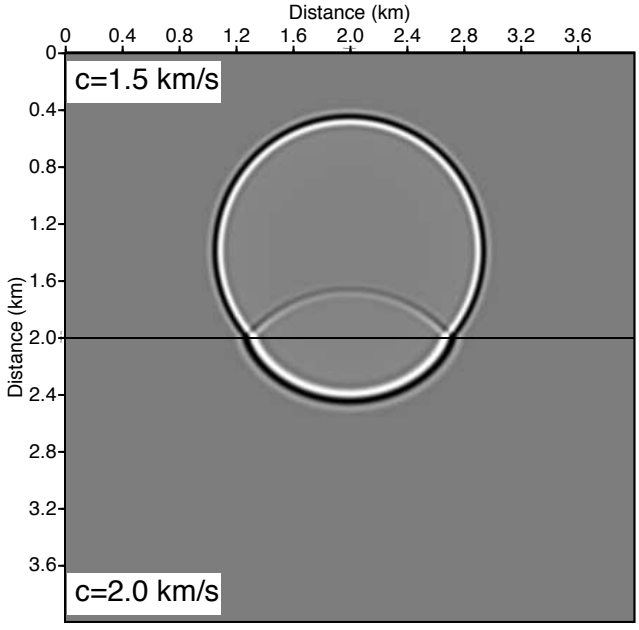

(b)

Figure 2.4: Snapshots computed at 700 ms for variable velocity and constant density medium separated by an interface (equation using rapid expansion method for (a) $Q = 5$ (b) $Q = 40$.

Figure 2.4 represents a comparison between the analytical and the numerical solutions of equation (2.8) for $Q = 5$. The analytical and numerical solutions are computed at an offset of 60 m for a source with dominant frequency of 15 Hz and velocity $c = 1527$m/s. Figure 2.4 clearly shows a good agreement between the numerical and analytical solution with an L^2-norm error of 0.4%.

Figure 2.5 represents the snapshot of wave field, computed by solving the equation (2.8) in an attenuative heterogeneous medium, comprising two layers of different velocity. Figure 2.5a and 2.5b represent the snapshot of wavefield at 700 ms for $Q = 5$ and $Q = 40$, respectively. The simulation is based on 400×400 mesh with grid size of 10 m. The time response of forcing function is a Ricker wavelet with the dominant frequency of 18 Hz. The velocity (c) of top and bottom layer is 1.5 km/s and 2.0 km/s respectively. The phenomena of the velocity varying with Q is very clear; in more attenuating medium ($Q = 5$, Figure 2.5a) the traversed distance of wavefield is less in comparison to the the less attenuating medium ($Q = 40$, Figure 2.5b).

In order to show the efficiency of REM over second-order finite-difference scheme, we compared the number of the Laplacian calculation required in finite difference and REM. In finite difference scheme, the time step for stable explicit-integration is computed using Courant–Friedrichs–Lewy (CFL) condition. CFL condition is the necessary condition, ensuring the convergence and stability of numerical solution, and also based on the fact that numerical speed $\left(\frac{\Delta t}{\Delta x}\right)$ is always less than the physical speed of the wave. The CFL condition is given as

$$\alpha = \frac{c_{max}\Delta t}{\Delta x} \leq \left(\frac{\sqrt{2}}{\pi}\right) \ , \tag{2.18}$$

where Δt is time step, Δx is grid size in space and c_{max} in maximum velocity.

For the finite-difference scheme, the number of the Laplacian is computed by dividing the maximum time of propagation (t_{max}) with time step (Δt), whereas the number of the Laplacian calculation for REM is $> t_{max}R/2$. For the case shown in the Figure 5.5, the number of the Laplacian calculation for the second-order finite-difference ($\alpha = 0.2$) and the REM is 349 and 311, respectively. As the propagation time and the domain size are very small, the difference in the number of the Laplacian computation is not substantial though for the long simulation, the difference is very evident and shown in the subsequent section of the paper.

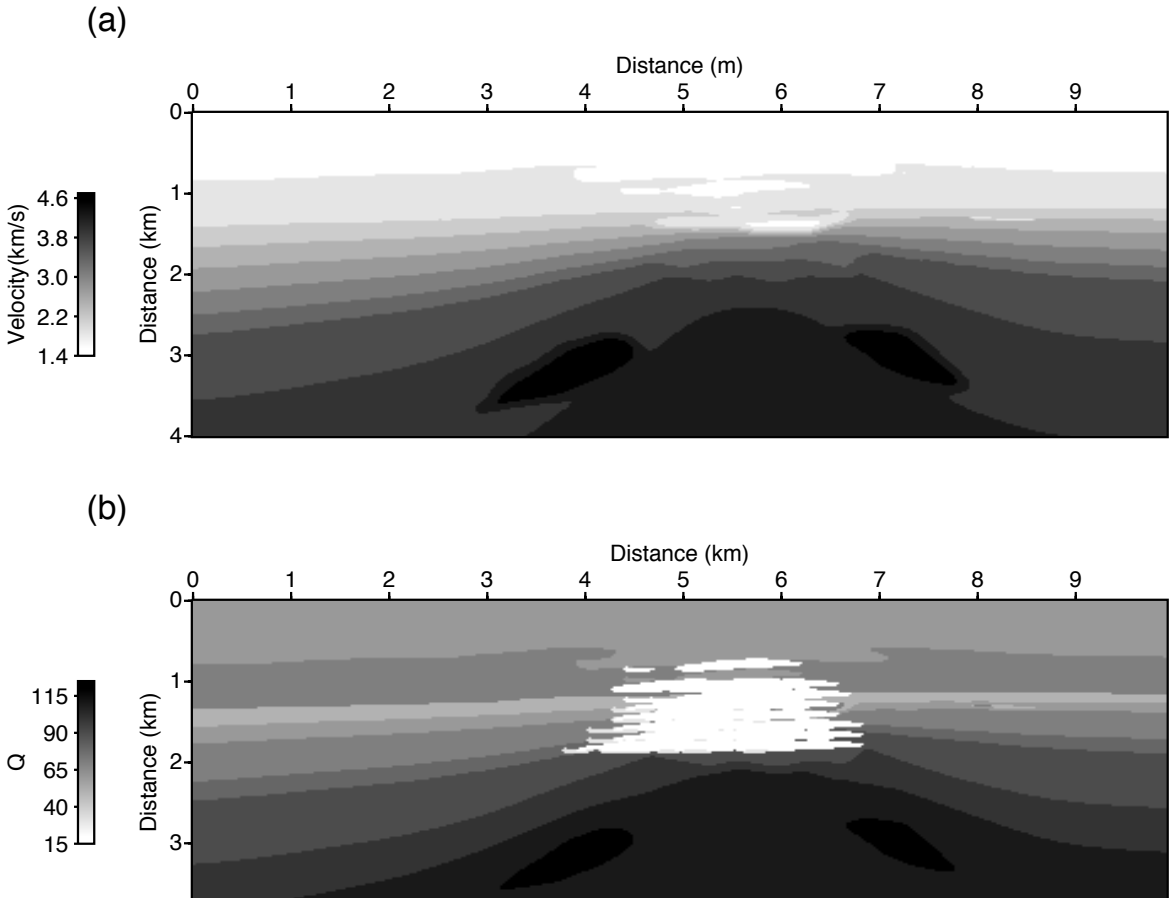

Figure 2.5: Large scale synthetic reservoir model with (a) P-wave velocity and (b) Q model

Numerical solution of the equation (2.8) is computed for a large synthetic reservoir model, containing a gas chimney. The P-wave velocity (Figure 2.6a) and Q model (Figure 2.6b) is adopted from [63]. In this model, the gas chimney is differentiated from the surrounding by a low value of velocity (Figure 2.6a) and $Q(\approx 15)$ (Figure 2.6b). The velocity and Q models comprise 398 and 161 grid points in the x- and the z-direction, respectively. The grid spacing in both the direction is 25 m ($dx = dz$). In the model, P-wave velocity varies from 1500 m/s (c_{min}) to 4500 m/s (c_{max}), which guarantees a max frequency of propagation ($c_{min}/2\Delta x$) to be bounded below by the 30 Hz. A Ricker point source of 18 Hz central frequency is used as a forcing function. Figure 2.7a represents the snapshot of stress-field (σ) at 1.5 s with the Q model (Figure 2.6b) incorporated in the computation. To show the effect of Q on the wave propagation, the numerical solution of the equation (2.8) is also computed for a lossless medium. A lossless condition is achieved by considering

$\beta = 1$ in the equation (2.8). Figure 2.7b represents the snapshot of the wave field at 1.5 s for the lossless medium. A comparison between Figure 2.7a and 2.7b reflects the fact that the dispersion due to the rheology of the model is incorporated accurately.

Figure 2.8a and 2.8b represent the shot gathers in a lossy (corresponding to simulation shown in Figure 2.7a) and lossless (corresponding to simulation shown in Figure 2.7b) medium, respectively. To show the effect of Q on shot gathers, a comparison between amplitude spectra of Figure 2.8a and 2.8b is shown the Figure 2.8c. Figure 2.8c clearly shows the effect of attenuation on the amplitudes. In Figure 2.8c, as expected, the effect of attenuation is more evident at high frequencies, which is reflected by the steeper rate of decay in amplitude in lossy case than in lossless case. The dominant frequency is ≈ 14.5 Hz for both the cases. Figure 2.8d represents a plot of comparison between traces extracted at 250 m offset from the source. The effect of attenuation is clearly reflected in terms of amplitude and phases (a shift in time) between the traces.

Table 2.1: Number of Laplace calculations using second-order finite-difference ($\mathrm{FD_L}$) and REM ($\mathrm{REM_L}$), with maximum time of propagation, $t_{max} = 1.5$ s

α	Freq. (Hz)	Δx (m)	Δt (s)	$\mathrm{FD_L}$	$\mathrm{REM_L}$
0.4	15.0	25.0	0.00217391	690	613
0.2	15.0	25.0	0.00434783	1380	613
0.4	45.0	15.0	0.00130435	1150	1022
0.2	45.0	15.0	0.00260870	2300	1022

A comparison between the number of the Laplacian calculation required for REM and the finite-difference scheme, is shown in Table 2.1. Table 2.1 proves the fact that for all cases of α and frequency, the REM is more efficient than the second-order finite-difference scheme.

A representative spectrogram (time-frequency) analysis of shot gathers, computed in the lossy (Figure 2.9a) and the lossless media (Figure 2.9b), is shown in Figure 2.9. The spectrogram essentially calculate the short-time Fourier transform of the trace resulting into the amplitude at time-localized frequency. The basic reason behind these computation is to represent distribution of the amplitude and phase (represented in term of time on $y-$ axis) at a fixed time and for an entire frequency range ($x-$ axis).

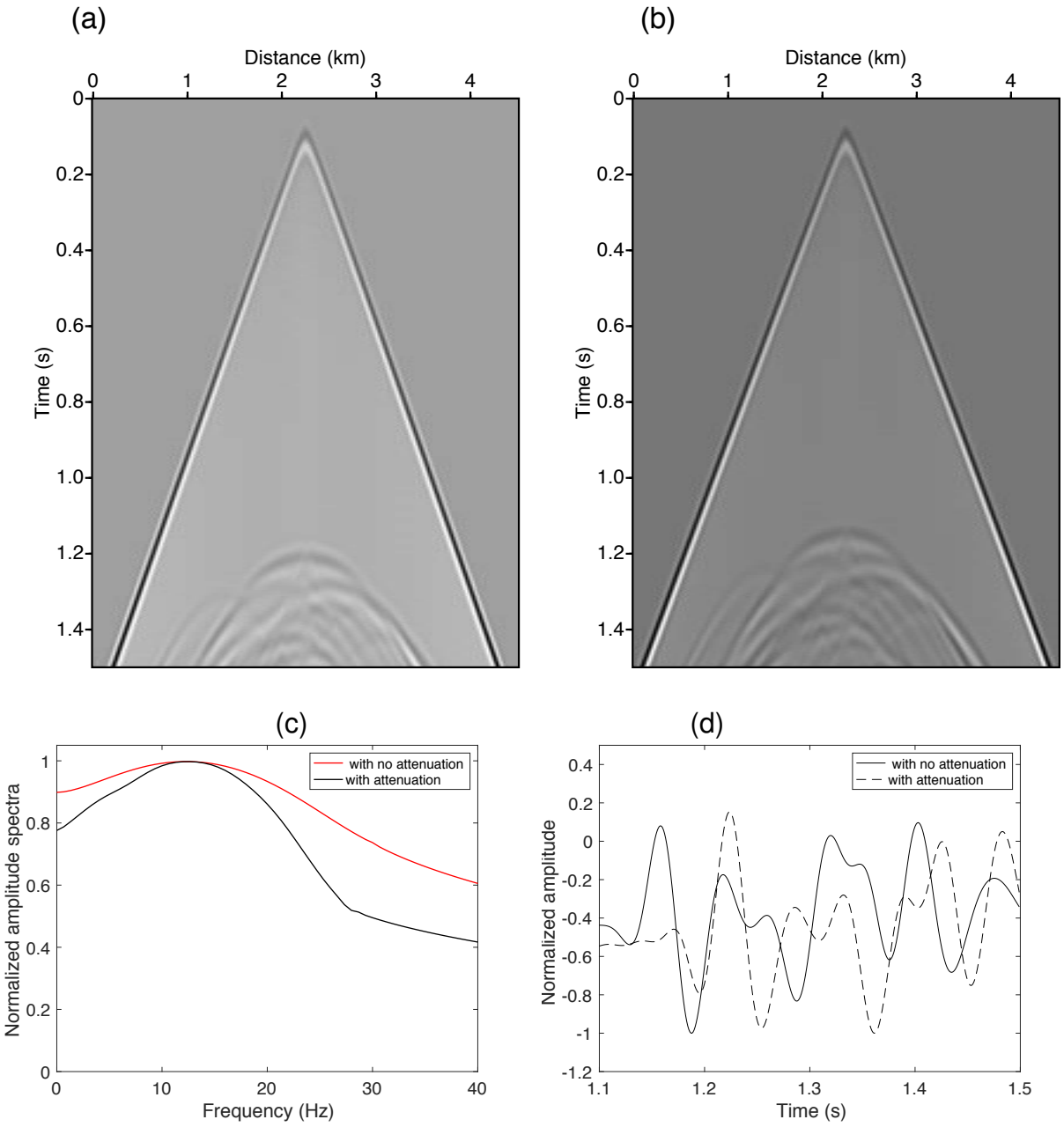

Figure 2.6: Shot gathers extracted from simulations shown in the Figure 7a and 7b. Shot gather in a (a) lossy medium (b) lossless medium and (c) a comparison between normalized amplitude spectra of (a) and (b), and (d) pressure seismograms at 250 m from the source location extracted for lossy and loss-less medium. The wave equation involves a fractional power of the Laplacian for the lossy case.

Figure 2.9a and 2.9b represent the time-frequency analysis for a trace for an offset of 750 m

in the lossy and the lossless media, respectively. It is worth to note that in a lossy media (Figure 2.9a) the onset of dominant power of the signal is delayed (> 0.4 s) in comparison to that in lossless medium (Figure 2.9b), which starts at ≈ 0.4 s. Thus, this time difference also confirms with the phase difference in attenuative media, as reported by [44]. Figure 2.9a also shows that in lossy media, the variation of the amplitude with the frequency and time is notable than in the lossless media (Figure 2.9b).

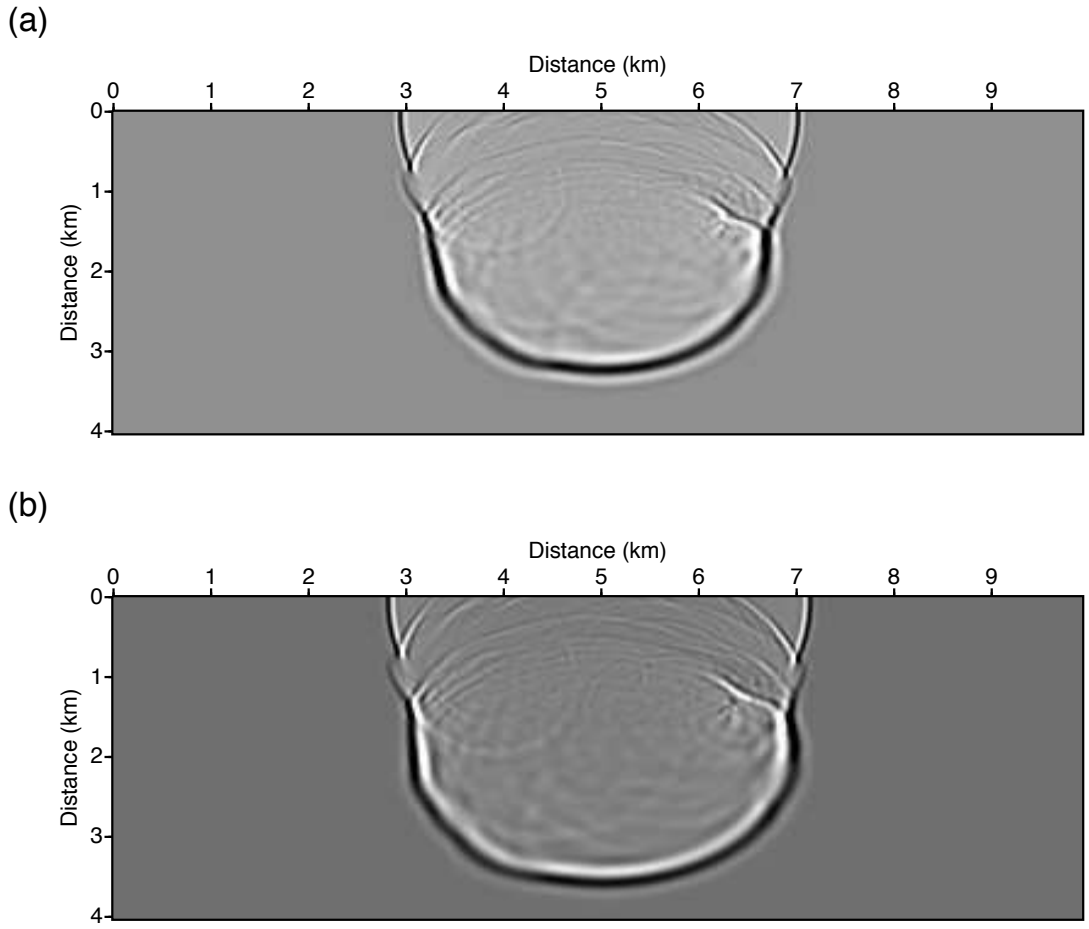

Figure 2.7: Wave field simulation for a reservoir model (a) Snapshot of the wave field at 1.5 s with $Q-$ and (b) wave field snapshot computed at 1.5 s with out $Q-$ (lossless medium).

2.6 Discussion

The implementation of the REM to compute the time derivative operator in equation (2.8), provides freedom in choosing the size of time step Δt (as shown in Figures 2.1-2.9) with an increased accuracy in the numerical solution. The efficiency along with accuracy achieved from the REM will be very useful in various seismic imaging algorithms. In particular, the reverse time migration (RTM) algorithm which requires two-way solutions of the wave equation.

In another in-line study, [64] computed the numerical solution for viscoacoustic equation, described by the fractional space derivatives with constant$-Q$, using a low rank approximation method [65]. The method of the low rank approximation does not impose any constraint on the size of Δt. [64] uses the constitutive equation of [66], which is based on approximation of freezing-unfreezing theory of heterogeneous medium [67]. [66] approximated the wave equation in the constant$-Q$ medium using four Laplacians and two of them with the fractional order. Numerical solution of such equations will require four 2D FFT operations at each time step. However, in present study we just require two (one forward and one inverse) 2D-FFT operation at each time step. Thus a comparison between the efficiency of numerical scheme presented in this paper with the study carried out by [64] will not be appropriate.

To show the efficiency of the algorithm, we have analyzed the numerical scheme using the approach of basic algorithmic-complexity [68]. To compute the spatial operator in 3D, we require six runs of the FFT algorithm (three forward and three inverse). The computational complexity of one run of the FFT algorithm is $\mathcal{O}(n \log n)$, with n being the total number of nodes, used to discretized the domain in x, y and z directions. Thus the time complexity (2D or 3D), for computation of spatial derivatives is $\mathcal{O}(n \log n)$. Any algorithm with the complexity of $\mathcal{O}(n \log n)$ suggests that the run time grows slowly as n increases in comparison to algorithms with exponential and quadratic complexity. The time complexity for computing the time derivative is dominated by evaluation of the modified Chebyshev polynomials in equation (2.13). Since, we have used the recursive approach to compute the modified Chebyshev polynomials, the time complexity for the computation of the time derivative would be $\mathcal{O}(M)$. Thus, at each time step, the total computational complexity would be $\mathcal{O}(M) + \mathcal{O}(n \log n)$.

Figure 2.10 shows a comparison between the theoretical run time, described by $\mathcal{O}(M) + \mathcal{O}(n \log n)$ and actual run time, computed for a 2D case. The run times are plotted against number of grid points in one direction. The run times are computed on a single node machine, comprising MacBookPro 2018 laptop with 8 cores and 2.3 GHz clock frequency.

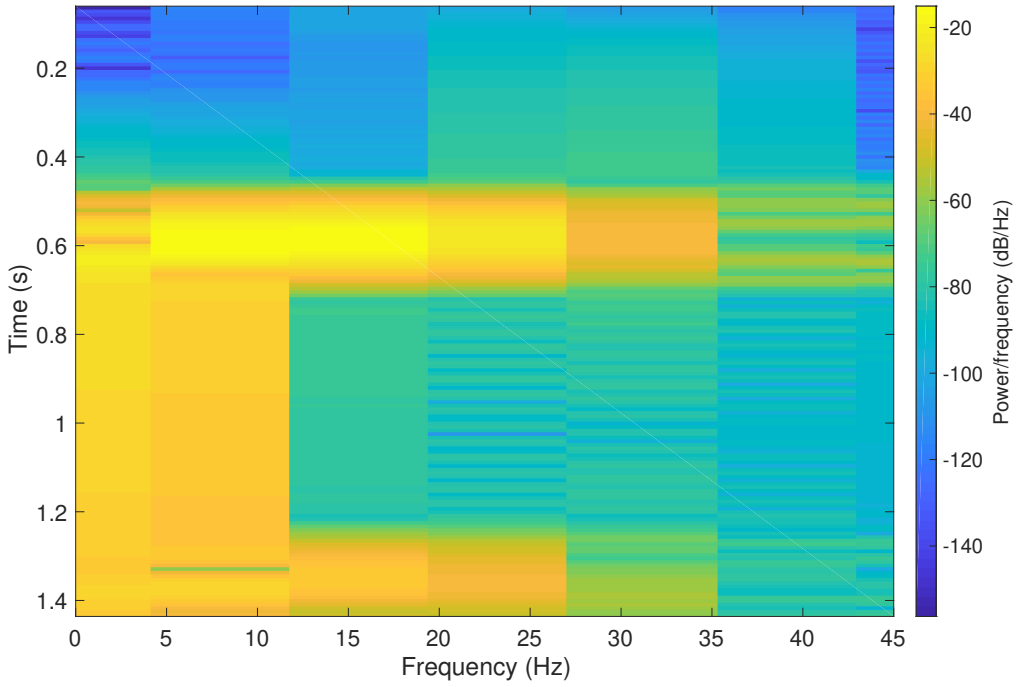

(a)

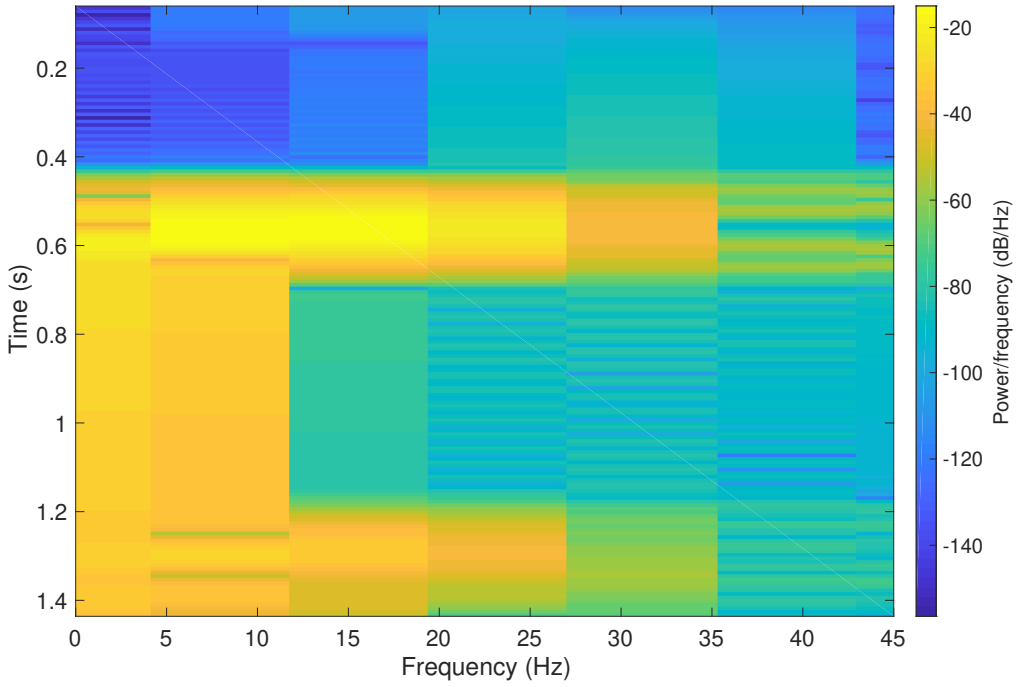

(b)

Figure 2.8: Spectrogram or time-frequency plot of shot gather in (a) lossy medium, (Figure 8a) (b) lossless medium (Figure 8b). Spectrogram is computed for a trace at an offset of 750 m.

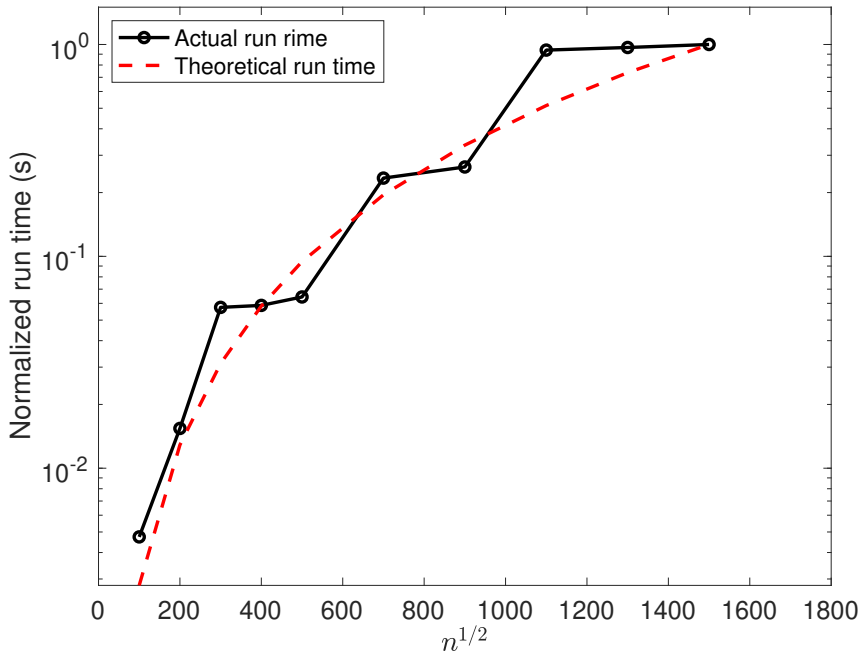

Figure 2.9: A comparison between the theoretical and actual run time of the code written in the current work.

The comparison clearly shows a very good agreement between the theoretical and actual runtime, considering the fact that the code is not optimized, substantially.

As confirmed by Figure 2.10, it is concluded that the efficiency of the presented numerical scheme will be primarily dominated by the scalability of the FFT algorithm on a multinode architecture with a distributed memory hierarchy. The FFT has been already proven to be a strong scale algorithm [69], which guarantees strong scalability of the presented numerical scheme on a multinode machine.

Chapter III

A nodal discontinuous Galerkin finite element method for the poroelastic wave equation

3.1 Abstract

We use the nodal discontinuous Galerkin me-thod with a Lax-Friedrich flux to model the wave propagation in transversely isotropic and poroelastic media. The effect of dissipation due to global fluid flow causes a stiff relaxation term, which is incorporated in the numerical scheme through an operator splitting approach. The well-posedness of the poroelastic system is proved by adopting an approach based on characteristic variables. An error analysis for a plane wave propagating in poroelastic media shows a convergence rate of $O(h^{n+1})$. Computational experiments are shown for various combinations of homogeneous and heterogeneous poroelastic media.

Keywords— Waves, poroelasticity, Lax-Friedrich, attenuation, numerical flux

3.2 Introduction

The dynamics of fluid-saturated porous media is modeled by the poroelasticity theory, pioneered by Maurice Biot and presented in a series of seminal work during the 1930s to 1960s [32]. Porous media acoustics, modeling the propagation of waves in a porous media saturated with a fluid, is an important field of research in various science and engineering disciplines e.g., geophysics, soil mechanics, medical science and civil engineering [70, 71]. In particular, in the exploration of oil and gas reservoirs, the quantitative estimation of porosity and permeability of rocks is very important to understand the direction of the fluid flow. In general, seismic modeling is performed by approximating the medium as a single phase (solid or fluid). These approximations are described by the acoustic [33, 34] and elastic [72, 73] rheologies and do not account for the loss of energy

resulting from the fluid flow. To describe the wave propagation in the porous media, filled with a single phase fluid with an ability to flow through pore networks, Biot proposed the theory of poroelasticity [8, 9, 10].

Poroelasticity is a homogenized model of a porous medium, using linear elasticity (Hooke's law) to describe the solid (or skeleton) portion of the medium, linear compressible fluid dynamics to represent the fluid portion, and Darcy's law to model the flow through the pores. Thus, the poroelastic wave equation combines the constitutive relations with the equations of conservation of the momentum and Darcy's law. The global fluid flow results into the dissipation of energy due to the relative motion between the solid and fluid particles. Dissipation is incorporated in the equations of motion through a frequency dependent viscodynamic operator ($\psi(t)$). The behavior of the viscodynamic operator depends on the relaxation frequency (ω_c) [32] of the material. For frequencies lower than the relaxation frequency, $\psi(t)$ is independent of the frequency and compactly supported. In the high frequency range ($\geq \omega_c$) , $\psi(t)$ becomes frequency dependent and incorporated in the equation of motion through convolution [3]. Our current work focuses on the poroleasticity in the low-frequency range ($< \omega_c$). This problem has already been solved by Carcione [3] using the pseudo-spectral method.

Unlike the acoustic and elastic approximations, wave propagation in a porous medium is a complex phenomenon. In poroelastic materials, three different types of waves appear: 1) A P wave, similar to an elastic P wave, with in-phase relative motion between the solid and the fluid; (2) A shear wave, similar to elastic S waves, and (3) A slow P wave or Biot's mode with out-of-phase relative motion between the solid and the fluid. Dissipation of energy in the poroelastic system, caused by the relative motion between solid and fluid, causes very low attenuation (and velocity dispersion) in the low-frequency range for P and S waves whereas a very strong effect is seen in the slow P wave [3, 32, 2]. Thus, propagation of the slow P wave can be seen as a diffusion, which attenuates very rapidly. The slow P wave propagates at different time scales than those the of P and S waves, resulting in a stiff system of equations [2].

A wide variety of numerical methods have been used to solve the system of poroelastic wave equations. A detailed review is presented by Carcione et al. [17]. Most of the methods presented in this paper regard pseudospectral [2, 3], staggered pseudospectral [74] and finite-difference methods [18, 21] and are based on structured meshes. Santos and Oreña [23] used the finite-element method to solve the poroelastic wave equation using quadrilateral meshes for spatial discretization. Recent work on the numerical solution of orthotropic poroelasticity is reported by Lemoine et al [27], using a finite-volume method on structured meshes. In our work, we develop a high-order discontinuous

Galerkin (DG) method, which is well-suited for simulation of time-domain wave propagation, due to their low dispersion and the ability to accommodate unstructured meshes [75], unlike the finite-difference method.

The time-domain wave propagation, described by a hyperbolic system of partial differential equations, can be solved with an explicit time integration scheme if a stability condition is used on the time step length. In general, the finite element method, coupled with explicit time integrator, requires the inversion of a global mass matrix. Spectral element methods avoids the inversion of the global mass matrix for hexahedral elements by choosing the nodal basis function, resulting in a diagonal mass matrix [76]. Inversion of the global mass matrix is avoided in the high order DG method which produces locally invertible matrices. High order DG methods are often used for seismic simulation (elastic approximation) through the use of simplicial meshes [77, 78, 79].

An inherent challenge in solving the poroelastic system is the treatment of the viscosity-dependent dissipation term. The poroelastic system of equations has the form $\dot{\boldsymbol{q}} = \boldsymbol{M}\boldsymbol{q}$, where $\boldsymbol{q}$ is the wave field vector and $\boldsymbol{M}$ is a propagation matrix. Since the system is dissipative, the eigenvalues of $\boldsymbol{M}$ will have a negative real part. The fastest wave in the system will have a small real part whereas the slowest mode (quasi-static) will have a large real part, making the differential equation stiff. The stiffness is more apparent in the low-frequency regime, whereas in the high frequency regime, separation between the time-scales of the dissipation term and the wave motion is small. The stiffness can be handled in the the poroelastic system by using an implicit scheme for time integration but this will not be a computationally efficient approach. Nevertheless, the viscous term, responsible for the quasi-static mode, is easy to solve analytically, which makes operator splitting a natural choice to handle the stiffness. Carcione and Quiroga-Goode [2] solved the poroacoustic system with operator splitting paired with the pseudo-spectral method. The operator splitting approach in a DG method is also explored by de la Puente et al. [4] but to maintain the fast rate of convergence they solved the system of low-frequency poroelastic wave equations (in stress-velocity form) in the diffusive limit by adopting a local space-time DG method [80]. The space-time DG method employs an expensive local implicit time-integration scheme, based on the high-order derivatives (ADER) of the polynomial approximation functions. de la Puente et al. [4] also used a weak form of the numerical scheme in modal form, which requires smoothness on the test functions, generally suited for the non-linear conservation laws. However, the weak and strong, used in this work, formulations are mathematically equivalent but computationally very different.

In the same line of work, Dupuy et al. [29] solved the porolelastic wave equations in frequency domain using the discontinuous Galerkin method. The system of equation is solved for displacement

field variables, expressed by a set of second order partial differential equations. Unlike the poroelastic model used in here, Dupuy et al. [29] used a frequency dependent permeability to deal with the entire frequency range in the numerical simulations. The rock physics model used by Dupuy et al. [29] closely follows the work of Pride [81]. Discontinuous Galerkin method used in [29] employs a central numerical flux. The central numerical flux is non-dissipative but makes the scheme unstable in heterogenous media. The stability and convergence of the numerical scheme is not discussed by Dupuy et al. [29]. The frequency-domain implementation circumvents the problem of stiffness implicitly but at the cost of solving the system at each frequency.

In another study, [82] solved the system of poroelastic wave equations, expressed in the strain-velocity formulation, using the upwind flux in an isotropic acoustic-poroelastic combination. In DG methods, the flux is applied at the shared edges of elements to recover the global solution. The application of upwind flux causes less dissipation but is more computer intensive as it requires an eigenvalue decomposition of Jacobian matrices. The eigenvalues and eigenvectors of the Jacobian, corresponding to a generic poroelastic medium is not trivial and poses a computational challenge. Furthermore, the upwind flux for an anisotropic medium requires the rotation of eigenvectors along normals of each edges of elements, although this can be avoided by using the Lax-Friedrich flux. To justify the choice of the Lax-Friedrich flux, we use the claim of Cockburn and Shu [83], which states that the *particular choice of the flux does not play an important role for high order simulations.* Furthermore, this claim is also substantiated for the poroelastic system. (discussed in subsection 5.5).

In this work, we have used a Lax-Friedrich flux [6] which requires knowledge of the maximum speed present in the system to stabilize the numerical scheme. We used a plane-wave approach to compute the maximum speed. Unlike an upwind flux, Lax-Friedrich flux is very generic and can be extended from an isotropic to an anisotropic medium. We have used the 4^{th}-order accurate low storage explicit Runge-Kutta scheme for time integration of the non-dissipative (i.e non-stiff part) part of the system. The novelties of our approach are i) We use a coupled first-order low-frequency poroelastic wave equation in conservation form for a transversely anisotropic media. ii) We prove well-posedness of the poroelastic system. In the usual sense, well-posedness of the system admits a unique solution of the system bounded in L^2 of the boundary or forcing data. iii) We derive a self-consistent DG strong formulation with a Lax-Friedrich flux. iv) We verify the method by comparing the analytical and numerical solutions. v) We perform various computational experiments to study the slow P wave in isotropic and anisotropic media.

3.3 System of equations describing poroelastic wave equation in transversely isotropic medium

In this section, we discuss Biot's equations of poroelasticity but readers are advised to refer to Biot's original papers [8, 9, 10] and [32] for further detail.

3.3.1 Stress-strain relations

The constitutive equations for an inhomogeneous and transversely isotropic poroelastic media is expressed as [3, 84]

$$\partial_t \tau_{xx} = c^u_{11}\partial_x v_x + c^u_{13}\partial_z v_z + \alpha_1 M(\partial_x q_x + \partial_z q_z) + \partial_t s_{11}, \tag{3.1}$$

$$\partial_t \tau_{zz} = c^u_{13}\partial_x v_x + c^u_{33}\partial_z v_z + \alpha_3 M(\partial_x q_x + \partial_z q_z) + \partial_t s_{33}, \tag{3.2}$$

$$\partial_t \tau_{xz} = c^u_{55}\left(\partial_z v_x + \partial_x v_z\right) + \partial_t s_{55}, \tag{3.3}$$

$$\partial_t p = -\alpha_1 M\partial_x v_x - \alpha_3 M\partial_z v_z - M(\partial_x q_x + \partial_z q_z) + \partial_t s_f, \tag{3.4}$$

where $\tau_{xx},\ \tau_{zz}$ and τ_{xz} are the total stresses, p is fluid pressure, the $v's$ and $q's$ are the solid and fluid (relative to solid) particle velocities, respectively, $c^u_{ij},\ i,j = 1,...,6$ are the undrained components of the elastic stiffness tensor, M is an elastic modulus and $\alpha_k,\ k = 1,3$ are Biot's effective coefficients. s_{ij} and s_f are the solid and fluid forcing functions, respectively. The conventions are that ∂_t, ∂_x and ∂_z denote time derivative and spatial derivative operator in x and z directions, respectively. The basic underlying assumption in estimating the coefficients is that anisotropy of the porous solid frame is caused by the directional arrangement of the grains. The undrained coefficients c^u_{ij} are expressed in terms of drained coefficients, c_{ij}, as

$$c^u_{11} = c_{11} + \alpha_1^2 M, \tag{3.5}$$

$$c^u_{33} = c_{33} + \alpha_3^2 M, \tag{3.6}$$

$$c^u_{13} = c_{13} + \alpha_1\alpha_3 M, \tag{3.7}$$

$$c^u_{55} = c_{55}. \tag{3.8}$$

Effective coefficients α and modulus M are given by [32]

$$\alpha_1 = 1 - \frac{c_{11} + c_{12} + c_{13}}{3K_s}, \tag{3.9}$$

$$\alpha_3 = 1 - \frac{2c_{13} + c_{33}}{3K_s}, \tag{3.10}$$

$$M = \frac{K_s^2}{D - (2c_{11} + c_{33} + 2c_{12} + 4c_{13})}, \tag{3.11}$$

where K_s is the bulk modulus of the grains and

$$D = Ks(1 - \phi + \phi K_s K_f^{-1}), \tag{3.12}$$

with K_f being the fluid bulk modulus and ϕ the porosity.

3.3.2 Dynamical equations and Darcy's law

The dynamic equations describing the wave propagation in a transversely isotropic heterogeneous porous medium, are given by [10, 32]

$$\partial_x \tau_{xx} + \partial_z \tau_{xz} = \rho \partial_t v_x + \rho_f \partial_t q_x, \tag{3.13}$$

$$\partial_x \tau_{xz} + \partial_z \tau_{zz} = \rho \partial_t v_z + \rho_f \partial_t q_z, \tag{3.14}$$

where $\rho = (1 - \phi)\rho_s + \phi\rho_f$ is the bulk density, and ρ_s and ρ_f are the solid and fluid density, respectively.

The generalized dynamic Darcy's law, governing the fluid flow in an anisotropic porous media, is expressed as [3]

$$-\partial_x p = \rho_f \partial_t v_x + \psi_1 * \partial_t q_x, \tag{3.15}$$

$$-\partial_z p = \rho_f \partial_t v_z + \psi_3 * \partial_t q_z, \tag{3.16}$$

where " $*$ " denotes the time convolution operators and ψ_i, i=1,3 are the time-dependent Biot's viscodynamic operator in the x and z directions. In the low frequency range, i.e., for frequencies lower than $\omega_c = \min\left(\frac{\eta\phi}{\rho_f T_i \kappa_i}\right)$, ψ_i can be expressed as

$$\psi_i(t) = m_i \delta(t) + (\eta/\kappa_i)\, H(t), \tag{3.17}$$

where $m_i = T_i \rho_f / \phi$, with T_i being the tortuosity, η the fluid viscosity, and κ_1 and κ_3 the principal components of the global permeability tensor, while $\delta(t)$ is Dirac's function and $H(t)$ the Heaviside

step function. Substituting (3.17) in (3.15) and (3.16), we get

$$-\partial_x p = \rho_f \partial_t v_x + m_1 \partial_t q_x + \frac{\eta}{\kappa_1} q_x, \tag{3.18}$$

$$-\partial_z p = \rho_f \partial_t v_z + m_3 \partial_t q_z + \frac{\eta}{\kappa_1} q_z. \tag{3.19}$$

Equations (3.13), (3.14),(3.18) and (3.19) yield

$$\partial_t v_x = \beta_{11}^{(1)} \left(\partial_x \tau_{xx} + \partial_z \tau_{xz}\right) - \beta_{12}^{(1)} \left(\partial_x p + \frac{\eta}{\kappa_1} q_x\right), \tag{3.20}$$

$$\partial_t v_z = \beta_{11}^{(3)} \left(\partial_x \tau_{xz} + \partial_z \tau_{zz}\right) - \beta_{12}^{(3)} \left(\partial_z p + \frac{\eta}{\kappa_3} q_z\right), \tag{3.21}$$

$$\partial_t q_x = \beta_{21}^{(1)} \left(\partial_x \tau_{xx} + \partial_z \tau_{xz}\right) - \beta_{22}^{(1)} \left(\partial_x p + \frac{\eta}{\kappa_1} q_x\right), \tag{3.22}$$

$$\partial_t q_z = \beta_{21}^{(3)} \left(\partial_x \tau_{xz} + \partial_z \tau_{zz}\right) - \beta_{22}^{(3)} \left(\partial_z p + \frac{\eta}{\kappa_3} q_z\right), \tag{3.23}$$

where

$$\begin{bmatrix} \beta_{11}^{(k)} & \beta_{12}^{(k)} \\ \beta_{21}^{(k)} & \beta_{22}^{(k)} \end{bmatrix} = (\rho_f^2 - \rho m_k)^{-1} \begin{bmatrix} -m_k & \rho_f \\ \rho_f & -\rho \end{bmatrix}. \tag{3.24}$$

3.3.3 Equations in a system form

To simplify the notation, we introduce a system form of the equations by combining equations (3.1)-(3.4) and (3.20)-(3.23). The conservation form of the system of poroelastic wave equations is

$$\partial_t \boldsymbol{q} + \nabla \cdot (\boldsymbol{A}\boldsymbol{q}) = \boldsymbol{D}\boldsymbol{q} + \boldsymbol{f}, \tag{3.25}$$

where $\boldsymbol{q} = [p\ \tau_{xx}\ \tau_{zz}\ \tau_{xz}\ v_x\ v_z\ q_x\ q_z]^T$, $\boldsymbol{A} = [\boldsymbol{A_1}\ \boldsymbol{A_2}\ \boldsymbol{A_3}]$ with

$$\boldsymbol{A_1} = \begin{bmatrix} 0 & 0 & 0 & 0 & \alpha_1 M & 0 & M & 0 \\ 0 & 0 & 0 & 0 & -c_{11}^u & 0 & -\alpha_1 M & 0 \\ 0 & 0 & 0 & 0 & -c_{13}^u & 0 & -\alpha_3 M & 0 \\ 0 & 0 & 0 & 0 & 0 & c_{55}^u & 0 & 0 \\ \beta_{12}^{(1)} & -\beta_{11}^{(1)} & 0 & 0 & 0 & 0 & 0 & 0 \\ 0 & 0 & 0 & -\beta_{11}^{(3)} & 0 & 0 & 0 & 0 \\ \beta_{22}^{(1)} & -\beta_{21}^{(1)} & 0 & 0 & 0 & 0 & 0 & 0 \\ 0 & 0 & 0 & -\beta_{21}^{(3)} & 0 & 0 & 0 & 0 \end{bmatrix}, \tag{3.26}$$

$$\boldsymbol{A_2} = \begin{bmatrix} 0 & 0 & 0 & 0 & 0 & \alpha_3 M & 0 & M \\ 0 & 0 & 0 & 0 & 0 & -c_{13}^u & 0 & -\alpha_1 M \\ 0 & 0 & 0 & 0 & 0 & -c_{33}^u & 0 & -\alpha_3 M \\ 0 & 0 & 0 & 0 & -c_{55}^u & 0 & 0 & 0 \\ 0 & 0 & 0 & -\beta_{11}^{(1)} & 0 & 0 & 0 & 0 \\ \beta_{12}^{(3)} & 0 & -\beta_{11}^{(3)} & 0 & 0 & 0 & 0 & 0 \\ 0 & 0 & 0 & -\beta_{21}^{(1)} & 0 & 0 & 0 & 0 \\ \beta_{22}^{3} & 0 & -\beta_{21}^{(3)} & 0 & 0 & 0 & 0 & 0 \end{bmatrix}, \tag{3.27}$$

$$\boldsymbol{D} = \begin{bmatrix} 0 & 0 & 0 & 0 & 0 & 0 & 0 & 0 \\ 0 & 0 & 0 & 0 & 0 & 0 & 0 & 0 \\ 0 & 0 & 0 & 0 & 0 & 0 & 0 & 0 \\ 0 & 0 & 0 & 0 & 0 & 0 & 0 & 0 \\ 0 & 0 & 0 & 0 & 0 & 0 & \dfrac{-\beta_{12}^{(1)}\eta}{\kappa_1} & 0 \\ 0 & 0 & 0 & 0 & 0 & 0 & 0 & \dfrac{-\beta_{12}^{(3)}\eta}{\kappa_3} \\ 0 & 0 & 0 & 0 & 0 & 0 & \dfrac{-\beta_{22}^{(1)}\eta}{\kappa_1} & 0 \\ 0 & 0 & 0 & 0 & 0 & 0 & 0 & \dfrac{-\beta_{22}^{(3)}\eta}{\kappa_3} \end{bmatrix}, \tag{3.28}$$

and $\boldsymbol{f} = [\partial_t s_{11}\ \partial_t s_{33}\ \partial_t s_{55}\ \partial_t s_f]^T$ is a forcing function. In this work, the forcing function is assumed to be the product of a compactly supported function in space (specifically Dirac delta function) and

Ricker wavelet in the time domain.

3.4 Well-posedness of the poroelastic system of equations

In the velocity-stress formulation, the governing equations describing the wave propagation in a region Ω enclosed by its boundary $\partial\Omega$ and filled with heterogeneous transversely isotropic porous media, is expressed as

$$\begin{aligned} \boldsymbol{q}_t + \partial_x\left(\boldsymbol{A_1 q}\right) + \partial_z\left(\boldsymbol{A_2 q}\right) &= \boldsymbol{D q} + \boldsymbol{f(t)}, \\ \boldsymbol{x} = (x,z) \in \Omega,\ t > 0, \\ \boldsymbol{q} = \boldsymbol{h(x)}, \quad \boldsymbol{x} \in \Omega,\ t = 0, \\ \mathcal{B}\boldsymbol{q} = \boldsymbol{g}(\boldsymbol{x},t), \quad \boldsymbol{x} \in \partial\Omega,\ t \geq 0. \end{aligned} \tag{3.29}$$

To prove the well-posedness of the system (3.29), first, we seek a symmetrizer for $\boldsymbol{A_1}$ and $\boldsymbol{A_2}$. The strain or potential energy of the poroelastic system is [32],

$$E_s = \frac{1}{2}\boldsymbol{\tau}^T \boldsymbol{C}\boldsymbol{\tau}, \tag{3.30}$$

where $\boldsymbol{\tau} = [\tau_{xx}\ \tau_{zz}\ \tau_{xz}\ p]^T$ and $\boldsymbol{C}$ is a symmetric undrained compliance matrix,

$$\boldsymbol{C} = \begin{bmatrix} C_{11} & C_{12} & 0 & C_{14} \\ C_{12} & C_{22} & 0 & C_{24} \\ 0 & 0 & C_{33} & 0 \\ C_{14} & C_{24} & 0 & C_{44} \end{bmatrix}, \tag{3.31}$$

where $C_{11} = \dfrac{c_{33}}{c_{11}c_{33} - c_{13}^2}$, $C_{12} = -\dfrac{c_{13}}{c_{11}c_{33} - c_{13}^2}$, $C_{14} = \dfrac{\alpha_1 c_{33} - \alpha_3 c_{13}}{c_{11}c_{33} - c_{13}^2}$, $C_{22} = \dfrac{c_{11}}{c_{11}c_{33} - c_{13}^2}$, $C_{24} = \dfrac{\alpha_3 c_{11} - \alpha_1 c_{13}}{c_{11}c_{33} - c_{13}^2}$, $C_{33} = \dfrac{1}{c_{55}}$, and $C_{44} = \dfrac{\alpha_3 c_{11} - \alpha_1 c_{13}}{c_{11}c_{33} - c_{13}^2}$.

The kinetic energy of the poroelastic system can be written as [32]

$$E_v = \frac{1}{2}\left[\rho \boldsymbol{v}^T \boldsymbol{v} + 2\rho_f \boldsymbol{q}^T \boldsymbol{v} + \boldsymbol{q_f}^T \boldsymbol{m} \boldsymbol{q_f}\right], \tag{3.32}$$

where $\boldsymbol{v} = [v_x\ v_z]^T$, $\boldsymbol{q_f} = [q_x\ q_z]^T$ and $\boldsymbol{m} = \begin{pmatrix} m_1 & 0 \\ 0 & m_3 \end{pmatrix}$. To construct a simultaneous symmetrizer ($\mathcal{H}$, a symmetric positive definite operator) for Jacobians $\boldsymbol{A_1}$ and $\boldsymbol{A_2}$, a block-diagonal matrix with non-zero elements, being the Hessian of (3.30) and (3.32), is expressed as

$$\mathcal{H} = \begin{bmatrix} \boldsymbol{E}_{11} & 0 \\ 0 & \boldsymbol{E}_{22} \end{bmatrix}, \tag{3.33}$$

where $E_{11} = \text{Hessian}(E_s) = \Delta E_s(p\ \tau_{xx}\ \tau_{zz}\ \tau_{xz})$ and $E_{22} = \text{Hessian}(E_v) = \Delta E_s(v_x\ v_z\ q_x\ q_z)$. Hence $\boldsymbol{E}_{11}$.

$$\boldsymbol{E}_{11} = \begin{bmatrix} e_{11} & e_{12} & e_{13} & 0 \\ e_{21} & e_{22} & e_{23} & 0 \\ e_{13} & e_{23} & e_{33} & 0 \\ 0 & 0 & 0 & e_{44} \end{bmatrix}$$

and

$$\boldsymbol{E}_{22} = \begin{bmatrix} \rho & 0 & \rho_f & 0 \\ 0 & \rho & 0 & \rho_f \\ \rho_f & 0 & m_1 & 0 \\ 0 & \rho_f & 0 & m_3 \end{bmatrix},$$

where $e_{11} = \dfrac{\alpha_1^3 c_{33} + \alpha_3^2 c_{11} - 2\alpha_1\alpha_3 c_{13}}{c_{11}c_{33} - c_{13}^2} + \dfrac{1}{M}$, $e_{12} = \dfrac{\alpha_1 c_{33} - \alpha_3 c_{13}}{c_{11}c_{33} - c_{13}^2}$, $e_{13} = \dfrac{\alpha_3 c_{11} - \alpha_1 c_{13}}{c_{11}c_{33} - c_{13}^2}$, $e_{22} = \dfrac{c_{33}}{c_{11}c_{33} - c_{13}^2}$, $e_{23} = -\dfrac{c_{13}}{c_{11}c_{33} - c_{13}^2}$, $e_{33} = -\dfrac{c_{13}}{c_{11}c_{33} - c_{13}^2}$ and $e_{44} = \dfrac{1}{c_{55}}$.

Applying $\mathcal{H}$ to $\boldsymbol{A_1},\ \boldsymbol{A_2}$ and $\boldsymbol{D}$ yields

$$\mathcal{H}\boldsymbol{A_1} = \widetilde{\boldsymbol{A}}_1 = \begin{bmatrix} 0 & 0 & 0 & 0 & 0 & 0 & 1 & 0 \\ 0 & 0 & 0 & 0 & -1 & 0 & 0 & 0 \\ 0 & 0 & 0 & 0 & 0 & 0 & 0 & 0 \\ 0 & 0 & 0 & 0 & 0 & -1 & 0 & 0 \\ 0 & -1 & 0 & 0 & 0 & 0 & 0 & 0 \\ 0 & 0 & 0 & -1 & 0 & 0 & 0 & 0 \\ 1 & 0 & 0 & 0 & 0 & 0 & 0 & 0 \\ 0 & 0 & 0 & 0 & 0 & 0 & 0 & 0 \end{bmatrix}, \tag{3.34}$$

$$\mathcal{H}\boldsymbol{A_2} = \widetilde{\boldsymbol{A}}_2 = \begin{bmatrix} 0 & 0 & 0 & 0 & 0 & 0 & 0 & 1 \\ 0 & 0 & 0 & 0 & 0 & 0 & 0 & 0 \\ 0 & 0 & 0 & 0 & 0 & -1 & 0 & 0 \\ 0 & 0 & 0 & 0 & -1 & 0 & 0 & 0 \\ 0 & 0 & 0 & -1 & 0 & 0 & 0 & 0 \\ 0 & 0 & -1 & 0 & 0 & 0 & 0 & 0 \\ 0 & 0 & 0 & 0 & 0 & 0 & 0 & 0 \\ 1 & 0 & 0 & 0 & 0 & 0 & 0 & 0 \end{bmatrix}, \tag{3.35}$$

$$\mathcal{H}\boldsymbol{D} = \widetilde{\boldsymbol{D}} = \begin{bmatrix} 0 & 0 & 0 & 0 & 0 & 0 & 0 & 0 \\ 0 & 0 & 0 & 0 & 0 & 0 & 0 & 0 \\ 0 & 0 & 0 & 0 & 0 & 0 & 0 & 0 \\ 0 & 0 & 0 & 0 & 0 & 0 & 0 & 0 \\ 0 & 0 & 0 & 0 & 0 & 0 & 0 & 0 \\ 0 & 0 & 0 & 0 & 0 & 0 & 0 & 0 \\ 0 & 0 & 0 & 0 & 0 & 0 & -\frac{\eta}{\kappa_1} & 0 \\ 0 & 0 & 0 & 0 & 0 & 0 & 0 & -\frac{\eta}{\kappa_3} \end{bmatrix}, \tag{3.36}$$

where $\widetilde{\boldsymbol{A}}_1$ and $\widetilde{\boldsymbol{A}}_2$ are symmetric and $\widetilde{\boldsymbol{D}}$ is a negative semi-definite matrix. $\mathcal{H}$ is positive-definite and symmetrizes $\boldsymbol{A}_1$ and $\boldsymbol{A}_2$. Thus well-posedness of (3.29) follows by energy estimate $E(t)$, which

is expressed as

$$E(t) = \frac{1}{2}\boldsymbol{q}^T \mathcal{H} \boldsymbol{q}. \tag{3.37}$$

It suffices to consider (3.29) for $\eta = 0$ and $\boldsymbol{f} = \boldsymbol{0}$. Multiplying (3.29) with $\boldsymbol{q^T}\mathcal{H}$, integrating over Ω and using the divergence theorem, we recover,

$$\frac{dE(t)}{dt} = \oint_{\partial\Omega} \boldsymbol{q^T A(n) q}\; d\boldsymbol{x}, \tag{3.38}$$

where $\oint_{\partial\Omega}$ denotes the line integral over $\partial\Omega$ and

$$\boldsymbol{A(n)} = \sum_{i=1}^{2} n_i \widetilde{\boldsymbol{A}}_i = \begin{bmatrix} 0 & 0 & 0 & 0 & 0 & 0 & n_1 & n_2 \\ 0 & 0 & 0 & 0 & -n_1 & 0 & 0 & 0 \\ 0 & 0 & 0 & 0 & 0 & -n_2 & 0 & 0 \\ 0 & 0 & 0 & 0 & -n_2 & -n_1 & 0 & 0 \\ 0 & -n_1 & 0 & -n_2 & 0 & 0 & 0 & 0 \\ 0 & 0 & -n_2 & -n_1 & 0 & 0 & 0 & 0 \\ n_1 & 0 & 0 & 0 & 0 & 0 & 0 & 0 \\ n_2 & 0 & 0 & 0 & 0 & 0 & 0 & 0 \end{bmatrix}.$$

Since $\boldsymbol{A(n)}$ is symmetric, there exists an unitary matrix $\boldsymbol{S(n)}$ such that $\boldsymbol{A(n)} = \boldsymbol{S(n)^T \Lambda S(n)}$. The expression for $\boldsymbol{S}$ and Λ are given as

$$\boldsymbol{S(n)} = \begin{bmatrix} 0 & 0 & -\frac{1}{n_2} & \frac{1}{n_2} & 0 & 0 & 0 & 0 \\ 0 & -\frac{n_2}{n_1} & 0 & 0 & -\frac{n_1}{\alpha_-} & \frac{n_1}{\alpha_-} & \frac{n_1}{\alpha_+} & -\frac{n_1}{\alpha_+} \\ 0 & -\frac{n_1}{n_2} & 0 & 0 & \frac{n_2}{\alpha_-} & -\frac{n_2}{\alpha_-} & \frac{n_2}{\alpha_+} & -\frac{n_2}{\alpha_+} \\ 0 & 1 & 0 & 0 & -\frac{-n_1+n_2}{\alpha_-} & -\frac{n_1-n_2}{\alpha_-} & \frac{-n_1-n_2}{\alpha_+} & -\frac{n_1+n_2}{\alpha_+} \\ 0 & 0 & 0 & 0 & -1 & -1 & 1 & 1 \\ 0 & 0 & 0 & 0 & 1 & 1 & 1 & 1 \\ -\frac{n_2}{n_1} & 0 & \frac{n_1}{n_2} & \frac{n_1}{n_2} & 0 & 0 & 0 & 0 \\ 1 & 0 & 1 & 1 & 0 & 0 & 0 & 0 \end{bmatrix},$$

where $\boldsymbol{\Lambda} = \mathbf{diag}\begin{bmatrix} \lambda_1 & \lambda_2 & \lambda_3 & \lambda_4 & \lambda_5 & \lambda_6 & \lambda_7 & \lambda_8 \end{bmatrix} =$

$\mathbf{diag}\begin{bmatrix} 0 & 0-1 & 1 & -\alpha_- & \alpha_- & -\alpha_+ & \alpha_+ \end{bmatrix}$ with

$\alpha_\pm = \sqrt{1 \pm n_1 n_2}$.

The characteristic state vector $\boldsymbol{R}$ is expressed as

$$\boldsymbol{R(n)} = \boldsymbol{S^T(n) q} = [R_1, R_2, R_3, R_4, R_5, R_6, R_7, R_8]^T \ . \tag{3.39}$$

Thus we have

$$\boldsymbol{q}^T \boldsymbol{A}(\boldsymbol{n})\boldsymbol{q} = \boldsymbol{R}^T \Lambda(n)\boldsymbol{R}(\boldsymbol{n}) = \sum_{i=1}^{8} (\lambda_i R_i^2). \tag{3.40}$$

Substituting (3.40) in (3.38), we recover

$$\frac{dE(t)}{dt} = \sum_{i=1}^{8} IS_i, \quad IS_i = \oint_{\partial\Omega} (\lambda_i R_i^2)\ d\boldsymbol{x}. \tag{3.41}$$

Equation (3.41) implies that the net rate of change of the energy with respect to time is estimated by summing the surface integrals. Surface integrals for $i = 4, 6, 8$ contribute to the energy of the system from the boundary. Surface integrals for $i = 3, 5, 7$ extract out the energy from the system, if the integral is not zero. Thus $R_4,\ R_6,\ R_8$ are incoming characteristics and $R_3,\ R_5,\ R_7$ are outgoing characteristics. For $\lambda_1 = \lambda_2 = 0$ there is no addition or subtraction of energy to the system thus, characteristic variables $R_1,\ R_2$ are stationary characteristics. Since $\lambda_3, \lambda_5,$ and λ_7 are negative,

$$\frac{dE(t)}{dt} \leq \oint_{\partial\Omega} (R_4^2 + \alpha_- R_6^2 + \alpha_+ R_8^2)\ d\boldsymbol{x}, \tag{3.42}$$

which implies that if a boundary condition is of the form

$$\mathcal{B}\boldsymbol{q} = \begin{bmatrix} \boldsymbol{s}_4^T \\ \boldsymbol{s}_6^T \\ \boldsymbol{s}_8^T \end{bmatrix} \boldsymbol{q} = \boldsymbol{g}(\boldsymbol{x}, t) = \begin{bmatrix} \boldsymbol{g}_1(\boldsymbol{x}, t) \\ \boldsymbol{g}_2(\boldsymbol{x}, t) \\ \boldsymbol{g}_3(\boldsymbol{x}, t) \end{bmatrix} \text{ and } \boldsymbol{x} \in \partial\Omega\ , \tag{3.43}$$

and we have

$$\begin{aligned} \oint_{\partial\Omega} (R_4^2 + \alpha_- R_6^2 + \alpha_+ R_8^2) &\leq \max(1, \alpha_-, \alpha_+) \Bigg(\oint_{\partial\Omega} \boldsymbol{q}^T \boldsymbol{s_4} \boldsymbol{s_4}^T \boldsymbol{q} d\boldsymbol{x} \\ &\quad + \oint_{\partial\Omega} \boldsymbol{q}^T \boldsymbol{s_6} \boldsymbol{s_6}^T \boldsymbol{q} d\boldsymbol{x} + \oint_{\partial\Omega} \boldsymbol{q}^T \boldsymbol{s_8} \boldsymbol{s_8}^T \boldsymbol{q} d\boldsymbol{x} \Bigg) \\ &= \alpha \oint_{\partial\Omega} |\boldsymbol{g}(\boldsymbol{x}, t)|^2\ d\boldsymbol{x} = \alpha G(t), \end{aligned}$$

with $\alpha = \max(1, \alpha_-, \alpha_+)$.

Thus we recover

$$\frac{dE(t)}{dt} \leq G(t).$$

Integrating w.r.t. time yields

$$E(t) \leq \int_0^t G(\chi)d\chi + E(0) \leq E(0) + t \max_{\chi\in[0,t]} G(\chi).$$

Alternatively,

$$\int_\Omega \boldsymbol{q}^{\boldsymbol{T}}(\boldsymbol{x},t)\boldsymbol{H}\boldsymbol{q}(\boldsymbol{x},t)\ d\boldsymbol{x} \leq \int_{\partial\Omega} \boldsymbol{h}^T(\boldsymbol{x})\boldsymbol{H}\boldsymbol{h}(\boldsymbol{x})d\boldsymbol{x} + t\left(\max_{\chi\in[0,t]} G(\chi)\right). \tag{3.44}$$

Equation (3.44) states that the energy of the system is bounded by the initial condition $\boldsymbol{h}(\boldsymbol{x},t)$ and the boundary condition $\boldsymbol{g}(\boldsymbol{x},t)$, prescribed by (3.29).

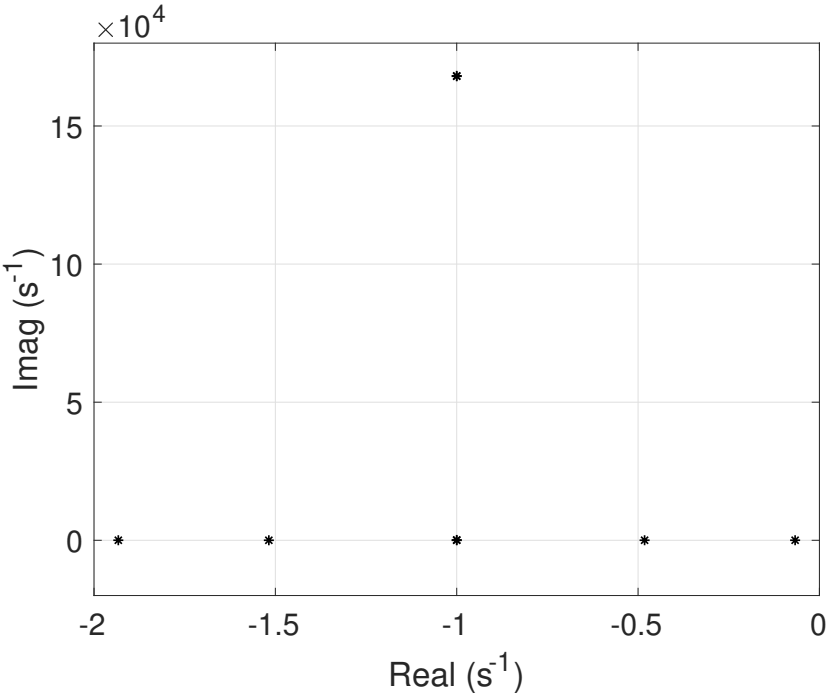

Figure 3.1: Eigenvalues of the propagator matrix $\boldsymbol{M}$ at 22 Hz.

Table 3.1: Material properties for sandstone saturated with brine [2]

Properties	Sandstone (Isotropic)
K_s (GPa)	40
ρ_s (kg/m^3)	2500
ϕ	0.2
κ (10^{-15} m^2)	600
K_f (GPa)	2.5
ρ_f (kg/m^3)	1040
T_1	3
T_3	3
η (10^{-3} Kg/m.s)	1
λ^* (m/s)	3800

* computed in this study.

Thus, the poroelastic system of equation, defined by equation (3.29), is a well-posed problem. This result is summarized in the theorem.

Theorem 1. *Assume there exist a smooth solution to (3.29). If the boundary condition is given of the form*

$$\mathcal{B}\boldsymbol{q} = \begin{bmatrix} \boldsymbol{s}_4^T \\ \boldsymbol{s}_6^T \\ \boldsymbol{s}_8^T \end{bmatrix} \boldsymbol{q} = \boldsymbol{g}(\boldsymbol{x},t) = \begin{bmatrix} \boldsymbol{g}_1(\boldsymbol{x},t) \\ \boldsymbol{g}_2(\boldsymbol{x},t) \\ \boldsymbol{g}_3(\boldsymbol{x},t) \end{bmatrix} \text{ and } \boldsymbol{x} \in \partial\Omega \ ,$$

then the IBVP (3.29) is well-posed and $\boldsymbol{q}$ *satisfies the estimate*

$$\int_\Omega \boldsymbol{q}^{\boldsymbol{T}}(t)\boldsymbol{H}\boldsymbol{q}(t)d\boldsymbol{x} \leq \int \boldsymbol{h}^T(\boldsymbol{x})\boldsymbol{H}\boldsymbol{h}(\boldsymbol{x})d\boldsymbol{x} + t \max_{\chi\in[0,t]} G(\chi),$$

with

$$G(t) = \alpha \oint_{\partial\Omega} |\boldsymbol{g}(\boldsymbol{x},\boldsymbol{t})|^2 d\boldsymbol{x}, \quad \alpha = \max_{\boldsymbol{x}\in\partial\Omega}(1,\alpha_+,\alpha_-). \tag{3.45}$$

3.5 Numerical scheme

In absence of a forcing function, the poroelastic system of equations (3.25) can be expressed as

$$\boldsymbol{q_t} = \boldsymbol{M}\boldsymbol{q}, \tag{3.46}$$

where $\boldsymbol{M}$ is the propagator matrix, containing the material properties and spatial derivative operators. The eigenvalues of $\boldsymbol{M}$ come in conjugate pairs. For an inviscid pore fluid ($\eta = 0$), the eigenvalues of $\boldsymbol{M}$ lie along the imaginary axis, which implies the absence of dissipation from the system. On the other hand, for the viscous pore fluid ($\eta \neq 0$), the eigenvalues of $\boldsymbol{M}$ also contain a negative real part. Furthermore, a substantial difference between the magnitude of the real part of eigenvalues of different wave modes in the system causes it to be stiff. Figure 1 shows the representative eigenvalues of (3.46) computed for an isotropic sandstone with material properties given in Table 1. Stiffness in the system causes instabilities in explicit time integration schemes unless a very small time step is used. Alternatively, an implicit time integration scheme can be an unconditionally stable, but not efficient for a linear hyperbolic system. Carcione and co-workers have used an explicit approach in time operator splitting, also known as Godunov splitting or fractional step [2, 3, 32], which separates the dissipative term from the conservation term at each time step. In our work we solve the stiff (dissipative) part of the system analytically and the non-stiff (conservation) part by using a nodal DG method, paired with a 4^{th}-order low-storage explicit Runge-Kutta scheme (LSERK) [6]. Equation (3.25) is split into stiff and non-stiff part as follows:

Stiff part:

$$\partial_t \boldsymbol{q} = \boldsymbol{D}\boldsymbol{q}. \tag{3.47}$$

Non-stiff part:

$$\partial_t \boldsymbol{q} + \nabla \cdot (\boldsymbol{A}\boldsymbol{q}) = \boldsymbol{f}. \tag{3.48}$$

At each time step, equation (3.47), which is a simple ordinary differential equation, is solved analytically [3] and these intermediate solutions are plugged into (3.48) as an initial solution. The analytical solution of equation (3.47) is given in B.1. The numerical solution of (3.48) is computed

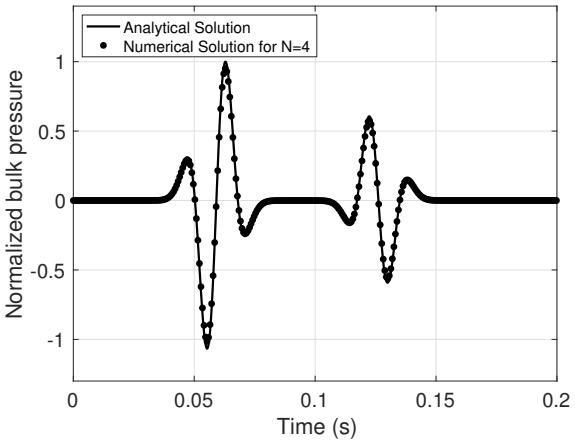

(a) Bulk pressure at $\eta = 0,\ f_c = 22$ Hz

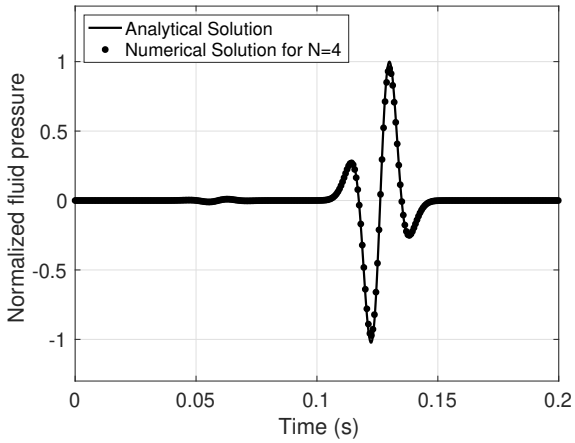

(b) Fluid pressure at $\eta = 0,\ f_c = 22$ Hz

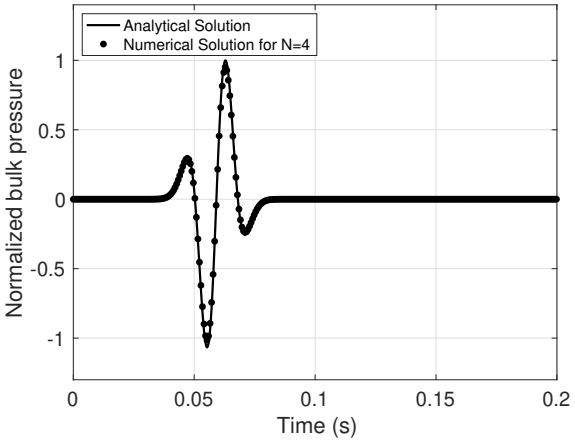

(c) Bulk pressure at $\eta = 0,\ f_c = 22$ Hz

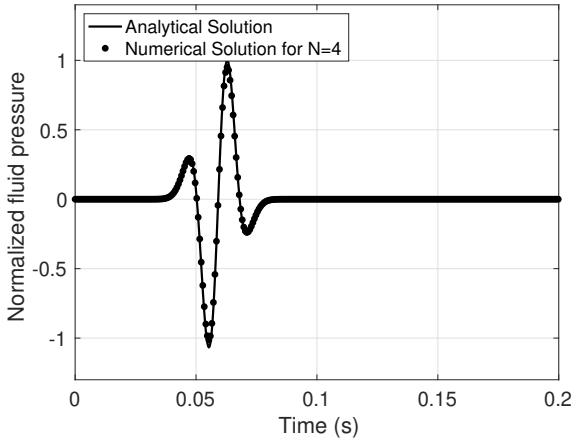

(d) Fluid pressure at $\eta = 0,\ f_c = 22$ Hz

Figure 3.2: A comparison between the analytical and the numerical solutions, computed in a poroacoustic media, at source-receiver offset of 250 m, and $f_c = 22\ Hz$, where (a) normalized bulk pressure ($\eta = 0$), (b) normalized fluid pressure, computed with ($\eta = 0$), (c) normalized bulk pressure ($\eta \neq 0$), and (d) normalized fluid pressure, computed with ($\eta \neq 0$).

using the nodal DG finite-element method, discussed next.

3.5.1 Nodal discontinuous Galerkin scheme for the poroelastic system

We consider that the domain Ω is Lipschitz and triangulated by D^k elements, where each element D^k is the image of a reference element $\hat{D}$ under the local mapping

$$\boldsymbol{x^k} = \Phi\hat{\boldsymbol{x}}, \tag{3.49}$$

Table 3.2: Material properties for several poroelastic media used in the examples [3, 4]

Properties	Sandstone (Orthotropic)	Epoxy-glass (Orthotropic)	Sandstone (Isotropic)	Shale (Isotropic)
K_s (GPa)	80	40	40	7.6
ρ_s (kg/m^3)	2500	1815	2500	2210
c_{11} (GPa)	71.8	39.4	36	11.9
c_{12} (GPa)	3.2	1.2	12	3.96
c_{13} (GPa)	1.2	1.2	12	3.96
c_{33} (GPa)	53.4	13.1	36	11.9
c_{55} (GPa)	26.1	3	12	3.96
ϕ	0.2	0.2	0.2	0.16
κ_1 (10^{-15} m^2)	600	600	600	100
κ_3 (10^{-15} m^2)	100	100	600	100
T_1	2	2	2	2
T_3	3.6	3.6	2	2
K_f (GPa)	2.5	2.5	2.5	2.5
ρ_f (Kg/m^3)	1040	1040	1040	1040
η (10^{-3} Kg/m.s)	1	1	1	1
λ^* (m/s)	6000	5240	4250	2480

* computed in this study.

where $\boldsymbol{x^k}$ and $\hat{\boldsymbol{x}}$ denote the physical and reference coordinates on D^k and $\hat{D}$, respectively. The approximate local solution over each element is expressed as

$$V_h(D^k) = \Phi^k \circ V_h(\hat{D}), \tag{3.50}$$

where $V_h(D^k)$ and $V_h(\hat{D})$ represent the approximation spaces for the physical and the reference element, respectively.

The global solution space $V_h(\Omega_h)$ is defined as the direct sum of the local approximation spaces

$$V_h(\Omega_h) = \bigoplus_{D^k} V_h(D^k). \tag{3.51}$$

In this work, we take $V_h(\hat{D}) = P^N(\hat{D})$, where $P^N(\hat{D})$ is the polynomial space of total degree N on the reference element.

Let f be the face of element D^k with neighboring element $D^{k,+}$ and unit outward normal vector $\boldsymbol{n}$. Let u be a function which is discontinuous across the element interface. The interior value

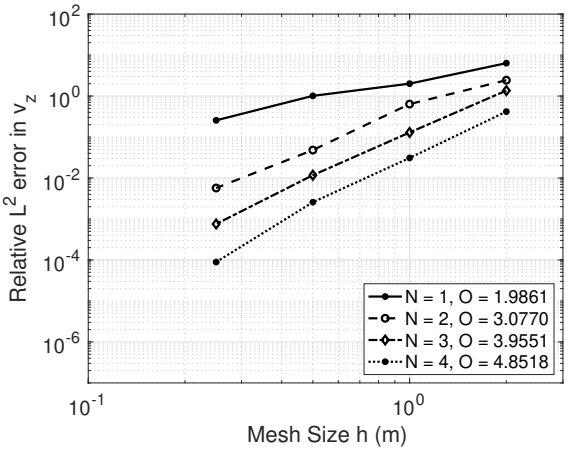

(a) Inviscid case($\eta = 0$)

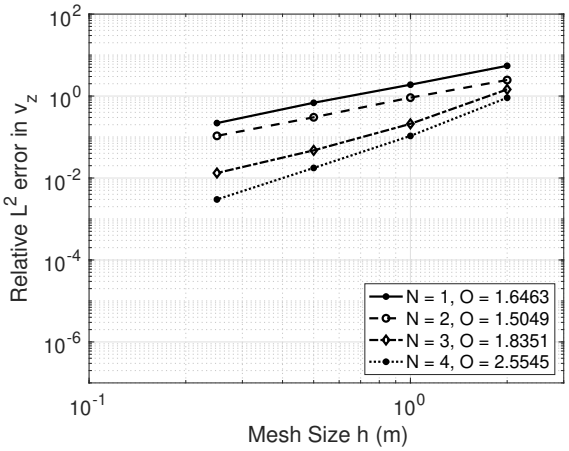

(b) Viscid case($\eta \neq 0$)

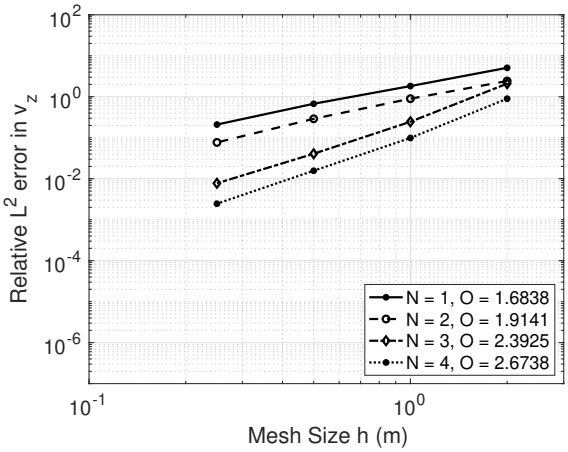

(c) Viscid case($\eta \neq 0$), fine δt

Figure 3.3: L^2 error of the solid particle velocity (v_z) (in a plane wave) as a function of the mesh size h computed at $N = 1,\ 2,\ 3$ and 4 for (a) inviscid case $\eta = 0$, (b) viscid case $\eta \neq 0$, and (c) viscid case $\eta \neq 0$ with very fine Δt.

u^- and exterior value u^+ on a face f of D^k are defined as

$$u^- = u|_{f \bigcap \partial D^k}, \quad u^+ = u|_{f \bigcap \partial D^{k,+}}.$$

Jump and average of a scalar function u over f is defined as

$$[\![u]\!] = u^+ - u^-, \qquad \{\!\{u\}\!\} = \frac{u^+ + u^-}{2}. \tag{3.52}$$

The jump and average of a vector valued functions are computed component wise.

The nodal DG scheme for (3.48) can be constructed by multiplying (3.48) with a basis function $\boldsymbol{p} \in P^N(\hat{D})$ and integrating by parts twice

$$\begin{aligned}\int_{D^k} \Big(\partial_t \boldsymbol{q_h} + \nabla \cdot (\boldsymbol{A q_h})\Big) \cdot \boldsymbol{p}\ d\boldsymbol{x} \\ + \int_{\partial D^k} ((\boldsymbol{A}_n \boldsymbol{q_h})^* - (\boldsymbol{A}_n \boldsymbol{q_h})^-) \cdot \boldsymbol{p}\ d\boldsymbol{x} \\ = \int_{D^k} \boldsymbol{f} \cdot \boldsymbol{p}\ d\boldsymbol{x},\end{aligned} \tag{3.53}$$

where $\boldsymbol{q_h}$ is the discretized solution, ($\boldsymbol{A}_n$ is the normal matrix defined on face f as $\boldsymbol{A}_n = n_1 A_1 + n_2 A_2$ and $(\boldsymbol{A}_n \boldsymbol{q_h})^*$ represents the numerical flux. Equation (3.53) represents the numerical scheme in strong form [6, p. 22] and thus does not require any smoothness on the basis function $\boldsymbol{p}$. To compute the basis function $\boldsymbol{p}$, we have utilized the nodal basis function approach, discussed in the following section.

3.5.2 Nodal basis function

The discretized solution $\boldsymbol{q_h}$ in (3.48) follows a component-wise expansion into $N_p = N_{dof}^{D^k} = N_{dof}^{D^k}(N)$ nodal trial basis function of order N [6],

$$\boldsymbol{q_h}(\boldsymbol{x}, t) = \bigoplus_{D^k} \sum_{n=1}^{N_p} \boldsymbol{q_{h,n}^{D^k}}(t) p_n(\boldsymbol{x}). \tag{3.54}$$

Here $\boldsymbol{q_{h,n}^{D^k}}$ indicates the local expansion of $\boldsymbol{q_h}$ within element D^k, $p_n(\boldsymbol{x})$ is a set of 2-D Lagrange polynomials associated with the nodal points, $\{x_n\}_{n=1}^{N_p}$. The explicit expression for computing the Lagrange polynomials in 2D space is not known, but can be constructed by expressing the approximated solution in modal and nodal form, simultaneously. Expressing the $\boldsymbol{q_{h,n}^{D^k}}$ in modal and nodal form simultaneously, yields

$$\mathcal{V}^T p_n(\boldsymbol{x}) = \boldsymbol{P_n(x)}, \tag{3.55}$$

where $\mathcal{V}$ is the Vandermonde matrix of basis functions, used for approximating the modal form $\boldsymbol{q_{h,n}^{D^k}}$ and $\boldsymbol{P_n(x)}$ is a 2D orthonormalized basis function, constructed from Jacobi polynomials.

We have used the warp and blend method [6] to determine the coordinates of the nodal points in a triangle; for order N interpolation, there are $N_p = \dfrac{(N+1)(N+2)}{2}$ such nodes.

3.5.3 Numerical flux

The numerical flux $(\boldsymbol{A}_n q_h)^*$ in (3.53) determines the unique solution at the shared edges of two elements. In this paper, we use the Lax-Friedrich flux [52] to compute $(\boldsymbol{A}_n q_h)^*$. The Lax-Friedrich flux is expressed as

$$(\boldsymbol{A}_n q_h)^* = \{\{\boldsymbol{A}_n q_h\}\} + \frac{\lambda}{2}[\![q_h]\!], \tag{3.56}$$

where λ is the maximum speed of the waves in the system. Substituting (3.56) into (3.53) and using the identities in (3.52), we recover the local strong form of the semi-discrete DG scheme as

$$\begin{aligned}\int_{D^k} \Big(\partial_t \boldsymbol{q_h} + \nabla \cdot (\boldsymbol{A}_n \boldsymbol{q_h})\Big) \cdot \boldsymbol{p}\ d\boldsymbol{x} \\ + \int_{\partial D^k} \left([\![\boldsymbol{A}_n \boldsymbol{q_h}]\!] + \frac{\lambda}{2}[\![\boldsymbol{q_h}]\!]\right) \cdot \boldsymbol{p}\ d\boldsymbol{x} \\ = \int_{D^k} \boldsymbol{f} \cdot\ \boldsymbol{p}\ d\boldsymbol{x}.\end{aligned} \tag{3.57}$$

The global representation of (3.57) is obtained by summing the local form of the semi-discrete DG scheme over all the elements in Ω_h, expressed as

$$\begin{aligned}\sum_{D^k \in \Omega_h} \left(\int_{D^k} \Big(\partial_t \boldsymbol{q_h} + \nabla \cdot (\boldsymbol{A}_n \boldsymbol{q_h})\Big) \cdot \boldsymbol{p}\ d\boldsymbol{x}\right) \\ + \int_{\partial D^k} \left([\![\boldsymbol{A}_n \boldsymbol{q_h}]\!] + \frac{\lambda}{2}[\![\boldsymbol{q_h}]\!]\right) \cdot \boldsymbol{p}\ d\boldsymbol{x} \\ = \sum_{D^k \in \Omega_h} \left(\int_{D^k} \boldsymbol{f} \cdot\ \boldsymbol{p}\ d\boldsymbol{x})\right).\end{aligned} \tag{3.58}$$

In order to compute λ, the maximum speed of the wave in the system, we have used a plane-wave approach [3]. A detailed formulation for computing λ is given in B.2.

3.5.4 Boundary conditions

The top surface of the domain is modeled as a free surface by assuming that stress components and pore-fluid pressure is zero,

$$p = 0, \quad \sigma_{xx} = 0, \quad \tau_{zz}, \quad \tau_{xz} = 0. \tag{3.59}$$

The free surface boundary conditions are imposed by computing the numerical flux by modifying the jump in stress variables, for example, the modified jump in variable τ_{xx} is expressed as

$$[\![\tau_{xx}]\!] = -2\tau_{xx}^{-}. \tag{3.60}$$

The other boundaries are modeled as absorbing boundaries. The absorbing boundaries are implemented as outflow boundaries by setting the flux (at the boundaries) equal to zero. We note that more accurate absorbing conditions can be also imposed, for example perfectly matched layers [85] but these implementation always come with the added computational cost.

3.5.5 Time discretization

In the present study, we have employed the low-storage explicit Runge-Kutta (LSERK) method [83]. The LSERK method is a single-step method but comprises of five intermediate stages. LSERK is preferred over other methods as it saves memory at the cost of computation time. A stable CFL condition depending on the polynomial degree N is derived by Cockburn and Shu [83] and employed here.

3.5.6 Variational crime

In many applications, the external forcing function $\boldsymbol{f}$ is considered as a point source or Dirac function. A Dirac delta function is not L^2 integrable and the term $\int_{D^k} \boldsymbol{f} \cdot \boldsymbol{p}\, d\boldsymbol{x}$ in (3.57) may not well defined. Thus we commit a variational crime while evaluating the $\boldsymbol{f(x)} = \delta(\boldsymbol{x} - \boldsymbol{x_0})$. A point source approximation is numerically implemented as

$$\sum_{D^k} \int_{D^k} \delta(\boldsymbol{x} - \boldsymbol{x_0}) \cdot \boldsymbol{p} = \int_{\Omega} \boldsymbol{p} \cdot \delta(\boldsymbol{x} - \boldsymbol{x_0}) = \boldsymbol{p(x_0)}.$$

3.6 Computational experiments

In this section, we illustrate the accuracy of our numerical scheme by comparing the analytical solution with the numerical solution and investigate the convergence. To check the accuracy between

the numerical and the analytical solutions, we started our computational experiments with a poroacoustic system [2], which is a simplified poroelastic system, obtained by setting the solid rigidity to zero. Thus poroacoustic simulation only models the dilatational deformation. The properties of a poroacoustic media have been used to to describe the kinematics of emulsions and gels [86]. A system of equations describing the poroacoustic wave equation is given in B.3.

3.6.1 Poroacoustic medium: Comparison of analytical and numerical solutions

The analytical solution of a point source in a 2D homogeneous poroacoustic medium is given by Carcione and Quiroga-Goode [2] and implemented here to evaluate the quality of the solution obtained from our nodal DG scheme. The forcing function $\boldsymbol{f}$ is the product of Dirac's delta in space and Ricker's wavelet in time, which is expressed as

$$f(t) = \exp\left[-\frac{1}{2}f_c^2(t-t_0)^2\right]\cos[\pi f_c(t-t_0)], \tag{3.61}$$

where f_c is the source central frequency of the source and $t_0 = 3/f_c$ is the wavelet delay.

Figure 3.2(a) and 3.2(b) present a comparison between the analytical and the numerical solutions of the bulk and the fluid pressure, computed at 22 Hz for an inviscid case ($\eta = 0$). We have used a polynomial degree $N = 4$. Table 1 shows the material properties of the poroacoustic medium used, an acoustic version of a brine saturated sandstone. Figure 3.2(a) and 3.2(b) show a good agreement between solutions with an L^2 error of 0.04 %. Figure 3.2(c) and 3.2(d) represent a comparison between the solutions of the bulk and the fluid pressure, computed at 22 Hz for a viscid case ($\eta \neq 0$). Figure 3.2(c) and 3.2(d) show a good agreement with an L^2 error of 0.05 %.

3.6.2 Poroelastic medium: Convergence test

An analytical solution for plane waves of the poroelastic system (3.25) is given by [32] and [4]. We implemented the solution computed by de la Puente et al. [4] to test the convergence of the numerical scheme in (3.57). The convergence analysis is performed in both regimes, non-stiff and stiff, with a periodic boundary condition. The convergence is computed for brine-filled (viscid and inviscid) isotropic sandstone. The properties are given in Table 2. The CFL value is 0.4 for the computation. Figure 3.3(a) shows a convergence plot of the L^2 error of v_z in the non-stiff regime. The rate of convergence shows an order of $O(h^{N+1})$. Figure 3.3(b) represents the convergence plot of the L^2 error of v_z in the stiff regime. The convergence reported in Figure 3.3 are the minimum rate of convergence. It is worth to note that the rate of convergence deteriorates due to the fact that

operator splitting is a first-order accurate in time. For $N = 1$, the rate of convergence is ≈ 2, which is expected rate for a nodal DG scheme. For higher orders ($N = 2,\ 3,\ 4$) the convergence rate is dominated by the accuracy of the time integration scheme. We also performed the convergence rate for a very fine time step (Δt), presented in Figure 3.3c, so that the operator splitting approach does not destroy the h convergence rate of the DG operator. Though, the minimum convergence rate improves over those in Figure 3.3b but it makes the computation very slow. The operator splitting approach will not provide a very high-accuracy as the operators associated with the non-stiff system $[\nabla \cdot \boldsymbol{A}]$ and stiff-system ($\boldsymbol{D}$) do not commute. Thus, it is imperative to suggest that the reasonable time step for the computation will be the maximum Δt allowed by the standard nodal DG scheme for the non-stiff case. However, in any case, the convergence rate is better than any low-order scheme.

3.6.3 Homogeneous poroacoustic medium: Wave-field simulation

We use the properties of the poroacoustic medium described in Table 3.1, which represents a brine-saturated sandstone. The Biot's characteristic frequency for this medium is 18 kHz. Thus, the system of equations (3.25) and the numerical scheme (3.57) used in this work is valid for a frequency of the forcing function ($\boldsymbol{f}$) less than 18 kHz. We have performed the simulations for the inviscid ($\eta = 0$) and viscid ($\eta \neq 0$) cases at frequencies varying from the seismic to the sonic range. The forcing function considered here is given in (3.61) and located at the center of the computational domain.

Figure 3.4 shows the numerical results with a forcing function of central frequency ($f_c =$ 22 Hz). The size of the computational domain is 2.5 km $\times$ 2.5 km. The minimum size of the edge of the equilateral triangles, used to mesh the domain, is 20 m. Figure 5(a) and 5(b) represent the snapshots of bulk and fluid pressures, respectively, computed at $t = 0.36$ s and $\eta = 0$ with a bulk forcing function. The bulk forcing function assumes that the energy is partitioned between the solid and fluid phases [2]. Figure 3.4(a) clearly shows both phases of P waves (fast and slow) whereas the fluid pressure in Figure 3.4(b) is dominated by a slow P wave, being the amplitude of the fast P wave very subtle. Since the results in Figure 3.4(a) and 3.4(b) are simulated for the inviscid case, the slow P wave is not attenuated. Figure 3.4(c) and 3.4(d) represents the bulk and fluid pressures at $t = 0.36$ s and $\eta \neq 0$. We remark that the slow P wave in Figure 3.4(c) and 3.4(d) attenuates faster than those in Figure 3.4(a) and 3.4(b). This is in agreement with the physics of Biot's theory, which states that for $\omega \leq \omega_c$, the slow P wave becomes a diffusive mode due to the dominance of viscous forces over the inertial forces.

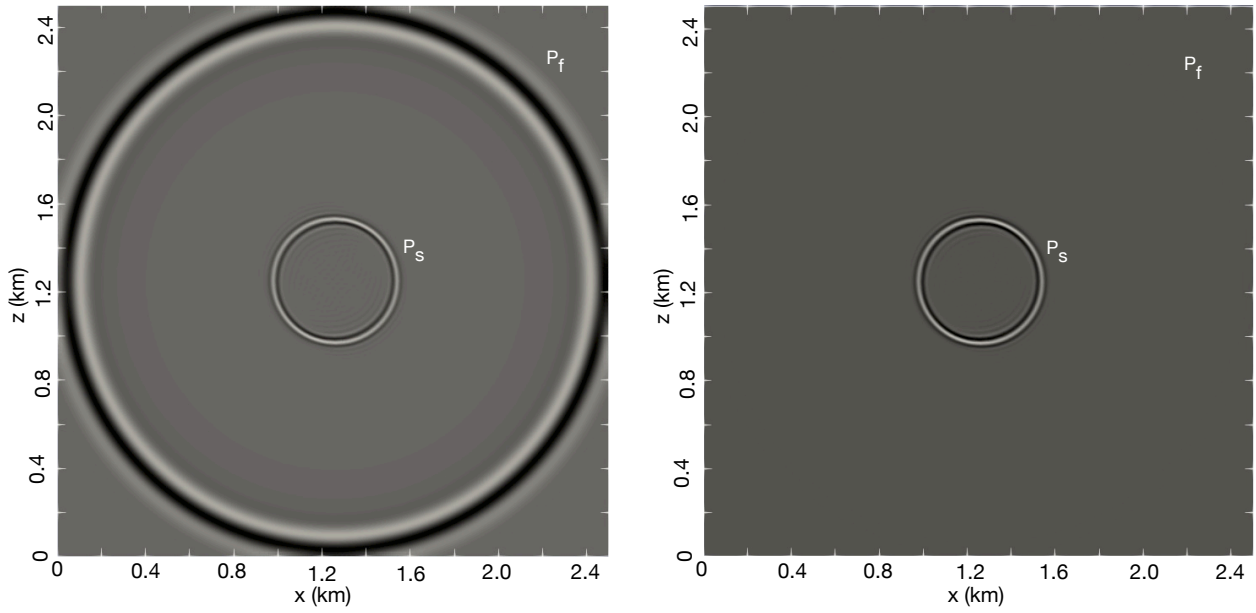

(a) Bulk pressure at $\eta = 0,\ f_c = 22$ Hz

(b) Fluid pressure at $\eta = 0,\ f_c = 22$ Hz

(c) Bulk pressure at $\eta \neq 0,\ f_c = 22$ Hz

(d) Fluid pressure at $\eta \neq 0,\ f_c = 22$ Hz

Figure 3.4: Snapshots of (a) bulk pressure p (b) fluid pressure p_f for the inviscid case ($\eta = 0$), computed at $t = 0.36$ s. Snapshots of (c) bulk pressure p (d) fluid pressure for viscid case ($\eta \neq 0$), computed at $t = 0.36$ s. The forcing function is a bulk source (energy is partitioned between solid and fluid) with a central frequency of 22 Hz. Numerical solution is computed for a polynomial of order 4. $\mathrm{P_f}$: Fast compressional wave, $\mathrm{P_s}$: slow wave (Biot mode).

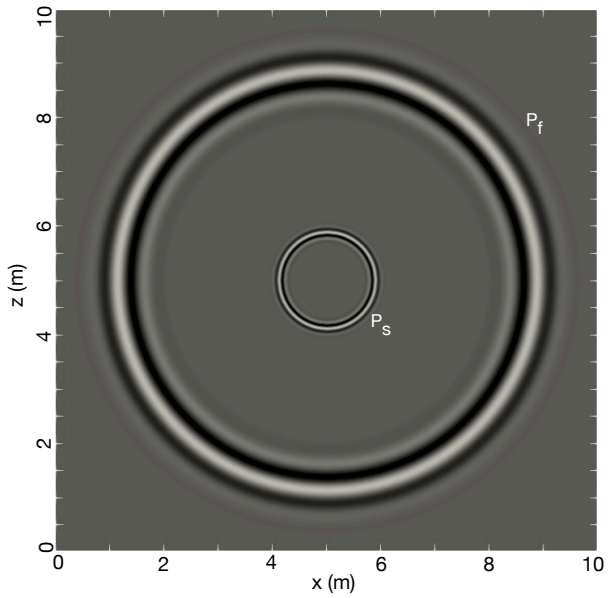

(a) Bulk pressure at $\eta = 0,\ f_c = 4.5$ kHz

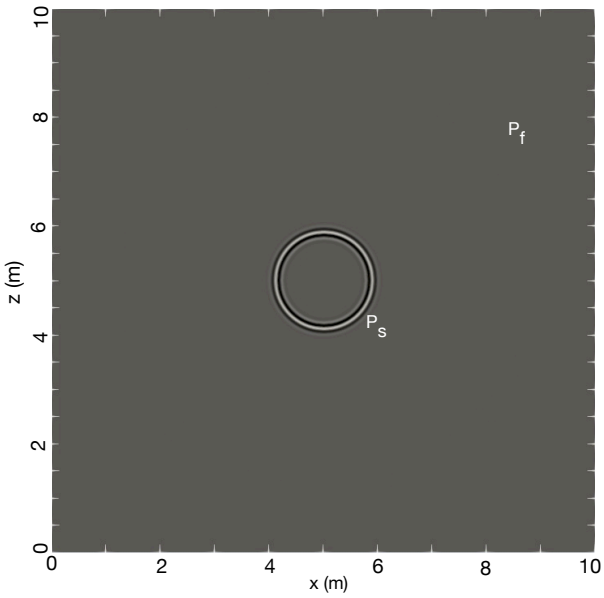

(b) Fluid pressure at $\eta = 0,\ f_c = 4.5$ kHz

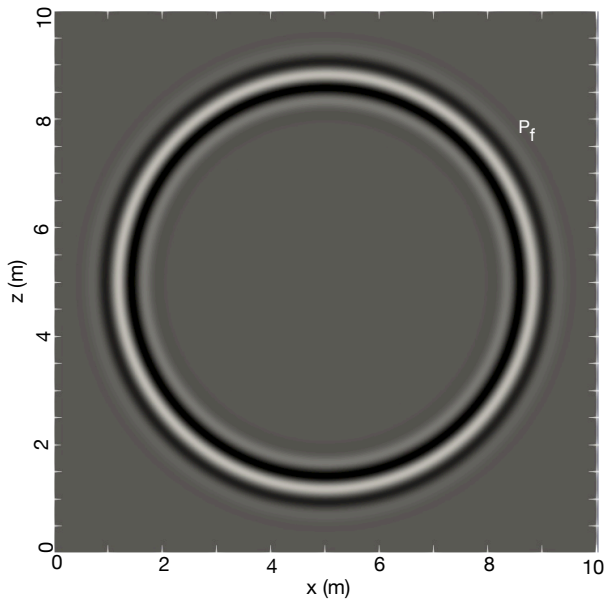

(c) Bulk pressure at $\eta \neq 0,\ f_c = 4.5$ kHz

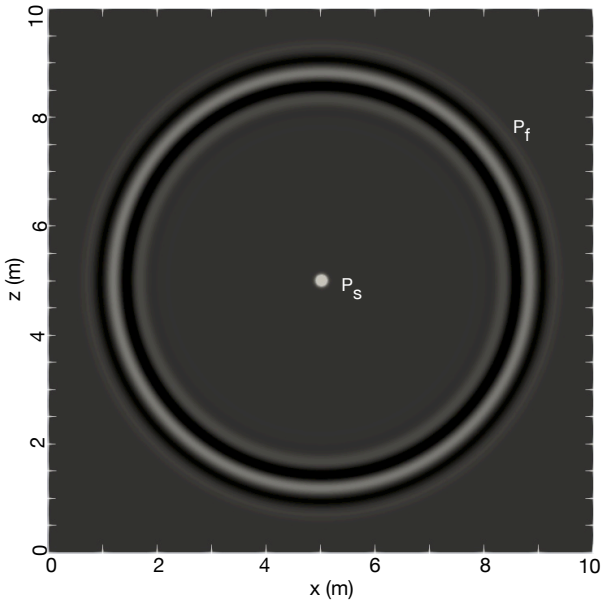

(d) Fluid pressure at $\eta \neq 0,\ f_c = 4.5$ kHz

Figure 3.5: Snapshots of (a) bulk pressure p (b) fluid pressure p_f for the inviscid case ($\eta = 0$), computed at $t = 1.2$ ms. Snapshots of (c) bulk pressure p (d) fluid pressure for viscid case ($\eta \neq 0$), computed at $t = 1.2$ ms. The forcing function is bulk source (energy is partitioned between solid and fluid) with a central frequency of 22 Hz. Numerical solution is computed for a polynomial of order 4. P_f: Fast compressional wave, P_s: slow wave (Biot mode).

Figure 3.5 shows the numerical results for the same poroacoustic medium but with a forcing function of central frequency ($f_c = 4.5$ kHz). The size of the computational domain in this case is 10 m $\times$ 10 m. The minimum size of the mesh is 0.04 m. Figure 3.5(a) and 3.5(b) represent the snapshots of the bulk and fluid pressures, respectively, computed at $t = 1.2$ ms and $\eta = 0$ with a bulk forcing function. Figure 3.5(c) and 3.5(d) are the bulk and fluid pressures, respectively, computed for a bulk forcing function at $t = 1.2$ ms and $\eta \neq 0$. The physical interpretation of Figure 5 is the same as that of the Figure 3.4, just at a different scale and the slow P wave propagates faster than those seen in Figure 3.4. The dispersion analysis also shows a non-zero velocity of the slow P wave at frequency 4.5 kHz [2].

3.6.4 Homogeneous poroelastic medium: Wave-field simulation

Here we illustrate the effect of anisotropy in (3.25) using our numerical scheme. We have considered, sandstone (orthotropic and isotropic), epoxy-glass and shale, brine filled, with the material properties given in Table 3.2. In order to have a detailed insight into the results of a poroelastic simulation, the energy velocity surfaces are computed for the materials with properties described in Table 3.2, solving the eigenvalue problem expressed in (2.10) of B.2. The surfaces include fast compressional, shear, and slow compressional waves with respect to azimuth. Figure 3.6a, 3.6b, 3.6c, and 3.6d show the energy velocities of the orthotropic sandstone, isotropic sandstone, epoxy-glass, and shale, respectively. The geometry of the energy velocity surface always agrees with the trajectory of the advancing wavefronts of the modes.

We have carried out numerical simulations with our scheme in order to compare with the energy velocity surfaces. In the subsequent discussions the field represents the center of mass particle velocity vector [87], which is expressed as

$$\boldsymbol{b} = \boldsymbol{v} + \left(\frac{\rho_f}{\rho}\right)\boldsymbol{q}. \tag{3.62}$$

The forcing function, in the subsequent simulation is given in (3.61) with a nonzero force corresponding to a vertical stress σ_{zz} and a fluid pressure p. The size of the computational domain is 18.25 m $\times$ 18.25 m. The minimum edge length is 5 cm.

Figure 3.7(a)-(d) represents the x and z components of the center of mass particle velocity of the orthotropic sandstone, where (a) and (b) correspond to the inviscid case ($\eta = 0$), and (c) and (d) to the viscid case ($\eta = 0$). The central frequency of the forcing function is $f_c = 3730$ Hz, and the basis functions have a polynomial degree $N = 4$. The propagation time is 1.6 ms. Three

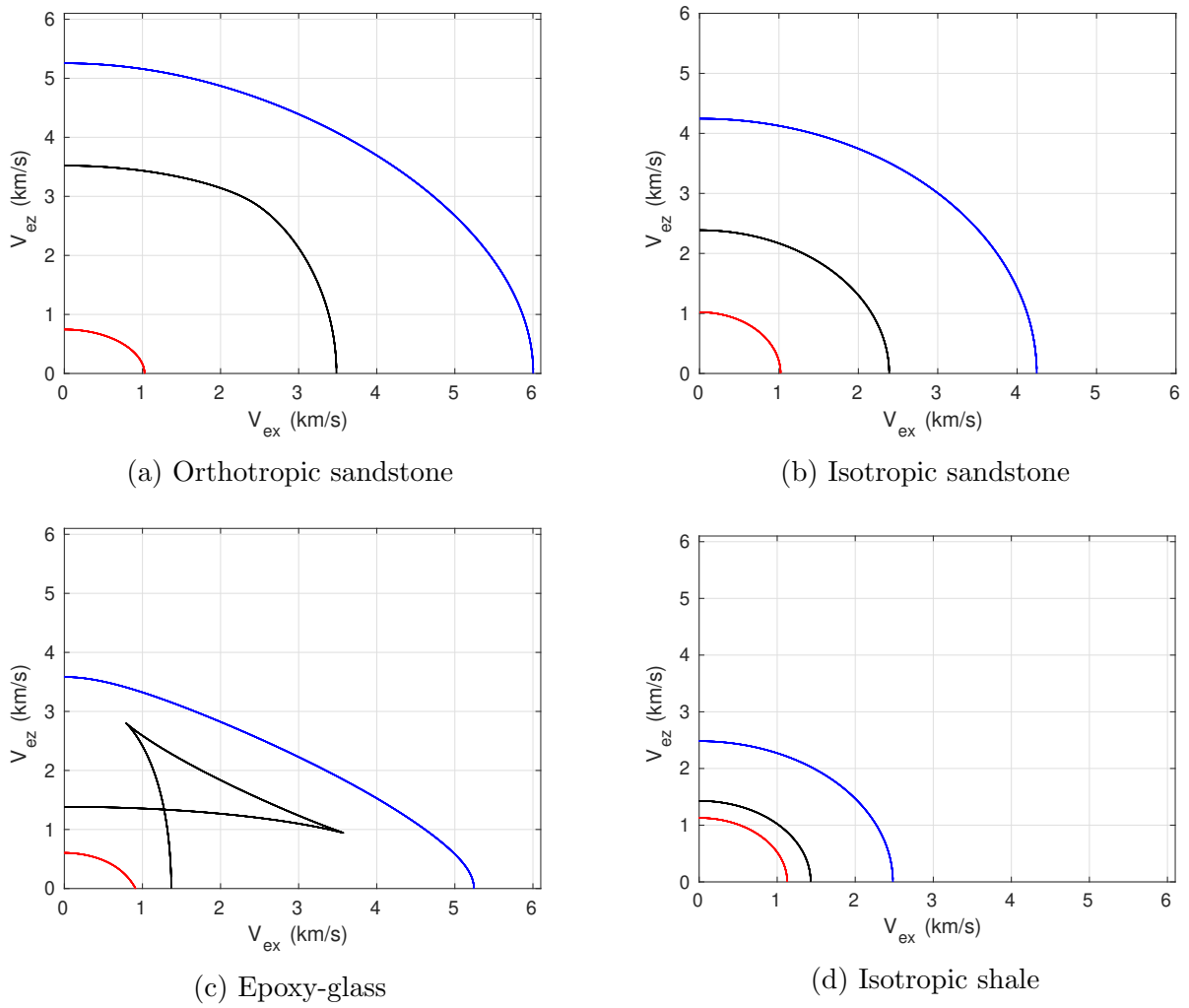

(a) Orthotropic sandstone

(b) Isotropic sandstone

(c) Epoxy-glass

(d) Isotropic shale

Figure 3.6: Energy velocity surface for $\eta = 0$, computed in a $x - z$ plane for (a) orthotropic sandstone, (b) isotropic sandstone, (c) epoxy-glass and (d) isotropic shale. The material properties are given in Table 2. For homogenous media, the geometry of the energy velocity surfaces resembles the wavefronts of the compressional, shear, and slow P waves. V_{ex} and V_{ez} are energy velocities in $x-$ and $z-$ directions, respectively.

events can be clearly observed: the fast P mode (P_f, outer wavefront), the shear wave (S, middle wavefront), and the slow P mode (P_s, inner wavefront). In the viscid case, the slow mode diffuses faster and the medium behaves almost as a single phase medium.

Figure 3.8(a)-(d) show the $x-$ and $z-$ components of the center of mass particle velocity in an isotropic sandstone, where (a) and (b) correspond to the inviscid case ($\eta = 0$), and (c) and (d) to the viscid case ($\eta = 0$). Figure 8 is produced with the same simulation parameters as those in Figure 7 except that the propagation time is 2.2 ms. The physical significance of Figure 3.8 is

the same as in Figure 3.7 except the fact that the radiation pattern is azimuthally invariant. The trajectory of the wavefronts mimics the surfaces of the energy velocity presented in Figure 3.6(b).

Snapshots of the $x-$ and $z-$ components of the center of mass particle velocity in the epoxy-glass porous medium are represented in Figure 3.9. Figures 3.9(a) and (b) correspond to the inviscid case ($\eta = 0$), and (c) and (d) to the viscid case ($\eta = 0$). The central frequency is $f_c = 3135$ Hz. The propagation time is 1.9 ms. It is worth noting the cuspidal triangles of S and $\mathrm{P_s}$ which is a typical phenomena in anisotropic materials. At 45^o, the polarization of the $\mathrm{P_s}$ mode wave is almost horizontal, which confirms the results shown in Figure 3(b) of [3].

3.6.5 Heterogeneous poroelastic medium: Wave-field simulation

With this last example, we illustrate the effect of an interface between two porous media. A two-layer model comprising shale and sandstone, both of them filled with brine, is constructed. The size of the computational domain is 1400 m $\times$ 1500 m in the x and z directions, respectively. The minimum size of the edge of the triangular element, used to triangulate the domain, is 8 m. The forcing function is located at (750 m, 900 m) The propagation time is 0.25 s. A Snapshot of the z component of the center of mass particle velocity is represented in Figure 10 for an inviscid case ($\eta = 0$). Figure 3.10 clearly shows the direct, reflected, and transmitted wavefronts, corresponding to all three modes. The slow P wave is more prominent in the shale.

To justify the choice of the flux, a comparison between the solutions, obtained from using the Lax-Friedrich flux and the local Lax-Friedrich flux, is presented in Figure 3.11. In the local Lax-Friedrich flux the λ [in (3.57)] is selected locally and thus resulting into a less dissipative scheme. The λ for local Lax-Friedrich is computed as

$$\lambda = \max\left(\lambda^-, \lambda^+\right). \tag{3.63}$$

Figure 3.11a and 3.11b show the comparison of solutions and residuals for b_x and b_z respectively, obtained from the Lax-Friedrich and the local Lax-Friedrich flux. The model and material parameters, used to compute the solutions in Figure 11, are same as that in Figure 3.10. The time history of the solution is retrieved at a node with $(x, z) = (900\text{ m}, 1100\text{ m})$. The residuals plot in Figure 3.11, magnified by a factor of ten, clearly shows that the choice of the flux does not make a significant difference. As a matter of fact, Cockburn and Shu [83] have also shown that the choice of the flux is not important for higher-order simulations, as long as the scheme is stable. This indicates that as the order of a simulation increases, the choice of numerical flux becomes less significant. This view

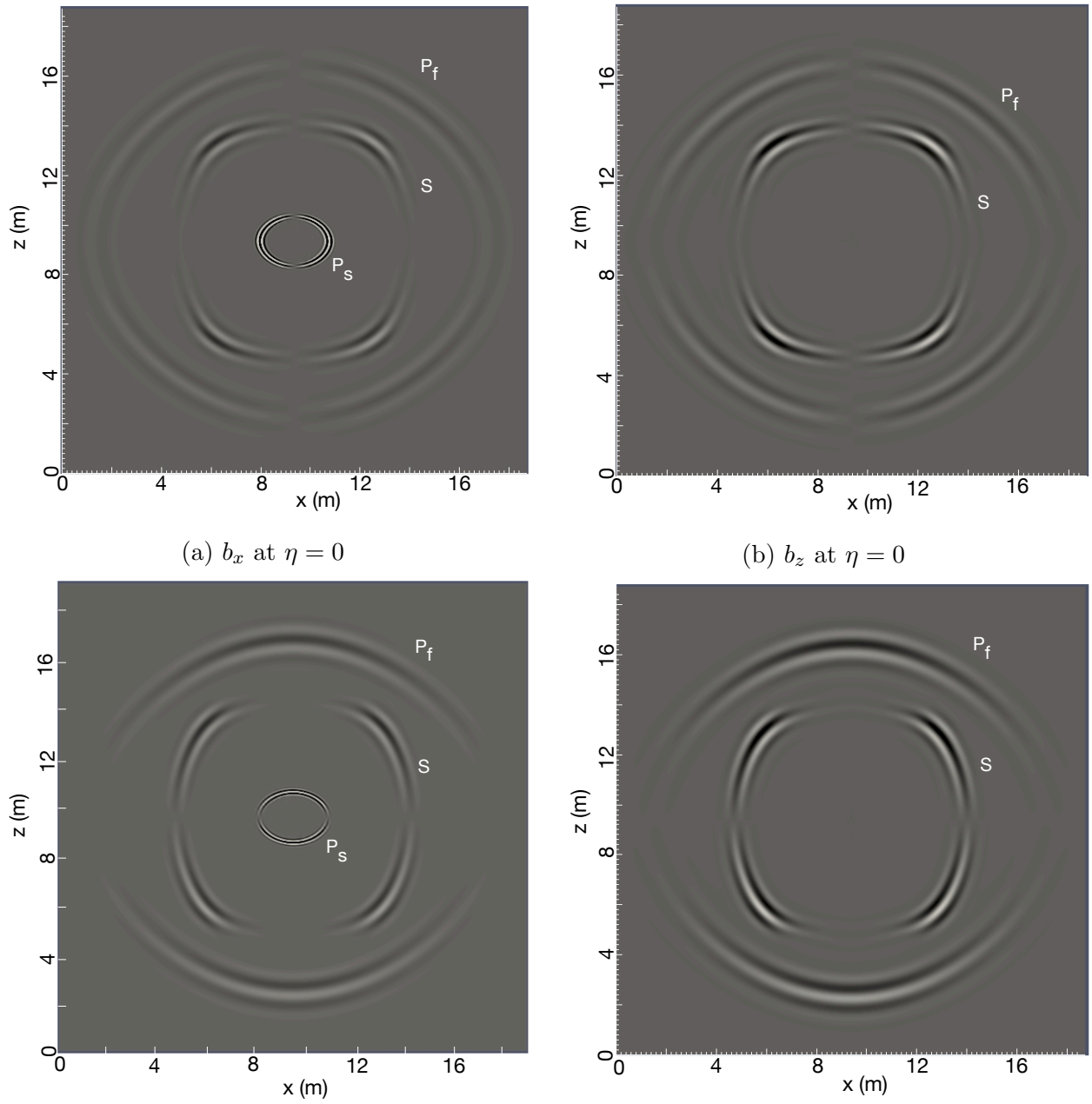

(a) b_x at $\eta = 0$

(b) b_z at $\eta = 0$

(c) b_x at $\eta \neq 0$

(d) b_z at $\eta \neq 0$

Figure 3.7: Snapshots of the centre of mass particle velocity in orthotropic sandstone, computed at $t =$ 1.6 ms, where (a) and (b) corresponds to $\eta = 0$, and (c) and (d) corresponds to $\eta \neq 0$. The central frequency of the forcing function is 3730 Hz. The solution is computed for a polynomial of order 4. P_f: Fast compressional wave, S: Shear wave, P_s: slow wave (Biot mode).

has lead to the simple and dissipative Lax-Friedrich (LF) flux being used within many DG methods. Furthermore, The findings of Cockburn and Shu [83] are also substantiated by Wheatley et al. [88]

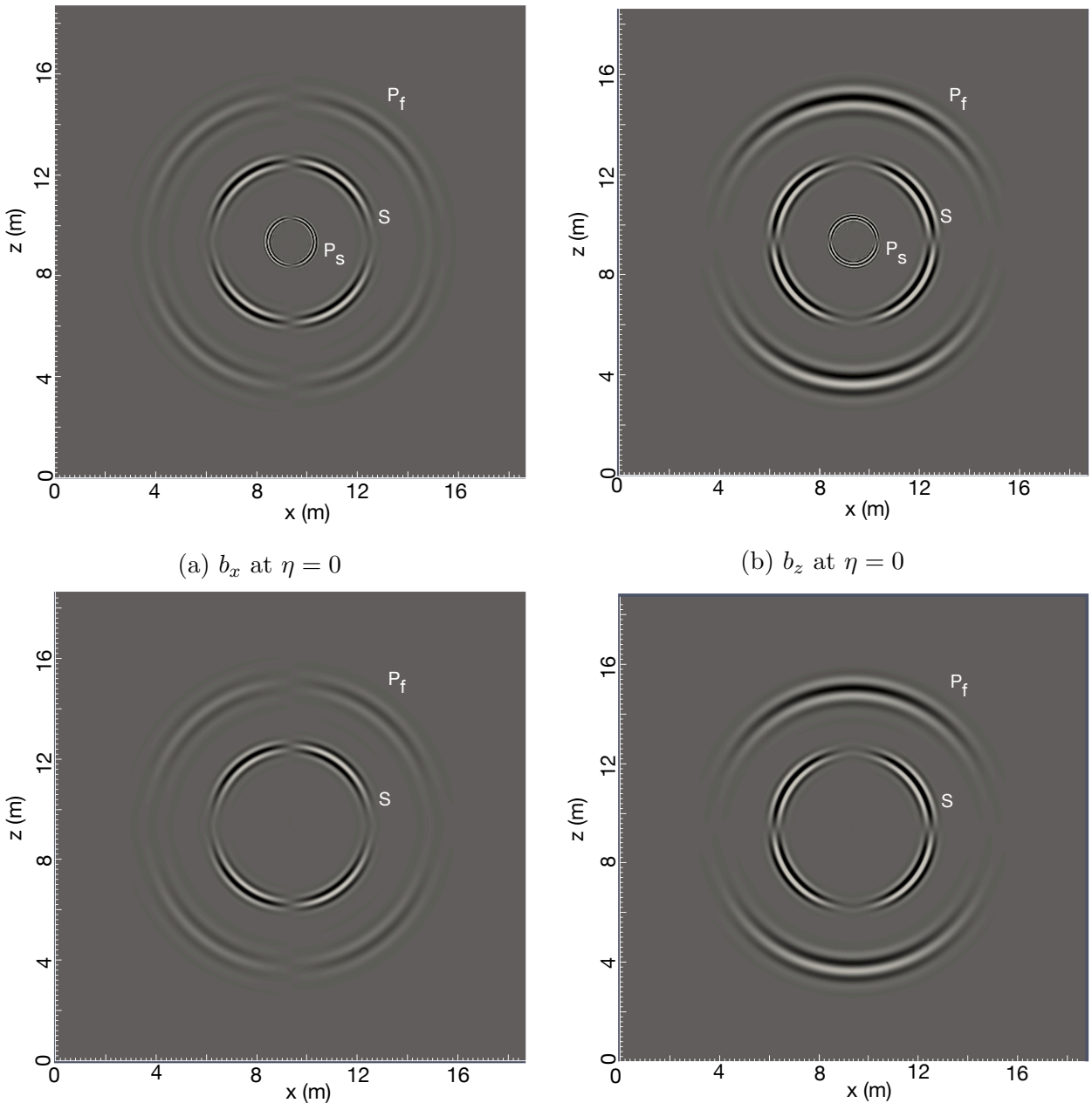

(a) b_x at $\eta = 0$

(b) b_z at $\eta = 0$

(c) b_x at $\eta \neq 0$

(d) b_z at $\eta \neq 0$

Figure 3.8: Snapshots of the centre of mass particle velocity in isotropic sandstone, computed at $t = 2.2$ ms, where (a) and (b) corresponds to $\eta = 0$, and (c) and (d) corresponds to $\eta \neq 0$. The central frequency of the forcing function is 3730 Hz. The solution is computed for a polynomial of order 4. P_f: Fast compressional wave, S: Shear wave, P_s: slow wave (Biot mode).

for a Magneto-hydrodynamic system.

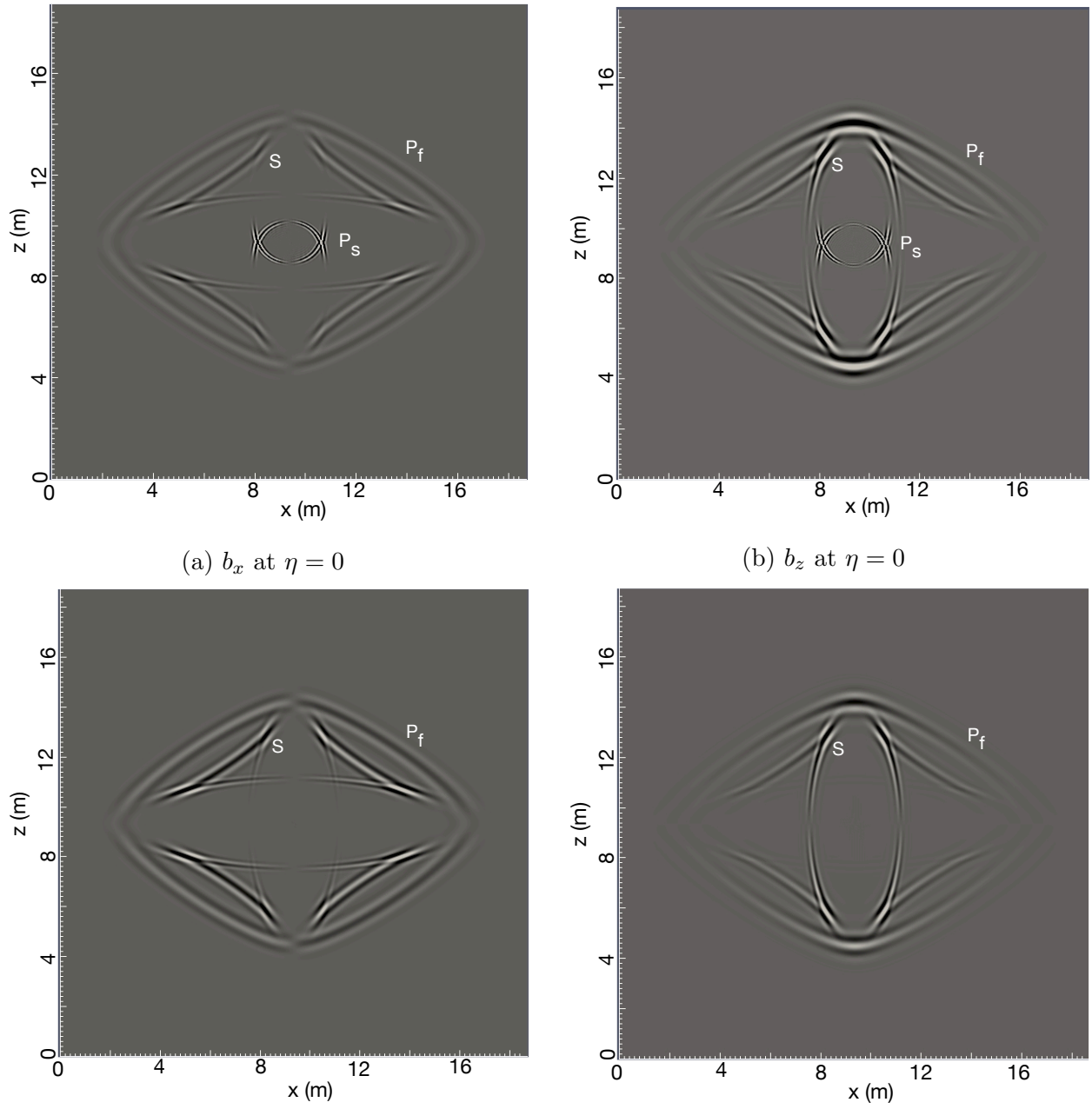

(a) b_x at $\eta = 0$

(b) b_z at $\eta = 0$

(c) b_x at $\eta \neq 0$

(d) b_z at $\eta \neq 0$

Figure 3.9: Snapshots of the centre of mass particle velocity in epoxy-glass, computed at $t = 1.8$ ms, where (a) and (b) corresponds to $\eta = 0$, and (c) and (d) corresponds to $\eta \neq 0$. The central frequency of the forcing function is 3730 Hz. The solution is computed for a polynomial of order 4. P_f: Fast compressional wave, S: Shear wave, P_s: slow wave (Biot mode).

3.7 Discussion

We have developed a nodal DG-method-based approach to simulate poroelastic wave phenomena and demonstrated its ability to generate correct solutions in both homogeneous and

heterogeneous domains. We use the Lax-Friedrich flux, which extends from isotropic to anisotropic media naturally, unlike the upwind flux used in [82].

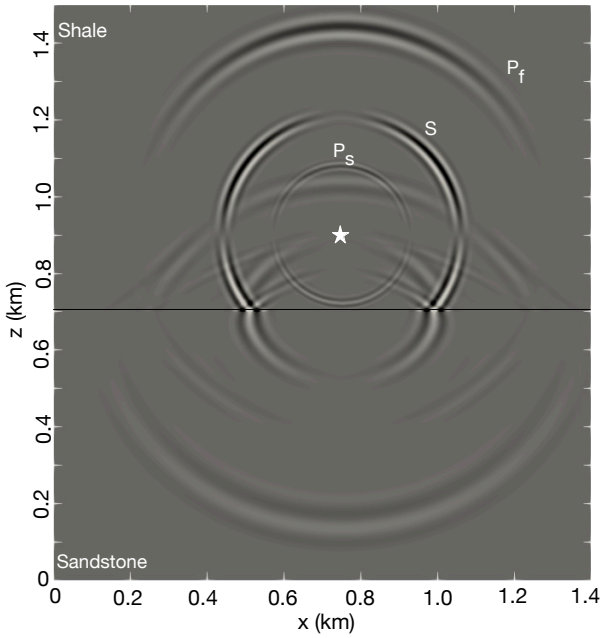

Figure 3.10: Snapshot of the z-component of the centre of mass particle velocity in an inviscid ($\eta = 0$) heterogenous medium, computed at $t = 0.25$ s .The central frequency of the forcing function is 45 Hz. The solution is computed for a polynomial of order 4. The star represents the location of the point source perturbation. P_f: Direct fast compressional wave, S: Direct shear wave, P_s: Direct slow wave (Biot mode).

The poroelastic system has very complex Jacobian matrices, which pose a computational challenge for the eigen-decomposition. Thus, the computation of the exact flux with such a complex wave structure will be very expensive. The Lax-Friedrich flux is slightly more dissipative than the upwind flux but the effects of numerical dissipation is less prominent at high order [6, 78]. We also compared the solutions obtained from global and local Lax-Friedrich flux and showed that the choice of flux does not have significant effects on the high-order simulations [83, 88]. Another challenge is to circumvent the effect of the stiffness, caused by strong dissipation at low frequencies. In the present work, we address the stiffness by using a first-order operator splitting approach. This operator deteriorates the convergence rate for a viscid case. We find that it works reasonably well for all spatial orders tested, i.e., $N = 1..4$. Existing alternatives, include [4] who use a locally implicit time integration scheme. Our scheme is simpler but fully explicit.

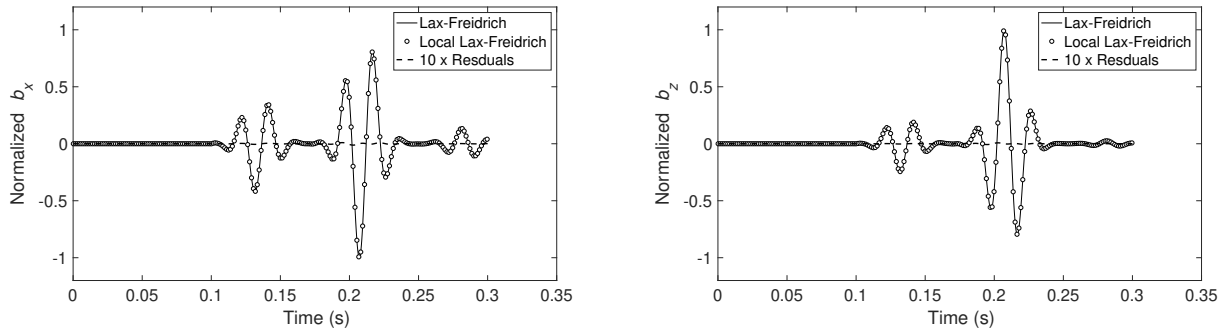

(a) Time-history of b_x

(b) Time-history of b_z

Figure 3.11: A comparison between numerical solutions obtained from Lax-Friedrich and local Lax-Friedrich flux, where (a) and (b) correspond to x and z components of normalized centre of mass particle velocity. The time-history of the solution is recovered at receiver located in model, same as in Figure 10, with coordinates $(x, z) = (900 \text{ m}, 1100 \text{ m})$. The residual between the solutions is magnified by the factor of 10.

Chapter IV

A weight-adjusted discontinuous Galerkin method for the poroelastic wave equation: penalty fluxes and micro-heterogeneities

4.1 Abstract

We introduce a high-order weight-adjusted discontinuous Galerkin (WADG) scheme for the numerical solution of three-dimensional (3D) wave propagation problems in anisotropic porous media. We use a coupled first-order symmetric stress-velocity formulation [27, 28]. Careful attention is directed at (a) the derivation of an energy-stable penalty-based numerical flux, which offers high-order accuracy in presence of material discontinuities, and (b) proper treatment of micro-heterogeneities (sub-element variations) in the numerical scheme. The use of a penalty-based numerical flux avoids the diagonalization of Jacobian matrices into polarized wave constituents necessary when solving element-wise Riemann problems. Micro-heterogeneities are accurately and stably incorporated in the numerical scheme using easily-invertible weight-adjusted mass matrices [89]. The convergence of the proposed numerical scheme is proven and verified by using convergence studies against analytical plane wave solutions. The proposed method is also compared against an existing implementation using the spectral element method to solve the poroelastic wave equation [5].

Keywords— WADG, Mass matrix, DG, Energy

4.2 Introduction

Theories of poroelasticity deal with the physics of elastic wave propagation in porous media. These physics are applicable where pore-filling materials are of interest, such as oil and gas

exploration, gas hydrate detection, hydrogeology, seismic monitoring of CO_2 storage, and medical imaging. The most popular theory of poroelastic wave propagation was pioneered by Maurice Biot [8, 10]. Biot obtained a dynamical system of equations describing wave propagation in a porous medium, saturated with a single phase fluid with an ability to flow through the pore networks. Biot's system of equations is divided in two categories, based on the material's characteristic frequency (ω_c) [10, 2, 74], which describes the nature of fluid flow (laminar or non-laminar) induced by wave motion. Biot's theory of poroelasticity predicts two compressional waves, the fast P wave and slow P wave, and one shear wave.

Biot's theory of poroelasticity predicts two compressional waves (a fast P wave and slow P wave) and one shear wave. In the fast P wave, the fluid and matrix are locked together and move in-phase. This locking arises through the action of viscous or inertial forces which result from wave-induced fluid flow. Viscous forces arise due to friction between the layers of the viscous fluid (laminar flow), whereas inertial forces result from the momentum of the fluid flow (non-laminar flow). The slow P wave results from relative motion between the fluid in the pores and the matrix. Biot's system of equations is divided in two categories based on the material's characteristic frequency (ω_c) [10, 2, 74], which describes the nature of fluid flow (laminar or non-laminar) induced by wave motion. Due to the relative motion between the solid and the fluid, a pore boundary layer is formed. The pore boundary layer is related to the viscous-skin depth, which is the distance where the fluid particle velocity attains a certain percentage of its maximum value.

A major cause of energy dissipation in porous media is a dissipative (or drag) "memory" force resulting from the relative motion between the solid skeleton and pore fluids. The dissipative force is incorporated in the equations of motion through a time dependent viscodynamic operator $\psi(t)$. In the low-frequency regime, the dissipative force is linearly proportional to the relative velocity between solid and fluid and $\psi(t)$ is compactly supported. This occurs because the viscous skin depth in the low-frequency regime is greater than the pore size, and thus does not form any pore boundary layer. However, in the high frequency regime, the dominance of inertial forces over viscous forces causes the formation of a pore boundary viscous layer. Thus, in principle, the relaxation mechanism of the medium due to drag force is expressed as a memory kernel and $\psi(t)$ is incorporated into the equation of motion through a convolution operator [3]. Our current work focuses on poroelasticity in the low-frequency regime (ω_c). In subsequent work, we will present numerical methods for the broad-band Biot system based on the Johnson-Koplik-Dashen (JKD) model of dynamic permeability [90], which will unify both the high and low frequency regime.

Numerical simulations of the poroelastic wave equation in the low-frequency regime have

been previously explored in the literature. The first numerical simulations were performed using the reflectivity method for flat layers [91, 92] and cylindrical structures [93]. Numerical simulation of the poroelastic wave equation using direct or grid based methods, such as finite difference (FD) and pseudo-spectral (PS) methods, dates back to the 1970s [17]. Most of the methods presented in [17] regard pseudospectral [2, 3], staggered pseudospectral [74] and finite-difference methods [18, 21] and are based on 2D structured meshes. Santos and Oreña [23] used a finite-element method to solve the poroelastic wave equation (second-order form) using quadrilateral meshes for spatial discretization. Recent work on the numerical solution of orthotropic poroelasticity is reported by Lemoine et al. [27], using a finite-volume method on structured meshes.

In the present study, we introduce a high-order numerical scheme based on the discontinuous Galerkin method to solve the 3D poroelastic wave equation on unstructured tetrahedral meshes. High order methods provide one avenue towards improving fidelity in numerical simulations while maintaining reasonable computational costs, and methods which can accommodate unstructured meshes are desirable for problems with complex geometries. Among such methods, high order discontinuous Galerkin (DG) methods are particularly well-suited to the solution of time-dependent hyperbolic problems on modern computing architectures [6, 94]. The accuracy of high order methods can be attributed in part to their low numerical dissipation and dispersion compared to low order schemes [95]. This accuracy has made them advantageous for the simulation of electro-magnetic and elastic wave propagation [6, 7].

Since the time-domain wave propagation is described by a hyperbolic system of partial differential equations, an explicit time integration can efficiently be applied. The finite-element methods, when coupled with an explicit time integrator, require the inversion of a global mass matrix, unless special techniques, such as diagonal mass lumping, are applied. Spectral element methods avoid the inversion of the global mass matrix for hexahedral elements by choosing nodal basis functions, which are discretely orthogonal with respect to an under-integrated L^2 inner product and result in a diagonal mass matrix. In contrast, high order DG methods produce block diagonal mass matrices, which are locally invertible. High order DG methods are often used for seismic simulation (elastic approximation) through the use of simplicial meshes [77, 78, 79].

DG methods impose inter-element continuity of approximate solutions between elements weakly through a numerical flux, of which several choices are common. de la Puente et al. [4] solved the poroelastic wave equation using a local space-time DG method with a Rusanov type flux, which tends to be dissipative. In another study, Ward et al. [82], derived an upwind flux by solving the exact Riemann problem on inter-element boundaries for the 2D isotropic strain-velocity form of the

poroelastic wave equations. Recently, Zhan et al. [96] also solved the poroelastic wave equation in 3D (formulated in stress-velocity form) using an upwind flux by solving the exact Riemann problem. The solution of Riemann problem requires diagonalization Jacobian matrices into polarized waves constituents, which is a computationally intensive process for the poroelastic system and does not extend naturally to anisotropic materials. Zhan et al. [96] addresses the complexity of the diagonalization by reducing the rank of Jacobian matrices by using the method of generalized wave impedances. Ye at al. [79] completely avoid the process of diagonalization for the coupled acoustic-elastic wave equation by using a penalty flux based on natural boundary conditions. In this study, we use a similar approach and derive an energy-stable penalty flux for the poroelastic wave equations.

A poroelastic material is defined by the static acoustic properties of fluid, solid and frame exclusively, e.g. fifteen physical properties are required to define an orthotropic medium. The spatial scale of variability of these properties can range from macro (piece-wise constant approximations) to micro-heterogeneities (sub-element variations) in the medium. Most high order methods for wave equations on simplical meshes assume that material coefficients are constant over each element. However, if the media is such that material gradients are non-zero in interior of the an element, piecewise constant approximations can yield inaccurate solutions [97]. This can be circumvented by incorporating sub-element heterogeneities into weighted mass matrices, which recovers a highly accurate and energy-stable DG method [98]. On tetrahedral meshes, this approach requires precomputation and storage of inverses for each local mass matrix, which increases the storage cost and data movement at high orders of approximations. Chan et al. [89] circumvented these storage costs for elastic wave propagation by approximating weighted mass matrices with easily invertible "weight-adjusted" approximations. We extend the same approach to the poroelastic wave equations, where matrix-valued weight functions arise after symmetrization of the system.

In brief, the novelties of our approach are the following:

1. We obtain a consistent DG weak formulation for the poroelastic wave equations without the diagonalization into polarized wave constituents required for upwind fluxes.

2. We introduce upwind-like dissipation through simple penalty terms in the numerical flux.

3. We implement an efficient "weight-adjusted" approximate mass matrix to address micro-heterogeneities at the sub-element level present in poroelastic materials.

4. We prove stability and high order accuracy of the proposed DG method.

The method is presented for tetrahedral meshes but extends naturally to quadrilateral and hexahedral meshes as well. The outline of the paper is as follows: Section 4.3 will discuss the system of equations describing the poroelastic wave equation along with interface conditions. Section 4.4 presents an energy stable formulation with simple penalty fluxes for the symmetric hyperbolic form of the poroelastic wave equations. Section 4.4 also discusses issues pertaining to storage and inversion of local mass matrices for material coefficients with micro-heterogeneities (sub-element variations). Section 4.5 incorporates weight-adjusted approximations of weighted L^2 inner products and mass matrices with matrix-valued weights into DG discretizations of the poroelastic wave equations. Finally, numerical results in Section 4.6 demonstrate the accuracy of this method for several problems in linear poroelasticity.

4.3 System of equations describing porelastic waves

Biot's theory describes wave propagation in a saturated porous medium i.e., a medium made up of a solid matrix (the skeleton or frame) fully saturated with single phase fluid. Biot also assumed that an infinitesimal transformation relates the reference and current states of deformation; thus the displacement, strains, and particle velocity are small. The concept of infinitesimal deformation allows the use of the Lagrangian and Hamilton's principle to derive the equations governing the propagation of waves in such a medium. In the following two subsections, we will review the constitutive equations, and equations of motions for a poroelastic medium. Readers are advised to refer to Biot's original papers [8, 9, 10], work of Lemoine et al. [27, 28] and [32] for further detail. For the following formulations, the variables specific to the poroelastic system are defined as

1. $\boldsymbol{u} = [u_1, u_2, u_3]$ and $\boldsymbol{U} = [U_1, U_2, U_3]$ are defined as displacement vectors of the solid and fluid matrix, respectively. These vectors are defined with respect to an orthogonal set of axes as denoted by the subscripts 1, 2 and 3.

2. $\boldsymbol{w} := \phi\,(\boldsymbol{U} - \boldsymbol{u})$ represent relative motion fluid scaled by porosity ϕ.

3. $\zeta := -\nabla \cdot \boldsymbol{w}$ represents the variation of fluid content.

4.3.1 Constitutive equations

Carcione [32, Ch. 7, p. 330] expresses the stress-strain relationship for an anisotropic poroelastic material. Using the Einstein summation notation, constitutive equations for an inhomogeneous

and anisotropic poroelastic medium are [27, 28]

$$\tau_I = c^u_{IJ} e_J - M\alpha_I \zeta, \tag{4.1}$$

$$p = M\left(\zeta - \alpha_I e_I\right), \tag{4.2}$$

where $\boldsymbol{\tau}_I$ is the I^{th} component of the total stress in poroelastic material, ordered as $\boldsymbol{\tau} = [\tau_{11},\ \tau_{22},\ \tau_{33},\ \tau_{23},\ \tau_{13},\ \tau_{12}]^T$. c^u_{IJ} is the undrained elastic stiffness tensor of the solid matrix defined as $c^u_{IJ} = c_{IJ} + \alpha_I \alpha_J M$, with c_{IJ} denoting the components of the elastic stiffness tensor. e_I is I^{th} component of strain ordered as $\boldsymbol{e} = [\epsilon_{11},\ \epsilon_{22},\ \epsilon_{33},\ 2\epsilon_{23},\ 2\epsilon_{13},\ 2\epsilon_{12}]^T$ with $\epsilon_{ii} = \dfrac{\partial u_i}{\partial x_i}$ and $\epsilon_{ij} = \dfrac{\partial u_i}{\partial x_j} + \dfrac{\partial u_j}{\partial x_i}$. α_I is I^{th} component of the effective stress coefficient defined as $\alpha_I = 1 - \dfrac{1}{3K_s}\displaystyle\sum_{J=1}^{3} c_{IJ}$, with K_s being the bulk modulus of the solid. M is the Biot's coefficient which relates the compressibility of the fluid to the compressibility of the solid and is defined as $M = \left(\phi\left(\dfrac{K_s}{K_f} - 1\right) + \left(1 - \dfrac{\widehat{K}}{K_s}\right)\right)$ with K_f being the bulk modulus of fluid and $\widehat{K} = \dfrac{1}{9}\displaystyle\sum_{I=1}^{3}\sum_{J=1}^{3} c_{IJ}$.

To derive the first-order velocity stress system, the relation between velocity and strain-rate is expressed as

$$\begin{aligned}
\frac{\partial e_1}{\partial t} &= \frac{\partial}{\partial x_1}\left(\frac{\partial u_1}{\partial t}\right) = \frac{\partial v_1}{\partial x_1} \\
\frac{\partial e_2}{\partial t} &= \frac{\partial}{\partial x_2}\left(\frac{\partial u_2}{\partial t}\right) = \frac{\partial v_2}{\partial x_2} \\
\frac{\partial e_3}{\partial t} &= \frac{\partial}{\partial x_3}\left(\frac{\partial u_3}{\partial t}\right) = \frac{\partial v_3}{\partial x_3} \\
\frac{\partial e_4}{\partial t} &= \frac{\partial}{\partial x_3}\left(\frac{\partial u_2}{\partial t}\right) + \frac{\partial}{\partial x_2}\left(\frac{\partial u_3}{\partial t}\right) = \frac{\partial v_2}{\partial x_3} + \frac{\partial v_3}{\partial x_2} \\
\frac{\partial e_5}{\partial t} &= \frac{\partial}{\partial x_3}\left(\frac{\partial u_1}{\partial t}\right) + \frac{\partial}{\partial x_1}\left(\frac{\partial u_3}{\partial t}\right) = \frac{\partial v_1}{\partial x_3} + \frac{\partial v_3}{\partial x_1} \\
\frac{\partial e_6}{\partial t} &= \frac{\partial}{\partial x_2}\left(\frac{\partial u_1}{\partial t}\right) + \frac{\partial}{\partial x_1}\left(\frac{\partial u_2}{\partial t}\right) = \frac{\partial v_1}{\partial x_2} + \frac{\partial v_2}{\partial x_1} \\
\frac{\partial \zeta}{\partial t} &= -\frac{\partial}{\partial x_1}\left(\frac{\partial U_1}{\partial t}\right) - \frac{\partial}{\partial x_2}\left(\frac{\partial U_2}{\partial t}\right) - \frac{\partial}{\partial x_3}\left(\frac{\partial U_3}{\partial t}\right) = -\frac{\partial q_1}{\partial x_1} - \frac{\partial q_2}{\partial x_2} - \frac{\partial q_3}{\partial x_3}
\end{aligned} \tag{4.3}$$

where $\boldsymbol{v}_s = [v_1,\ v_2,\ v_3]$ is velocity of the solid matrix relative to the inertial frame and $\boldsymbol{v}_f = [q_1,\ q_2,\ q_3]$ is the rate of the flow of the fluid relative to the matrix.

Now differentiating (4.1) and (4.2) with respect to time and using (4.3), the rate of change

of the stresses and fluid pressure are expressed as

$$\begin{aligned}
\frac{\partial \tau_{11}}{\partial t} &= c_{11}^u \frac{\partial v_1}{\partial x_1} + c_{12}^u \frac{\partial v_2}{\partial x_2} + c_{13}^u \frac{\partial v_3}{\partial x_3} + \alpha_1 M \frac{\partial q_1}{\partial x_1} + \alpha_1 M \frac{\partial q_2}{\partial x_2} + \alpha_1 M \frac{\partial q_3}{\partial x_3}, \\
\frac{\partial \tau_{22}}{\partial t} &= c_{12}^u \frac{\partial v_1}{\partial x_1} + c_{22}^u \frac{\partial v_2}{\partial x_2} + c_{23}^u \frac{\partial v_3}{\partial x_3} + \alpha_2 M \frac{\partial q_1}{\partial x_1} + \alpha_2 M \frac{\partial q_2}{\partial x_2} + \alpha_2 M \frac{\partial q_3}{\partial x_3}, \\
\frac{\partial \tau_{33}}{\partial t} &= c_{13}^u \frac{\partial v_1}{\partial x_1} + c_{23}^u \frac{\partial v_2}{\partial x_2} + c_{33}^u \frac{\partial v_3}{\partial x_3} + \alpha_3 M \frac{\partial q_1}{\partial x_1} + \alpha_3 M \frac{\partial q_2}{\partial x_2} + \alpha_3 M \frac{\partial q_3}{\partial x_3}, \\
\frac{\partial \tau_{23}}{\partial t} &= c_{44}^u \frac{\partial v_2}{\partial x_3} + c_{44}^u \frac{\partial v_3}{\partial x_2}, \\
\frac{\partial \tau_{13}}{\partial t} &= c_{55}^u \frac{\partial v_1}{\partial x_3} + c_{55}^u \frac{\partial v_3}{\partial x_1}, \\
\frac{\partial \tau_{12}}{\partial t} &= c_{66}^u \frac{\partial v_1}{\partial x_2} + c_{66}^u \frac{\partial v_2}{\partial x_1}, \\
\frac{\partial p}{\partial t} &= -M \left(\alpha_1 \frac{\partial v_1}{\partial x_1} + \alpha_2 \frac{\partial v_2}{\partial x_2} + \alpha_3 \frac{\partial v_3}{\partial x_3} + \frac{\partial q_1}{\partial x_1} + \frac{\partial q_2}{\partial x_2} + \frac{\partial q_3}{\partial x_3} \right),
\end{aligned} \tag{4.4}$$

4.3.2 Dynamical equations and Darcy's law

To build up the full set of wave equations, we require equations of motion which specify the dynamics of fluid and solid with respect to stress gradients. To define the dynamics of solid for anisotropic heterogeneous porous media, Newton's second law with zero external forces ($\boldsymbol{f} = 0$) is used and expressed as [32, Ch. 7, pp. 339-340]

$$\begin{aligned}
\frac{\partial \tau_{11}}{\partial x_1} + \frac{\partial \tau_{12}}{\partial x_2} + \frac{\partial \tau_{13}}{\partial x_3} &= \rho \frac{\partial v_1}{\partial t} + \rho_f \frac{\partial q_1}{\partial t}, \\
\frac{\partial \tau_{12}}{\partial x_1} + \frac{\partial \tau_{22}}{\partial x_2} + \frac{\partial \tau_{23}}{\partial x_3} &= \rho \frac{\partial v_2}{\partial t} + \rho_f \frac{\partial q_2}{\partial t}, \\
\frac{\partial \tau_{13}}{\partial x_1} + \frac{\partial \tau_{23}}{\partial x_2} + \frac{\partial \tau_{33}}{\partial x_3} &= \rho \frac{\partial v_3}{\partial t} + \rho_f \frac{\partial q_3}{\partial t},
\end{aligned} \tag{4.5}$$

where $\rho = (1 - \phi)\rho_s + \phi\rho_f$ is the bulk density, and ρ_s and ρ_f are the solid and fluid density, respectively. To define the dynamics of confined fluid flow in a porous media, Biot used Darcy's law. The generalized dynamic Darcy's law governing fluid flow in an anisotropic porous media, is

expressed as [32, Ch. 7, pp. 339-340]

$$\begin{aligned} -\frac{\partial p}{\partial x_1} &= \rho_f \frac{\partial v_1}{\partial t} + \psi_1(t) * \frac{\partial q_1}{\partial t}, \\ -\frac{\partial p}{\partial x_2} &= \rho_f \frac{\partial v_2}{\partial t} + \psi_2(t) * \frac{\partial q_2}{\partial t}, \\ -\frac{\partial p}{\partial x_3} &= \rho_f \frac{\partial v_3}{\partial t} + \psi_3(t) * \frac{\partial q_3}{\partial t}, \end{aligned} \tag{4.6}$$

where $\psi_i,\ i = 1...3$ are viscodynamic operators. Here, " $*$ " represents the convolution operation in time. In the low frequency range, i.e., for frequencies lower than $\omega_c = \min\left(\frac{\eta\phi}{\rho_f T_i \kappa_i}\right)$, ψ_i can be expressed as

$$\psi_i(t) = m_i \delta(t) + (\eta/\kappa_i)\, H(t), \tag{4.7}$$

where $m_i = T_i \rho_f / \phi$, with T_i being the tortuosity, η the fluid viscosity, and κ_is principal components of the global permeability tensor, while $\delta(t)$ is Dirac's function and $H(t)$ the Heaviside step function. The convolution operation in (4.6) represents the dissipation of energy due to fluid-flow induced by the wave motion. As this work focuses on the low-frequency regime, the convolution is approximated by viscosity-dependent damping terms, shown in (4.7).

Substituting (4.7) into (4.6) and using the convolution identity $\psi_i * \frac{\partial q_i}{\partial t} = q_i * \frac{\partial \psi_i}{\partial t}$, we get

$$\begin{aligned} -\frac{\partial p}{\partial x_1} &= \rho_f \frac{\partial v_1}{\partial t} + m_1 \frac{\partial q_1}{\partial t} + \frac{\eta}{\kappa_1} q_1, \\ -\frac{\partial p}{\partial x_2} &= \rho_f \frac{\partial v_2}{\partial t} + m_2 \frac{\partial q_2}{\partial t} + \frac{\eta}{\kappa_2} q_2, \\ -\frac{\partial p}{\partial x_3} &= \rho_f \frac{\partial v_3}{\partial t} + m_3 \frac{\partial q_3}{\partial t} + \frac{\eta}{\kappa_3} q_3. \end{aligned} \tag{4.8}$$

Solving the system of equations in (4.5) and (4.8) for $\left(\dfrac{\partial q_i}{\partial t} \text{ and } \dfrac{\partial v_i}{\partial t}\right)$ for each i, we recover the rate of change of solid and fluid velocity as

$$\begin{aligned}
\frac{\partial v_1}{\partial t} &= \frac{m_1}{\beta_1}\left(\frac{\partial \tau_{11}}{\partial x_1} + \frac{\partial \tau_{12}}{\partial x_2} + \frac{\partial \tau_{13}}{\partial x_3}\right) + \frac{\rho_f}{\beta_1}\frac{\partial p}{\partial x_1} + \frac{\rho_f \eta}{\beta_1 \kappa_1} q_1, \\
\frac{\partial v_2}{\partial t} &= \frac{m_2}{\beta_2}\left(\frac{\partial \tau_{12}}{\partial x_1} + \frac{\partial \tau_{22}}{\partial x_2} + \frac{\partial \tau_{23}}{\partial x_3}\right) + \frac{\rho_f}{\beta_2}\frac{\partial p}{\partial x_2} + \frac{\rho_f \eta}{\beta_2 \kappa_2} q_2, \\
\frac{\partial v_3}{\partial t} &= \frac{m_3}{\beta_3}\left(\frac{\partial \tau_{13}}{\partial x_1} + \frac{\partial \tau_{23}}{\partial x_2} + \frac{\partial \tau_{33}}{\partial x_3}\right) + \frac{\rho_f}{\beta_3}\frac{\partial p}{\partial x_3} + \frac{\rho_f \eta}{\beta_3 \kappa_3} q_3, \\
\frac{\partial q_1}{\partial t} &= -\frac{\rho_f}{\beta_1}\left(\frac{\partial \tau_{11}}{\partial x_1} + \frac{\partial \tau_{12}}{\partial x_2} + \frac{\partial \tau_{13}}{\partial x_3}\right) - \frac{\rho}{\beta_1}\frac{\partial p}{\partial x_1} - \frac{\rho \eta}{\beta_1 \kappa_1} q_1, \\
\frac{\partial q_2}{\partial t} &= -\frac{\rho_f}{\beta_2}\left(\frac{\partial \tau_{12}}{\partial x_1} + \frac{\partial \tau_{22}}{\partial x_2} + \frac{\partial \tau_{23}}{\partial x_3}\right) - \frac{\rho}{\beta_2}\frac{\partial p}{\partial x_2} - \frac{\rho \eta}{\beta_2 \kappa_2} q_2, \\
\frac{\partial q_3}{\partial t} &= -\frac{\rho_f}{\beta_3}\left(\frac{\partial \tau_{13}}{\partial x_1} + \frac{\partial \tau_{23}}{\partial x_2} + \frac{\partial \tau_{33}}{\partial x_3}\right) - \frac{\rho}{\beta_3}\frac{\partial p}{\partial x_3} - \frac{\rho \eta}{\beta_3 \kappa_3} q_3,
\end{aligned} \tag{4.9}$$

where $\beta_i = \rho m_i - \rho_f^2$.

4.3.3 The system of equations in matrix form

To simplify notation, we introduce a matrix form of the system of equations which accounts for anisotropy and heterogeneity. Combining (4.4) and (4.9) and adding an external forcing $\boldsymbol{f}$ to the velocity components, we get

$$\frac{\partial \boldsymbol{Q}}{\partial t} + \boldsymbol{A}\frac{\partial \boldsymbol{Q}}{\partial x_1} + \boldsymbol{B}\frac{\partial \boldsymbol{Q}}{\partial x_2} + \boldsymbol{C}\frac{\partial \boldsymbol{Q}}{\partial x_3} = \boldsymbol{D}\boldsymbol{Q} + \boldsymbol{f}, \tag{4.10}$$

where

$$\boldsymbol{Q} = \begin{bmatrix} \tau_{11}, & \tau_{22}, & \tau_{33}, & \tau_{23}, & \tau_{13}, & \tau_{12}, & p, & v_1, & v_2, & v_3, & q_1, & q_2, & q_3 \end{bmatrix}^T, \ \boldsymbol{A} = \left[\begin{array}{c|c} \mathbf{0}_{7\times 7} & \boldsymbol{A}_{11} \\ \hline \boldsymbol{A}_{21} & \mathbf{0}_{6\times 6} \end{array}\right],$$

$$\boldsymbol{B} = \left[\begin{array}{c|c} \mathbf{0}_{7\times 7} & \boldsymbol{B}_{11} \\ \hline \boldsymbol{B}_{21} & \mathbf{0}_{6\times 6} \end{array}\right], \ \boldsymbol{C} = \left[\begin{array}{c|c} \mathbf{0}_{7\times 7} & \boldsymbol{C}_{11} \\ \hline \boldsymbol{C}_{21} & \mathbf{0}_{6\times 6} \end{array}\right], \text{ and } \boldsymbol{D} = \left[\begin{array}{c|c} \mathbf{0}_{7\times 7} & \mathbf{0}_{6\times 7} \\ \hline \mathbf{0}_{6\times 7} & \boldsymbol{D}_{22} \end{array}\right], \text{ with}$$

$$\boldsymbol{A}_{11} = -\begin{bmatrix} c_{11}^u & 0 & 0 & \alpha_1 M & 0 & 0 \\ c_{12}^u & 0 & 0 & \alpha_2 M & 0 & 0 \\ c_{13}^u & 0 & 0 & \alpha_3 M & 0 & 0 \\ 0 & 0 & 0 & 0 & 0 & 0 \\ 0 & 0 & c_{55} & 0 & 0 & 0 \\ 0 & c_{66} & 0 & 0 & 0 & 0 \\ -M\alpha_1 & 0 & 0 & -M & 0 & 0 \end{bmatrix}, \; \boldsymbol{A}_{21} = -\begin{bmatrix} \frac{m_1}{\beta_1} & 0 & 0 & 0 & 0 & 0 & \frac{\rho_f}{\beta_1} \\ 0 & 0 & 0 & 0 & 0 & \frac{m_2}{\beta_2} & 0 \\ 0 & 0 & 0 & 0 & \frac{m_3}{\beta_3} & 0 & 0 \\ -\frac{\rho_f}{\beta_1} & 0 & 0 & 0 & 0 & 0 & -\frac{\rho}{\beta_1} \\ 0 & 0 & 0 & 0 & 0 & -\frac{\rho_f}{\beta_2} & 0 \\ 0 & 0 & 0 & 0 & -\frac{\rho_f}{\beta_3} & 0 & 0 \end{bmatrix},$$

$$\boldsymbol{B}_{11} = -\begin{bmatrix} 0 & c_{12}^u & 0 & 0 & \alpha_1 M & 0 \\ 0 & c_{22}^u & 0 & 0 & \alpha_2 M & 0 \\ 0 & c_{33}^u & 0 & 0 & \alpha_3 M & 0 \\ 0 & 0 & c_{44} & 0 & 0 & 0 \\ 0 & 0 & 0 & 0 & 0 & 0 \\ c_{66} & 0 & 0 & 0 & 0 & 0 \\ 0 & -M\alpha_2 & 0 & 0 & -M & 0 \end{bmatrix}, \; \boldsymbol{B}_{21} = -\begin{bmatrix} 0 & 0 & 0 & 0 & 0 & \frac{m_1}{\beta_1} & 0 \\ 0 & \frac{m_2}{\beta_2} & 0 & 0 & 0 & 0 & \frac{\rho_f}{\beta_2} \\ 0 & 0 & 0 & \frac{m_3}{\beta_3} & 0 & 0 & 0 \\ 0 & 0 & 0 & 0 & 0 & -\frac{\rho_f}{\beta_1} & 0 \\ 0 & -\frac{\rho_f}{\beta_2} & 0 & 0 & 0 & 0 & 0 \\ 0 & 0 & 0 & -\frac{\rho_f}{\beta_3} & 0 & 0 & 0 \end{bmatrix},$$

$$\boldsymbol{C}_{11} = -\begin{bmatrix} 0 & 0 & c_{13}^u & 0 & 0 & \alpha_1 M \\ 0 & 0 & c_{23}^u & 0 & 0 & \alpha_2 M \\ 0 & 0 & c_{33}^u & 0 & 0 & \alpha_3 M \\ 0 & 0 & c_{44} & 0 & 0 & 0 \\ c_{55} & 0 & 0 & 0 & 0 & 0 \\ 0 & 0 & 0 & 0 & 0 & 0 \\ 0 & 0 & -M\alpha_3 & 0 & 0 & -M \end{bmatrix}, \; \boldsymbol{C}_{21} = -\begin{bmatrix} 0 & 0 & 0 & 0 & \frac{m_1}{\beta_1} & 0 & 0 \\ 0 & 0 & 0 & \frac{m_2}{\beta_2} & 0 & 0 & 0 \\ 0 & 0 & \frac{m_3}{\beta_3} & 0 & 0 & 0 & \frac{\rho_f}{\beta_3} \\ 0 & 0 & 0 & 0 & -\frac{\rho_f}{\beta_1} & 0 & 0 \\ 0 & 0 & 0 & -\frac{\rho_f}{\beta_2} & 0 & 0 & 0 \\ 0 & 0 & -\frac{\rho_f}{\beta_3} & 0 & 0 & 0 & -\frac{\rho}{\beta_3} \end{bmatrix}, \text{ and}$$

$$\boldsymbol{D}_{22} = \begin{bmatrix} 0 & 0 & 0 & \frac{\rho_f \eta}{\beta_1 \kappa_1} & 0 & 0 \\ 0 & 0 & 0 & 0 & \frac{\rho_f \eta}{\beta_2 \kappa_2} & 0 \\ 0 & 0 & 0 & 0 & 0 & \frac{\rho_f \eta}{\beta_3 \kappa_3} \\ 0 & 0 & 0 & -\frac{\rho \eta}{\beta_1 \kappa_1} & 0 & 0 \\ 0 & 0 & 0 & 0 & -\frac{\rho \eta}{\beta_2 \kappa_2} & 0 \\ 0 & 0 & 0 & 0 & 0 & -\frac{\rho \eta}{\beta_3 \kappa_3} \end{bmatrix},$$

where $\boldsymbol{f}$ is the vector of forcing terms.

4.3.4 Symmetric form of system of poroelastic equations

To ensure the stability and convergence of the numerical scheme, we utilize a symmetric form of (4.10). The symmetric form of (4.10) for velocity and stress is expressed as

$$\boldsymbol{Q}_s \frac{\partial \boldsymbol{\tau}}{\partial t} = \sum_{i=1}^{d} \boldsymbol{A}_i \frac{\partial \boldsymbol{v}}{\partial \boldsymbol{x}_i}, \tag{4.11}$$

$$\boldsymbol{Q}_v \frac{\partial \boldsymbol{v}}{\partial t} = \sum_{i=1}^{d} \boldsymbol{A}_i^T \frac{\partial \boldsymbol{\tau}}{\partial \boldsymbol{x}_i} + \boldsymbol{D}\boldsymbol{v} + \boldsymbol{f}, \tag{4.12}$$

where

$$\boldsymbol{Q}_s = \left[\begin{array}{c|c} \boldsymbol{S} & \boldsymbol{S}\boldsymbol{\alpha} \\ \hline \boldsymbol{\alpha}^{\boldsymbol{T}}\boldsymbol{S} & \frac{1}{M} + \boldsymbol{\alpha}^T S \boldsymbol{\alpha} \end{array}\right], \quad \boldsymbol{Q}_v = \begin{bmatrix} \rho & 0 & 0 & \rho_f & 0 & 0 \\ 0 & \rho & 0 & 0 & \rho_f & 0 \\ 0 & 0 & \rho & 0 & 0 & \rho_f \\ \rho_f & 0 & 0 & m_1 & 0 & 0 \\ 0 & \rho_f & 0 & 0 & m_2 & 0 \\ 0 & 0 & \rho_f & 0 & 0 & m_3 \end{bmatrix},$$

with

$$\boldsymbol{S} = \begin{bmatrix} \frac{c_{11}c_{33}-c_{13}^2}{c_0} & \frac{c_{13}^2-c_{12}c_{33}}{c_0} & \frac{-c_{13}}{c_1} & 0 & 0 & 0 \\ \frac{c_{13}^2-c_{12}c_{33}}{c_0} & \frac{c_{11}c_{33}-c_{13}^2}{c_0} & \frac{-c_{13}}{c_1} & 0 & 0 & 0 \\ -\frac{c_{13}}{c_1} & -\frac{c_{13}}{c_1} & \frac{c_{11}+c_{12}}{c_1} & 0 & 0 & 0 \\ 0 & 0 & 0 & \frac{1}{c_{55}} & 0 & 0 \\ 0 & 0 & 0 & 0 & \frac{1}{c_{55}} & 0 \\ 0 & 0 & 0 & 0 & 0 & \frac{2}{c_{11}-c_{12}} \end{bmatrix}, \qquad \boldsymbol{\alpha} = \begin{bmatrix} \alpha_1 \\ \alpha_2 \\ \alpha_3 \\ 0 \\ 0 \\ 0 \end{bmatrix},$$

where $c_0 = c_{11}c_{33} - (c_{13}^2)$, and $\boldsymbol{\tau} = [\tau_{11},\ \tau_{22},\ \tau_{33},\ \tau_{23},\ \tau_{13},\ \tau_{12},\ p]^T$, $\boldsymbol{v} = [v_1,\ v_2,\ v_3,\ q_1,\ q_2,\ q_3]^T$, with

$$\boldsymbol{A}_1 = \begin{bmatrix} 1 & 0 & 0 & 0 & 0 & 0 \\ 0 & 0 & 0 & 0 & 0 & 0 \\ 0 & 0 & 0 & 0 & 0 & 0 \\ 0 & 0 & 0 & 0 & 0 & 0 \\ 0 & 0 & 1 & 0 & 0 & 0 \\ 0 & 1 & 0 & 0 & 0 & 0 \\ 0 & 0 & 0 & -1 & 0 & 0 \end{bmatrix}, \quad \boldsymbol{A}_2 = \begin{bmatrix} 0 & 0 & 0 & 0 & 0 & 0 \\ 0 & 1 & 0 & 0 & 0 & 0 \\ 0 & 0 & 0 & 0 & 0 & 0 \\ 0 & 0 & 1 & 0 & 0 & 0 \\ 0 & 0 & 0 & 0 & 0 & 0 \\ 1 & 0 & 0 & 0 & 0 & 0 \\ 0 & 0 & 0 & 0 & -1 & 0 \end{bmatrix},$$

$$\boldsymbol{A}_3 = \begin{bmatrix} 0 & 0 & 0 & 0 & 0 & 0 \\ 0 & 0 & 0 & 0 & 0 & 0 \\ 0 & 0 & 1 & 0 & 0 & 0 \\ 0 & 1 & 0 & 0 & 0 & 0 \\ 1 & 0 & 0 & 0 & 0 & 0 \\ 0 & 0 & 0 & 0 & 0 & 0 \\ 0 & 0 & 0 & 0 & 0 & -1 \end{bmatrix}, \quad \boldsymbol{D} = \begin{bmatrix} 0 & 0 & 0 & 0 & 0 & 0 \\ 0 & 0 & 0 & 0 & 0 & 0 \\ 0 & 0 & 0 & 0 & 0 & 0 \\ 0 & 0 & 0 & 0 & 0 & 0 \\ 0 & 0 & 0 & -\frac{\eta}{\kappa_1} & 0 & 0 \\ 0 & 0 & 0 & 0 & -\frac{\eta}{\kappa_2} & 0 \\ 0 & 0 & 0 & 0 & 0 & -\frac{\eta}{\kappa_3} \end{bmatrix}.$$

Explicit expressions for $\boldsymbol{Q}_s^{-1}$ and $\boldsymbol{Q}_v^{-1}$ are given by

$$\boldsymbol{Q}_s^{-1} = \begin{bmatrix} c_{11}+M\alpha_1^2 & c_{12}+M\alpha_1\alpha_2 & c_{13}+M\alpha_1\alpha_3 & 0 & 0 & 0 & -M\alpha_1 \\ c_{12}+M\alpha_1\alpha_2 & c_{11}+M\alpha_2^2 & c_{13}+M\alpha_2\alpha_3 & 0 & 0 & 0 & -M\alpha_2 \\ c_{13}+M\alpha_1\alpha_3 & c_{13}+M\alpha_2\alpha_3 & c_{33}+M\alpha_3^2 & 0 & 0 & 0 & -M\alpha_3 \\ 0 & 0 & 0 & c_{55} & 0 & 0 & 0 \\ 0 & 0 & 0 & 0 & c_{55} & 0 & 0 \\ 0 & 0 & 0 & 0 & 0 & \dfrac{c_{11}-c_{12}}{2} & 0 \\ -M\alpha_1 & -M\alpha_2 & -M\alpha_3 & 0 & 0 & 0 & M \end{bmatrix},$$

$$\boldsymbol{Q}_v^{-1} = \begin{bmatrix} \dfrac{m_1}{\rho m_1-\rho_f^2} & 0 & 0 & \dfrac{-\rho_f}{\rho m_1-\rho_f^2} & 0 & 0 \\ 0 & \dfrac{m_2}{\rho m_2-\rho_f^2} & 0 & 0 & \dfrac{-\rho_f}{\rho m_2-\rho_f^2} & 0 \\ 0 & 0 & \dfrac{m_3}{\rho m_3-\rho_f^2} & 0 & 0 & \dfrac{-\rho_f}{\rho m_3-\rho_f^2} \\ \dfrac{-\rho_f}{\rho m_1-\rho_f^2} & 0 & 0 & \dfrac{\rho}{\rho m_1-\rho_f^2} & 0 & 0 \\ 0 & \dfrac{-\rho_f}{\rho m_2-\rho_f^2} & 0 & 0 & \dfrac{\rho}{\rho m_2-\rho_f^2} & 0 \\ 0 & 0 & \dfrac{-\rho_f}{\rho m_3-\rho_f^2} & 0 & 0 & \dfrac{\rho}{\rho m_3-\rho_f^2} \end{bmatrix}.$$

The matrices $\boldsymbol{Q}_s$ and $\boldsymbol{Q}_v$ are Hessians of the potential and kinetic energy, respectively, computed with respect to state variables in $\boldsymbol{Q}$. Since the energy of the poroelastic system is quadratic positive-definite [3], the Hessians ($\boldsymbol{Q_s}$, $\boldsymbol{Q}_v$) are symmetric positive-definite. We also assume the Hessians are bounded as follows

$$0 < s_{\min} \leq \boldsymbol{u}^T \boldsymbol{Q}_s(\boldsymbol{x})\boldsymbol{u} \leq s_{\max} < \infty$$

$$0 < \tilde{s}_{\min} \leq \boldsymbol{u}^T \boldsymbol{Q}_s^{-1}(\boldsymbol{x})\boldsymbol{u} \leq \tilde{s}_{\max} < \infty$$

$$0 < v_{\min} \leq \boldsymbol{u}^T \boldsymbol{Q}_v(\boldsymbol{x})\boldsymbol{u} \leq v_{\max} < \infty$$

$$0 < \tilde{v}_{\min} \leq \boldsymbol{u}^T \boldsymbol{Q}_v^{-1}(\boldsymbol{x})\boldsymbol{u} \leq \tilde{v}_{\max} < \infty$$

for $\forall\ \boldsymbol{x} \in \mathbb{R}^d$ and $\forall\ \boldsymbol{u} \in \mathbb{R}^{N_d}$. Note that in (3.9), the dissipation matrix $\boldsymbol{D}$ is negative-definite.

Using the expressions for $\boldsymbol{Q}_s$ and $\boldsymbol{Q}_v$, the kinetic (K) and potential energy (V) of the

poroelastic system are expressed as

$$K = \frac{1}{2}\boldsymbol{\tau}^T \boldsymbol{Q}_s \boldsymbol{\tau}, \quad V = \frac{1}{2}\boldsymbol{v}^T \boldsymbol{Q}_v \boldsymbol{v}. \tag{4.13}$$

4.4 An energy stable discontinuous Galerkin formulation for poroelastic wave propgation

Energy stable discontinuous Galerkin methods for elastic wave propagation have been constructed based on symmetric formulations of the elastodynamic equations [97], and it is straightforward to extend such discontinuous Galerkin formulations to the symmetric poroelastic system. We assume that the domain Ω is exactly triangulated by a mesh Ω_h which consists of elements D^k which are images of a reference element $\hat{D}$ under the local affine mapping.

$$\boldsymbol{x}^k = \Phi^k \widehat{\boldsymbol{x}},$$

where $\boldsymbol{x}^k = \{x^k, y^k\}$ for $d = 2$ and $\boldsymbol{x}^k = \{x^k, y^k, z^k\}$ for $d = 3$ denote the physical coordinates on D^k and $\hat{\boldsymbol{x}} = \{\hat{x}, \hat{y}\}$ for $d = 2$ and $\widehat{\boldsymbol{x}} = \{\widehat{x}, \widehat{y}, \widehat{z}\}$ for $d = 3$ denote coordinates on the reference element. We denote the determinant of the Jacobian of Φ^k as J.

Solutions over each element D^k are approximated from a local approximation space $V_h(D^k)$, which is defined as composition of mapping Φ^k and reference approximation space $V_h(\widehat{D})$

$$V_h(D^k) = V_h(\widehat{D}) \circ \left(\Phi^k\right)^{-1}.$$

Subsequently, the global approximation space $V_h(\Omega_h)$ is defined as

$$V_h(\Omega_h) = \bigoplus_k V_h(D^k).$$

In this work, we will take $V_h(\widehat{D}) = P^N(\widehat{D})$, with $P^N(\widehat{D})$ being the space of polynomials of total degree N on the reference simplex. In two dimensions, P^N on a triangle is

$$P^N(\widehat{D}) = \{\widehat{x}^i \widehat{y}^j, 0 \leq i + j \leq N\},$$

and in three dimensions, P^N on a tetrahedron is

$$P^N(\widehat{D}) = \{\widehat{x}^i \widehat{y}^j \widehat{x}^k, 0 \leq i + j + k \leq N\}.$$

The L^2 inner product and norm over D^k is represented as

$$(\boldsymbol{g},\boldsymbol{h}) = \int_{D^k} \boldsymbol{g}\cdot\boldsymbol{h}\; d\boldsymbol{x} = \int_{\hat{D}} \left(\boldsymbol{g}\circ\Phi^k\right)\cdot\left(\boldsymbol{h}\circ\Phi^k\right) J\; d\hat{\boldsymbol{x}}, \qquad ||\boldsymbol{g}||^2_{L^2(\Omega)} = (\boldsymbol{g},\boldsymbol{g})_{L^2(D^k)},$$

where $\boldsymbol{g}$ and $\boldsymbol{h}$ are real vector-valued functions. Global L^2 inner products and squared norms are defined as the sum of local L^2 inner products and squared norms over each elements. The L^2 inner product and norm over the boundary ∂D^k of an element are similarly defined as

$$\langle \boldsymbol{u},\boldsymbol{v}\rangle_{L^2(\partial D^k)} = \int_{\partial D^k} \boldsymbol{u}\cdot\boldsymbol{v}\; d\boldsymbol{x} = \sum_{f\in\partial D^k}\int_{\hat{f}} \boldsymbol{u}\cdot\boldsymbol{v}J^f\; d\hat{\boldsymbol{x}}, \qquad ||\boldsymbol{u}||^2_{L^2(\partial D^k)} = \langle \boldsymbol{u},\boldsymbol{u}\rangle\,,$$

where J^f is the Jacobian of the mapping from a reference face $\hat{f}$ to a physical face f of an element.

Let f be a face of an element D^k with neighboring element $D^{k,+}$ and unit outward normal $\boldsymbol{n}$. Let u be a function with discontinuities across element interfaces. We define the interior value u^- and exterior value u^+ on face f of D^k

$$u^- = u|_{f\cap\partial D^k}, \qquad u^+ = u|_{f\cap\partial D^{k,+}}.$$

The jump and average of a scalar function $u\in V_h(\Omega_h)$ over f are then defined as

$$[\![u]\!] = u^+ - u^-, \qquad \{\!\{u\}\!\} = \frac{u^+ + u^-}{2}.$$

Jumps and averages of vector-valued functions $\boldsymbol{u}\in\mathbb{R}^m$ and and matrix-valued functions $\tilde{\boldsymbol{S}}\in\mathbb{R}^{m\times n}$ are defined component-wise.

$$([\![\boldsymbol{u}]\!])_i = [\![\boldsymbol{u}_i]\!], \qquad 1\le i\le m \qquad \left([\![\tilde{\boldsymbol{S}}]\!]\right)_{ij} = [\![\tilde{\boldsymbol{S}}]\!]$$

We can now specify a DG formulation for poroelastic wave equation (4.10). The symmetric hyperbolic system in (4.10) readily admits a DG formulation based on a penalty flux [99, 97]. For

the symmetric first order poroelastic wave equation, the DG formulation in strong form is given as

$$\begin{aligned}
\sum_{D^k\in\Omega_h}\left(\boldsymbol{Q}_s\frac{\partial\boldsymbol{\tau}}{\partial t},\boldsymbol{h}\right)_{L^2(D^k)} &= \sum_{D^k\in\Omega_h}\left(\left(\sum_{i=1}^{d}\boldsymbol{A}_i\frac{\partial\boldsymbol{v}}{\partial\boldsymbol{x}_i},\boldsymbol{h}\right)_{L^2(D^k)}+\left\langle\frac{1}{2}\boldsymbol{A_n}[\![\boldsymbol{v}]\!]+\frac{\alpha_{\boldsymbol{\tau}}}{2}\boldsymbol{A_n}\boldsymbol{A}_n^T[\![\boldsymbol{\tau}]\!],\boldsymbol{h}\right\rangle_{L^2(\partial D^k)}\right)\\
\sum_{D^k\in\Omega_h}\left(\boldsymbol{Q}_v\frac{\partial\boldsymbol{v}}{\partial t},\boldsymbol{g}\right)_{L^2(D^k)} &= \sum_{D^k\in\Omega_h}\left(\left(\sum_{i=1}^{d}\boldsymbol{A}_i{}^T\frac{\partial\boldsymbol{\tau}}{\partial\boldsymbol{x}_i}+\boldsymbol{f},\boldsymbol{g}\right)_{L^2(D^k)}\right.\\
&\qquad\left.+\left\langle\frac{1}{2}\boldsymbol{A}_{\boldsymbol{n}}^T[\![\boldsymbol{\tau}]\!]+\frac{\alpha_{\boldsymbol{v}}}{2}\boldsymbol{A}_n^T\boldsymbol{A_n}[\![\boldsymbol{v}]\!],\boldsymbol{g}\right\rangle_{L^2(\partial D^k)}+(\boldsymbol{D}\boldsymbol{v},\boldsymbol{g})\right),
\end{aligned}\tag{4.14}$$

for all $\boldsymbol{h},\ \boldsymbol{g}\in V_h(\Omega_h)$. Here, $\boldsymbol{A}_n$ is the normal matrix defined on a face f of an element

$$\boldsymbol{A}_n=\sum_{i=1}^{d}n_i\boldsymbol{A}_i=\begin{bmatrix}n_x&0&0&0&0&0\\0&n_y&0&0&0&0\\0&0&n_z&0&0&0\\0&n_z&n_y&0&0&0\\n_z&0&n_x&0&0&0\\n_y&n_x&0&0&0&0\\0&0&0&-n_x&-n_y&-n_z\end{bmatrix}.$$

The factors $\alpha_{\boldsymbol{\tau}}$ and $\alpha_{\boldsymbol{v}}$ are penalty parameters and defined on element interfaces. We assume that $\alpha_{\boldsymbol{\tau}},\ \alpha_{\boldsymbol{v}}\geq 0$ and are piecewise constant over each shared face between two elements. These penalty constants can be taken to be zero, which results in a non-dissipative central flux, while $\alpha_{\boldsymbol{\tau}},\ \alpha_{\boldsymbol{v}}>0$ results in energy dissipation similar to the upwind flux [6]. The stability of DG formulations are independent of the magnitude of these penalty parameters. However, a naive choice of these parameters will result in a stiffer semi-discrete system of ODEs and necessitates a smaller time under explicit time integration schemes. In this work, we take $\alpha_\tau,\alpha_v=O(1)$ unless stated otherwise.

We note that for most DG formulations, the material parameters are expected to be present in the numerical flux and in the penalty parameters α_τ,α_v. However, for the presented formulation, the scheme is stable and high order accurate even when the penalty parameters are zero. The difference in the presented formulation is that the material data has been factored out onto the mass matrix multiplying the time derivative. Multiplying by the inverse mass matrix incorporates material parameters through an appropriate combination and scaling of the flux terms.

Remark. *For several problems in Section 4.6, $\boldsymbol{f}$ is taken as a scaled point source perturbation or*

Dirac delta function $\boldsymbol{f(x)} = \boldsymbol{\beta}(\boldsymbol{x})\Delta(\boldsymbol{x}-\boldsymbol{x_0})$ *(with* $\boldsymbol{\beta(x)} \in \mathbb{R}$*). In this setting,* $\boldsymbol{f}$ *is not* L^2 *integrable and thus* $(\boldsymbol{f},\boldsymbol{g})_{L^2(D^k)}$ *may not be well-defined. In such cases, we commit a variation crime and evaluate its contribution as*

$$\sum_k (\boldsymbol{\beta}(\boldsymbol{x})\delta(\boldsymbol{x}-\boldsymbol{x}_0),\boldsymbol{g})_{L^2((D^k)} = \int_\Omega \boldsymbol{g}\cdot\boldsymbol{\beta}\delta(\boldsymbol{x}-\boldsymbol{x_0})d\boldsymbol{x} = \boldsymbol{g(x_0)}\cdot\boldsymbol{\beta}(\boldsymbol{x}_0)$$

4.4.1 Physical interpretation of central flux terms

Apart from providing the global solution of the system, the central flux terms corresponding to the velocity ($\boldsymbol{A}_n[\![\boldsymbol{v}]\!]$) and the stress ($\boldsymbol{A}_n^T[\![\boldsymbol{\tau}]\!]$) also enforce natural boundary conditions at the interface between two poroelastic media. These conditions are related to the phenomena of reflection, refraction, and diffraction of waves in the presence of inhomogeneities and interfaces. The component-wise expressions of the central flux terms $\boldsymbol{A}_n^T[\![\boldsymbol{\tau}]\!]$ and $\boldsymbol{A}_n[\![\boldsymbol{v}]\!]$ correspond to

$$\boldsymbol{\tau_s}^+\cdot\boldsymbol{n} - \boldsymbol{\tau_s}^-\cdot\boldsymbol{n} = 0, \tag{4.15}$$

$$\boldsymbol{v}^+ - \boldsymbol{v}^- = 0,, \tag{4.16}$$

$$\boldsymbol{q}^+\cdot\boldsymbol{n} - \boldsymbol{q}^-\cdot\boldsymbol{n} = 0, \tag{4.17}$$

$$p^+ - p^- = 0, \tag{4.18}$$

where the "±" convention is determined by the outward interface normal, $\boldsymbol{n}$. In this work, the outer normal vector is assumed point in the direction of the "+" side of the interface.

The physical significance of the above conditions are:

1. (4.15) describes the continuity of traction across the interface.
2. (4.16) states that the medium across the interface stays intact.
3. (4.17) implies that all fluid entering the interface should exit the other side.
4. (4.18) assumes perfect hydraulic conductivity across the interface, providing continuity of pore-fluid pressure.

These interface conditions are also consistent with the open-pore boundary conditions of [100, 101] between two different poroelastic media.

4.4.2 Boundary conditions

In many applications, the boundary condition for the top surface of a domain is assumed to be a free surface (stress free), with the remaining surfaces taken to be absorbing boundaries. We impose boundary conditions on the DG formulation by choosing appropriate exterior values which result in modified boundary numerical fluxes. Boundary conditions on the normal component of the stress can be imposed by noting that that the numerical flux contain the term $[\![\boldsymbol{A}_n^T\boldsymbol{\tau}]\!] = [\![\widetilde{\boldsymbol{S}}\boldsymbol{n}]\!]$ with

$$\widetilde{\boldsymbol{S}} = \begin{bmatrix} \tau_{11} & \tau_{12} & \tau_{13} & 0 \\ \tau_{21} & \tau_{22} & \tau_{23} & 0 \\ \tau_{31} & \tau_{32} & \tau_{33} & 0 \\ 0 & 0 & 0 & p \end{bmatrix}.$$

For a face which lies on the top surface of the domain, the free surface boundary or zero traction boundary conditions can be imposed by setting

$$[\![\boldsymbol{A}_n^T\boldsymbol{\tau}]\!] = [\![\widetilde{\boldsymbol{S}}\boldsymbol{n}]\!] = -2\widetilde{\boldsymbol{S}}^{-}\boldsymbol{n} = -2\boldsymbol{A}_n^T\boldsymbol{\tau}^{-}, \quad \boldsymbol{v}^{+} = \boldsymbol{v}^{-} \implies [\![\boldsymbol{v}]\!] = 0.$$

For problems which require the truncation of infinite or large domains, basic absorbing boundary conditions can be imposed by setting

$$[\![\boldsymbol{A}_n^T\boldsymbol{\tau}]\!] = [\![\widetilde{\boldsymbol{S}}\boldsymbol{n}]\!] = -\widetilde{\boldsymbol{S}}^{-}\boldsymbol{n} = -\boldsymbol{A}_n^T\boldsymbol{\tau}^{-}, \quad \boldsymbol{v}^{+} = 0 \implies [\![\boldsymbol{v}]\!] = -\boldsymbol{v}^{-}.$$

In addition to the above boundary conditions, more accurate absorbing boundary conditions can be also imposed using perfectly matching layers (PML) [85] or high order absorbing boundary conditions (HABC) [102, 103]. However, the implementation of such boundary conditions results in an augmented system of PDEs which can become very expensive. For example, the implementation of PML for the poroelastic wave equations results in a system of thirty PDEs [85].

In all cases, the boundary conditions are imposed by computing the numerical fluxes based on the modified jumps. This imposition guarantees energy stability for free surface and absorbing boundary conditions.

4.4.3 Energy stability

One can show that the DG formulation in (4.14) is energy stable in the absence of external forces ($\boldsymbol{f} = 0$), and free-surface and absorbing boundary conditions. Integrating by parts the velocity

equation in (4.14) gives

$$\begin{aligned}
\sum_{D^k\in\Omega_h}\left(\boldsymbol{Q}_s\frac{\partial\boldsymbol{\tau}}{\partial t},\boldsymbol{h}\right)_{L^2(D^k)} &= \sum_{D^k\in\Omega_h}\left(\left(\sum_{i=1}^{d}\boldsymbol{A}_i\frac{\partial\boldsymbol{v}}{\partial\boldsymbol{x}_i},\boldsymbol{h}\right)_{L^2(D^k)}+\left\langle\frac{1}{2}\boldsymbol{A_n}[\![\boldsymbol{v}]\!]+\frac{\alpha_{\boldsymbol{\tau}}}{2}\boldsymbol{A_n}\boldsymbol{A}_n^T[\![\boldsymbol{\tau}]\!],\boldsymbol{h}\right\rangle_{L^2(\partial D^k)}\right)\\
\sum_{D^k\in\Omega_h}\left(\boldsymbol{Q}_v\frac{\partial\boldsymbol{v}}{\partial t},\boldsymbol{g}\right)_{L^2(D^k)} &= \sum_{D^k\in\Omega_h}\left(-\left(\sum_{i=1}^{d}\boldsymbol{\tau},\boldsymbol{A}_i\frac{\partial\boldsymbol{g}}{\partial\boldsymbol{x}_i}\right)_{L^2(D^k)}\right.\\
&\qquad\left.+\left\langle\boldsymbol{A_n}^T\{\!\{\boldsymbol{\tau}\}\!\}+\frac{\alpha_{\boldsymbol{v}}}{2}\boldsymbol{A}_n^T\boldsymbol{A_n}[\![\boldsymbol{v}]\!],\boldsymbol{g}\right\rangle_{L^2(\partial D^k)}+(\boldsymbol{Dv},\boldsymbol{v})_{L^2(D^k)}\right)
\end{aligned}\tag{4.19}$$

Taking $(\boldsymbol{h},\boldsymbol{g})=(\boldsymbol{\tau},\boldsymbol{v})$ and adding both equations together yields

$$\begin{aligned}
&\sum_{D^k\in\Omega_h}\frac{1}{2}\frac{\partial}{\partial t}\left((\boldsymbol{Q}_s\boldsymbol{\tau},\boldsymbol{\tau})_{L^2(D^k)}+(\boldsymbol{Q}_v\boldsymbol{v},\boldsymbol{v})_{L^2(D^k)}\right)\\
&\quad=\sum_{D^k\in\Omega_h}\left\langle\frac{1}{2}\boldsymbol{A_n}[\![\boldsymbol{v}]\!]+\frac{\alpha_{\boldsymbol{\tau}}}{2}\boldsymbol{A_n}\boldsymbol{A}_n^T[\![\boldsymbol{\tau}]\!],\boldsymbol{h}\right\rangle_{L^2(\partial D^k)}+\left\langle\boldsymbol{A_n}^T\{\!\{\boldsymbol{\tau}\}\!\}+\frac{\alpha_{\boldsymbol{v}}}{2}\boldsymbol{A}_n^T\boldsymbol{A_n}[\![\boldsymbol{v}]\!],\boldsymbol{g}\right\rangle_{L^2(\partial D^k)}\\
&\qquad+(\boldsymbol{Dv},\boldsymbol{v})_{L^2(D^k)}\\
&\quad=\sum_{D^k\in\Omega_h}\sum_{f\in\partial D^k}\int_f\left(\frac{1}{2}\boldsymbol{\tau}^T\boldsymbol{A}_n[\![\boldsymbol{v}]\!]+\frac{\alpha_{\boldsymbol{\tau}}}{2}\boldsymbol{\tau}^T\boldsymbol{A_n}\boldsymbol{A}_n^T[\![\tau]\!]+\boldsymbol{v}^T\boldsymbol{A}_n^T\{\!\{\boldsymbol{\tau}\}\!\}+\frac{\alpha_{\boldsymbol{v}}}{2}\boldsymbol{v}^T\boldsymbol{A}_n^T\boldsymbol{A}_n[\![\boldsymbol{v}]\!]\right)\mathrm{d}\boldsymbol{x}\\
&\qquad+\sum_{D^k\in\Omega_h}\int_{D^k}\boldsymbol{v}^T\boldsymbol{Dv}\ \mathrm{d}\boldsymbol{x},
\end{aligned}$$

where the term

$$\sum_{D^k\in\Omega_h}\frac{1}{2}\frac{\partial}{\partial t}\left((\boldsymbol{Q}_s\boldsymbol{\tau},\boldsymbol{\tau})_{L^2(D^k)}+(\boldsymbol{Q}_v\boldsymbol{v},\boldsymbol{v})_{L^2(D^k)}\right)$$

is the total energy of the system. Let Γ_h denote the set of unique faces in Ω_h and let $\Gamma_{\boldsymbol{\tau}}$, Γ_{abc} denote boundaries where free-surface and absorbing boundary conditions are imposed, respectively. We separate surface terms into contributions from interior shared faces and from boundary faces. On interior shared faces, we sum the contributions from the two adjacent elements to yield

$$\begin{aligned}
&\sum_{f\in\Gamma_h\setminus\partial\Omega}\int_f\left(\frac{1}{2}\boldsymbol{\tau}^T\boldsymbol{A}_n[\![\boldsymbol{v}]\!]+\frac{\alpha_{\boldsymbol{\tau}}}{2}\boldsymbol{\tau}^T\boldsymbol{A_n}\boldsymbol{A}_n^T[\![\tau]\!]+\boldsymbol{v}^T\boldsymbol{A}_n^T\{\!\{\boldsymbol{\tau}\}\!\}+\frac{\alpha_{\boldsymbol{v}}}{2}\boldsymbol{v}^T\boldsymbol{A}_n^T\boldsymbol{A}_n[\![\boldsymbol{v}]\!]\right)\mathrm{d}\boldsymbol{x}+\sum_{D^k\in\Omega_h}\int_{D^k}\boldsymbol{v}^T\boldsymbol{Dv}\ \mathrm{d}\boldsymbol{x}\\
&=-\sum_{f\in\Gamma_h\setminus\partial\Omega}\int_f\left(\frac{\alpha_{\boldsymbol{\tau}}}{2}\left|\boldsymbol{A}_n^T[\![\boldsymbol{\tau}]\!]\right|^2+\frac{\alpha_{\boldsymbol{v}}}{2}\left|\boldsymbol{A}_n[\![\boldsymbol{v}]\!]\right|^2\right)\mathrm{d}\boldsymbol{x}+\sum_{D^k\in\Omega_h}\int_{D^k}\boldsymbol{v}^T\boldsymbol{Dv}\ \mathrm{d}\boldsymbol{x},
\end{aligned}$$

where $\boldsymbol{v}^T\boldsymbol{D}\boldsymbol{v} < 0$, since $\boldsymbol{D}$ is a negative semi-definite matrix. For faces which lie on $\Gamma_{\boldsymbol{\tau}}$, $\boldsymbol{A}_n^T = -2\boldsymbol{A}_n^T\boldsymbol{\tau}^-$, $\boldsymbol{A}_n^T\{\{\tau\}\} = 0$ and $[\![\boldsymbol{v}]\!] = 0$ yielding

$$\sum_{f\in\Gamma_{\boldsymbol{\tau}}}\int_f\left(\frac{1}{2}\boldsymbol{\tau}^T\boldsymbol{A}_n[\![\boldsymbol{v}]\!] + \frac{\alpha_{\boldsymbol{\tau}}}{2}\boldsymbol{\tau}^T\boldsymbol{A}_{\boldsymbol{n}}\boldsymbol{A}_n^T[\![\tau]\!] + \boldsymbol{v}^T\boldsymbol{A}_n^T\{\{\boldsymbol{\tau}\}\} + \frac{\alpha_{\boldsymbol{v}}}{2}\boldsymbol{v}^T\boldsymbol{A}_n^T\boldsymbol{A}_n[\![\boldsymbol{v}]\!]\right)\mathrm{d}\boldsymbol{x}$$
$$= -\sum_{f\in\Gamma_{\boldsymbol{\tau}}}\int_f\left(\alpha_{\boldsymbol{\tau}}\left|\boldsymbol{A}_n^T\boldsymbol{\tau}^-\right|^2\right)\,\mathrm{d}\boldsymbol{x}.$$

Finally, for faces in Γ_{abc}, we have $\boldsymbol{A}_n^T\{\{\tau\}\} = \frac{1}{2}\boldsymbol{A}_n^T\tau^-$, $\boldsymbol{A}_n^T[\![\tau]\!] = -\boldsymbol{A}_n^T\boldsymbol{\tau}^-$ and $[\![\boldsymbol{v}]\!] = -\boldsymbol{v}^-$, yielding

$$\sum_{f\in\Gamma_h\backslash\partial\Omega}\int_f\left(\frac{1}{2}\boldsymbol{\tau}^T\boldsymbol{A}_n[\![\boldsymbol{v}]\!] + \frac{\alpha_{\boldsymbol{\tau}}}{2}\boldsymbol{\tau}^T\boldsymbol{A}_{\boldsymbol{n}}\boldsymbol{A}_n^T[\![\tau]\!] + \boldsymbol{v}^T\boldsymbol{A}_n^T\{\{\boldsymbol{\tau}\}\} + \frac{\alpha_{\boldsymbol{v}}}{2}\boldsymbol{v}^T\boldsymbol{A}_n^T\boldsymbol{A}_n[\![\boldsymbol{v}]\!]\right)\mathrm{d}\boldsymbol{x}$$
$$= -\sum_{f\in\Gamma_{\text{abc}}}\int_f\left(\frac{\alpha_{\boldsymbol{\tau}}}{2}\left|\boldsymbol{A}_n^T\boldsymbol{\tau}^-\right|^2 + \frac{\alpha_{\boldsymbol{v}}}{2}\left|\boldsymbol{A}_n\boldsymbol{v}^-\right|^2\right)\mathrm{d}\boldsymbol{x},$$

Combining contributions from all faces and dissipation in the system yields the following result:

Theorem 2. *The DG formulation in (4.14) is energy stable for $\alpha_{\boldsymbol{\tau}}, \alpha_{\boldsymbol{v}} \geq 0$ such that*

$$\sum_{D^k\in\Omega_h}\frac{1}{2}\frac{\partial}{\partial t}\left((\boldsymbol{Q}_s\boldsymbol{\tau},\boldsymbol{\tau})_{L^2(D^k)} + (\boldsymbol{Q}_v\boldsymbol{v},\boldsymbol{v})_{L^2(D^k)}\right) = -\sum_{f\in\Gamma_h\backslash\partial\Omega}\int_f\left(\frac{\alpha_{\boldsymbol{\tau}}}{2}\left|\boldsymbol{A}_n^T[\![\boldsymbol{\tau}]\!]\right|^2 + \frac{\alpha_{\boldsymbol{v}}}{2}\left|\boldsymbol{A}_n[\![\boldsymbol{v}]\!]\right|^2\right)d\boldsymbol{x}$$
$$-\sum_{f\in\Gamma_{\boldsymbol{\tau}}}\int_f\left(\alpha_{\boldsymbol{\tau}}\left|\boldsymbol{A}_n^T\boldsymbol{\tau}^-\right|^2\right)\,d\boldsymbol{x} - \sum_{f\in\Gamma_{abc}}\int_f\left(\frac{\alpha_{\boldsymbol{\tau}}}{2}\left|\boldsymbol{A}_n^T\boldsymbol{\tau}^-\right|^2 + \frac{\alpha_{\boldsymbol{v}}}{2}\left|\boldsymbol{A}_n\boldsymbol{v}^-\right|^2\right)d\boldsymbol{x}$$
$$+\sum_{D^k\in\Omega_h}\int_{D^k}\boldsymbol{v}^T\boldsymbol{D}\boldsymbol{v}\;d\boldsymbol{x} \leq 0. \tag{4.20}$$

Since $\boldsymbol{Q}_s$ and $\boldsymbol{Q}_v$ are positive definite, the left hand side of (5.29) is an L^2-equivalent norm on $(\boldsymbol{\tau},\boldsymbol{v})$ and Theorem 1 implies that magnitude of the DG solution is non-increasing in time. This also shows that dissipation is present for positive penalization parameters, i.e. $\alpha_{\boldsymbol{\tau}}, \alpha_{\boldsymbol{v}} > 0$.

4.4.4 The semi-discrete matrix system for DG

Let $\{\phi_i\}_{i=1}^{N_p}$ be a basis for $P^N\left(\widehat{D}\right)$. In our implementation, we use nodal basis functions located at Warp and Blend interpolation points [6], which are defined implicitly using an orthogonal polynomial basis on the reference simplex. We define the reference mass matrix $\widehat{\boldsymbol{M}}$ and the physical

mass matrix $\boldsymbol{M}$ for an element D^k as

$$\left(\widehat{\boldsymbol{M}}\right)_{ij} = \int_{\widehat{D}} \phi_j \phi_i \, \mathrm{d}\boldsymbol{x}, \qquad (\boldsymbol{M}_{ij}) = \int_{D^k} \phi_j \phi_i \, \mathrm{d}\boldsymbol{x} = \int_{\widehat{D}} \phi_j \phi_i J \, \mathrm{d}\widehat{\boldsymbol{x}}.$$

For affine mappings, J is constant and $\boldsymbol{M} = J\widehat{\boldsymbol{M}}$. We also define weak differentiation matrices $\boldsymbol{S}_k$ and face mass matrices $\boldsymbol{M}_f$ such that

$$(\boldsymbol{S}_k)_{ij} = \int_{D^k} \frac{\partial \phi_j}{\partial \boldsymbol{x}_k} \phi_i \, \mathrm{d}\boldsymbol{x}, \quad (\boldsymbol{M}_f)_{ij} = \int_f \phi_j \phi_i \mathrm{d}\boldsymbol{x} = \int_{\hat{f}} \phi_j \phi_i J^f \mathrm{d}\hat{\boldsymbol{x}},$$

where J^f is the Jacobian of the mapping from the reference face $\widehat{f}$ to f. For affinely mapped simplices, J^f is also constant and $M_f = J^f \widehat{\boldsymbol{M}}_f$, where the definition of the reference face mass matrix $\widehat{\boldsymbol{M}}_f$ is analogous to the definition of the reference mass matrix $\widehat{\boldsymbol{M}}$.

Finally, we introduce weighted mass matrices. Let $w(\boldsymbol{x}) \in \mathbb{R}$ and $\boldsymbol{W}(\boldsymbol{x}) \in \mathbb{R}^{m \times n}$. Then, scalar and matrix-weighted mass matrices $\boldsymbol{M}_w$ and $\boldsymbol{M}_{\boldsymbol{W}}$ are defined as

$$(\boldsymbol{M}_w)_{ij} = \int_{D^k} w(\boldsymbol{x}) \phi_j(\boldsymbol{x}) \phi_i(\boldsymbol{x}) \, \mathrm{d}\boldsymbol{x}, \qquad \boldsymbol{M}_{\boldsymbol{W}} = \begin{bmatrix} \boldsymbol{M}_{\boldsymbol{W}_{\mathbf{1},\mathbf{1}}} & \dots & \boldsymbol{M}_{\boldsymbol{W}_{\mathbf{1},\boldsymbol{n}}} \\ \vdots & \ddots & \vdots \\ \boldsymbol{M}_{\boldsymbol{W}_{\boldsymbol{m},\mathbf{1}}} & \dots & \boldsymbol{M}_{\boldsymbol{W}_{\boldsymbol{m},\boldsymbol{n}}}, \end{bmatrix} \tag{4.21}$$

where $\boldsymbol{M}_{\boldsymbol{W}_{\boldsymbol{i},\boldsymbol{j}}}$ is the scalar weighted mass matrix weighted by the $(i,j)^{\text{th}}$ element of $\boldsymbol{W}$. Note that $\boldsymbol{M}_w, \boldsymbol{M}_{\boldsymbol{W}}$ are positive definite if $w(x), \boldsymbol{W}$ are pointwise positive definite.

Local contributions to the DG variational form may be evaluated in a quadrature-free manner using matrix-weighted mass matrices as defined above. Let $\boldsymbol{\Sigma_i}$, $\boldsymbol{V}_i$ denote vectors containing degrees of freedom for solutions components $\boldsymbol{\tau}_i$ and $\boldsymbol{v}_i$, such that

$$\begin{aligned} \boldsymbol{v}_i(\boldsymbol{x}, t) &= \sum_{j=1}^{N_p} (\boldsymbol{V}_i(t))_j \phi_j(\boldsymbol{x}), & 1 \le i \le 6 \\ \boldsymbol{\tau}_i(\boldsymbol{x}, t) &= \sum_{j=1}^{N_p} (\boldsymbol{\Sigma_i(t)})_j \phi_j(\boldsymbol{x}), & 1 \le i \le 7 \end{aligned}$$

Then, the local DG formulation can be written as a block system of ordinary differential equations by concatenating $\boldsymbol{\Sigma}_i$, $\boldsymbol{V}_i$ into single vectors $\boldsymbol{\Sigma}$ and $\boldsymbol{V}$ and using the Kronecker product $\otimes$

$$\boldsymbol{M}_{\boldsymbol{Q}_s} \frac{\partial \boldsymbol{\Sigma}}{\partial t} = \sum_{i=1}^{d} \left(\boldsymbol{A}_i \otimes \boldsymbol{S_i}\right) \boldsymbol{V} + \sum_{f \in \partial D^k} \left(\boldsymbol{I} \otimes \boldsymbol{M}_f\right) \boldsymbol{F}_\tau \tag{4.22}$$

$$\boldsymbol{M}_{\boldsymbol{Q}_v}\frac{\partial \boldsymbol{V}}{\partial t} = \sum_{i=1}^{d}\left(\boldsymbol{A}_i{}^T \otimes \boldsymbol{S_i}\right)\boldsymbol{\Sigma} + \sum_{f\in\partial D^k}\left(\boldsymbol{I}\otimes \boldsymbol{M}_f\right)\boldsymbol{F}_v + \boldsymbol{M_D V}, \tag{4.23}$$

where $\boldsymbol{F}_v$ and $\boldsymbol{F}_\tau$ denote the degrees of freedom for the velocity and stress numerical fluxes.

In order to apply a time integrator, we must invert $\boldsymbol{M}_{\boldsymbol{Q}_s}$ and $\boldsymbol{M}_{\boldsymbol{Q}_v}$. While the inversion of $\boldsymbol{M}_{\boldsymbol{Q}_s}$ and $\boldsymbol{M}_{\boldsymbol{Q}_v}$ can be parallelized from element to element, doing so typically requires either the precomputation and storage of the dense matrix inverses or on-the-fly construction and solution of a large dense matrix system at every time step. The former option requires a large amount of storage, while the latter option is computationally expensive and difficult to parallelize among degrees of freedom. This cost can be avoided when $\boldsymbol{Q}_s$ and $\boldsymbol{Q}_v$ are constant over an element D^k. In this case, $\boldsymbol{M}_{\boldsymbol{Q}_s}$ reduces to

$$\boldsymbol{M}_{\boldsymbol{Q}_s}^{-1} = \begin{bmatrix} \boldsymbol{Q}_{s(1,1)}\boldsymbol{M} & \dots & \boldsymbol{Q}_{s(1,N_d)}\boldsymbol{M} \\ \vdots & \ddots & \vdots \\ \boldsymbol{Q}_{s(N_d,1)}\boldsymbol{M} & \dots & \boldsymbol{Q}_{s(N_d,N_d)}\boldsymbol{M} \end{bmatrix}^{-1} = \left(\boldsymbol{Q}_s \otimes \boldsymbol{M}\right)^{-1} = \boldsymbol{Q}_s{}^{-1} \otimes \left(\frac{1}{J}\widehat{\boldsymbol{M}}^{\boldsymbol{-1}}\right).$$

Similarly $\boldsymbol{M}_{\boldsymbol{Q}_v}^{-1}$ and $\boldsymbol{M}_{\boldsymbol{D}}^{-1}$ can be expressed as $\boldsymbol{M}_{\boldsymbol{Q}_v}^{-1} = \boldsymbol{Q}_v{}^{-1} \otimes \left(\frac{1}{J}\widehat{\boldsymbol{M}}^{\boldsymbol{-1}}\right)$, and $\boldsymbol{M}_{\boldsymbol{D}}^{-1} = \boldsymbol{D}^{-1} \otimes \left(\frac{1}{J}\widehat{\boldsymbol{M}}^{\boldsymbol{-1}}\right)$ respectively. Applying these observations to (4.22) and (4.23) yields the following sets of local ODEs over each element

$$\frac{\partial \boldsymbol{\Sigma}}{\partial t} = \sum_{i=1}^{d}\left(\boldsymbol{Q}_s{}^{-1}\boldsymbol{A}\otimes \boldsymbol{D_i}\right)\boldsymbol{V} + \sum_{f\in\partial D^k}\left(\boldsymbol{Q}_s{}^{-1}\otimes \boldsymbol{M}_f\right)\boldsymbol{F}_\tau, \tag{4.24}$$

$$\frac{\partial \boldsymbol{V}}{\partial t} = \sum_{i=1}^{d}\left(\boldsymbol{Q}_v{}^{-1}\boldsymbol{A}^T\otimes \boldsymbol{D_i}\right)\boldsymbol{\Sigma} + \sum_{f\in\partial D^k}\left(\boldsymbol{I}\otimes \boldsymbol{M}_f\right)\boldsymbol{F}_v + \boldsymbol{M}_{\boldsymbol{Q}_v}^{-1}\boldsymbol{M_D V}, \tag{4.25}$$

where we have introduced the differentiation matrix $\boldsymbol{D}_i = \boldsymbol{M}^{-1}\boldsymbol{S}_i$ and lift matrix $\boldsymbol{L}_f = \boldsymbol{M}^{-1}\boldsymbol{M}_f$. For affine elements, both derivative and lift matrices are applied using products of geometric factors and reference derivative and lift matrices.

Unfortunately, if $\boldsymbol{Q}_s$ and $\boldsymbol{Q}_v$ varies spatially within the element, then the above approach can no longer be used to invert $\boldsymbol{Q}_s$ and $\boldsymbol{Q}_v$. Here, we follow the approach of [89], where $\boldsymbol{M}_{\boldsymbol{Q}_s}, \boldsymbol{M}_{\boldsymbol{Q}_v}$ are replaced with weight-adjusted approximations. These approximations are low storage, simple to invert, and yield an energy stable and high order accurate DG method to approximate the matrix-weighted L^2 inner product (and corresponding matrix-weighted mass-matrices $\boldsymbol{Q}_s$ and $\boldsymbol{Q}_v$).

We also note that, material coefficients $\boldsymbol{Q_s}$, $\boldsymbol{Q}_v$ appear only the left hand side of (4.10).

The right hand side of (4.10) is equivalent to the discretization of a constant coefficient system. This provides additional advantages in that the right hand side can be evaluated using efficient techniques for DG discretizations of constant-coefficient problems [104, 105].

4.5 Weight-adjusted discontinuous Galerkin (WADG) formulation for poroelastic wave propagation

We wish to apply weight-adjusted approximations to avoid the inversion of $\boldsymbol{M}_{\boldsymbol{Q}_s}$ and $\boldsymbol{M}_{\boldsymbol{Q}_v}$. Weight-adjusted inner products are high order approximations of weighted L^2 inner products. These weight-adjusted inner products result in weight-adjusted mass matrices whose inverses approximate the inverses of weighted L^2 mass matrices. We briefly review scalar and matrix-valued weight-adjusted mass matrices in the following section. Matrix weight-adjusted inner products and weight-adjusted approximations with matrix weights are discussed in more detail in C.1 and C.2.

4.5.1 Approximation of weighted mass matrix inverses

The advantage of weighted-adjusted inner products is that the corresponding weight-adjusted mass matrices are straightforward to invert. For scalar weights, weight-adjusted mass matrices are given as follows [89]

$$\boldsymbol{M}_w \approx \boldsymbol{M}\boldsymbol{M}_{\boldsymbol{1/w}}^{\boldsymbol{-1}}\boldsymbol{M}, \qquad \boldsymbol{M}_w^{-1} \approx \boldsymbol{M}^{-1}\boldsymbol{M}_{1/w}\boldsymbol{M}^{-1}.$$

By evaluating $\boldsymbol{M}_{1/w}$ in a matrix-free fashion using a sufficiently accurate quadrature rule, the inverse of the weight-adjusted mass matrix $\boldsymbol{M}^{-1}\boldsymbol{M}_{1/w}\boldsymbol{M}^{-1}$ yields a low storage implementation. Let $\hat{\boldsymbol{x}}_i, \hat{\boldsymbol{w}}_i$ denote quadrature points and weights on the reference element, and let $\boldsymbol{V}_q$ denote the generalized Vandermonde matrix

$$(\boldsymbol{V}_q)_{ij} = \phi_j(\hat{\boldsymbol{x}}_i)$$

whose columns correspond to evaluations of basis functions at quadrature points. Then, for affine elements, $M = J\widehat{\boldsymbol{M}} = J\boldsymbol{V}_q^T \mathrm{diag}(\hat{\boldsymbol{w}}_i)\boldsymbol{V}_q$, where $\widehat{\boldsymbol{M}}$ is the reference mass matrix and J is the determinant of the Jacobian of the reference-to-physical mapping, which is constant for affine mappings. Additionally,

$$\boldsymbol{M}_{1/w} = J\boldsymbol{V}_q{}^T \mathrm{diag}\left(\hat{\boldsymbol{w}}_i / w(\hat{\boldsymbol{x}}_i)\right)\boldsymbol{V}_q,$$

where $w(\hat{\boldsymbol{x}}_i)$ denotes the evaluation of the weight function $w(\boldsymbol{x})$ at quadrature points. Thus, for a vector $\boldsymbol{u}$, the inverse of the weight-adjusted mass matrix can be applied as follows

$$\boldsymbol{M}^{-1}\boldsymbol{M}_{1/w}\boldsymbol{M}^{-1}\boldsymbol{u} = \boldsymbol{M}^{-1}\boldsymbol{V}_q^T \text{diag}(\hat{\boldsymbol{w}}_i)\text{diag}\left(\frac{1}{w(\boldsymbol{x}_i)}\right)\boldsymbol{V}_q\boldsymbol{M}^{-1}\boldsymbol{u} = \boldsymbol{P}_q\text{diag}\left(\frac{1}{w(\widehat{\boldsymbol{x}}_i)}\right)\boldsymbol{V}_q\frac{1}{J}\widehat{\boldsymbol{M}}^{-1}\boldsymbol{u},$$

where $\boldsymbol{P}_q = \widehat{\boldsymbol{M}}^{-1}\boldsymbol{V}_q^T\text{diag}(\widehat{\boldsymbol{w}}_i)$ is the quadrature-based L^2 projection operator on the reference element.

For weight-adjusted inner products with matrix-valued weights, the corresponding weight-adjusted mass matrices approximate weighted L^2 mass matrices in a similar fashion

$$\begin{aligned}\boldsymbol{M}_{\boldsymbol{W}} &\approx (\boldsymbol{I}\otimes\boldsymbol{M})\boldsymbol{M}_{\boldsymbol{W}^{-1}}^{-1}(\boldsymbol{I}\otimes\boldsymbol{M}),\\ \boldsymbol{M}_{\boldsymbol{W}}^{-1} &\approx (\boldsymbol{I}\otimes\boldsymbol{M}^{-1})\boldsymbol{M}_{\boldsymbol{W}^{-1}}(\boldsymbol{I}\otimes\boldsymbol{M}^{-1}),\end{aligned}$$

where $\boldsymbol{M}_{\boldsymbol{W}}$ is the matrix-weighted mass matrix defined in (5.30). We note that $\boldsymbol{M}_{\boldsymbol{W}}$ can be applied in a quadrature based fashion component by component.

In the context of DG with explicit time-stepping, the factor of $\widehat{\boldsymbol{M}}^{-1}$ can be pre-multiplied into the right hand side (the spatial discretization). The application of the weight-adjusted mass matrices then requires only two reference matrices $\boldsymbol{V}_q$ and $\boldsymbol{P}_q$ and the values of the weight function at quadrature points $w(\widehat{\boldsymbol{x}}_i)$. In this study the number of quadrature points is $O(N^3)$ [106]. The overall storage cost for applying weight-adjusted mass matrices using the above implementation is $O(N^3)$ per element, while the pre-computation and storage of DG operators involving inverses of weighted mass matrices require $O(N^6)$ storage per element.

We derive a weight-adjusted DG method by replacing the L^2 inner products in the left hand side of the DG formulation (4.14) with weight-adjusted approximations. The right hand side of the WADG formulation is similar to the right hand side of the DG formulation (4.14), and preserves a variant of the energy stability in Theorem 1 i.e.,

$$\sum_{D^k\in\Omega_h}\frac{1}{2}\frac{\partial}{\partial t}\left(\left(T_{\boldsymbol{Q}_s{}^{-1}}\boldsymbol{\tau},\boldsymbol{\tau}\right)_{L^2(D^k)} + \left(T_{\boldsymbol{Q}_v{}^{-1}}\boldsymbol{v},\boldsymbol{v}\right)_{L^2(D^k)}\right) \leq 0,$$

where $T_{\boldsymbol{Q}_s{}^{-1}}$ are $T_{\boldsymbol{Q}_v{}^{-1}}$ are weighting operators defined in C.2.

We replace the weighted L^2 mass matrices in (4.22) and (4.23) by their weight-adjusted approximations. Inverting these weight-adjusted mass matrices yields the following local system of

Table 4.1: Material properties for several poroelastic media used in the examples [3]

Properties	Sandstone (Orthotropic)	Epoxy-glass (Orthotropic)	Sandstone (Isotropic)	Shale (Isotropic)
K_s (GPa)	80	40	40	7.6
ρ_s (kg/m^3)	2500	1815	2500	2210
c_{11} (GPa)	71.8	39.4	36	11.9
c_{12} (GPa)	3.2	1.2	12	3.96
c_{13} (GPa)	1.2	1.2	12	3.96
c_{33} (GPa)	53.4	13.1	36	11.9
c_{55} (GPa)	26.1	3	12	3.96
ϕ	0.2	0.2	0.2	0.16
κ_1 (10^{-15} m^2)	600	600	600	100
κ_3 (10^{-15} m^2)	100	100	600	100
T_1	2	2	2	2
T_3	3.6	3.6	2	2
K_f (GPa)	2.5	2.5	2.5	2.5
ρ_f (Kg/m^3)	1040	1040	1040	1040
η (10^{-3} Kg/m.s)	1	1	1	1

ODEs for $\boldsymbol{\Sigma}$ and $\boldsymbol{V}$:

$$\frac{\partial \boldsymbol{\Sigma}}{\partial t} = \left(\boldsymbol{I} \otimes \boldsymbol{M}^{-1}\right) \boldsymbol{M}_{\boldsymbol{Q}_s^{-1}} \left(\sum_{i=1}^{d} \left(\boldsymbol{A}_i \otimes \boldsymbol{S_i}\right) \boldsymbol{V} + \sum_{f \in \partial D^k} \left(\boldsymbol{I} \otimes \boldsymbol{M}_f\right) \boldsymbol{F}_\tau \right),$$

$$\frac{\partial \boldsymbol{V}}{\partial t} = \left(\boldsymbol{I} \otimes \boldsymbol{M}^{-1}\right) \boldsymbol{M}_{\boldsymbol{Q}_v^{-1}} \left(\sum_{i=1}^{d} \left(\boldsymbol{A}_i{}^T \otimes \boldsymbol{S_i}\right) \boldsymbol{\Sigma} + \sum_{f \in \partial D^k} \left(\boldsymbol{I} \otimes \boldsymbol{M}_f\right) \boldsymbol{F}_v + \boldsymbol{M_D V} \right).$$

Matrices $\left(\boldsymbol{I} \otimes \boldsymbol{M}^{-1}\right) \boldsymbol{M}_{\boldsymbol{Q}_s^{-1}}$ and $\left(\boldsymbol{I} \otimes \boldsymbol{M}^{-1}\right) \boldsymbol{M}_{\boldsymbol{Q}_v^{-1}}$ are applied in a matrix-free fashion using reference element matrices and values of $\boldsymbol{Q}_s^{-1}$ and $\boldsymbol{Q}_v^{-1}$ at quadrature points in (4.11) and (4.12). The convergence analysis of the numerical scheme is performed in C.3.

4.6 Numerical experiments

In this section, we present several numerical experiments validating the stability and accuracy of proposed method in two and three dimensions. The convergence of the new DG formulation in piecewise constant isotropic poroelastic media is confirmed. Finally, the method is applied to problems with anisotropy and micro-heterogeneities (sub-element variations).

In all experiments, we follow [107] and compute the application of weight-adjusted mass

matrices using a quadrature which is exact for polynomials of degree $(2N+1)$. Time integration is performed using the low-storage 4^{th} order five-stage Runge-Kutta scheme of Carpenter and Kennedy [108], and the time step is chosen based on the global estimate

$$dt = \min_k \frac{C_{CFL}}{\sup_{x\in\Omega} \|\boldsymbol{C}(\boldsymbol{x})\|_2 \, C_N \, \|J^f\|_{L^\infty(\partial D^k)} \, \|J^{-1}\|_{L^\infty(D^k)}} \tag{4.26}$$

where $C_N = O(N^2)$ is the order-dependent constant in the surface polynomial trace inequality [109] and C_{CFL} is a tunable global CFL constant. This estimate is derived by bounding the eigenvalues of the spatial DG discretization matrix appearing in the semi-discrete system of ODEs. This choice of dt is very conservative as it is derived based on an upper bound on the spectral radius.

4.6.1 Spectra and choice of penalty parameter

We first verify the energy stability of proposed DG formulation. Let $\boldsymbol{A}_h$ denote the matrix induced by the global semi-discrete DG formulation, such that time evolution of the solution $\boldsymbol{\tau}, \boldsymbol{v}$ is governed by

$$\frac{\partial \boldsymbol{Q}}{\partial t} = \boldsymbol{A}_h \boldsymbol{Q},$$

where $\boldsymbol{Q}$ denotes a vector of degrees of freedom for $(\boldsymbol{\tau}, \boldsymbol{v})$. We show in Figure 4.1 eigenvalues of $\boldsymbol{A}_h$ for $\alpha_{\boldsymbol{\tau}} = \alpha_{\boldsymbol{v}} = 0$ and $\alpha_{\boldsymbol{\tau}} = \alpha_{\boldsymbol{v}} = 1$ with material parameters of isotropic sandstone (given in Table 4.1). The discretization parameters are $N = 3$ and $h = 1/2$. In both cases, the largest real part of any eigenvalues is $O(10^{-14})$, which suggests that the semi-discrete scheme is indeed energy stable.

For practical simulations, the choice of $\alpha_{\boldsymbol{\tau}}, \alpha_{\boldsymbol{v}}$ remains to be specified. Taking $\alpha_{\boldsymbol{\tau}}, \alpha_{\boldsymbol{v}} > 0$ results in damping of of under-resolved spurious components of the solutions. However, a naive selection of $\alpha_{\boldsymbol{\tau}}, \alpha_{\boldsymbol{v}}$ can result in an overly restrictive time-step restriction for stability. A guiding principle for determining appropriate values of the penalty parameters $\alpha_{\boldsymbol{\tau}}, \alpha_{\boldsymbol{v}}$ is to ensure that the spectral radius is the same magnitude as the case when $\alpha_{\boldsymbol{\tau}} = \alpha_{\boldsymbol{v}} = 0$. For example, the spectral radius of $\boldsymbol{A}_h$, $\rho(\boldsymbol{A}_h)$ is 18.0034 for $\alpha_{\boldsymbol{\tau}}, \alpha_{\boldsymbol{v}} = 0$ which is $O(N^2/h)$. The spectral radius $\rho(\boldsymbol{A}_h)$ is 19.1217 for $\alpha_{\boldsymbol{\tau}}, \alpha_{\boldsymbol{v}} = 0.5$, while the spectral radius for $\alpha_{\boldsymbol{\tau}}, \alpha_{\boldsymbol{v}} = 1$ is $\rho(\boldsymbol{A}_h) = 44.44$. Since the maximum stable timestep is proportional to the spectral radius, taking $\alpha_{\boldsymbol{\tau}}, \alpha_{\boldsymbol{v}} = 1$ in this case results in a more restrictive CFL condition. This phenomena is related to observations in [99] that large penalty parameters result in extremal eigenvalues of $\boldsymbol{A}_h$ with very large negative real parts. The optimal choice of scaling also depends on the media heterogeneities on elements adjacent to an interface.

In all following experiments, we use $\alpha_{\boldsymbol{\tau}} = \alpha_{\boldsymbol{v}} = 1$ unless specified otherwise.

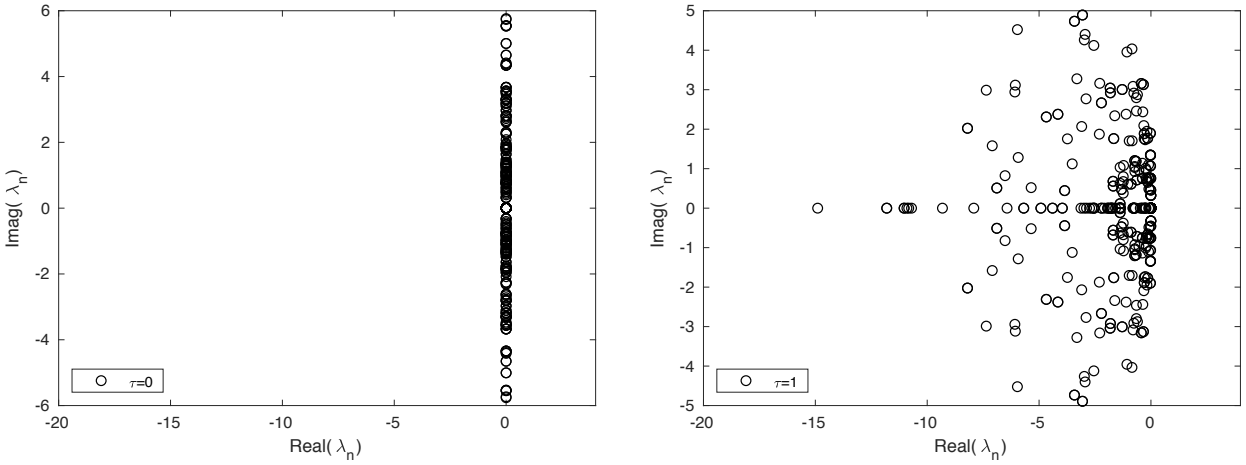

(a) $\alpha_{\boldsymbol{\tau}} = \alpha_{\boldsymbol{v}} = 0$ (b) $\alpha_{\boldsymbol{\tau}} = \alpha_{\boldsymbol{v}} = 1$

Figure 4.1: Spectra for $N = 3$ and $h = 1/2$ with a material property of isotropic Sandstone (Table 4.1). For $\alpha_{\boldsymbol{\tau}} = \alpha_{\boldsymbol{v}} = 0$ and $\alpha_{\boldsymbol{\tau}} = \alpha_{\boldsymbol{v}} = 1$, the largest real part of spectra are 1.6431e-14 and 6.3412e-15, respectively.

Next, we study the accuracy and convergence of the our DG method for a plane wave propagating in an isotropic porous sandstone with material properties given in Table 4.1 (Column 4). Unless otherwise stated, we report relative L^2 errors for all components of the solution $\boldsymbol{U} = (\boldsymbol{\tau}, \boldsymbol{v})$

$$\frac{\|\boldsymbol{U} - \boldsymbol{U}_h\|_{L^2(\Omega)}}{\|\boldsymbol{U}\|_{L^2(\Omega)}} = \frac{\left(\sum_{i=1}^{m} \|\boldsymbol{U_i} - \boldsymbol{U_{i,h}}\|^2_{L^2(\Omega)}\right)^{1/2}}{\left(\sum_{i=1}^{m} \|\boldsymbol{U}_i\|^2_{L^2(\Omega)}\right)^{1/2}}.$$

4.6.2 Plane wave in a poroelastic medium

The analytical solution to (4.10) for a plane wave is given as

$$\boldsymbol{Q}_n(\boldsymbol{x}, t) = \boldsymbol{Q}_n^0 \exp[\mathrm{i} \cdot (\omega t - \boldsymbol{k} \cdot \boldsymbol{x})], \qquad n = 1...13, \tag{4.27}$$

where $\boldsymbol{Q}_n^0$ is the initial amplitude vector of stress and velocity components; ω are wave frequencies; $\boldsymbol{k} = (k_x, k_y, k_z)$ is the wave-number vector. To achieve realistic poroelastic behavior, we superimpose three plane waves, of the form given by (4.27), corresponding to a fast P-wave, an S-wave and a slow P-wave.

Now, we briefly describe how we determine the the wave frequencies ω. Substituting (4.27)

into (4.10) yields

$$\omega \boldsymbol{Q}_n^0 = (\boldsymbol{A}k_x + \boldsymbol{B}k_y + \boldsymbol{C}k_z - \mathrm{i}\boldsymbol{E})\boldsymbol{Q}_n^0 \tag{4.28}$$

Solving the three eigenvalues problem for in (4.27) for each wave mode l yields in matrix of right eigenvectors ($R_{mn}^{(l)}$) and eigenvalue (ω_l). Following [110, 4], the solution of (4.10) can be constructed as

$$\boldsymbol{Q}_n(\boldsymbol{x}, t) = \sum_{l=1}^{3} R_{mn}^{(l)} \gamma_n^{(l)} \exp[\mathrm{i} \cdot (\omega^{(l)} t - \boldsymbol{k^{(l)}} \cdot \boldsymbol{x})], \tag{4.29}$$

where $\gamma_n^{(l)}$ is a amplitude coefficient with $\gamma_1^{(1)} = \gamma_2^{(2)} = \gamma_4^{(3)} = 100$.

For completeness, we perform convergence analyses for inviscid and viscid media separately.

4.6.2.1 Inviscid case ($\eta = 0$)

The error is computed for an inviscid brine-filled ($\eta = 0$) isotropic sandstone. The inviscid nature of the fluid implies that $\boldsymbol{D} = \boldsymbol{0}$. We show in Figure 4.2 the L^2 errors computed at T=1 and CFL=1, using uniform triangular meshes constructed by bisecting an uniform mesh of quadrilaterals along the diagonal. Figure 4.2a and 2b show the convergence plot using the central flux ($\alpha_{\boldsymbol{v}} = \alpha_{\boldsymbol{\tau}} = 0$) and penalty flux ($\alpha_{\boldsymbol{v}} = \alpha_{\boldsymbol{\tau}} = 1$) respectively. Plots of error, showing the convergence for stress and velocity individually, are shown in Figure 4.2c and 4.2d. For $N = 1, ..., 5$, $O(h^{N+1})$, rates of convergence are observed. We note that for $N = 4$ and $N = 5$, we observe results for both fluxes which are better than the 4^{th} order accuracy of our time-stepping scheme. This is most likely due to the benign nature of the solution in time and the choice of time step (5.35) which scales as $O(h/N^2)$. For $N = 4, 5$, the results of Figure 4.2 suggest that the resulting time step is small enough such that temporal errors of $O(dt^4)$ are small relative to spatial discretization errors of $O(h^{N+1})$.

4.6.2.2 Viscid case ($\eta \neq 0$)

The poroelastic formulations used by Carcione [3] and de la Puente et al. [4] produce a stiff system of ODEs due to the presence of the dissipative matrix $\boldsymbol{D}$. Consequently, Carcione used a Strang's 2^{nd} order operator splitting approach [111] to avoid small Δt, while de la Puente et al. [4] circumvented the effect of stiffness using a local implicit time-stepping approach to achieve the convergence rate of $O(h^{N+1})$. The poroelastic formulation and numerical discretization used in this study do not appear to produce equally stiff systems of ODEs, and Strang splitting is not required.

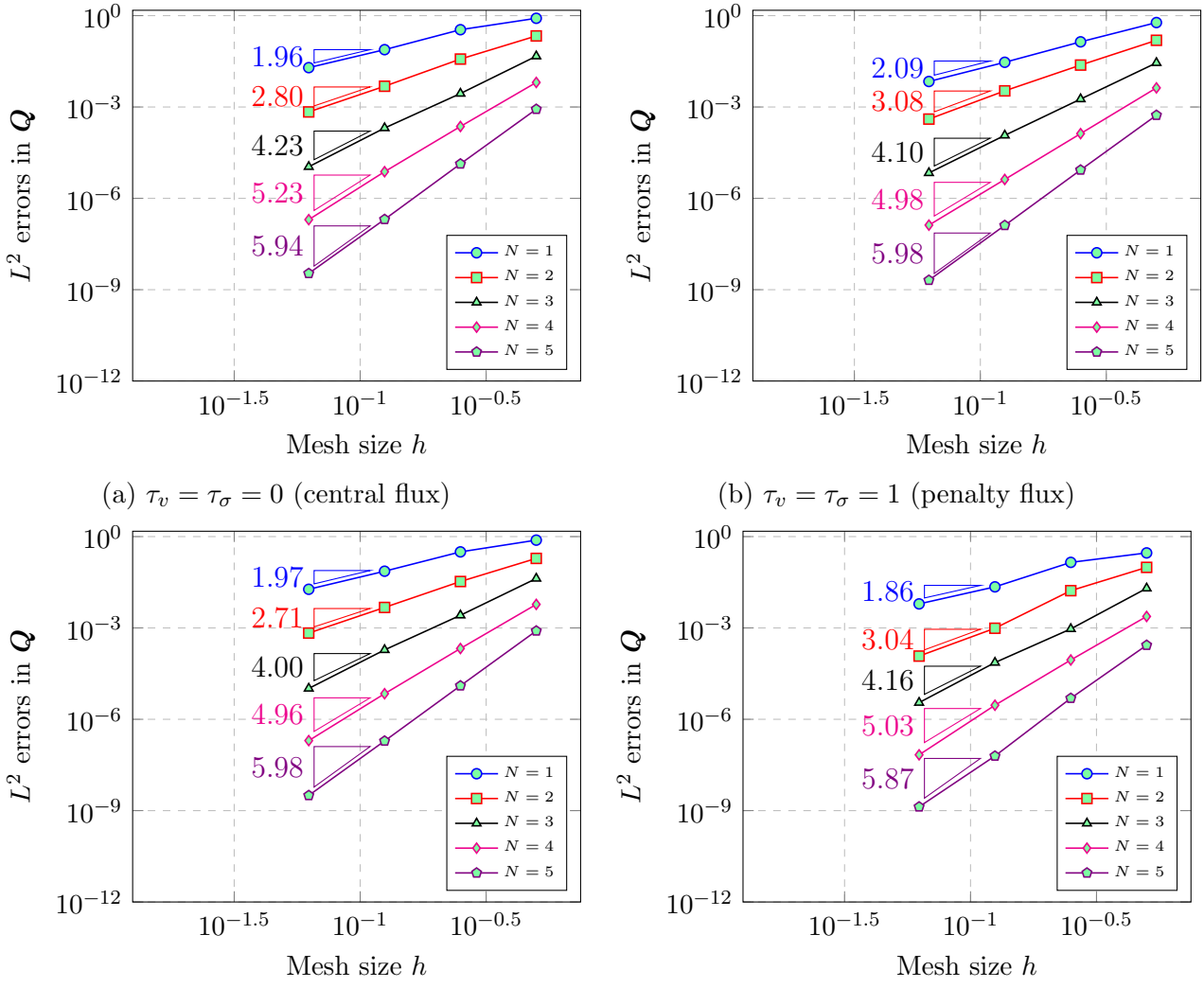

(a) $\tau_v = \tau_\sigma = 0$ (central flux)

(b) $\tau_v = \tau_\sigma = 1$ (penalty flux)

(c) $\tau_v = \tau_\sigma = 0$ (central flux) for velocity ($\boldsymbol{v}$)

(d) $\tau_v = \tau_\sigma = 0$ (central flux) for stress ($\boldsymbol{\tau}$)

Figure 4.2: Convergence of L^2 error for plane wave in porolastic media with $\eta = 0$-inviscid case

However, for a complete analysis, the convergence of the proposed DG formulation in viscid case is studied using both a unified DG scheme (where we incorporate the dissipative matrix $\boldsymbol{D}$ directly into the explicit time-stepping scheme) as well as a second order Strang operator splitting [111].

Operator splitting separates the dissipative term from the conservative term at each time step. We solve the dissipative part (stiff) part of the system analytically and solve the conservative part by using the proposed DG formulation. We rewrite the system with non-zero forcing function as follows

$$\frac{\partial \boldsymbol{Q}}{\partial t} = \boldsymbol{A}_h \boldsymbol{Q} + \boldsymbol{f}, \tag{4.30}$$

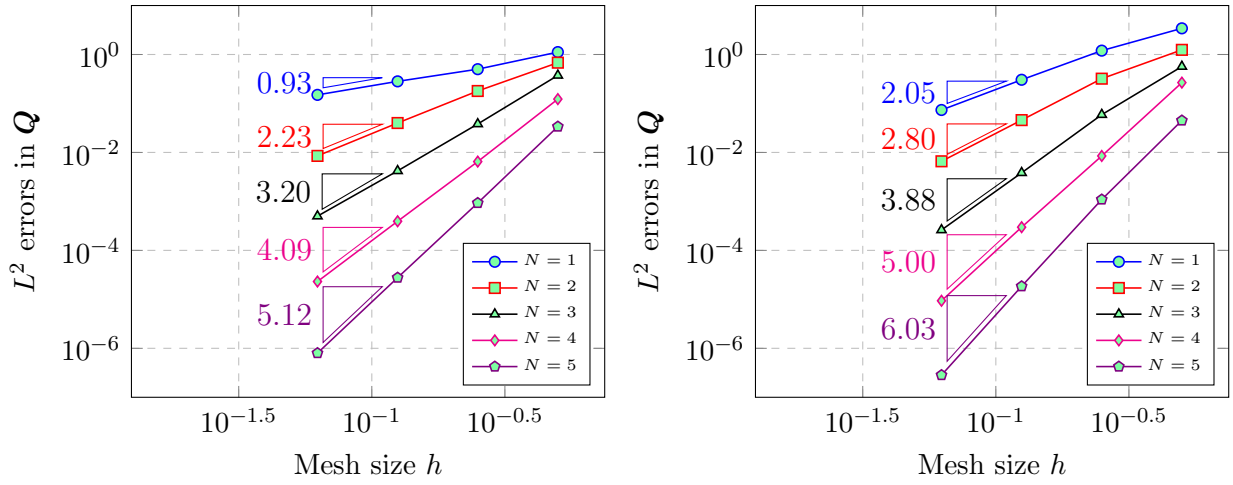

(a) $\tau_v = \tau_\sigma = 0$ (central flux)

(b) $\tau_v = \tau_\sigma = 1$ (penalty flux)

Figure 4.3: Convergence of L^2 error for plane wave in poroelastic media for viscid case ($\eta \neq 0$) with unified DG scheme

The formal solution of (4.30) is given as

$$\boldsymbol{Q}(t) = \exp(\boldsymbol{A}_h t)\boldsymbol{Q_0} + \int_0^t \exp(\tau \boldsymbol{A}_h)\boldsymbol{f}(t-\tau)d\tau, \tag{4.31}$$

where $\exp(\boldsymbol{A}_h t)$ is an evolution operator.

Using the operator splitting approach, the propagation matrix can be partitioned as

$$\boldsymbol{A}_h = \boldsymbol{A}_c + \boldsymbol{A}_d, \tag{4.32}$$

where the subscript c indicates the matrix representing the conservative part of the system, and the subscript d indicates the diffusive matrix, representing low order terms coupled with the viscosity (η). Subsequently, the evolution operator can be expressed as

$$\exp(\boldsymbol{A}_h t) = \exp[(\boldsymbol{A}_{h_c} + \boldsymbol{A}_{h_d})t]. \tag{4.33}$$

By using the product formula, (4.33) is expressed as

$$\exp(\boldsymbol{A}_h dt) = \exp\left(\frac{1}{2}\boldsymbol{A}_{h_d} dt\right) \exp(\boldsymbol{A}_{h_c} dt) \exp\left(\frac{1}{2}\boldsymbol{A}_{h_d} dt\right). \tag{4.34}$$

It can be shown that (4.33) is second order accurate in dt. Thus, (4.34) allows us to solve the stiff

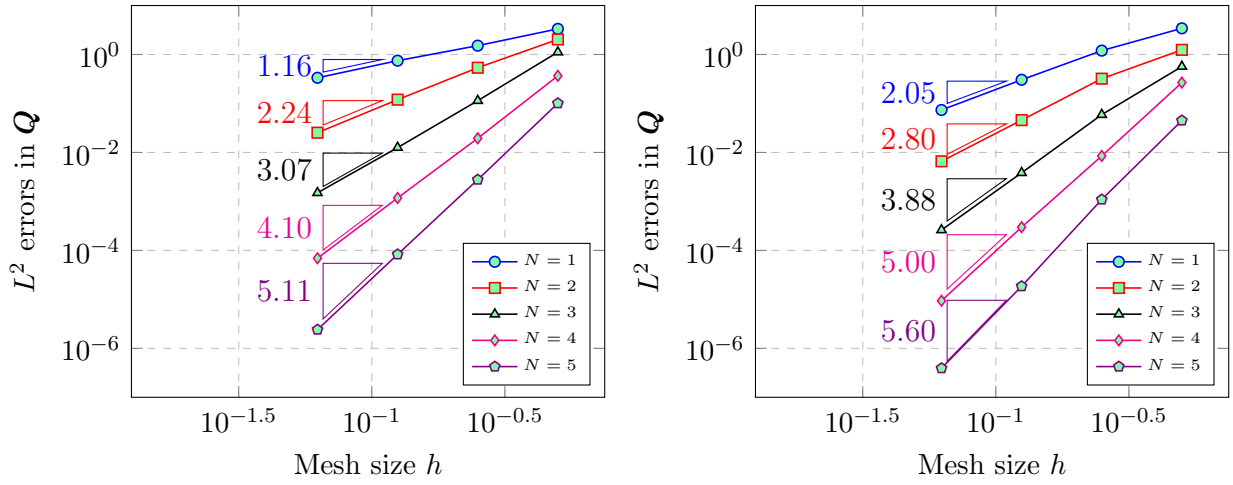

(a) $\tau_v = \tau_\sigma = 0$ (central flux)

(b) $\tau_v = \tau_\sigma = 1$ (penalty flux)

Figure 4.4: Convergence of L^2 error for plane wave in poroelastic media for viscid case ($\eta \neq 0$) with paired DG and Strang splitting approach

part separately. The solution of the stiff part of the system can be derived analytically and is shown in C.4.

We show in Figure 4.3 the L^2 errors for viscid case, computed at T=1 and CFL=1 using uniform triangular meshes. Figure 4.3a and 3b show convergence plots using the central flux ($\alpha_{\boldsymbol{v}} = \alpha_{\boldsymbol{\tau}} = 0$) and penalty flux ($\alpha_{\boldsymbol{v}} = \alpha_{\boldsymbol{\tau}} = 1$), respectively. For $N = 1, ..., 5$, $O(h^{N+1})$ rate of convergence are observed when using the penalty flux $\alpha_{\boldsymbol{v}} = \alpha_{\boldsymbol{\tau}} = 1$. When using a central flux ($\alpha_{\boldsymbol{v}} = \alpha_{\boldsymbol{\tau}} = 0$), we observe a so-called "even-odd" pattern [6, 98], with convergence rate $O(h^N)$ for odd N and between $O(h^{N+1/2})$ and $O(h^{N+1})$ for even N.

Similar to the inviscid case, for $N = 4$ and $N = 5$, we observe results for both fluxes which are better than the 4^{th} order accuracy of our time-stepping, due to the fact that temporal error are small relative to spatial discretization error. Furthermore, the spectral radius $\rho(\boldsymbol{A}_h)$ for $N = 4$ and $h = 1/2$ is 25.91 which is of $O(N^2/h)$. Since $N^2/h > ||\boldsymbol{D} = 1.667||$, the dissipative term does not increase the stiffness of the high order DG scheme.

We show in Figure 4.4 the L^2 errors for the viscid case using Strang splitting, computed at T=1 and CFL=1. Figure 4.4a and 4.4b show convergence plots using the central flux ($\alpha_{\boldsymbol{v}} = \alpha_{\boldsymbol{\tau}} = 0$) and penalty flux ($\alpha_{\boldsymbol{v}} = \alpha_{\boldsymbol{\tau}} = 1$), respectively. Observations on convergence are similar to those in the unified DG scheme. Here, it is worth noting that for $N = 5$ the convergence rate is 5.60, which does not match the optimal theoretical rate of $O(h^{N+1})$. This is may be due to the second order accuracy of the splitting scheme resulting in larger temporal errors relative to the spatial discretization errors $O(h^{N+1})$.

4.6.3 Application examples

We next demonstrate the accuracy and flexibility of the proposed DG for several application-based problems in linear poroelasticity with micro heterogeneities and anisotropy. All computations are done using penalty parameters $\alpha_{\boldsymbol{v}} = \alpha_{\boldsymbol{\tau}} = 1$ unless specified otherwise. In the subsequent sections, the field $\boldsymbol{b}$ represents the center of mass particle velocity vector [87], which is expressed as

$$\boldsymbol{b} = \boldsymbol{v} + \left(\frac{\rho_f}{\rho}\right)\boldsymbol{q}. \tag{4.35}$$

In subsequent simulations, the forcing is applied to both the $z-$ component of stress τ_{zz} and the fluid pressure p by a Ricker wavelet point source

$$f(\boldsymbol{x}, t) = (1 - 2(\pi f_0(t - t_0))^2)\exp[-(\pi f_0(t - t_0))^2]\delta(\boldsymbol{x} - \boldsymbol{x}_0), \tag{4.36}$$

where $\boldsymbol{x}_0$ is the position of the point source and f_0 is the central frequency.

In the following simulations, three types of poroelastic waves are observed: the fast P wave, S wave, and slow P wave. The fast P wave has solid and fluid motion in phase, while the slow P wave (Biot's mode) has the solid and fluid motion out of phase with one another. At low frequencies, the slow P wave is diffusive in character as viscous forces dominate over inertial forces. However, at high frequencies, the dominance of inertial forces over viscous forces results in the propagation of the slow P wave.

4.6.3.1 Orthotropic sandstone

To illustrate the effect of anisotropy on poroelastic wave propagation, we perform a computational experiment in orthotropic sandstone with material properties given in Table 4.1. The size of the computational domain is 18.25 m $\times$ 18.25 m. The domain is discretized with uniform triangular element with a minimum edge length of 5 cm. Figures 4.5(a)-(d) represent the $x-$ and $z-$ components of the center of mass particle velocity of the orthotropic sandstone, where (a) and (b) correspond to the inviscid case ($\eta = 0$), and (c) and (d) to the viscid case ($\eta \neq 0$). The central frequency of the forcing function is $f_0 = 3730$ Hz, and polynomials of degree $N = 4$ are used. The propagation time is 1.56 ms. Three events can be observed: the fast P mode ($\mathrm{P_f}$, outer wavefront), the shear wave (S, middle wavefront), and the slow P mode ($\mathrm{P_s}$, inner wavefront). In the viscid case, the slow mode diffuses faster and the medium behaves almost as a single phase medium.

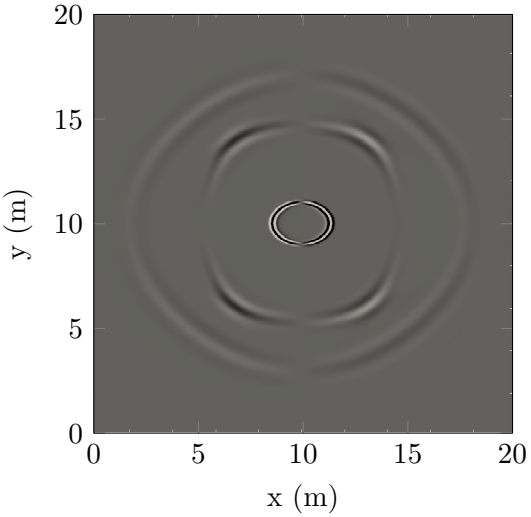

(a) Orthotropic Sandstone, b_x with $\eta = 0$

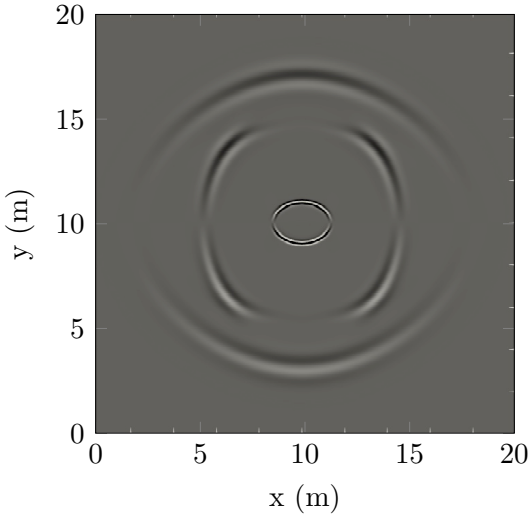

(b) Orthotropic Sandstone, b_z with $\eta = 0$

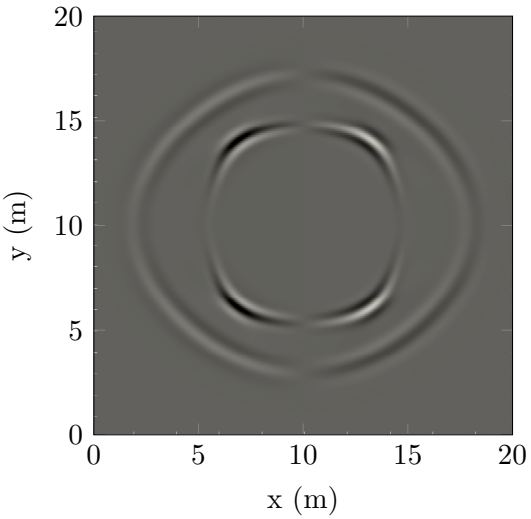

(c) Orthotropic Sandstone, b_x with $\eta \neq 0$

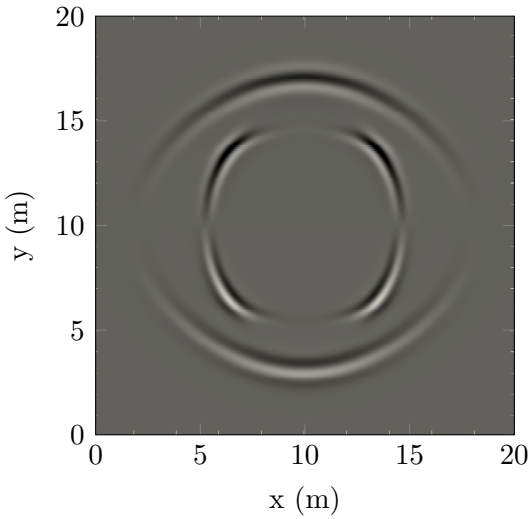

(d) Orthotropic Sandstone, b_z with $\eta \neq 0$

Figure 4.5: Snapshots of the centre of mass particle velocity in orthotropic sandstone, computed at $t = 1.56$ ms, where (a) and (b) corresponds to $\eta = 0$, and (c) and (d) corresponds to $\eta \neq 0$. The central frequency of the forcing function is 3730 Hz. The solution is computed using polynomials of degree $N = 4$.

4.6.3.2 Epoxy-glass material

Snapshots of the $x-$ and $z-$ components of the center of mass particle velocity in the epoxy-glass porous medium are shown in Figure 4.6. Figures 4.6(a) and (b) correspond to the inviscid case ($\eta = 0$), and (c) and (d) to the viscid case ($\eta \neq 0$). The central frequency is $f_c = 3135$ Hz and the propagation time is 1.8 ms. It is worth noting the cuspidal triangles of S and P_s, which are phenomena typical in anisotropic materials. At 45^o, the polarization of the P_s mode wave is almost horizontal, which confirms the results shown in Figure 4.3(b) of [3].

4.6.3.3 Isotropic-isotropic and isotropic-anisotropic layered model

In this example, we illustrate the effect of an interface between two layers of porous media. We constructed two models, each with two layers. In the first model, the top and bottom layer are isotropic and made of shale and sandstone. In second model, the sandstone is replaced by orthotropic sand stone. The detailed material properties are given in Table 4.1. These models are considered to be filled with brine ($\eta = 0$). The size of the computational domain is 1400 m $\times$ 1500 m in the x and z directions, respectively. The minimum edge size of the triangular elements used to mesh the domain is 8 m. The point source is located at (750 m, 900 m) with a Ricker wavelet of frequency 45 Hz. The propagation time for isotropic and anisotropic model are 0.25 s and 0.22 s, respectively. The simulation is performed using polynomials of degree $N = 4$. Snapshots of the z component of the center of mass particle velocity are shown in Figures 4.7a and 4.7b for inviscid ($\eta = 0$) and viscid fluid ($\eta \neq 0$), respectively. Figure 4.7 clearly shows the direct, reflected, and transmitted wavefront, corresponding to all three modes. The slow P wave is more prominent in the shale. The effect of anisotropy on all three modes is clearly seen as wavefronts moves with different phase velocities.

Here, we illustrate the effect of viscosity of fluid on a slow P wave using an isotropic two layer model with the same discretization parameters as those used in Figure 4.7a. We compute numerical solutions for two cases. In first case, both layers are assumed to be brine filled with ($\eta = 0$) and are represented by inviscid-inviscid model. However, in the second case we assume that the bottom layer is filled with a viscous fluid and represented as inviscid-viscid model. Figure 4.8a shows the snapshot of the z component of the center of mass particle velocity for the inviscid-inviscid model, which shows a direct, reflected, and transmitted slow P wave. On the other hand, Figure 4.8b shows a snapshot of the z component of the center of mass particle velocity for the inviscid-viscid model, which shows only a direct and reflected slow P wave. The transmitted slow P wave is missing in

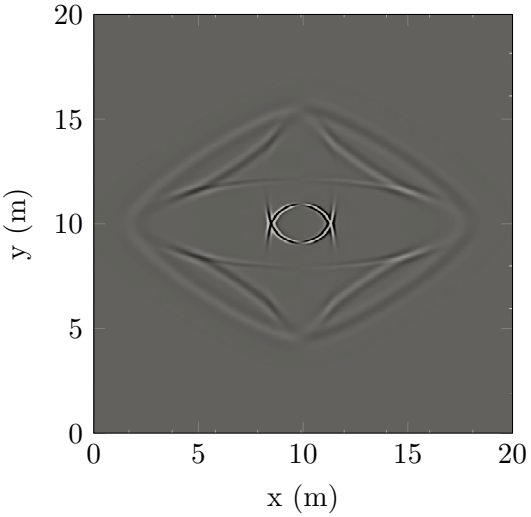

(a) Epoxy-glass, b_x with $\eta = 0$

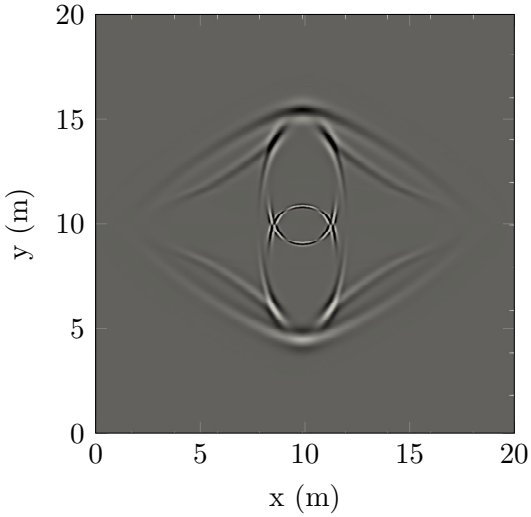

(b) Epoxy-glass, b_z with $\eta = 0$

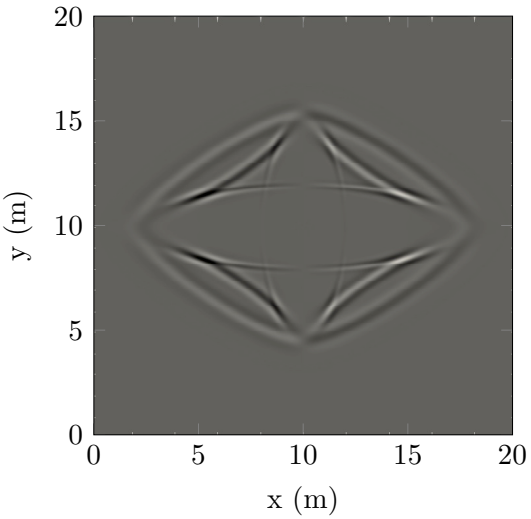

(c) Epoxy-glass, b_x with $\eta \neq 0$

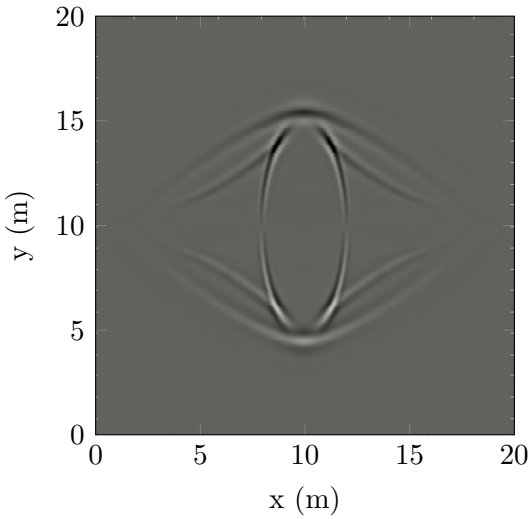

(d) Epoxy-glass, b_z with $\eta \neq 0$

Figure 4.6: Snapshots of the centre of mass particle velocity in epoxy-glass, computed at $t = 1.8$ ms, where (a) and (b) corresponds to $\eta = 0$, and (c) and (d) corresponds to $\eta \neq 0$. The central frequency of the forcing function is 3135 Hz. The solution is computed using polynomials of degree $N = 4$.

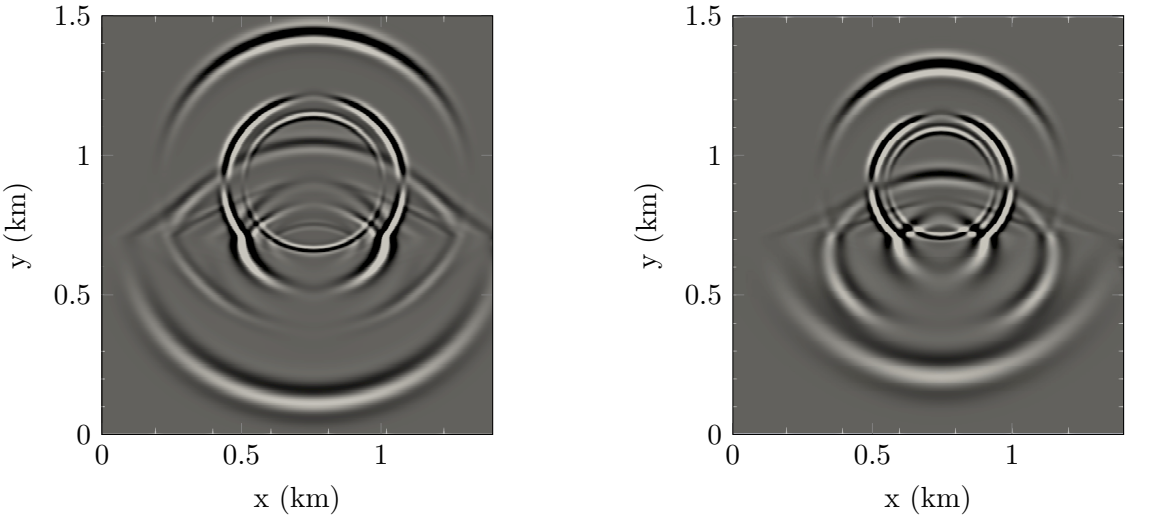

(a) Isotropic layered model, b_z (b) Anisotropic layered model, b_z

Figure 4.7: Snapshots of the $z-$ component of centre of mass particle velocity in (a) isotropic layered model computed at $t = 0.25$ s (b) anisotropic layered model computed at $t = 0.22$ s. The central frequency of the forcing function is 45 Hz. The solution is computed using polynomials of degree $N = 4$.

the inviscid-viscid model, which confirms Biot's observation on slow P waves for the low frequency regime [8].

4.6.3.4 Piecewise constant vs sub-cell heterogeneities

To address the effect of micro-heterogenities on poroelastic wave propagation, we illustrate the efficacy of WADG method over a traditional DG method using piecewise constant coefficients on each element. We modulate the material properties contained in $\boldsymbol{Q}_s^{-1}$ and $\boldsymbol{Q}_v^{-1}$ with

$$\rho = 1 + .5 \sin(2\pi \boldsymbol{x}) \sin(2\pi \boldsymbol{y}),$$

where $\boldsymbol{x}$ and $\boldsymbol{y}$ are coordinates of of cubature nodes. We construct piecewise constant approximations to $\boldsymbol{Q}_s^{-1}$ and $\boldsymbol{Q}_v^{-1}$ by taking the local average over each element.

Figure 4.9a and 4.9b show piecewise smooth and high order heterogeneous approximations of bulk density, respectively. To demonstrate the effect of subelement variations on wave propagation, we first compute the solutions approximated by polynomials of degree $N = 2$ with $K_{1\mathrm{D}} = 64$, where $K_{1\mathrm{D}}$ denotes the number of elements in one direction. These solutions are shown in Figures 4.10a (piecewise constant) and 10b (WADG). The solutions are similar, as the lower resolution due to the piecewise constant approximation of media is offset by the larger number of elements. Next,

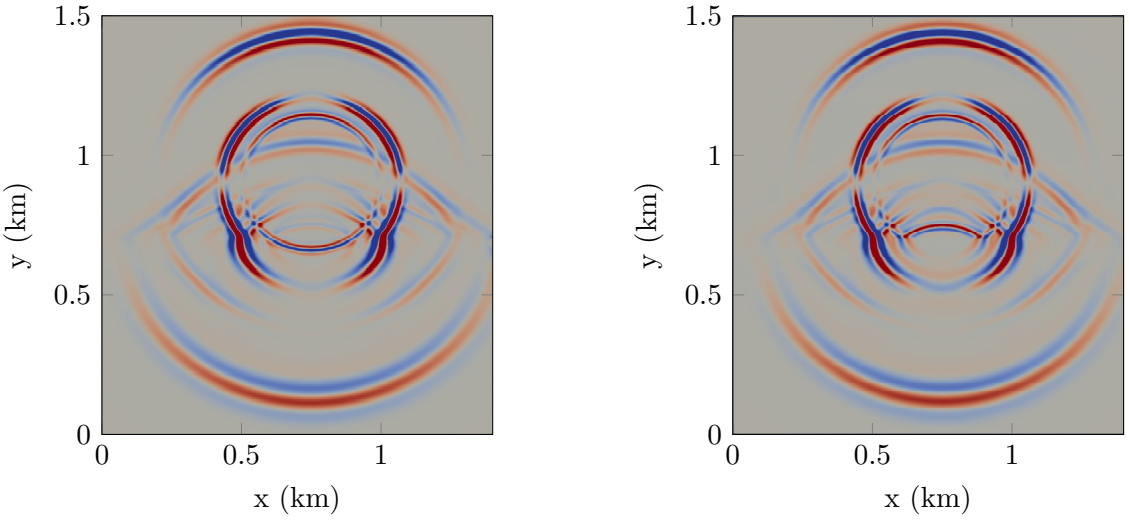

(a) Inviscid-inviscid layered model, b_z (b) Inviscid-viscid layered model, b_z

Figure 4.8: Snapshots of the $z-$ component of centre of mass particle velocity in (a) Inviscid-inviscid layered model (b) Inviscid-viscid layered model, computed at $t = 0.25$ s. The central frequency of the forcing function is 45 Hz for a viscid case ($\eta = 0$). The solution is computed using polynomials of degree $N = 4$.

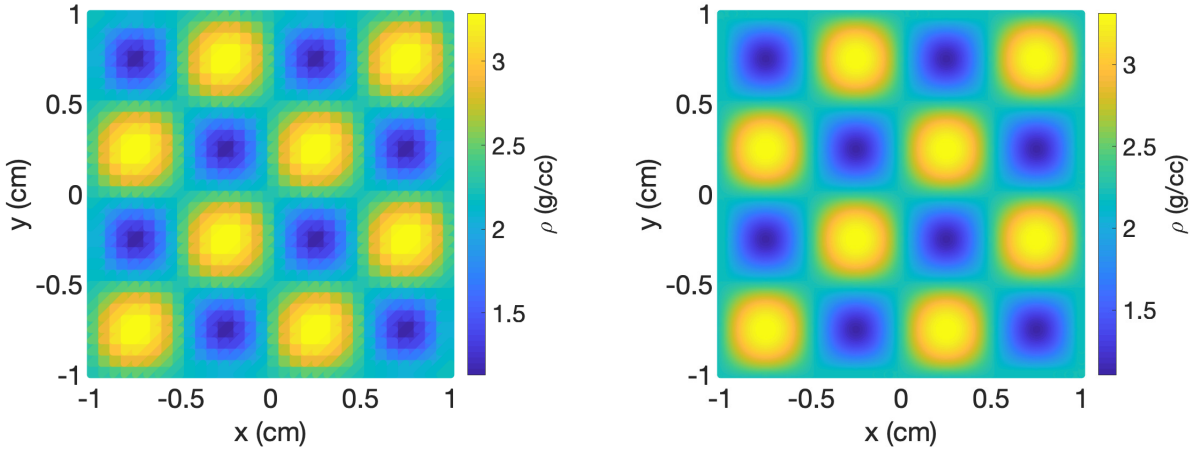

(a) Piecewise smooth bulk-density $\boldsymbol{\rho}$ (b) Heterogeneous bulk-density $\boldsymbol{\rho}$

Figure 4.9: Heterogeneous model of bulk density (ρ) (a) obtained from piecewise approximation with high order sub-cell variations, used for the piecewise constant solution (b) high order sub-cell heterogeneous distribution, used for WADG solution.

we compute the solutions for $N = 4$ and $K_{1\mathrm{D}} = 32$. The effects of subelement variations are now clearly marked by spurious reflections in Figures 4.10c and 4.10d. These effects are more prominent for higher orders as shown in Figures 4.10e and f, which display the piecewise constant and WADG solutions for $N = 8$ and $K_{1D} = 16$.

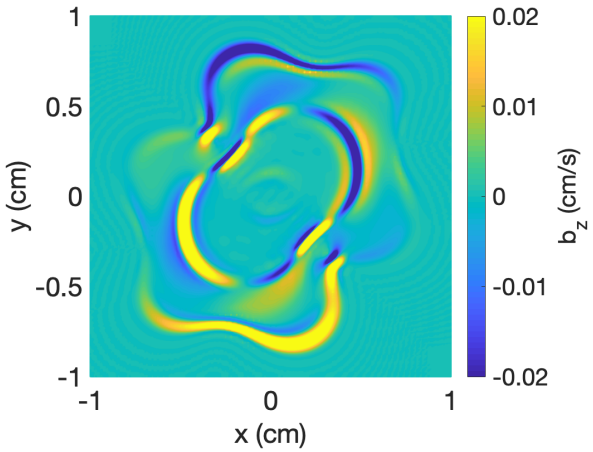

(a) $N = 2,\ K_{1D} = 64$, and piecewise constant

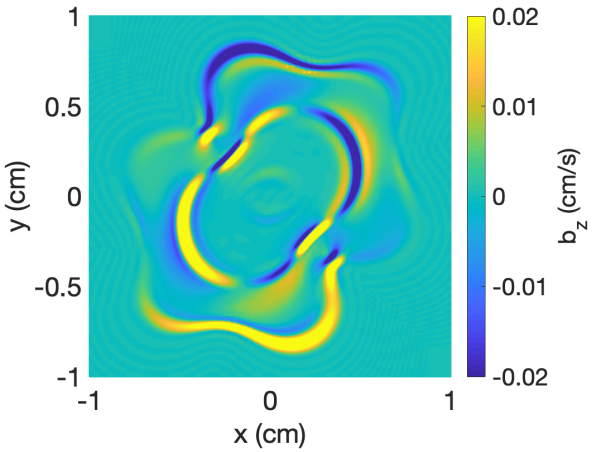

(b) $N = 2,\ K_{1D} = 64$, and WADG

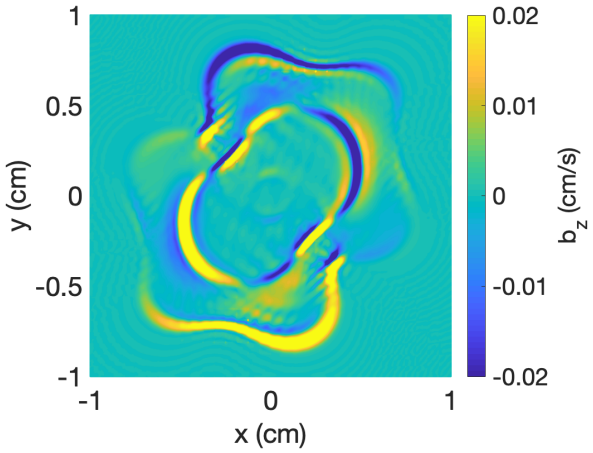

(c) $N = 4,\ K_{1D} = 32$, and piecewise constant

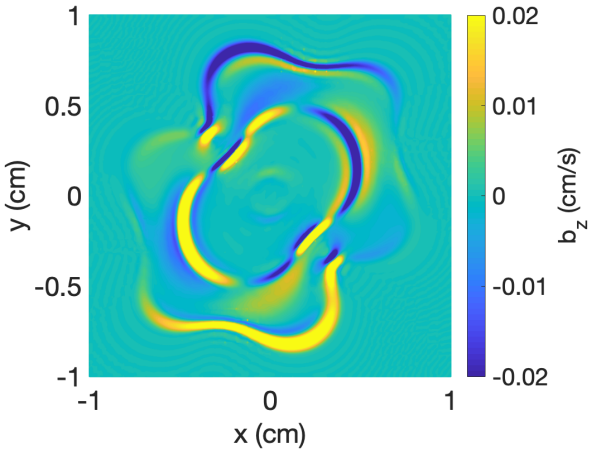

(d) $N = 4,\ K_{1D} = 32$, and WADG

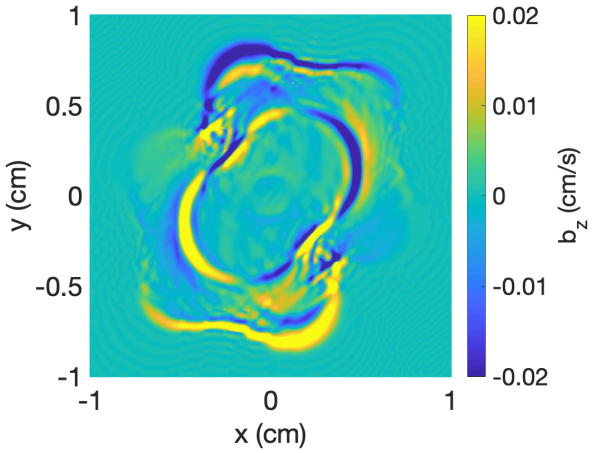

(e) $N = 8,\ K_{1D} = 16$, and piecewise constant

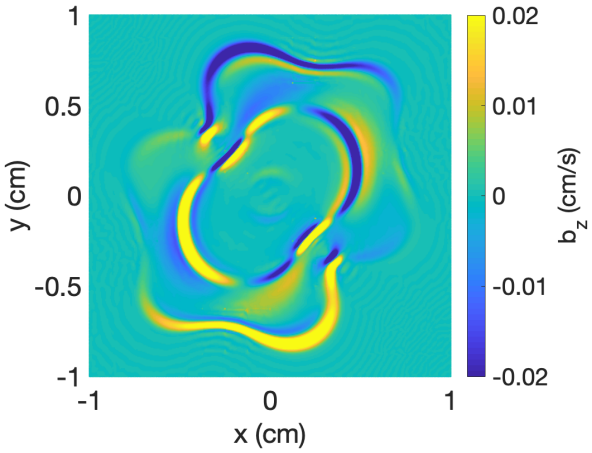

(f) $N = 8,\ K_{1D} = 16$, and WADG

Figure 4.10: A comparison between the solutions obtained from piecewise constant media and sub-cell heterogeneities treated using WADG.

Table 4.2: Material properties used for comparison of solution with SPECFEM implementations [5]

Properties	Medium I	Medium II	Medium III
ρ_s (kg/m^3)	2650	2200	2650
ρ_f (kg/m^3)	880	950	750
ϕ	0.1	0.4	0.2
T_1	2	2	2
T_3	2	2	2
K_s (GPa)	12.2	6.9	6.9
K_f (GPa)	1.985	2.0	2.0
κ_{fr} (GPa)*	9.6	6.7	6.7
μ_{fr}^{**} (GPa)**	5.1	3.0	3.0
η (10^{-3} Kg/m.s)	0	0	0

*: Frame bulk modulus, **: Frame shear modulus.

4.6.3.5 Validation of numerical solution

Here, we show comparisons between numerical solutions of the poroelastic wave equation obtained from the proposed DG method and from the spectral element method [5]. Morency and Tromp [5] used the spectral element method to solve the poroelastic wave equation in second order displacement form for 2D isotropic porous materials. First, we perform a validation study in a homogeneous porous medium. The domain dimensions are 1000 m $\times$ 1000 m. The domain is discretized with triangular and quadrilateral elements with minimum edge length 5 m for the DG and spectral element method, respectively.

Mornecy and Tromp implemented a pure dilatational explosive source as an external forcing function. To match the assumption of the dilatational explosive source, we have set the forcing functions corresponding to τ_{11} and τ_{22} to be equal, while the forcing function corresponding to τ_{12} is set to zero since a pure dilatational source does not radiate shear waves. It was also assumed in [5] that the fluid and the solid contain equal energy, and thus the forcing function corresponding to the pressure variable p is the same as for τ_{11} and τ_{12}.

The time domain response of the forcing function is a Ricker wavelet with a central frequency of $f_c = 30$ Hz. The material properties of the medium are given in column 2 of Table 4.2. In [3], the material properties were represented using Lame constants κ_{fr}, μ_{fr}. These can be converted to compliance coefficients as follows:

$$c_{55} = \mu_{fr}, \quad c_{11} = \kappa_{fr} + \frac{4}{3}\mu_{fr}, \quad c_{12} = c_{13} = \kappa_{fr} - \frac{2}{3}\mu_{fr}.$$

Figure 4.11a shows a snapshot of the solid particle velocity v_3, computed at $t = 0.14$ s. P_f and P_s represent the modes corresponding to fast and slow P waves, respectively. The point source is located at $\boldsymbol{x}_0 = (500 \text{ m}, 300 \text{ m})$, marked by a white star in Figure 4.11a. Figure 4.11b shows a comparison between the normalized solid vertical particle velocity (v_3) obtained from both the DG method and spectral-element method. The time history of the solution is recorded at (600 m, 400 m), denoted by the red diamond in Figure 4.11a. The agreement between the solutions is good. The root mean square error (RMSE) between the solutions is $8.68\text{e}-03$. A comparison between the solution obtained from the DG method and a pseudo-spectral method [3] is also shown in Figure 4.11c. The comparison shows a good agreement between the solutions except at the onset time 0.06 s. The RMS misfit between the solution is $3.18\text{e}-02$.

Next, we validate numerical solutions obtained from the DG method with a spectral-element method for a heterogenous medium. A two layer medium is constructed with material properties given in column 2 (top layer) and 3 (bottom layer) of Table 4.2. The size of the computational domain is (4800 m $\times$ 4800 m) and discretized with the triangular and quadrilateral elements for DG and spectral-element method, respectively. The minimum size of the edge of the element is taken as 200 m. Figure 4.12a represents the snapshot of solid particle velocity at $t = 0.73$ s. The pure dilatational point source is located at $\boldsymbol{x}_0 = (1600 \text{ m}, 2900 \text{ m})$, denoted by white star in Figure 4.12a, and implemented in same way as discussed for homogeneous medium. Figure 4.12b shows a comparison between solutions obtained from the DG and spectral-element methods. The time history of the solutions is recorded at (2000 m, 1867 m), marked by a red diamond in Figure 4.12a. The comparison shows a good overall agreement, though some discrepancies are present around time $T = 1$. The RMS misfit between the solutions is $6.65\text{e}-02$.

4.6.3.6 3D models and computational results

Finally, we present numerical solutions of the poroelastic wave equation on 3D domains. First, we compute the solution in an homogeneous medium and then extend the computation to a realistic synthetic reservoir model constructed from a varying layer with an undulated topography.

4.6.4 Epoxy-glass model

First, we compute the solution for a 3D cube made of epoxy-glass with material properties given in column 3 of Table 4.1. The size of the computational domain is 2 km $\times$ 2 km $\times$ 2 km in x, y and z directions, respectively. The domain is discretized with tetrahedral elements with a minimum edge length of 45 m. Figure 4.13(a)-(b) represents the $x-$ and $z-$ components of the

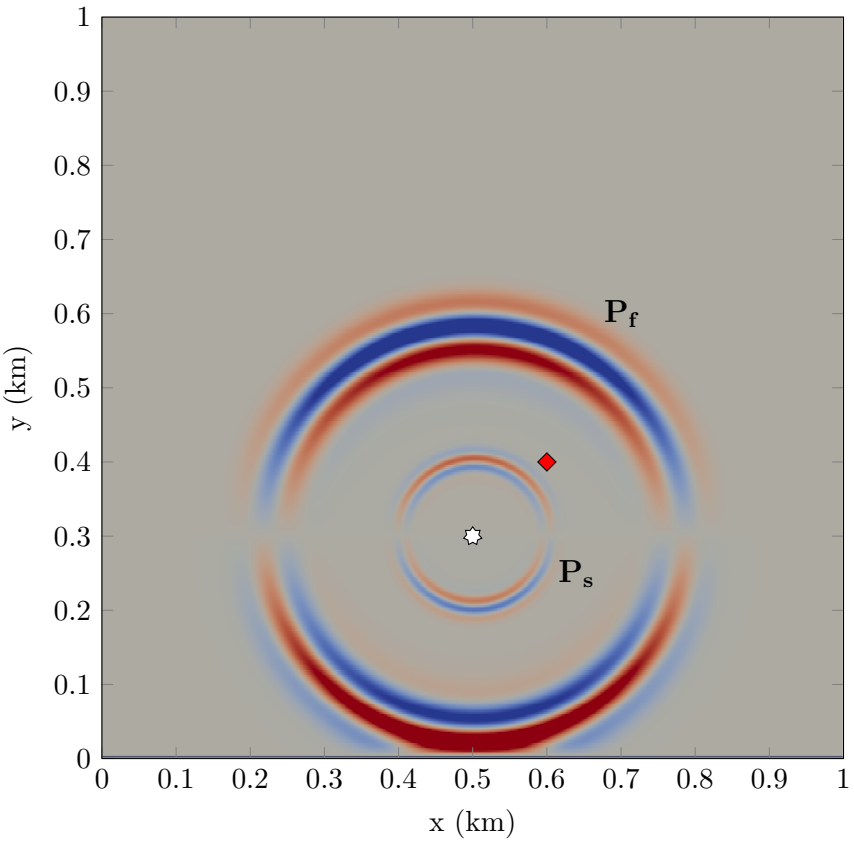

(a) Snapshot of vertical solid particle velocity, v_3 at $t = 0.14$ s

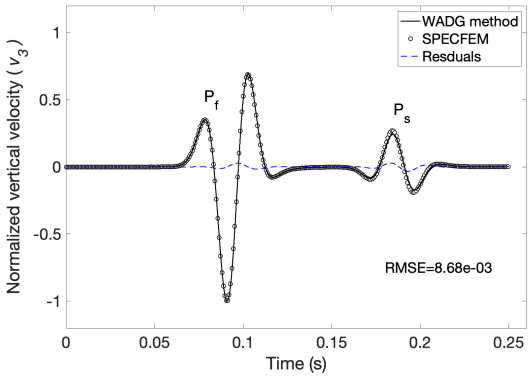

(b) SPECFEM vs WADG

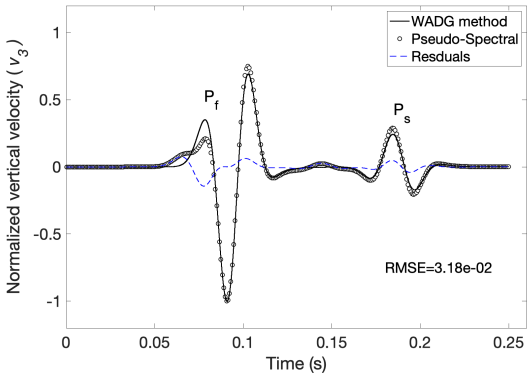

(c) Pseudo-spectral method vs WADG

Figure 4.11: A comparison between the solutions obtained from the proposed DG method and spectral-element method in a homogeneous porous medium with (a) showing the snapshot of the solutions obtained from the DG method computed with polynomials of degree $N = 4$. Figures (b) and (c) show comparisons between the solutions obtained from the DG/spectral element methods and the DG/pseudo-spectral methods, respectively. $\mathrm{P_f}$ and $\mathrm{P_s}$ represent fast and slow P wave, respectively.

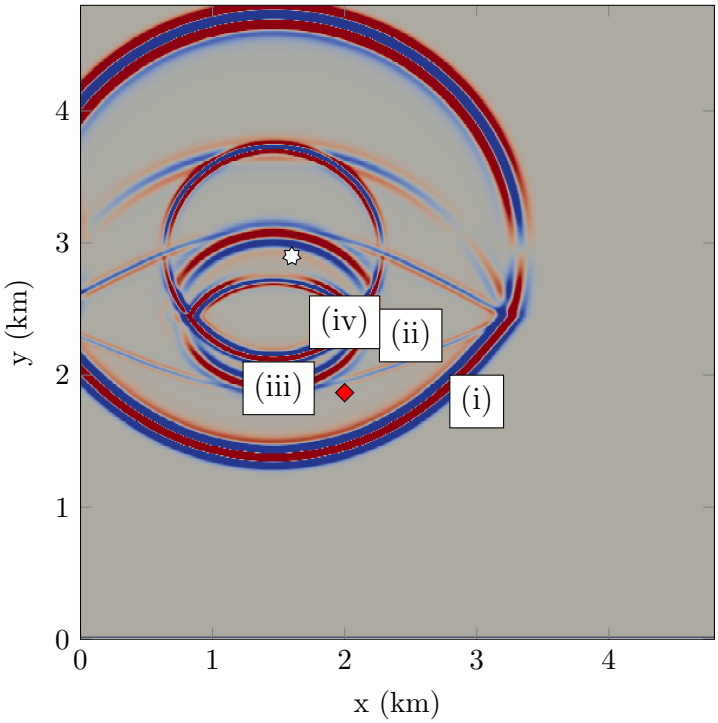

(a) Snapshot of vertical solid particle velocity, v_3 at $t = 0.73$ s

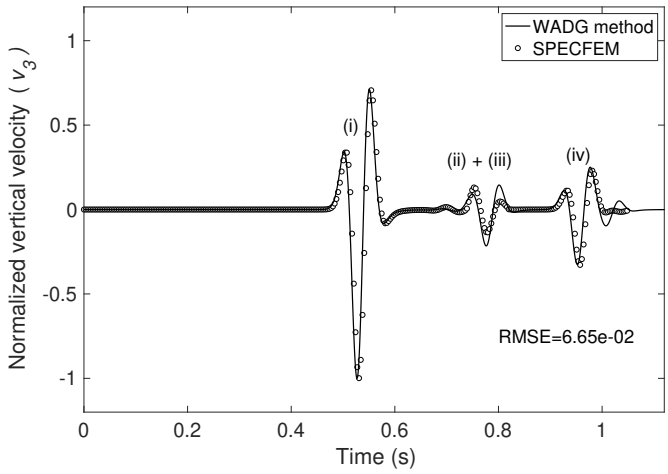

(b) SPECFEM vs WADG

Figure 4.12: A comparison between the solutions obtained from the proposed DG method and spectral-element method in a heterogeneous porous medium with (a) showing the snapshot of the solutions obtained from the DG method computed with polynomials of degree $N = 4$. Figure (b) shows a comparison between the solutions obtained from the DG/spectral element methods. The labels (i)-(iv) correspond to different transmitted wave modes as follows: (i) denotes the transmitted fast P wave, (ii) denotes the conversion of fast P to S and slow P waves, (iii) denotes converted slow P to S waves, and (iv) denotes converted slow P waves to fast P waves.

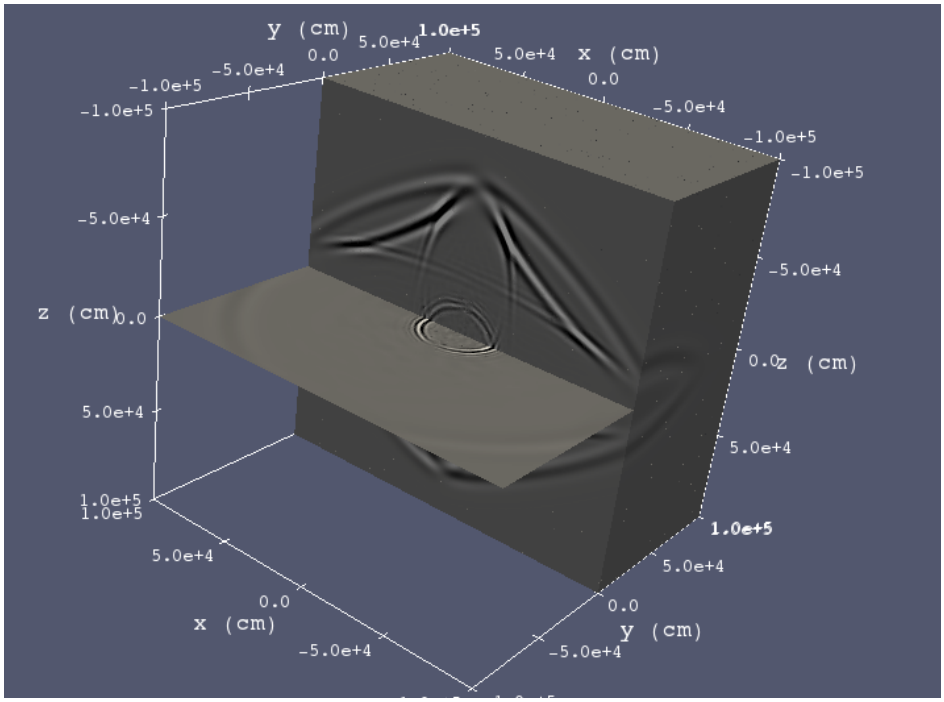

(a) Snapshot of horizontal solid particle velocity, v_1 at $t = 0.25$ s

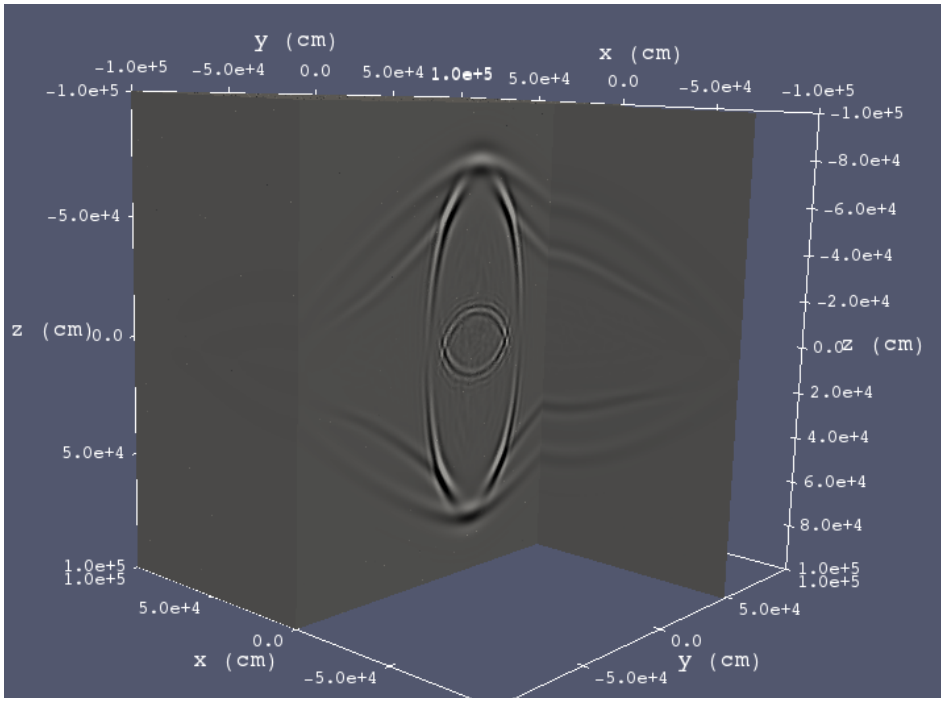

(b) Snapshot of vertical solid particle velocity, v_3 at $t = 0.25$ s

Figure 4.13: Snapshots of the x and z components of solid particle velocity in a 3D epoxy-glass material. (a) and (b) corresponds to the snapshots of v_1 and v_3 at $t = 0.25$ s. The central frequency of the forcing function is 25 Hz. The solution is computed using polynomials of degree $N = 5$.

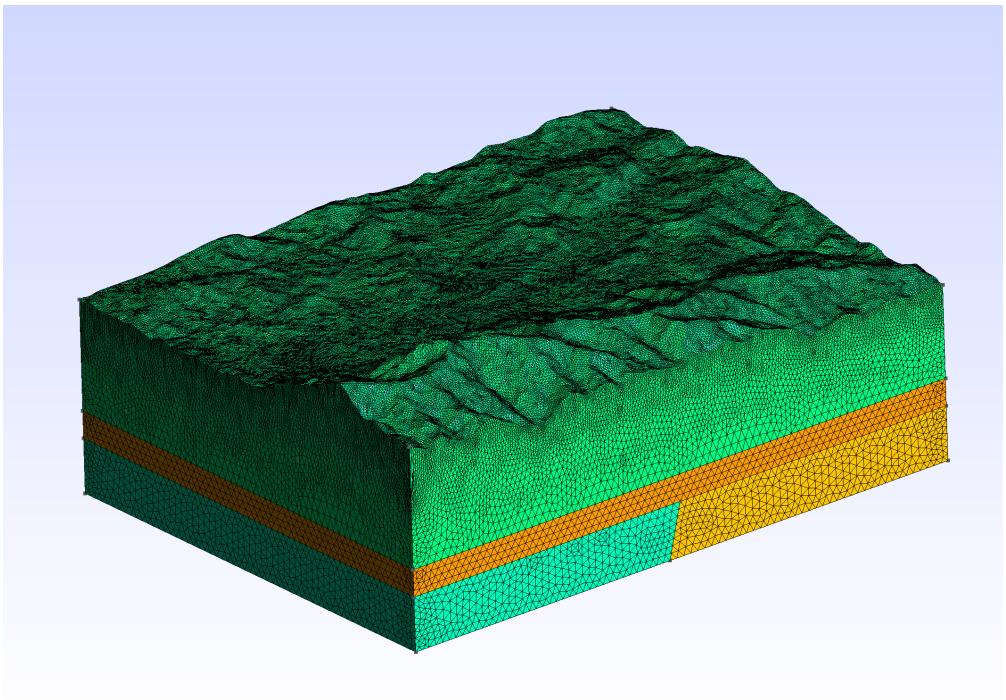

(a) Discretized reservoir model

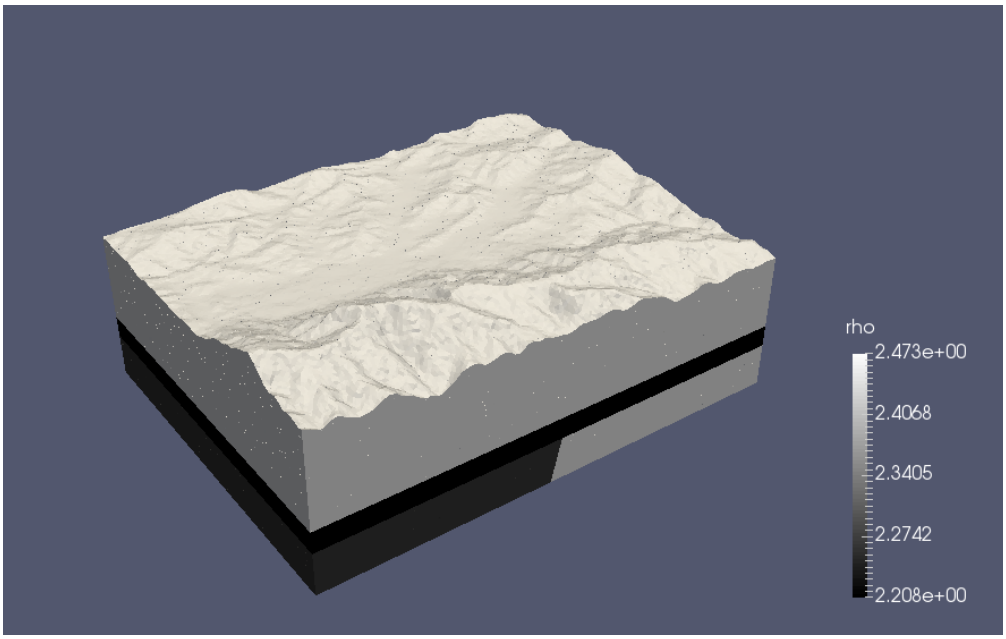

(b) Density (ρ) model

Figure 4.14: 3D Reservoir model (a) model discretized with tetrahedral elements and (b) distribution of the density (ρ) in the model.

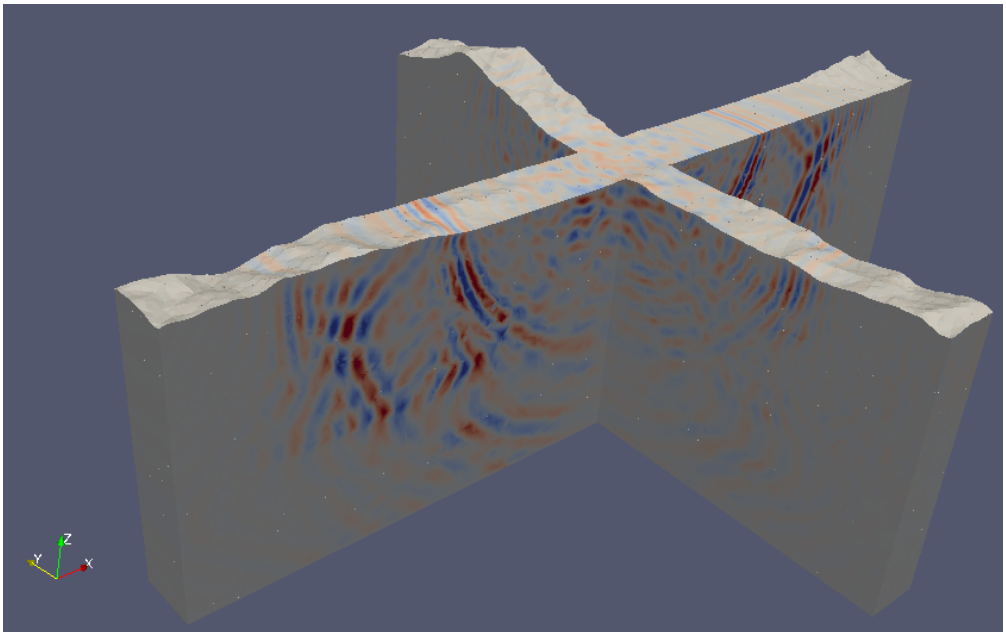

(a) Snapshot of horizontal solid particle velocity, v_1 at $t = 3.5$ s

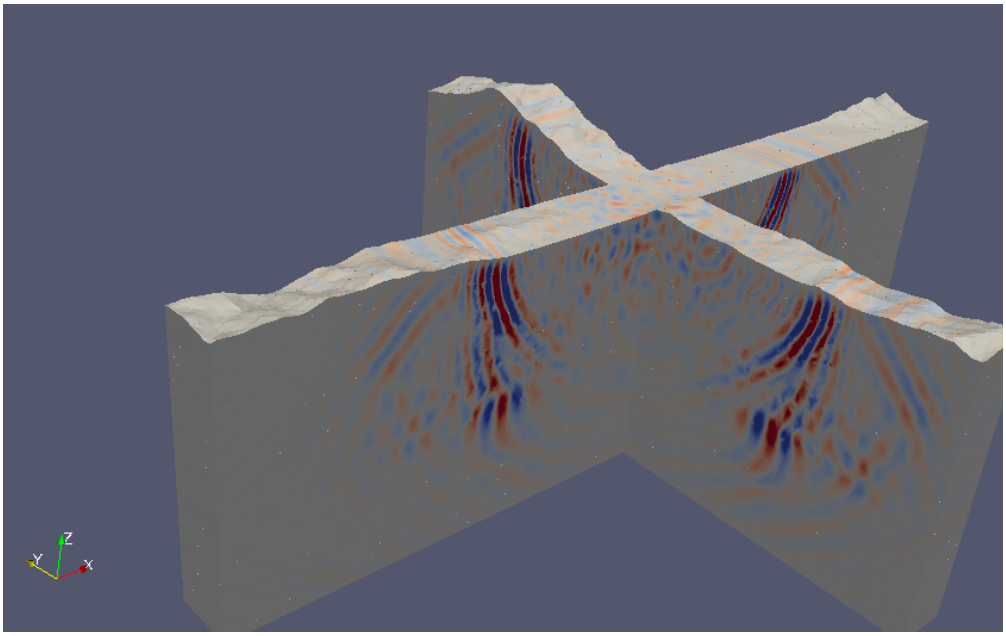

(b) Snapshot of vertical solid particle velocity, v_3 at $t = 3.5$ s

Figure 4.15: Snapshots of the x and z components of solid particle velocity in a reservoir model. (a) and (b) corresponds to the snapshots of v_1 and v_3 at $t = 3.5$ s. The central frequency of the forcing function is 10 Hz. The solution is computed using polynomials of degree $N = 3$.

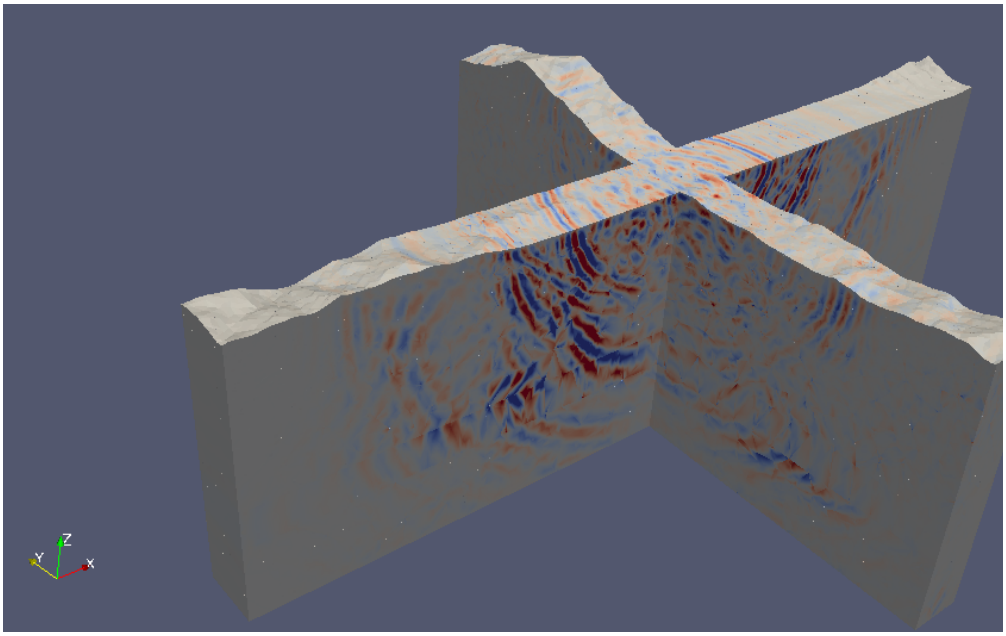

(a) Snapshot of horizontal fluid particle velocity, q_1 at $t = 3.5$ s

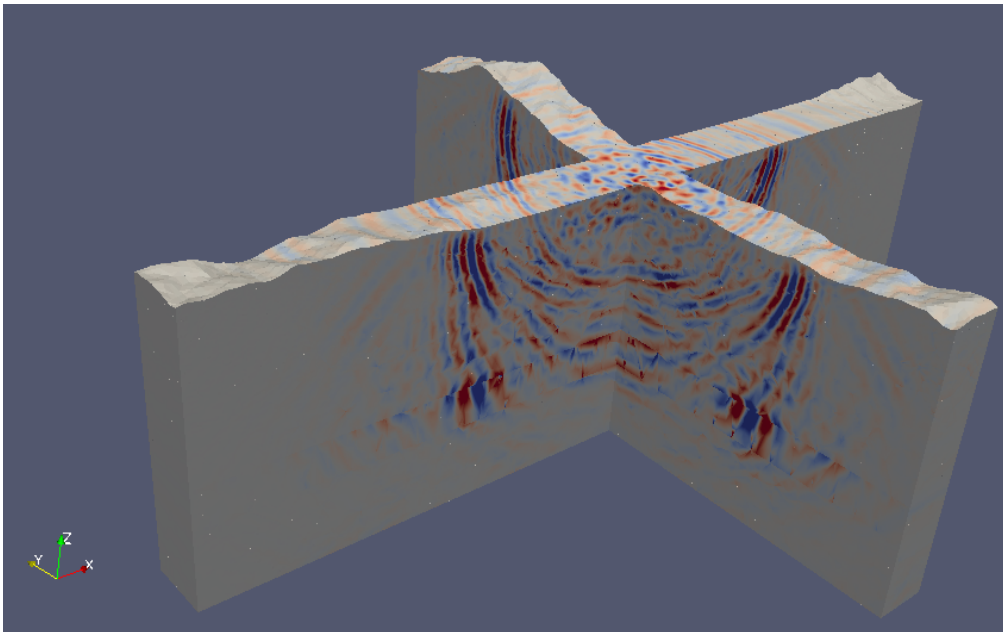

(b) Snapshot of vertical fluid particle velocity, q_3 at $t = 3.5$ s

Figure 4.16: Snapshots of the x and z components of fluid particle velocity in a reservoir model. (a) and (b) corresponds to the snapshots of q_1 and q_3 at $t = 3.5$ s. The central frequency of the forcing function is 10 Hz. The solution is computed using polynomials of degree $N = 3$.

solid particle velocity in the epoxy-glass medium at 0.25 s. The central frequency of the forcing function is $f_0 = 35$ Hz, and polynomials of degree $N = 5$ are used.

Three events can be observed: the fast P mode (P_f, outer wavefront), the shear wave (S, middle wavefront), and the slow P mode (inner wavefront). In an orthotropic material, the effect of anisotropy on wave propagation is observed in two orthogonal planes, whereas isotropic effects are observed only in one plane. Figure 4.13a clearly shows the effect of anisotropy on wave propagation with an isotropic effect in the plane parallel to the y axis.

4.6.5 Reservoir model

We construct a 3D reservoir model characterized by rock layers, discontinuity, and a surface with undulated topography. The discretized model along with the density distribution is shown in Figures 4.14a and 4.14b, respectively. The dimension of the model is 22.8 km $\times$ 17.4 km $\times$ 7.0 km in x, y and z directions, respectively. The domain is discretized with tetrahedral elements with a minimum edge length of 125 m. The top surface of the model is perturbed so that the effects of the topography, assumed as a free surface, could be incorporated into numerical simulations. Figure 4.15(a)-(b) represent the $x-$ and $z-$ components of the solid particle velocity at 3.5 s. The central frequency of the forcing function is $f_0 = 10$ Hz, and polynomials of degree $N = 3$ are used. The various modes of transmissions, reflections and scattering can be clearly seen in Figures 4.15a and 4.15b. Figure 4.16(a)-(b) show the $x-$ and $z-$ components of the fluid particle velocity at 3.5 s.

Chapter V

A weight-adjusted discontinuous Galerkin method for the broad-band Biot's equation

5.1 Abstract

We introduce a system of hyperbolic partial differential equations describing Biot's poroelastic wave equation for quasi-static Poisseulle and potential flow. To incorporate effects from micro-heterogeneities due to pores, we have used the Johnson-Koplik-Dashen (JKD) model [90] of dynamic permeability, which also account for frequency-dependent viscous dissipation caused by wave-induced pore fluids. Coupling the JKD model with the equations of motion recasts the dissipative forces in terms of a fractional derivative operator of order 1/2. Numerical solutions of the system are obtained using a high-order discontinuous Galerkin discretization with an energy-stable penalty-based numerical flux [112]. The convergence of the proposed numerical scheme is proven and verified by using convergence studies against analytical plane wave solutions. Computational experiments are performed on various realistic models.

5.2 Introduction

Theories of poroelasticity deal with the physics of elastic wave propagation in porous media where pore-filling materials are of interest, such as in oil and gas exploration, gas hydrate detection, hydrogeology, and seismic monitoring of CO_2 storage. The most popular theory dealing with poroelastic wave propagation was given by Maurice Biot in seminal work presented in [8], [10]. Biot obtained a dynamical system of equations describing the wave propagation in a porous medium saturated with a single phase fluid. Biot's system of equations is classified on the basis of a material's characteristic frequency (ω_c) [10], [2].

Biot's theory of poroelasticity predicts two compressional waves, a fast P wave and slow P wave, and one shear wave. The fast P wave has solid and fluid motion in phase, while the slow P wave (Biot's mode) has the solid and fluid motion out of phase with one another. At low frequencies, the slow P wave is diffusive in character, as viscous forces dominate over inertial forces. However, at high frequencies, the dominance of inertial forces over viscous forces results in the propagation of the slow P wave.

A major cause of energy dissipation in porous media is a dissipative (or drag) "memory" force resulting from the relative motion between the solid skeleton and pore fluid. In the low-frequency regime, the dissipative force is linearly proportional to relative velocity between solid and fluid. This occurs because the viscous skin depth in the low-frequency regime is greater than the pore size, and thus does not form any pore boundary layer. However, in the high frequency regime, the dominance of inertial forces over viscous forces causes the formation of a pore boundary viscous layer with thickness less than the pore-radius. The relaxation mechanism of the medium due to drag force is expressed as a memory kernel and is incorporated into the equation of motion through a convolution operator [3]. In [3], drag force is approximated by simple exponential memory kernel. However, the Johnson-Koplik-Dashen (JKD) model of dynamic permeability [90] and [10] has shown that the dissipative drag force should be consistent with the thickness of a pore boundary layer, which a simple exponential memory kernel will not correctly reproduce at high frequencies.

Numerical simulations of the poroelastic wave equation have primarily focused on the low-frequency regime. A detailed review of computational poroelasticity is presented by Carcione et al. [17]. The first numerical simulations were performed using the reflectivity method for flat layers [91, 92] and cylindrical structures [93]. Numerical simulation of the poroelastic wave equation using direct or grid based methods, such as finite difference (FD) and pseudo-spectral (PS) methods, dates back to the 1970s. In [18], the damped 1D Green's function is computed artificially for low-frequency poroelasticity using a FD scheme. In [19], low-frequency poroelasticity is solved in cylindrical coordinates using a Hankel transform in radial directions and a FD grid in the vertical direction with accuracy of order 2 in space and time, which we refer to as order $\mathcal{O}(2,2)$. The first numerical simulation of the low-frequency poroacoustic wave equation in dilatation form was presented in[20], using a FD scheme of order $\mathcal{O}(2,2)$. In [113], the low-frequency poroelastic wave equation in displacement form was solved using a FD scheme of $\mathcal{O}(2,2)$. The first implementtion of the free surface boundary condition for low-frequency poroelasticity was presented in [21] using McCormack's scheme based on a dimensional splitting method [41]. Santos and Oreña [23] used a finite-element method to solve the poroelastic wave equation in second-order form using quadrilateral

meshes for spatial discretization. In [2], a numerical solution of low-frequency poroacoustic equation in pressure-velocity form was presented using a pseudo-spectral scheme. The first numerical simulation of low-frequency anisotropic poroelastic wave propagation was presented in [3], which showed that slow P waves can develop cusps similar to those present in shear waves. In [114] and [115], pseudo-spectral methods are applied to the equations of poro-viscoelasticity. More recently, Lemoine et al. [27] have used a finite-volume method on structured meshes for numerical simulations of wave propagation in orthotropic poroelastic media.

We are interested in combining the dynamic permeability model of [90] with Biot's dynamical equations to formulate a 3D Biot's system which we refer to as the "broad-band Biot's" equations. These equations account for frequencies varying from the seismic to the ultrasonic scale. The JKD model describes the dissipative force for a random pore geometry, whereas Biot's original model [8] was valid only for a circular pore geometry. The original dynamic permeability $\kappa(\omega)$ is expressed in the frequency domain and coupled with Biot's time domain equation, resulting in a dissipation force defined by a fractional derivative operator of order $\frac{1}{2}$. A numerical discretization of the fractional derivative operator is achieved by recasting it into integral form using Caputo's formula [116] and subsequently converting it into differential equations involving auxiliary variables [114, 1].

Until recently, numerical solutions of the poroelastic system and its variants have been achieved using either low order or structured grid numerical schemes, with most of the aforementioned numerical simulations using simple geometries consisting of a homogeneous or two-layered medium. In this paper, we obtain numerical solutions of the broad-band Biot's equation on unstructured meshes using a high order discontinuous Galerkin (DG) [6] scheme. High order methods provide one avenue towards improving fidelity in numerical simulations while maintaining reasonable computational costs, and methods which can accommodate unstructured meshes are desirable for problems with complex geometries. Among such methods, high order discontinuous Galerkin (DG) methods are particularly well-suited to the solution of time-dependent hyperbolic problems on modern computing architectures [6, 94]. The accuracy of high order methods can be attributed in part to their low numerical dissipation and dispersion compared to low order schemes [95]. This accuracy has made them advantageous for the simulation of electro-magnetic and elastic wave propagation [6, 7].

DG methods impose inter-element continuity of approximate solutions between elements weakly through a numerical flux, of which several choices are common. de la Puente et al. [4] solved the low-frequency poroelastic wave equation using a local space-time DG method with a Rusanov type flux, which tends to be dissipative. In another study, Ward et al. [82], derived an

upwind flux by solving the exact Riemann problem on inter-element boundaries for the 2D isotropic strain-velocity form of the poroelastic wave equations. Recently, Zhan et al. [96] also solved the poroelastic wave equation in 3D (formulated in stress-velocity form) using an upwind flux by solving the exact Riemann problem. The solution of Riemann problem requires diagonalization Jacobian matrices into polarized waves constituents, which is a computationally intensive process for the poroelastic system and does not extend naturally to anisotropic materials. Zhan et al. [96] addresses the complexity of the diagonalization by reducing the rank of Jacobian matrices by using the method of generalized wave impedances.

In this work, we follow [112] and avoid the process of diagonalization for the anisotropic poroelastic wave equation by using an upwind-like penalty flux based on natural boundary conditions [79, 117]. Micro-heterogeneities (sub-element variations) in materials properties were also treated in [112] by approximating weighted mass matrices [98] with easily invertible "weight-adjusted" approximations [97]. We extend the same approach for broad-band Biot's eqaution , where matrix-valued weight functions arise after symmetrization of the system. This resulting method is energy-stable for the broad-band Biot's equations in both anisotropic media and spatially varying media with micro-heterogeneities. In brief, the novelties of our approach are the following:

1. We formulate the 3D broad-band Biot's system of equations (which describes elastic wave propagation in porous media for all frequencies) by incorporating the dynamic permeability $\boldsymbol{\kappa}(\omega)$ in the fluid-flow equations

2. We introduce upwind-like dissipation through simple penalty terms in the numerical flux.

3. We obtain a consistent DG weak formulation for the broad-band Biot's equations without the diagonalization into polarized wave constituents required for upwind fluxes.

Section 5.3 will introduce the system of equations describing poroelastic wave propagation, as well as physical interface conditions. Section 5.4 presents an energy stable DG formulation with penalty fluxes for the symmetric hyperbolic form of the poroelastic wave equations. Finally, numerical results in Section 5.5 demonstrate the accuracy of this method for problems in linear poroelasticity for higher frequencies.

5.3 Biot's System of Equations

Biot's theory describes wave propagation in a saturated porous medium i.e., a medium made up of a solid matrix (the skeleton, or frame) fully saturated with fluid. Biot also assumed

Table 5.1: List of symbols

Symbols	Physical meaning	Ref. eq. no.
$i,\ j = 1...6$	index of stress and strain tensor matrix	(5.1)
$\sigma_{ij}^{(m)}$	element of stress tensor for matrix of poroelastic medium	(5.1)
$\sigma_{(f)}$	fluid stress	(5.1)
τ_{ij}	element of effective stress tensor for poroelastic medium	(5.1)
σ_{ij}^{m}	element of stress tensor for matrix	(5.1)
p	pore pressure	(5.2)
ϕ	porosity	(5.2)
$\mathbf{u^{(f)}}$	displacement vector of fluid particle	(5.3)
$\mathbf{u^{(s)}}$	displacement vector of solid particle	(5.3)
ω_c	Biot's characteristic frequency	(5.6)
η	fluid viscosity	(5.6)
ϕ	porosity of material	(5.6)
$\rho_{\mathbf{f}}$	pore fluid density	(5.7)
$\mathbf{a}_\infty$	tortuosity	(5.7)
$\kappa_{\mathbf{0}}$	static permeability	(5.10)
$\mathbf{q}$	velocity vector of fluid particle	(5.7)
ρ	bulk density $[\phi\rho_f + (1-\phi)\rho_s]$; ρ_s: solid density	(5.7)

that an infinitesimal transformation relates the reference and current states of deformation; thus displacement, strains and particle velocity are small. The concept of infinitesimal deformation allows the use of the Lagrangian and Hamilton's principle [8] to derive the equations governing the propagation of waves in such a medium. In this section we have formulated Biot's equation in 3D by combining the constitutive equations, equation of motion and dissipative force, defined by the concept of dynamic permeability [90]. Application of dynamic permeability to dissipation forces allows us to express a unique Biot's system defining wave propagation across all frequencies.

5.3.1 Constitutive Equations

Stress-strain relations can be interpreted as a relation between incremental fields, where stress and strain are increments with respect to a reference stress and strain, such as in the case of wave propagation, or, as relations between the absolute fields. Effective stress and effective pressure play an important role in rock physics. The pore pressure, p, and confining pressure, p_c, tend to have an opposite effect on acoustic and transport properties of porous media, so it is convenient to characterize these properties with a single pressure, the effective pressure, p_e [118]. Terzaghi defined $p_e = p_c - \phi p$, and subsequently Biot utilized the concept of effective pressure to obtain the effective

stress-strain law for poroelastic materials. In the following discussions the superscripts m and f are used for the solid matrix and fluid phase, respectively.

Consider a unit cube of bulk material with the components $\sigma_{ij}^{(m)}$ representing the force applied to the solid part of the faces, and suppose $\sigma^{(f)}$ represents the force applied to the fluid part of these faces. The total stress component τ_{ij} on the bulk material can be expressed as:

$$\tau_{ij} = \sigma_{ij}^{(m)} + \delta_{ij}\sigma^{(f)}, \tag{5.1}$$

$$\sigma^{(f)} = -\phi p. \tag{5.2}$$

The variation of fluid content is expressed as

$$\zeta = -\nabla \cdot [\phi(\boldsymbol{u}^{(f)} - \boldsymbol{u}^{(s)})]. \tag{5.3}$$

The variation of fluid content, ζ, represents the amount of fluid which has flowed in and out of each element attached to the solid frame.

Equations (4.1)–(4.2) can be expressed using the deviatoric strain [8, 10] as

$$\tau_{ij} = c_{ijkl}^{u}\epsilon_{kl}^{(m)} - M\alpha_i\zeta, \tag{5.4}$$

$$p = M(\zeta - \alpha_k\epsilon_{kk}^{(m)}), \tag{5.5}$$

where c_{ijkl}^{u} is the undrained stiffness constant, which can be expressed as $c_{ijkl}^{u} = c_{ijkl}^{(m)} + M\alpha_i\alpha_j$ with $c_{ijkl}^{(m)}$ representing the elements of the stiffness tensor of the solid matrix. The Biot effective stress coefficient α and Biot's parameter M are derived experimentally from the bulk moduli of the solid and fluid [32]. Finally, $\epsilon_{kl}^{(m)}$ signifies the strain.

5.3.2 Equation of motion

Biot's theory assumes that a porous medium is fully saturated with a single phase fluid, and that pores are connected. Thus, solid and fluid phases belong to same continuum. Biot divided the poroelastic system into two categories, based on the material's characteristic frequency ω_c (also known as the Biot's frequency). The frequency can be expressed as

$$\omega_c = \frac{\eta\phi}{\rho_f a_\infty \kappa_0}, \tag{5.6}$$

where κ_0 is limit of permeability for steady flow.

The system of equations for frequencies below ω_c assumes quasi-static laminar flow, for which viscous forces dominate over inertial force. For frequencies above f_c, the fluid flow is quasi-static potential flow, where inertial forces dominate over viscous forces. Dissipation in the poroelastic system is due to fluid motion relative to solid motion, which is known as filtration velocity and defined by $\mathbf{q} = \phi[\frac{\partial}{\partial t}(\boldsymbol{u}^{(f)} - \boldsymbol{u}^{(s)})]$.

The equation describing the solid particles' velocity is

$$\rho \frac{\partial \boldsymbol{v}}{\partial t} + \rho_f \frac{\partial \boldsymbol{q}}{\partial t} = \nabla \cdot \boldsymbol{\tau}, \tag{5.7}$$

and the equation describing the motion of fluid particles relative to solid particles is

$$\rho_f \frac{\partial \boldsymbol{v}}{\partial t} + \boldsymbol{F_i} \frac{\partial \boldsymbol{q}}{\partial t} + \boldsymbol{F_d} * \boldsymbol{q} = -\nabla p, \tag{5.8}$$

where $\boldsymbol{F}_i$ and $\boldsymbol{F}_d$ are matrices describing the inertial and time dependent dissipative forces. where $\boldsymbol{F}_i$ and $\boldsymbol{F}_d$ are matrices describing the inertial and time dependent dissipative forces. Here, $*$ represents the convolution operation in time.

5.3.3 Dynamic Permeability

In this section, we derive explicit formulas for $\boldsymbol{F}_i$ and $\boldsymbol{F}_d$ described in (5.8). The frequency domain representation of Darcy's law [14] with the inertial effect of the fluid is

$$\hat{\boldsymbol{q}} = \frac{\hat{\kappa}(\omega)}{\eta}(-\nabla \hat{p} + i\omega\rho_f \hat{\boldsymbol{v}}), \tag{5.9}$$

where ω is the frequency. Here, $\hat{\cdot}$ denotes the frequency representation of the variables.

The frequency-dependent permeability is given by $\hat{\kappa}(\omega)$, and differentiates the nature of fluid flow below and above Biot's characteristic frequency. In this paper we consider the anisotropic Johnson-Koplik-Dashen (JKD) model of dynamic permeability [90] for $\hat{\kappa}(\omega)$, which is expressed as

$$\hat{\kappa}(\omega) = \kappa_{0_i} \left[\left(1 + \mathrm{i} \frac{4a_{\infty_i}^2 \kappa_{0_i}^2 \rho_f \omega}{\Lambda^2 \phi^2 \eta} \right)^{1/2} + \mathrm{i} \frac{\omega a_{\infty_i} \rho_f \kappa_0}{\phi \eta} \right]^{-1}, \tag{5.10}$$

where Λ is a structural parameter defining the ratio of pore to surface volume. Geometric parameters

K_i, m_i, and a_{s_i} are defined as

$$K_i = \frac{4a_\infty \kappa_0}{\Lambda^2 \phi}, \qquad m_i = \frac{a_\infty \rho_f}{\phi}, \qquad a_{s_i} = (\omega_c / K_i). \tag{5.11}$$

Substituting (5.10) into (5.9), we recover

$$-\nabla \hat{p} = (i\omega)\rho_f \hat{\boldsymbol{v}} + (i\omega) m_i \hat{\boldsymbol{q}} + \frac{\eta}{\kappa_{0_i}} a_s^{\frac{1}{2}} (a_{s_i} + i\omega)^{1/2} i\omega \hat{\boldsymbol{q}}. \tag{5.12}$$

The transformation of (5.12) into the time domain yields [119]

$$-\nabla p = \rho_f \frac{\partial \mathbf{v}}{\partial t} + m \frac{\partial \mathbf{q}}{\partial t} + \frac{\eta}{\kappa_0} a_{s_i}^{-\frac{1}{2}} (D + a_s)^{1/2} \mathbf{q}, \tag{5.13}$$

The derivation of (5.13) is given in the Appendix D.1.

In (5.13), the terms $m_i \frac{\partial \boldsymbol{q}}{\partial t}$ and $\frac{\eta}{\kappa_{0_i}} a_{s_i}^{-\frac{1}{2}} (D + a_s)^{1/2} \boldsymbol{q}$ represent the inertial and dissipative forces, respectively. Collecting the two sets of coefficients, we have:

$$\text{Inertial coefficients} \quad \boldsymbol{F}_i = \begin{bmatrix} m_1 & 0 & 0 \\ 0 & m_2 & 0 \\ 0 & 0 & m_3 \end{bmatrix}, \tag{5.14}$$

$$\text{Dissipative coefficients} \quad \boldsymbol{F}_d = \begin{bmatrix} \frac{\eta}{\kappa_1}\Psi_1 & 0 & 0 \\ 0 & \frac{\eta}{\kappa_2}\Psi_2 & 0 \\ 0 & 0 & \frac{\eta}{\kappa_3}\Psi_3 \end{bmatrix}, \tag{5.15}$$

where $\Psi_i = \frac{\eta}{\kappa_i} a_{s_i}^{-\frac{1}{2}} (D + a_{s_i})^{1/2}$ with $i = 1..3$ is a shifted fractional derivative operator in along i^{th} axis.

5.3.4 The system of equations in matrix form

To simplify notation, we introduce a matrix form of the system of equations while accounting for anisotropy and heterogeneity. Combining (5.4), (5.5), (5.7) and (5.13), we get

$$\frac{\partial \boldsymbol{Q}}{\partial t} + \boldsymbol{A}\frac{\partial \boldsymbol{Q}}{\partial x_1} + \boldsymbol{B}\frac{\partial \boldsymbol{Q}}{\partial x_2} + \boldsymbol{C}\frac{\partial \boldsymbol{Q}}{\partial x_3} = \boldsymbol{D}\boldsymbol{Q} + \boldsymbol{f}, \tag{5.16}$$

where

$$\boldsymbol{Q} = \left[\begin{array}{cccccccccccc} \tau_{11}, & \tau_{22}, & \tau_{33}, & \tau_{23}, & \tau_{13}, & \tau_{12}, & p, & v_1, & v_2, & v_3, & q_1, & q_2, & q_3 \end{array} \right]^T, \; \boldsymbol{A} = \left[\begin{array}{c|c} \boldsymbol{0}_{7\times 7} & \boldsymbol{A}_{11} \\ \hline \boldsymbol{A}_{21} & \boldsymbol{0}_{6\times 6} \end{array} \right],$$

$$\boldsymbol{B} = \left[\begin{array}{c|c} \boldsymbol{0}_{7\times 7} & \boldsymbol{B}_{11} \\ \hline \boldsymbol{B}_{21} & \boldsymbol{0}_{6\times 6} \end{array} \right], \; \boldsymbol{C} = \left[\begin{array}{c|c} \boldsymbol{0}_{7\times 7} & \boldsymbol{C}_{11} \\ \hline \boldsymbol{C}_{21} & \boldsymbol{0}_{6\times 6} \end{array} \right], \text{ and } \boldsymbol{D} = \left[\begin{array}{c|c} \boldsymbol{0}_{7\times 7} & \boldsymbol{0}_{6\times 7} \\ \hline \boldsymbol{0}_{6\times 7} & \boldsymbol{D}_{22} \end{array} \right], \text{ with}$$

$$\boldsymbol{A}_{11} = -\begin{bmatrix} c_{11}^u & 0 & 0 & \alpha_1 M & 0 & 0 \\ c_{12}^u & 0 & 0 & \alpha_2 M & 0 & 0 \\ c_{13}^u & 0 & 0 & \alpha_3 M & 0 & 0 \\ 0 & 0 & 0 & 0 & 0 & 0 \\ 0 & 0 & c_{55} & 0 & 0 & 0 \\ 0 & c_{66} & 0 & 0 & 0 & 0 \\ -M\alpha_1 & 0 & 0 & -M & 0 & 0 \end{bmatrix}, \; \boldsymbol{A}_{21} = -\begin{bmatrix} \frac{m_1}{\beta_1} & 0 & 0 & 0 & 0 & 0 & \frac{\rho_f}{\beta_1} \\ 0 & 0 & 0 & 0 & 0 & \frac{m_2}{\beta_2} & 0 \\ 0 & 0 & 0 & 0 & \frac{m_3}{\beta_3} & 0 & 0 \\ -\frac{\rho_f}{\beta_1} & 0 & 0 & 0 & 0 & 0 & -\frac{\rho}{\beta_1} \\ 0 & 0 & 0 & 0 & 0 & -\frac{\rho_f}{\beta_2} & 0 \\ 0 & 0 & 0 & 0 & -\frac{\rho_f}{\beta_3} & 0 & 0 \end{bmatrix},$$

$$\boldsymbol{B}_{11} = -\begin{bmatrix} 0 & c_{12}^u & 0 & 0 & \alpha_1 M & 0 \\ 0 & c_{22}^u & 0 & 0 & \alpha_2 M & 0 \\ 0 & c_{33}^u & 0 & 0 & \alpha_3 M & 0 \\ 0 & 0 & c_{44} & 0 & 0 & 0 \\ 0 & 0 & 0 & 0 & 0 & 0 \\ c_{66} & 0 & 0 & 0 & 0 & 0 \\ 0 & -M\alpha_2 & 0 & 0 & -M & 0 \end{bmatrix}, \; \boldsymbol{B}_{21} = -\begin{bmatrix} 0 & 0 & 0 & 0 & 0 & \frac{m_1}{\beta_1} & 0 \\ 0 & \frac{m_2}{\beta_2} & 0 & 0 & 0 & 0 & \frac{\rho_f}{\beta_2} \\ 0 & 0 & 0 & \frac{m_3}{\beta_3} & 0 & 0 & 0 \\ 0 & 0 & 0 & 0 & 0 & -\frac{\rho_f}{\beta_1} & 0 \\ 0 & -\frac{\rho_f}{\beta_2} & 0 & 0 & 0 & 0 & 0 \\ 0 & 0 & 0 & -\frac{\rho_f}{\beta_3} & 0 & 0 & 0 \end{bmatrix},$$

$$\boldsymbol{C}_{11} = -\begin{bmatrix} 0 & 0 & c_{13}^u & 0 & 0 & \alpha_1 M \\ 0 & 0 & c_{23}^u & 0 & 0 & \alpha_2 M \\ 0 & 0 & c_{33}^u & 0 & 0 & \alpha_3 M \\ 0 & 0 & c_{44} & 0 & 0 & 0 \\ c_{55} & 0 & 0 & 0 & 0 & 0 \\ 0 & 0 & 0 & 0 & 0 & 0 \\ 0 & 0 & -M\alpha_3 & 0 & 0 & -M \end{bmatrix},\ \boldsymbol{C}_{21} = -\begin{bmatrix} 0 & 0 & 0 & 0 & \frac{m_1}{\beta_1} & 0 & 0 \\ 0 & 0 & 0 & \frac{m_2}{\beta_2} & 0 & 0 & 0 \\ 0 & 0 & \frac{m_3}{\beta_3} & 0 & 0 & 0 & \frac{\rho_f}{\beta_3} \\ 0 & 0 & 0 & 0 & -\frac{\rho_f}{\beta_1} & 0 & 0 \\ 0 & 0 & 0 & -\frac{\rho_f}{\beta_2} & 0 & 0 & 0 \\ 0 & 0 & -\frac{\rho_f}{\beta_3} & 0 & 0 & 0 & -\frac{\rho}{\beta_3} \end{bmatrix},\ \text{and}$$

$$\boldsymbol{D}_{22} = \begin{bmatrix} 0 & 0 & 0 & \frac{\rho_f}{\rho}\chi_1(D+a_{s_1})^{1/2} & 0 & 0 \\ 0 & 0 & 0 & 0 & \frac{\rho_f}{\rho}\chi_2(D+a_{s_2})^{1/2} & 0 \\ 0 & 0 & 0 & 0 & 0 & \frac{\rho_f}{\rho}\chi_3(D+a_{s_3})^{1/2} \\ 0 & 0 & 0 & -\chi_1(D+a_{s_1})^{1/2} & 0 & 0 \\ 0 & 0 & 0 & 0 & -\chi_2(D+a_{s_2})^{1/2} & 0 \\ 0 & 0 & 0 & 0 & 0 & -\chi_3(D+a_{s_3})^{1/2} \end{bmatrix},$$

where $\beta_i = \rho m_i - \rho_f^2,\ \chi_i = \left(\frac{\rho}{\rho m_i - \rho_f^2}\right)\frac{\eta}{\kappa_i} a_{s_i}^{-1/2}$, and $\boldsymbol{f}$ denotes the vector of forcing terms.

5.3.5 Approximation of fractional derivative term

Using the Caputo's definition of fractional derivative [116, 1]

$$\begin{aligned}(D+a_{s_i})^{1/2} q_i &= \int_0^t \frac{e^{-a_{s_i}(t-\tau)}}{\Gamma(1/2)}(t-\tau)^{-1/2}\left[a_{s_i} q_i(\tau) + \dot{q}_i(\tau)\right] d\tau, \\ &= \frac{1}{\sqrt{\pi}}\int_0^t \frac{e^{-a_{s_i}(t-\tau)}}{\sqrt{t-\tau}}\left[a_{s_i} q_i(\tau) + \dot{q}_i(\tau)\right] d\tau,\end{aligned} \tag{5.17}$$

where we have used the identity $\Gamma(1/2) = \pi$.

The montone function $\dfrac{1}{\sqrt{t-\tau}}$ is approximated as [1]

$$\frac{1}{\sqrt{(t-\tau)}} = \frac{1}{\sqrt{\pi}}\int_0^\infty \frac{1}{\sqrt{\alpha}} e^{-\alpha(t-\tau)} d\alpha. \tag{5.18}$$

Substituting (5.18) into (5.17) results

$$(D + a_{s_i})^{1/2} q_i = \frac{1}{\pi} \int_0^\infty \frac{1}{\sqrt{\alpha}} \phi(\alpha, t)\ d\alpha \tag{5.19}$$

where

$$\phi(\alpha, t) = \int_0^t e^{-(t-\tau)(\alpha + a_{s_i})} \left[a_s q_i(\tau) + \dot{q}_i(\tau) \right]\ d\tau$$

with $\phi(\alpha, t)$ satisfying the following ODE

$$\partial_t \phi - \partial_t q_i = -(a_{s_i} + \alpha)\phi + a_{s_1} q_1 \tag{5.20}$$

$$\phi(\alpha, 0) = 0 \tag{5.21}$$

The improper integral in (5.19) can be expressed as

$$(D + a_{s_i})^{1/2} q_i = \sum_{l=1}^{N} a_l^i \phi_l^i(t) \quad \text{with} \quad \phi_l = \phi(\alpha_l^i, t) \tag{5.22}$$

with each ϕ_l satisfying equations (5.20) as follows

$$\begin{aligned} \partial_t \phi_l^i - \partial_t q_i &= -(a_{s_i} + \alpha_l^i)\phi_l^i + a_{s_i} q_i \\ \phi(\alpha_l, 0) &= 0 \end{aligned} \tag{5.23}$$

A modified Gauss-Jacobi quadrature approximation is used to compute the a_l and α_l. A brief review of the Gauss-Jacobi approximation is given in D.2. The computed values of a_l and α_l for $l = 5$ are provided in Table 5.1.

Augmenting the system of equations in (5.16) with (5.20) and (5.22) will result in a system with $3N + 13$ partial differential equations and is written as

$$\frac{\partial \widehat{\boldsymbol{Q}}}{\partial t} + \widehat{\boldsymbol{A}} \frac{\partial \widehat{\boldsymbol{Q}}}{\partial x_1} + \widehat{\boldsymbol{B}} \frac{\partial \widehat{\boldsymbol{Q}}}{\partial x_2} + \widehat{\boldsymbol{C}} \frac{\partial \widehat{\boldsymbol{Q}}}{\partial x_3} = \widehat{\boldsymbol{D}} \widehat{\boldsymbol{Q}} + \boldsymbol{f}, \tag{5.24}$$

where

$$\widehat{\boldsymbol{Q}} = \left[\begin{array}{cccccccccccccc} \tau_{11}, & \tau_{22}, & \tau_{33}, & \tau_{23}, & \tau_{13}, & \tau_{12}, & p, & v_1, & v_2, & v_3, & q_1, & q_2, & q_3, \\ & \psi_1^x, & \psi_1^y, & \psi_1^z, & \ldots..\ , & \psi_N^x, & \psi_N^y, & \psi_N^z & & & & & & \end{array} \right]^T,$$

with $\psi_l^i = \phi_l^i - q_i$ and

$$\widehat{\boldsymbol{A}} = \left[\begin{array}{c|c|c} \mathbf{0}_{7\times 7} & \boldsymbol{A}_{11} & \mathbf{0}_{7\times 3N} \\ \hline \boldsymbol{A}_{21} & \mathbf{0}_{6\times 6} & \mathbf{0}_{6\times 3N} \\ \hline \mathbf{0}_{3N\times 7} & \boldsymbol{A}_{32} & \mathbf{0}_{3N\times 3N} \end{array}\right], \quad \widehat{\boldsymbol{B}} = \left[\begin{array}{c|c|c} \mathbf{0}_{7\times 7} & \boldsymbol{B}_{11} & \mathbf{0}_{7\times 3N} \\ \hline \boldsymbol{B}_{21} & \mathbf{0}_{6\times 6} & \mathbf{0}_{6\times 3N} \\ \hline \mathbf{0}_{3N\times 7} & \boldsymbol{B}_{32} & \mathbf{0}_{3N\times 3N} \end{array}\right],$$

$$\widehat{\boldsymbol{C}} = \left[\begin{array}{c|c|c} \mathbf{0}_{7\times 7} & \boldsymbol{C}_{11} & \mathbf{0}_{7\times 3N} \\ \hline \boldsymbol{C}_{21} & \mathbf{0}_{6\times 6} & \mathbf{0}_{6\times 3N} \\ \hline \mathbf{0}_{3N\times 7} & \boldsymbol{C}_{32} & \mathbf{0}_{3N\times 3N} \end{array}\right], \quad \widehat{\boldsymbol{D}} = \left[\begin{array}{c|c|c} \mathbf{0}_{7\times 7} & \mathbf{0}_{7\times 6} & \mathbf{0}_{7\times 3N} \\ \hline \mathbf{0}_{6\times 7} & \boldsymbol{D}_{22} & \boldsymbol{D}_{23} \\ \hline \mathbf{0}_{3N\times 7} & \boldsymbol{D}_{32} & \boldsymbol{D}_{33} \end{array}\right], \text{ with}$$

$$\boldsymbol{A}_{32} = -\begin{bmatrix} -\frac{\rho_f}{\beta_1} & 0 & 0 & 0 & 0 & 0 & -\frac{\rho}{\beta_1} \\ 0 & 0 & 0 & 0 & 0 & -\frac{\rho_f}{\beta_2} & 0 \\ 0 & 0 & 0 & 0 & -\frac{\rho_f}{\beta_3} & 0 & 0 \\ \vdots & \vdots & \vdots & \vdots & \vdots & \vdots & \vdots \\ \vdots & \vdots & \vdots & \vdots & \vdots & \vdots & \vdots \\ \vdots & \vdots & \vdots & \vdots & \vdots & \vdots & \vdots \\ -\frac{\rho_f}{\beta_1} & 0 & 0 & 0 & 0 & 0 & -\frac{\rho}{\beta_1} \\ 0 & 0 & 0 & 0 & 0 & -\frac{\rho_f}{\beta_2} & 0 \\ 0 & 0 & 0 & 0 & -\frac{\rho_f}{\beta_3} & 0 & 0 \end{bmatrix},$$

$$\boldsymbol{B}_{32} = -\begin{bmatrix} 0 & 0 & 0 & 0 & 0 & -\frac{\rho_f}{\beta_1} & 0 \\ 0 & -\frac{\rho_f}{\beta_2} & 0 & 0 & 0 & 0 & 0 \\ 0 & 0 & 0 & -\frac{\rho_f}{\beta_3} & 0 & 0 & 0 \\ \vdots & \vdots & \vdots & \vdots & \vdots & \vdots & \vdots \\ \vdots & \vdots & \vdots & \vdots & \vdots & \vdots & \vdots \\ \vdots & \vdots & \vdots & \vdots & \vdots & \vdots & \vdots \\ 0 & 0 & 0 & 0 & 0 & -\frac{\rho_f}{\beta_1} & 0 \\ 0 & -\frac{\rho_f}{\beta_2} & 0 & 0 & 0 & 0 & 0 \\ 0 & 0 & 0 & -\frac{\rho_f}{\beta_3} & 0 & 0 & 0 \end{bmatrix},$$

$$\boldsymbol{C}_{32} = -\begin{bmatrix} 0 & 0 & 0 & 0 & -\frac{\rho_f}{\beta_1} & 0 & 0 \\ 0 & 0 & 0 & -\frac{\rho_f}{\beta_2} & 0 & 0 & 0 \\ 0 & 0 & -\frac{\rho_f}{\beta_3} & 0 & 0 & 0 & -\frac{\rho}{\beta_3} \\ \vdots & \vdots & \vdots & \vdots & \vdots & \vdots & \vdots \\ \vdots & \vdots & \vdots & \vdots & \vdots & \vdots & \vdots \\ \vdots & \vdots & \vdots & \vdots & \vdots & \vdots & \vdots \\ 0 & 0 & 0 & 0 & -\frac{\rho_f}{\beta_1} & 0 & 0 \\ 0 & 0 & 0 & -\frac{\rho_f}{\beta_2} & 0 & 0 & 0 \\ 0 & 0 & -\frac{\rho_f}{\beta_3} & 0 & 0 & 0 & -\frac{\rho}{\beta_3} \end{bmatrix}, \quad \boldsymbol{D}_{32} = -\begin{bmatrix} 0 & 0 & 0 & \alpha_1^x & 0 & 0 \\ 0 & 0 & 0 & 0 & \alpha_1^y & 0 \\ 0 & 0 & 0 & 0 & 0 & \alpha_1^z \\ \vdots & \vdots & \vdots & \vdots & \vdots & \vdots \\ \vdots & \vdots & \vdots & \vdots & \vdots & \vdots \\ \vdots & \vdots & \vdots & \vdots & \vdots & \vdots \\ 0 & 0 & 0 & \alpha_N^x & 0 & 0 \\ 0 & 0 & 0 & 0 & \alpha_N^x & 0 \\ 0 & 0 & 0 & 0 & 0 & \alpha_N^x \end{bmatrix},$$

$$\boldsymbol{D}_{22} = \begin{bmatrix} 0 & 0 & 0 & \frac{\rho_f}{\rho}\chi_1 \sum_{l=1}^{N} \alpha_l^x & 0 & 0 \\ 0 & 0 & 0 & 0 & \frac{\rho_f}{\rho}\chi_2 \sum_{l=1}^{N} \alpha_l^y & 0 \\ 0 & 0 & 0 & 0 & 0 & \frac{\rho_f}{\rho}\chi_3 \sum_{l=1}^{N} \alpha_l^z \\ 0 & 0 & 0 & -\chi_1 \sum_{l=1}^{N} \alpha_l^x & 0 & 0 \\ 0 & 0 & 0 & 0 & -\chi_2 \sum_{l=1}^{N} \alpha_l^y & 0 \\ 0 & 0 & 0 & 0 & 0 & -\chi_3 \sum_{l=1}^{N} \alpha_l^z \end{bmatrix}, \text{ and}$$

$$\boldsymbol{D}_{23} = \begin{bmatrix} \frac{\rho_f}{\rho}\chi_1\alpha_1^x & 0 & 0 & \cdots & \cdots & \frac{\rho_f}{\rho}\chi_1\alpha_N^x & 0 & 0 \\ 0 & \frac{\rho_f}{\rho}\chi_2\alpha_1^y & 0 & \cdots & \cdots & 0 & \frac{\rho_f}{\rho}\chi_2\alpha_N^y & 0 \\ 0 & 0 & \frac{\rho_f}{\rho}\chi_3\alpha_1^z & \cdots & \cdots & 0 & 0 & \frac{\rho_f}{\rho}\chi_3\alpha_N^z \\ -\chi_1\alpha_1^x & 0 & 0 & \cdots & \cdots & -\chi_1\alpha_N^x & 0 & 0 \\ 0 & -\chi_2\alpha_1^y & 0 & \cdots & \cdots & 0 & -\chi_2\alpha_N^y & 0 \\ 0 & 0 & -\chi_3\alpha_1^z & \cdots & \cdots & 0 & 0 & -\chi_3\alpha_N^z \end{bmatrix}, \text{ and}$$

$$\boldsymbol{D}_{33} = -\begin{bmatrix} a_{s_1}+\alpha_1^x & 0 & 0 & \cdots & 0 & 0 & 0 \\ 0 & a_{s_2}+\alpha_1^y & 0 & \cdots & 0 & 0 & 0 \\ 0 & 0 & a_{s_3}+\alpha_1^z & \cdots & 0 & 0 & 0 \\ \vdots & \vdots & \vdots & \vdots & \vdots & \vdots & \\ \vdots & \vdots & \vdots & \vdots & \vdots & \vdots & \\ \vdots & \vdots & \vdots & \vdots & \vdots & \vdots & \\ 0 & 0 & 0 & \cdots & a_{s_1}+\alpha_N^x & 0 & 0 \\ 0 & 0 & 0 & \cdots & 0 & a_{s_2}+\alpha_N^x & 0 \\ 0 & 0 & 0 & \cdots & 0 & 0 & a_{s_3}+\alpha_N^x \end{bmatrix}.$$

From here onwards, the system in (5.24) is referred as "broad-band Biot's equations".

5.3.6 Symmetric form of the system of broad-band Biot's equations

We utilize a symmetric form of (5.24), which ensures the stability and convergence of the numerical scheme. The symmetric form of (5.24) for velocity (including auxiliary variable) and stress is expressed as

$$\boldsymbol{Q}_s \frac{\partial \boldsymbol{\tau}}{\partial t} = \sum_{i=1}^{d} \boldsymbol{A}_i \frac{\partial \boldsymbol{v}}{\partial \boldsymbol{x}_i}, \tag{5.25}$$

$$\boldsymbol{Q}_v \frac{\partial \boldsymbol{v}}{\partial t} = \sum_{i=1}^{d} \boldsymbol{A}_i^T \frac{\partial \boldsymbol{\tau}}{\partial \boldsymbol{x}_i} + \boldsymbol{D}\boldsymbol{v} + \boldsymbol{f}, \tag{5.26}$$

where

$$\boldsymbol{Q}_s = \left[\begin{array}{c|c} \boldsymbol{S} & \boldsymbol{S\alpha} \\ \hline \boldsymbol{\alpha^T S} & \dfrac{1}{M} + \boldsymbol{\alpha}^T S \boldsymbol{\alpha} \end{array}\right], \quad \boldsymbol{Q}_v = \begin{bmatrix} \rho & 0 & 0 & \rho_f & 0 & 0 & \cdots & 0 & 0 & 0 \\ 0 & \rho & 0 & 0 & \rho_f & 0 & \cdots & 0 & 0 & 0 \\ 0 & 0 & \rho & 0 & 0 & \rho_f & \cdots & 0 & 0 & 0 \\ \rho_f & 0 & 0 & m_1 & 0 & 0 & \cdots & 0 & 0 & 0 \\ 0 & \rho_f & 0 & 0 & m_2 & 0 & \cdots & 0 & 0 & 0 \\ 0 & 0 & \rho_f & 0 & 0 & m_3 & \cdots & 0 & 0 & 0 \\ \vdots & \vdots & \vdots & \vdots & \vdots & \vdots & & & & \\ 0 & 0 & 0 & 0 & 0 & 0 & \cdots & 1 & 0 & 0 \\ 0 & 0 & 0 & 0 & 0 & 0 & \cdots & 0 & 1 & 0 \\ 0 & 0 & 0 & 0 & 0 & 0 & \cdots & 0 & 0 & 1 \end{bmatrix},$$

with

$$\boldsymbol{S} = \begin{bmatrix} \dfrac{c_{11}c_{33} - c_{13}^2}{c_0} & \dfrac{c_{13}^2 - c_{12}c_{33}}{c_0} & \dfrac{-c_{13}}{c_1} & 0 & 0 & 0 \\ \dfrac{c_{13}^2 - c_{12}c_{33}}{c_0} & \dfrac{c_{11}c_{33} - c_{13}^2}{c_0} & \dfrac{-c_{13}}{c_1} & 0 & 0 & 0 \\ -\dfrac{c_{13}}{c_1} & -\dfrac{c_{13}}{c_1} & \dfrac{c_{11} + c_{12}}{c_1} & 0 & 0 & 0 \\ 0 & 0 & 0 & \dfrac{1}{c_{55}} & 0 & 0 \\ 0 & 0 & 0 & 0 & \dfrac{1}{c_{55}} & 0 \\ 0 & 0 & 0 & 0 & 0 & \dfrac{2}{c_{11} - c_{12}} \end{bmatrix}, \quad \boldsymbol{\alpha} = \begin{bmatrix} \alpha_1 \\ \alpha_2 \\ \alpha_3 \\ 0 \\ 0 \\ 0 \end{bmatrix},$$

and

$$\boldsymbol{\tau} = [\tau_{11},\ \tau_{22},\ \tau_{33},\ \tau_{23},\ \tau_{13},\ \tau_{12},\ p]^T,$$
$$\boldsymbol{v} = [v_1,\ v_2,\ v_3,\ q_1,\ q_2,\ q_3,\ \psi_1^x,\ \psi_1^y,\ \psi_1^z,\ \ldots..\ ,\ \psi_N^x,\ \psi_N^y,\ \psi_N^z]^T,$$

with

$$\boldsymbol{A}_i = \left[\ \widehat{\boldsymbol{A}}_i \ \middle|\ \boldsymbol{0}_{7\times 3N}\ \right],$$

$$\widehat{\boldsymbol{A}}_1 = \begin{bmatrix} 1 & 0 & 0 & 0 & 0 & 0 \\ 0 & 0 & 0 & 0 & 0 & 0 \\ 0 & 0 & 0 & 0 & 0 & 0 \\ 0 & 0 & 0 & 0 & 0 & 0 \\ 0 & 0 & 1 & 0 & 0 & 0 \\ 0 & 1 & 0 & 0 & 0 & 0 \\ 0 & 0 & 0 & -1 & 0 & 0 \end{bmatrix}, \quad \widehat{\boldsymbol{A}}_2 = \begin{bmatrix} 0 & 0 & 0 & 0 & 0 & 0 \\ 0 & 1 & 0 & 0 & 0 & 0 \\ 0 & 0 & 0 & 0 & 0 & 0 \\ 0 & 0 & 1 & 0 & 0 & 0 \\ 0 & 0 & 0 & 0 & 0 & 0 \\ 1 & 0 & 0 & 0 & 0 & 0 \\ 0 & 0 & 0 & 0 & -1 & 0 \end{bmatrix},$$

$$\widehat{\boldsymbol{A}}_3 = \begin{bmatrix} 0 & 0 & 0 & 0 & 0 & 0 \\ 0 & 0 & 0 & 0 & 0 & 0 \\ 0 & 0 & 1 & 0 & 0 & 0 \\ 0 & 1 & 0 & 0 & 0 & 0 \\ 1 & 0 & 0 & 0 & 0 & 0 \\ 0 & 0 & 0 & 0 & 0 & 0 \\ 0 & 0 & 0 & 0 & 0 & -1 \end{bmatrix}, \qquad \boldsymbol{D} = \boldsymbol{Q}_v \widehat{\boldsymbol{D}}.$$

Explicit expressions for $\boldsymbol{Q}_s^{-1}$ and $\boldsymbol{Q}_v^{-1}$ are given by

$$\boldsymbol{Q}_s^{-1} = \begin{bmatrix} c_{11} + M\alpha_1^2 & c_{12} + M\alpha_1\alpha_2 & c_{13} + M\alpha_1\alpha_3 & 0 & 0 & 0 & -M\alpha_1 \\ c_{12} + M\alpha_1\alpha_2 & c_{11} + M\alpha_2^2 & c_{13} + M\alpha_2\alpha_3 & 0 & 0 & 0 & -M\alpha_2 \\ c_{13} + M\alpha_1\alpha_3 & c_{13} + M\alpha_2\alpha_3 & c_{33} + M\alpha_3^2 & 0 & 0 & 0 & -M\alpha_3 \\ 0 & 0 & 0 & c_{55} & 0 & 0 & 0 \\ 0 & 0 & 0 & 0 & c_{55} & 0 & 0 \\ 0 & 0 & 0 & 0 & 0 & \dfrac{c_{11} - c_{12}}{2} & 0 \\ -M\alpha_1 & -M\alpha_2 & -M\alpha_3 & 0 & 0 & 0 & M \end{bmatrix},$$

$$\boldsymbol{Q}_v^{-1} = \begin{bmatrix} \frac{m_1}{\rho m_1 - \rho_f^2} & 0 & 0 & \frac{-\rho_f}{\rho m_1 - \rho_f^2} & 0 & 0 & \cdots & 0 & 0 & 0 \\ 0 & \frac{m_2}{\rho m_2 - \rho_f^2} & 0 & 0 & \frac{-\rho_f}{\rho m_2 - \rho_f^2} & 0 & \cdots & 0 & 0 & 0 \\ 0 & 0 & \frac{m_3}{\rho m_3 - \rho_f^2} & 0 & 0 & \frac{-\rho_f}{\rho m_3 - \rho_f^2} & \cdots & 0 & 0 & 0 \\ \frac{-\rho_f}{\rho m_1 - \rho_f^2} & 0 & 0 & \frac{\rho}{\rho m_1 - \rho_f^2} & 0 & 0 & \cdots & 0 & 0 & 0 \\ 0 & \frac{-\rho_f}{\rho m_2 - \rho_f^2} & 0 & 0 & \frac{\rho}{\rho m_2 - \rho_f^2} & 0 & \cdots & 0 & 0 & 0 \\ 0 & 0 & \frac{-\rho_f}{\rho m_3 - \rho_f^2} & 0 & 0 & \frac{\rho}{\rho m_3 - \rho_f^2} & \cdots & 0 & 0 & 0 \\ \vdots & \vdots & \vdots & \vdots & \vdots & \vdots & \vdots & \vdots & \vdots & \vdots \\ 0 & 0 & 0 & 0 & 0 & 0 & \cdots & 1 & 0 & 0 \\ 0 & 0 & 0 & 0 & 0 & 0 & \cdots & 0 & 1 & 0 \\ 0 & 0 & 0 & 0 & 0 & 0 & \cdots & 0 & 0 & 1 \end{bmatrix}.$$

The matrices $\boldsymbol{Q}_s$ and $\boldsymbol{Q}_v$ are Hessians of the potential and kinetic energy, respectively, computed with respect to state variables in $\boldsymbol{Q}$. Since the energy of the poroelastic system is quadratic positive-definite [3], the Hessians ($\boldsymbol{Q_s}$, $\boldsymbol{Q}_v$) are symmetric positive-definite. We also assume the Hessians are bounded as follows

$$0 < s_{\min} \leq \boldsymbol{u}^T \boldsymbol{Q}_s(\boldsymbol{x}) \boldsymbol{u} \leq s_{\max} < \infty$$

$$0 < \tilde{s}_{\min} \leq \boldsymbol{u}^T \boldsymbol{Q}_s^{-1}(\boldsymbol{x}) \boldsymbol{u} \leq \tilde{s}_{\max} < \infty$$

$$0 < v_{\min} \leq \boldsymbol{u}^T \boldsymbol{Q}_v(\boldsymbol{x}) \boldsymbol{u} \leq v_{\max} < \infty$$

$$0 < \tilde{v}_{\min} \leq \boldsymbol{u}^T \boldsymbol{Q}_v^{-1}(\boldsymbol{x}) \boldsymbol{u} \leq \tilde{v}_{\max} < \infty$$

for $\forall\ \boldsymbol{x} \in \mathbb{R}^d$ and $\forall\ \boldsymbol{u} \in \mathbb{R}^{N_d}$. Note that in (5.24), the dissipation matrix $\widehat{\boldsymbol{D}}$ is negative-definite.

Using the expressions for $\boldsymbol{Q}_s$ and $\boldsymbol{Q}_v$, the kinetic (K) and potential energy (V) of the poroelastic system are expressed as

$$K = \frac{1}{2} \boldsymbol{\tau}^T \boldsymbol{Q}_s \boldsymbol{\tau}, \quad V = \frac{1}{2} \boldsymbol{v}^T \boldsymbol{Q}_v \boldsymbol{v}. \tag{5.27}$$

5.4 An energy stable discontinuous Galerkin formulation for poroelastic wave propgation

Energy stable discontinuous Galerkin methods for elastic wave propagation have been constructed based on symmetric formulations of the elastodynamic equations [97, 89], and it is straightforward to extend such discontinuous Galerkin formulations to the symmetric poroelastic system [112]. We assume that the domain Ω is exactly triangulated by a mesh Ω_h which consists of elements D^k which are images of a reference element $\hat{D}$ under the local affine mapping.

$$\boldsymbol{x}^k = \Phi^k \widehat{\boldsymbol{x}},$$

where $\boldsymbol{x}^k = \{x^k, y^k\}$ for $d = 2$ and $\boldsymbol{x}^k = \{x^k, y^k, z^k\}$ for $d = 3$ denote the physical coordinates on D^k and $\hat{\boldsymbol{x}} = \{\hat{x}, \hat{y}\}$ for $d = 2$ and $\widehat{\boldsymbol{x}} = \{\widehat{x}, \widehat{y}, \widehat{z}\}$ for $d = 3$ denote coordinates on the reference element. We denote the determinant of the Jacobian of Φ^k as J.

Solutions over each element D^k are approximated from a local approximation space $V_h(D^k)$, which is defined as composition of mapping Φ^k and reference approximation space $V_h(\widehat{D})$

$$V_h(D^k) = \Phi^k \circ V_h(\widehat{D}).$$

Subsequently, the global approximation space $V_h(\Omega_h)$ is defined as

$$V_h(\Omega_h) = \bigoplus_k V_h(D^k).$$

In this work, we will take $V_h(\widehat{D}) = P^N(\widehat{D})$, with $P^N(\widehat{D})$ being the space of polynomials of total degree N on the reference simplex. In two dimensions, P^N on a triangle is

$$P^N(\widehat{D}) = \{\widehat{x}^i \widehat{y}^j, 0 \leq i + j \leq N\},$$

and in three dimensions, P^N on a tetrahedron is

$$P^N(\widehat{D}) = \{\widehat{x}^i \widehat{y}^j \widehat{x}^k, 0 \leq i + j + k \leq N\}.$$

The L^2 inner product and norm over D^k is represented as

$$(\boldsymbol{g}, \boldsymbol{h}) = \int_{D^k} \boldsymbol{g} \cdot \boldsymbol{h} \; d\boldsymbol{x} = \int_{\hat{D}} \boldsymbol{g} \cdot \boldsymbol{h} J \; d\hat{\boldsymbol{x}}, \qquad ||\boldsymbol{g}||^2_{L^2\Omega} = (\boldsymbol{g}, \boldsymbol{g})_{L^2(D^k)},$$

where $\boldsymbol{g}$ and $\boldsymbol{h}$ are real vector-valued functions. Global L^2 inner products and squared norms are defined as the sum of local L^2 inner products and squared norms over each elements. The L^2 inner product and norm over the boundary ∂D^k of an element are similarly defined as

$$\langle \boldsymbol{u}, \boldsymbol{v} \rangle_{L^2(\partial D^k)} = \int_{\partial D^k} \boldsymbol{u} \cdot \boldsymbol{v} \; d\boldsymbol{x} = \sum_{f \in \partial D^k} \int_{\hat{f}} \boldsymbol{u} \cdot \boldsymbol{v} J^f \; d\hat{\boldsymbol{x}}, \qquad ||\boldsymbol{u}||^2_{L^2(\partial D^k)} = \langle \boldsymbol{u}, \boldsymbol{u} \rangle ,$$

where J^f is the Jacobian of the mapping from a reference face $\hat{f}$ to a physical face f of an element.

Let f be a face of an element D^k with neighboring element $D^{k,+}$ and unit outward normal $\boldsymbol{n}$. Let u be a function with discontinuities across element interfaces. We define the interior value u^- and exterior value u^+ on face f of D^k

$$u^- = u|_{f \cap \partial D^k}, \qquad u^+ = u|_{f \cap \partial D^{k,+}}.$$

The jump and average of a scalar function $u \in V_h(\Omega_h)$ over f are then defined as

$$[\![u]\!] = u^+ - u^-, \qquad \{\!\{ u \}\!\} = \frac{u^+ + u^-}{2}.$$

Jumps and averages of vector-valued functions $\boldsymbol{u} \in \mathbb{R}^m$ and and matrix-valued functions $\tilde{\boldsymbol{S}} \in \mathbb{R}^{m \times n}$ are defined component-wise.

$$([\![\boldsymbol{u}]\!])_i = [\![\boldsymbol{u}_i]\!], \qquad 1 \leq i \leq m \qquad \left([\![\tilde{\boldsymbol{S}}]\!]\right)_{ij} = [\![\tilde{\boldsymbol{S}}]\!]$$

We can now specify a DG formulation for poroelastic wave equation (5.24). The symmetric hyperbolic system in (5.25 and 5.26) readily admits a DG formulation based on a penalty flux [99, 97]. For the symmetric first order poroelastic wave equation, the DG formulation in strong form is given as

$$\begin{aligned}
\sum_{D^k \in \Omega_h} \left(\boldsymbol{Q}_s \frac{\partial \boldsymbol{\tau}}{\partial t}, \boldsymbol{h} \right)_{L^2(D^k)} &= \sum_{D^k \in \Omega_h} \left(\left(\sum_{i=1}^{d} \boldsymbol{A}_i \frac{\partial \boldsymbol{v}}{\partial \boldsymbol{x}_i}, \boldsymbol{h} \right)_{L^2(D^k)} + \left\langle \frac{1}{2} \boldsymbol{A}_{\boldsymbol{n}} [\![\boldsymbol{v}]\!] + \frac{\alpha_{\boldsymbol{\tau}}}{2} \boldsymbol{A}_{\boldsymbol{n}} \boldsymbol{A}_n^T [\![\boldsymbol{\tau}]\!], \boldsymbol{h} \right\rangle_{L^2(\partial D^k)} \right) \\
\sum_{D^k \in \Omega_h} \left(\boldsymbol{Q}_v \frac{\partial \boldsymbol{v}}{\partial t}, \boldsymbol{g} \right)_{L^2(D^k)} &= \sum_{D^k \in \Omega_h} \left(\left(\sum_{i=1}^{d} {\boldsymbol{A}_i}^T \frac{\partial \boldsymbol{\tau}}{\partial \boldsymbol{x}_i} + \boldsymbol{f}, \boldsymbol{g} \right)_{L^2(D^k)} \right. \\
&\qquad \left. + \left\langle \frac{1}{2} \boldsymbol{A}_{\boldsymbol{n}}^T [\![\boldsymbol{\tau}]\!] + \frac{\alpha_{\boldsymbol{v}}}{2} \boldsymbol{A}_n^T \boldsymbol{A}_{\boldsymbol{n}} [\![\boldsymbol{v}]\!], \boldsymbol{g} \right\rangle_{L^2(\partial D^k)} + (\boldsymbol{D}\boldsymbol{v}, \boldsymbol{g}) \right),
\end{aligned} \tag{5.28}$$

for all $\boldsymbol{h},\ \boldsymbol{g} \in V_h(\Omega_h)$. Here, $\boldsymbol{A}_n$ is the normal matrix defined on a face f of an element

$$\boldsymbol{A}_n = \sum_{i=1}^{d} n_i \boldsymbol{A}_i.$$

The factors $\alpha_{\boldsymbol{\tau}}$ and $\alpha_{\boldsymbol{v}}$ are penalty parameters and defined on element interfaces. We assume that $\alpha_{\boldsymbol{\tau}},\ \alpha_{\boldsymbol{v}} \geq 0$ and are piecewise constant over each shared face between two elements. These penalty constants can be taken to be zero, which results in a non-dissipative central flux, while $\alpha_{\boldsymbol{\tau}},\ \alpha_{\boldsymbol{v}} > 0$ results in energy dissipation similar to the upwind flux [6]. The stability of DG formulations are independent of the magnitude of these penalty parameters. However, a naive choice of these parameters will result in a stiffer semi-discrete system of ODEs and necessitates a smaller time under explicit time integration schemes. In this work, we take $\alpha_\tau, \alpha_v = O(1)$ unless stated otherwise.

The boundary conditions in this study are the same as those used in [112].

5.4.1 Energy stability

The DG formulation in (5.28) is energy stable in the absence of external forces ($f = 0$), and for free-surface and absorbing boundary conditions. The proof of energy stability extends naturally from the work by Shukla et al. [112] and summarized as follows

Theorem 3. *The DG formulation in (5.28) is energy stable for $\alpha_{\boldsymbol{\tau}}, \alpha_{\boldsymbol{v}} \geq 0$ such that*

$$\begin{aligned}
\sum_{D^k \in \Omega_h} \frac{1}{2}\frac{\partial}{\partial t}\left((\boldsymbol{Q}_s\boldsymbol{\tau},\boldsymbol{\tau})_{L^2(D^k)} + (\boldsymbol{Q}_v\boldsymbol{v},\boldsymbol{v})_{L^2(D^k)} \right) &= -\sum_{f\in\Gamma_h\setminus\partial\Omega} \int_f \left(\frac{\alpha_{\boldsymbol{\tau}}}{2} \left|\boldsymbol{A}_n^T[\![\boldsymbol{\tau}]\!]\right|^2 + \frac{\alpha_{\boldsymbol{v}}}{2} \left|\boldsymbol{A}_n[\![\boldsymbol{v}]\!]\right|^2 \right) d\boldsymbol{x} \\
&- \sum_{f\in\Gamma_{\boldsymbol{\tau}}} \int_f \left(\alpha_{\boldsymbol{\tau}} \left|\boldsymbol{A}_n^T\boldsymbol{\tau}^-\right|^2 \right)\ d\boldsymbol{x} - \sum_{f\in\Gamma_{abc}} \int_f \left(\frac{\alpha_{\boldsymbol{\tau}}}{2} \left|\boldsymbol{A}_n^T\boldsymbol{\tau}^-\right|^2 + \frac{\alpha_{\boldsymbol{v}}}{2} \left|\boldsymbol{A}_n\boldsymbol{v}^-\right|^2 \right) d\boldsymbol{x} \\
&+ \sum_{D^k\in\Omega_h} \int_{D^k} \boldsymbol{v}^T\boldsymbol{D}\boldsymbol{v}\ d\boldsymbol{x} \leq 0.
\end{aligned} \tag{5.29}$$

Since $\boldsymbol{Q}_s$ and $\boldsymbol{Q}_v$ are positive definite, the left hand side of (5.29) is an L^2-equivalent norm on $(\boldsymbol{\tau}, \boldsymbol{v})$ and Theorem 1 implies that magnitude of the DG solution is non-increasing in time. This also shows that dissipation is present for positive penalization parameters, i.e. $\alpha_{\boldsymbol{\tau}}, \alpha_{\boldsymbol{v}} > 0$.

5.4.2 The semi-discrete matrix system for DG

Let $\{\phi_i\}_{i=1}^{N_p}$ be a basis for $P^N\left(\widehat{D}\right)$. In our implementation, we use nodal basis functions located at Warp and Blend interpolation points [6], which are defined implicitly using an orthogonal polynomial basis on the reference simplex. We define the reference mass matrix $\widehat{\boldsymbol{M}}$ and the physical mass matrix $\boldsymbol{M}$ for an element D^k as

$$\left(\widehat{\boldsymbol{M}}\right)_{ij} = \int_{\widehat{D}} \phi_j \phi_i \, \mathrm{d}\boldsymbol{x}, \qquad (\boldsymbol{M}_{ij}) = \int_{D^k} \phi_j \phi_i \, \mathrm{d}\boldsymbol{x} = \int_{\widehat{D}} \phi_j \phi_i J \, \mathrm{d}\widehat{\boldsymbol{x}}.$$

For affine mappings, J is constant and $\boldsymbol{M} = J\widehat{\boldsymbol{M}}$. We also define weak differentiation matrices $\boldsymbol{S}_k$ and face mass matrices $\boldsymbol{M}_f$ such that

$$(\boldsymbol{S}_k)_{ij} = \int_{D^k} \frac{\partial \phi_j}{\partial \boldsymbol{x}_k} \phi_i \, \mathrm{d}\boldsymbol{x}, \quad (\boldsymbol{M}_f)_{ij} = \int_f \phi_j \phi_i \mathrm{d}\boldsymbol{x} = \int_{\hat{f}} \phi_j \phi_i J^f \mathrm{d}\hat{\boldsymbol{x}},$$

where J^f is the Jacobian of the mapping from the reference face $\widehat{f}$ to f. For affinely mapped simplices, J^f is also constant and $M_f = J^f \widehat{\boldsymbol{M}}_f$, where the definition of the reference face mass matrix $\widehat{\boldsymbol{M}}_f$ is analogous to the definition of the reference mass matrix $\widehat{\boldsymbol{M}}$.

Finally, we introduce weighted mass matrices. Let $w(\boldsymbol{x}) \in \mathbb{R}$ and $\boldsymbol{W}(\boldsymbol{x}) \in \mathbb{R}^{m \times n}$. Then, scalar and matrix-weighted mass matrices $\boldsymbol{M}_w$ and $\boldsymbol{M}_{\boldsymbol{W}}$ are defined as

$$(\boldsymbol{M}_w)_{ij} = \int_{D^k} w(\boldsymbol{x}) \phi_j(\boldsymbol{x}) \phi_i(\boldsymbol{x}) \, \mathrm{d}\boldsymbol{x}, \qquad \boldsymbol{M}_{\boldsymbol{W}} = \begin{bmatrix} \boldsymbol{M}_{\boldsymbol{W}_{\mathbf{1},\mathbf{1}}} & \dots & \boldsymbol{M}_{\boldsymbol{W}_{\mathbf{1},\boldsymbol{n}}} \\ \vdots & \ddots & \vdots \\ \boldsymbol{M}_{\boldsymbol{W}_{\boldsymbol{m},\mathbf{1}}} & \dots & \boldsymbol{M}_{\boldsymbol{W}_{\boldsymbol{m},\boldsymbol{n}}}, \end{bmatrix} \tag{5.30}$$

where $\boldsymbol{M}_{\boldsymbol{W}_{\boldsymbol{i},\boldsymbol{j}}}$ is the scalar weighted mass matrix weighted by the $(i,j)^{\text{th}}$ element of $\boldsymbol{W}$. Note that $\boldsymbol{M}_w, \boldsymbol{M}_{\boldsymbol{W}}$ are positive definite if $w(x), \boldsymbol{W}$ are pointwise positive definite.

Local contributions to the DG variational form may be evaluated in a quadrature-free manner using matrix-weighted mass matrices as defined above. Let $\boldsymbol{\Sigma}_{\boldsymbol{i}}$, $\boldsymbol{V}_i$ denote vectors containing degrees of freedom for solutions components $\boldsymbol{\tau}_i$ and $\boldsymbol{v}_i$, such that

$$\boldsymbol{v}_i(\boldsymbol{x},t) = \sum_{j=1}^{N_p} (\boldsymbol{V}_i(t))_j \phi_j(\boldsymbol{x}), \qquad 1 \le i \le 6$$

$$\boldsymbol{\tau}_i(\boldsymbol{x},t) = \sum_{j=1}^{N_p} (\boldsymbol{\Sigma}_{\boldsymbol{i}}(\boldsymbol{t}))_j \phi_j(\boldsymbol{x}), \qquad 1 \le i \le 7$$

Then, the local DG formulation can be written as a block system of ordinary differential equations by concatenating $\boldsymbol{\Sigma}_i$, $\boldsymbol{V}_i$ into single vectors $\boldsymbol{\Sigma}$ and $\boldsymbol{V}$ and using the Kronecker product $\otimes$

$$\boldsymbol{M}_{\boldsymbol{Q}_s}\frac{\partial \boldsymbol{\Sigma}}{\partial t} = \sum_{i=1}^{d}\left(\boldsymbol{A}_i \otimes \boldsymbol{S}_{\boldsymbol{i}}\right)\boldsymbol{V} + \sum_{f\in\partial D^k}\left(\boldsymbol{I}\otimes \boldsymbol{M}_f\right)\boldsymbol{F}_\tau \tag{5.31}$$

$$\boldsymbol{M}_{\boldsymbol{Q}_v}\frac{\partial \boldsymbol{V}}{\partial t} = \sum_{i=1}^{d}\left({\boldsymbol{A}_i}^T \otimes \boldsymbol{S}_{\boldsymbol{i}}\right)\boldsymbol{\Sigma} + \sum_{f\in\partial D^k}\left(\boldsymbol{I}\otimes \boldsymbol{M}_f\right)\boldsymbol{F}_v + \boldsymbol{M}_{\boldsymbol{D}}\boldsymbol{V}, \tag{5.32}$$

where $\boldsymbol{F}_v$ and $\boldsymbol{F}_\tau$ denote the degrees of freedom for the velocity and stress numerical fluxes.

In order to apply a time integrator, we must invert $\boldsymbol{M}_{\boldsymbol{Q}_s}$ and $\boldsymbol{M}_{\boldsymbol{Q}_v}$. While the inversion of $\boldsymbol{M}_{\boldsymbol{Q}_s}$ and $\boldsymbol{M}_{\boldsymbol{Q}_v}$ can be parallelized from element to element, doing so typically requires either the precomputation and storage of the dense matrix inverses or on-the-fly construction and solution of a large dense matrix system at every time step. The former option requires a large amount of storage, while the latter option is computationally expensive and difficult to parallelize among degrees of freedom. This cost can be avoided when $\boldsymbol{Q}_s$ and $\boldsymbol{Q}_v$ are constant over an element D^k. In this case, $\boldsymbol{M}_{\boldsymbol{Q}_s}$ reduces to

$$\boldsymbol{M}_{\boldsymbol{Q}_s}^{-1} = \begin{bmatrix} \boldsymbol{Q}_{s(1,1)}\boldsymbol{M} & \dots & \boldsymbol{Q}_{s(1,N_d)}\boldsymbol{M} \\ \vdots & \ddots & \vdots \\ \boldsymbol{Q}_{s(N_d,1)}\boldsymbol{M} & \dots & \boldsymbol{Q}_{s(N_d,N_d)}\boldsymbol{M} \end{bmatrix}^{-1} = \left(\boldsymbol{Q}_s \otimes \boldsymbol{M}\right)^{-1} = {\boldsymbol{Q}_s}^{-1} \otimes \left(\frac{1}{J}\widehat{\boldsymbol{M}}^{\boldsymbol{-1}}\right).$$

Similarly $\boldsymbol{M}_{\boldsymbol{Q}_v}^{-1}$ and $\boldsymbol{M}_{\boldsymbol{D}}^{-1}$ can be expressed as $\boldsymbol{M}_{\boldsymbol{Q}_v}^{-1} = {\boldsymbol{Q}_v}^{-1} \otimes \left(\frac{1}{J}\widehat{\boldsymbol{M}}^{\boldsymbol{-1}}\right)$, and $\boldsymbol{M}_{\boldsymbol{D}}^{-1} = \boldsymbol{D}^{-1} \otimes \left(\frac{1}{J}\widehat{\boldsymbol{M}}^{\boldsymbol{-1}}\right)$ respectively. Applying these observations to (5.31) and (5.32) yields the following sets of local ODEs over each element

$$\frac{\partial \boldsymbol{\Sigma}}{\partial t} = \sum_{i=1}^{d}\left({\boldsymbol{Q}_s}^{-1}\boldsymbol{A} \otimes \boldsymbol{D}_{\boldsymbol{i}}\right)\boldsymbol{V} + \sum_{f\in\partial D^k}\left({\boldsymbol{Q}_s}^{-1} \otimes \boldsymbol{M}_f\right)\boldsymbol{F}_\tau, \tag{5.33}$$

$$\frac{\partial \boldsymbol{V}}{\partial t} = \sum_{i=1}^{d}\left({\boldsymbol{Q}_v}^{-1}\boldsymbol{A}^T \otimes \boldsymbol{D}_{\boldsymbol{i}}\right)\boldsymbol{\Sigma} + \sum_{f\in\partial D^k}\left(\boldsymbol{I}\otimes \boldsymbol{M}_f\right)\boldsymbol{F}_v + \boldsymbol{M}_{\boldsymbol{Q}_v}^{-1}\boldsymbol{M}_{\boldsymbol{D}}\boldsymbol{V}, \tag{5.34}$$

where we have introduced the differentiation matrix $\boldsymbol{D}_i = \boldsymbol{M}^{-1}\boldsymbol{S}_i$ and lift matrix $\boldsymbol{L}_f = \boldsymbol{M}^{-1}\boldsymbol{M}_f$. For affine elements, both derivative and lift matrices are applied using products of geometric factors and reference derivative and lift matrices.

Unfortunately, if $\boldsymbol{Q}_s$ and $\boldsymbol{Q}_v$ varies spatially with in the element, then above approach can

no longer be used to invert $\boldsymbol{Q}_s$ and $\boldsymbol{Q}_v$. Here, we follow the approach of [97], where $\boldsymbol{M}_{\boldsymbol{Q}_s}, \boldsymbol{M}_{\boldsymbol{Q}_v}$ are replaced with weight-adjusted approximations. These approximations are low storage, simple to invert, and yield an energy stable and high order accurate DG method to approximate the matrix-weighted L^2 inner product (and corresponding matrix-weighted mass-matrices $\boldsymbol{Q}_s$ and $\boldsymbol{Q}_v$).

We also note that, material coefficients $\boldsymbol{Q_s}$, $\boldsymbol{Q}_v$ appear only the left hand sides of (5.25) and (5.26). The right hand sides of (5.25) and (5.26) is equivalent to the discretization of a constant coefficient system. This provides additional advantages in that the right hand side can be evaluated using efficient techniques for DG discretizations of constant-coefficient problems [120, 105].

Table 5.2: Weights and quadratures points for Gauss-Jacobi and modified Gauss-Jacobi approximation

	Gauss-Jacobi	Modified Gauss-Jacobi
α_1	20.32	116.04
α_2	3.332	7.65
α_3	1.00	1.00
α_4	3.00	0.13124
α_5	0.04921	0.00860
a_1	3.80	12.23
a_1	0.784	1.95
a_1	0.362	0.622
a_1	0.235	0.255
a_5	0.187	0.105

5.5 Numerical experiments

In this section, we present several numerical experiments validating the stability and accuracy of proposed new DG method in two dimensional homogeneous isotropic poroelastic media. All experiments utilize the parameters given in Table 5.3.

In all experiments, we follow [107] and compute the application of weight-adjusted mass matrices using a quadrature which is exact for polynomials of degree $(2N + 1)$. Time integration is performed using the low-storage 4^{th} order five-stage Runge-Kutta scheme of Carpenter and Kennedy

Table 5.3: Material properties for several poroelastic media used in the examples [3]

Properties	Sandstone (Isotropic)
K_s (GPa)	40
ρ_s (kg/m^3)	2500
c_{11} (GPa)	36
c_{12} (GPa)	12
c_{13} (GPa)	12
c_{33} (GPa)	36
c_{55} (GPa)	12
ϕ	0.2
κ_1 (10^{-15} m^2)	600
κ_3 (10^{-15} m^2)	600
a_∞	2
T_3	2
K_f (GPa)	2.5
ρ_f (Kg/m^3)	1040
η (10^{-3} Kg/m.s)	1
Λ (10^{-4} (m^2)	0.219

[108], and the time step is chosen based on the global estimate

$$dt = \min_k \frac{C_{CFL}}{\sup_{x\in\Omega} \|\boldsymbol{C}(\boldsymbol{x})\|_2 \, C_N \, \|J^f\|_{L^\infty(\partial D^k)} \, \|J^{-1}\|_{L^\infty(D^k)}} \tag{5.35}$$

where $C_N = O(N^2)$ is the order-dependent constant in the surface polynomial trace inequality [109] and C_{CFL} is a tunable global CFL constant. This estimate is derived by bounding the eigenvalues of the spatial DG discretization matrix appearing in the semi-discrete system of ODEs. This choice of dt is very conservative as it is derived based on an upper bound on the spectral radius.

5.5.1 Spectra and choice of penalty parameter

We first verify the energy stability of proposed DG formulation. Let $\boldsymbol{A}_h$ denote the matrix induced by the global semi-discrete DG formulation, such that time evolution of the solution $\boldsymbol{\tau}, \boldsymbol{v}$ is governed by

$$\frac{\partial \boldsymbol{Q}}{\partial t} = \boldsymbol{A}_h \boldsymbol{Q},$$

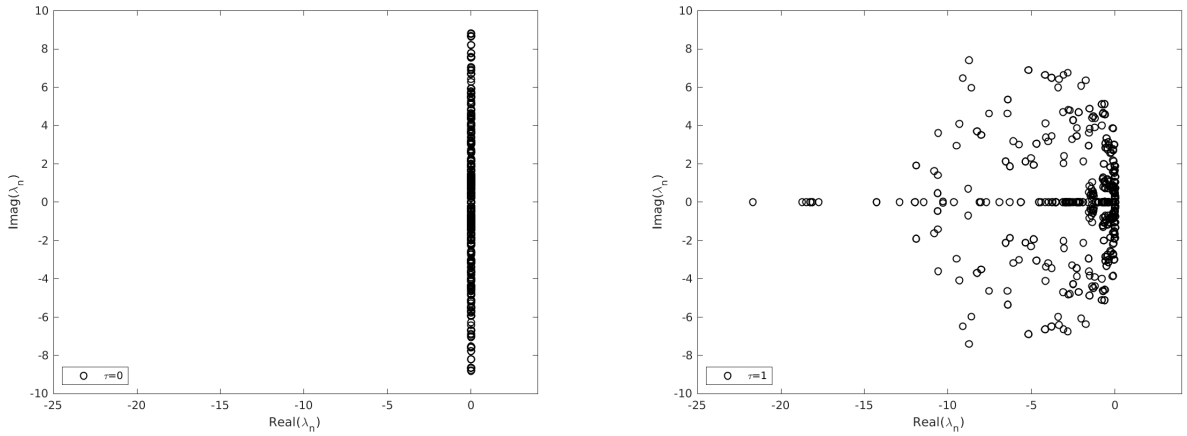

(a) $\alpha_{\boldsymbol{\tau}} = \alpha_{\boldsymbol{v}} = 0$ (b) $\alpha_{\boldsymbol{\tau}} = \alpha_{\boldsymbol{v}} = 1$

Figure 5.1: Spectra for $N = 3$ and $h = 1/2$ with a material property of isotropic Sandstone (Table 5.1). For $\alpha_{\boldsymbol{\tau}} = \alpha_{\boldsymbol{v}} = 0$ and $\alpha_{\boldsymbol{\tau}} = \alpha_{\boldsymbol{v}} = 1$, the largest real part of spectra are 6.54698e-13 and 8.22466e-13, respectively.

where $\boldsymbol{Q}$ denotes a vector of degrees of freedom for $(\boldsymbol{\tau}, \boldsymbol{v})$. We show in Figure 1 eigenvalues of $\boldsymbol{A}_h$ for $\alpha_{\boldsymbol{\tau}} = \alpha_{\boldsymbol{v}} = 0$ and $\alpha_{\boldsymbol{\tau}} = \alpha_{\boldsymbol{v}} = 1$ with material parameters of isotropic sandstone (given in Table 5.1). The discretization parameters are $N = 3$ and $h = 1/2$. In both cases, the largest real part of any eigenvalues is $O(10^{-14})$, which suggests that the semi-discrete scheme is indeed energy stable.

For practical simulations, the choice of $\alpha_{\boldsymbol{\tau}}, \alpha_{\boldsymbol{v}}$ remains to be specified. Taking $\alpha_{\boldsymbol{\tau}}, \alpha_{\boldsymbol{v}} > 0$ results in damping of of under-resolved spurious components of the solutions. However, a naive selection of $\alpha_{\boldsymbol{\tau}}, \alpha_{\boldsymbol{v}}$ can result in an overly restrictive time-step restriction for stability. A guiding principle for determining appropriate values of the penalty parameters $\alpha_{\boldsymbol{\tau}}, \alpha_{\boldsymbol{v}}$ is to ensure that the spectral radius is the same magnitude as the case when $\alpha_{\boldsymbol{\tau}} = \alpha_{\boldsymbol{v}} = 0$. For example, the spectral radius of $\boldsymbol{A}_h$, $\rho(\boldsymbol{A}_h)$ is 9.017 for $\alpha_{\boldsymbol{\tau}}, \alpha_{\boldsymbol{v}} = 0$ which is $O(N^2/h)$. The spectral radius $\rho(\boldsymbol{A}_h)$ is 10.1189 for $\alpha_{\boldsymbol{\tau}}, \alpha_{\boldsymbol{v}} = 0.5$, while the spectral radius for $\alpha_{\boldsymbol{\tau}}, \alpha_{\boldsymbol{v}} = 1$ is $\rho(\boldsymbol{A}_h) = 22.88$. Since the maximum stable timestep is proportional to the spectral radius, taking $\alpha_{\boldsymbol{\tau}}, \alpha_{\boldsymbol{v}} = 1$ in this case results in a more restrictive CFL condition. This phenomena is related to observations in [99] that large penalty parameters result in extremal eigenvalues of $\boldsymbol{A}_h$ with very large negative real parts. The optimal choice of scaling also depends on the media heterogeneities on elements adjacent to an interface.

5.5.2 Analytic solution

Next, we study the accuracy and convergence of the our DG method for a plane wave propagating in an isotropic porous sandstone with material properties given in Table 5.3. Unless

otherwise stated, we report relative L^2 errors for all components of the solution $\boldsymbol{U} = (\boldsymbol{\tau}, \boldsymbol{v})$

$$\frac{\|\boldsymbol{U} - \boldsymbol{U}_h\|_{L^2(\Omega)}}{\|\boldsymbol{U}\|_{L^2(\Omega)}} = \frac{\left(\sum_{i=1}^{m} \|\boldsymbol{U_i} - \boldsymbol{U_{i,h}}\|^2_{L^2(\Omega)}\right)^{1/2}}{\left(\sum_{i=1}^{m} \|\boldsymbol{U}_i\|^2_{L^2(\Omega)}\right)^{1/2}}.$$

5.5.3 Plane wave in a poroelastic medium

The analytical solution to (5.24) for a plane wave is given as

$$\boldsymbol{Q}_n(\boldsymbol{x}, t) = \boldsymbol{Q}_n^0 \exp[\mathrm{i} \cdot (\omega t - \boldsymbol{k} \cdot \boldsymbol{x})], \qquad n = 1...13, \tag{5.36}$$

where $\boldsymbol{Q}_n^0$ is the initial amplitude vector of stress and velocity components; ω are wave frequencies; $\boldsymbol{k} = (k_x, k_y, k_z)$ is the wave-number vector. To achieve realistic poroelastic behavior, we superimpose three plane waves, of the form given by (5.36), corresponding to a fast P-wave, an S-wave and a slow P-wave.

Now, we briefly describe how we determine the the wave frequencies ω. Substituting (5.36) into (5.24) yields

$$\omega \boldsymbol{Q}_n^0 = (\boldsymbol{A}k_x + \boldsymbol{B}k_y + \boldsymbol{C}k_z - \mathrm{i}\boldsymbol{E})\boldsymbol{Q}_n^0 \tag{5.37}$$

Solving the three eigenvalues problem for in (5.36) for each wave mode l yields in matrix of right eigenvectors ($R_{mn}^{(l)}$) and eigenvalue (ω_l). Following [110, 4], the solution of (5.24) can be constructed as

$$\boldsymbol{Q}_n(\boldsymbol{x}, t) = \sum_{l=1}^{3} R_{mn}^{(l)} \gamma_n^{(l)} \exp[\mathrm{i} \cdot (\omega^{(l)} t - \boldsymbol{k^{(l)}} \cdot \boldsymbol{x})], \tag{5.38}$$

where $\gamma_n^{(l)}$ is a amplitude coefficient with $\gamma_1^{(1)} = \gamma_2^{(2)} = \gamma_4^{(3)} = 100$.

For completeness, we perform convergence analyses for inviscid and viscid media separately.

5.5.3.1 Inviscid case ($\eta = 0$)

The error is computed for an inviscid brine-filled ($\eta = 0$) isotropic sandstone. The inviscid nature of the fluid implies that $\boldsymbol{D} = \boldsymbol{0}$. We show in Figure 2 the L^2 errors computed at T=1 and CFL=1, using uniform triangular meshes constructed by bisecting an uniform mesh of quadrilaterals along the diagonal. Figure 5.2a and 5.2b show the convergence plot using the central flux ($\alpha_{\boldsymbol{v}} = \alpha_{\boldsymbol{\tau}} =$

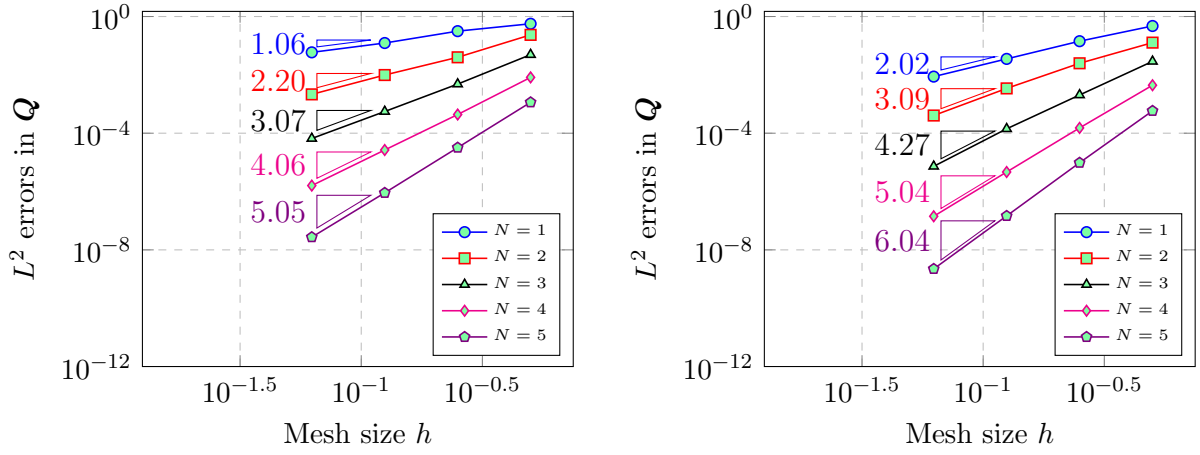

(a) $\tau_v = \tau_\sigma = 0$ (central flux)

(b) $\tau_v = \tau_\sigma = 1$ (penalty flux)

Figure 5.2: Convergence of L^2 error for plane wave in porolastic media with $\eta = 0$-inviscid case

0) and penalty flux ($\alpha_{\boldsymbol{v}} = \alpha_{\boldsymbol{\tau}} = 1$) respectively. For $N = 1, ..., 5$, $O(h^{N+1})$, rates of convergence are observed. We note that for $N = 4$ and $N = 5$, we observe results for both fluxes which are better than the 4^{th} order accuracy of our time-stepping scheme. This is most likely due to the benign nature of the solution in time and the choice of time step (5.35) which scales as $O(h/N^2)$. For $N = 4, 5$, the results of Figure 5.2 suggest that the resulting time step is small enough such that temporal errors of $O(dt^4)$ are small relative to spatial discretization errors of $O(h^{N+1})$.

5.5.3.2 Viscid case ($\eta \neq 0$)

We show in Figure 5.3 the L^2 errors for viscid case, computed at T=1 and CFL=1 using uniform triangular meshes. Figure 5.3a and 5.3b show convergence plots using the central flux ($\alpha_{\boldsymbol{v}} = \alpha_{\boldsymbol{\tau}} = 0$) and penalty flux ($\alpha_{\boldsymbol{v}} = \alpha_{\boldsymbol{\tau}} = 1$), respectively. For $N = 1, ..., 5$, $O(h^{N+1})$ rate of convergence are observed when using the penalty flux $\alpha_{\boldsymbol{v}} = \alpha_{\boldsymbol{\tau}} = 1$. When using a central flux ($\alpha_{\boldsymbol{v}} = \alpha_{\boldsymbol{\tau}} = 0$), we observe a so-called "even-odd" pattern [6, 98], with convergence rate $O(h^N)$ for odd N and between $O(h^{N+1/2})$ and $O(h^{N+1})$ for even N.

Similar to the inviscid case, for $N = 4$ and $N = 5$, we observe results for both fluxes which are better than the 4^{th} order accuracy of our time-stepping, due to the fact that temporal error are small relative to spatial discretization error.

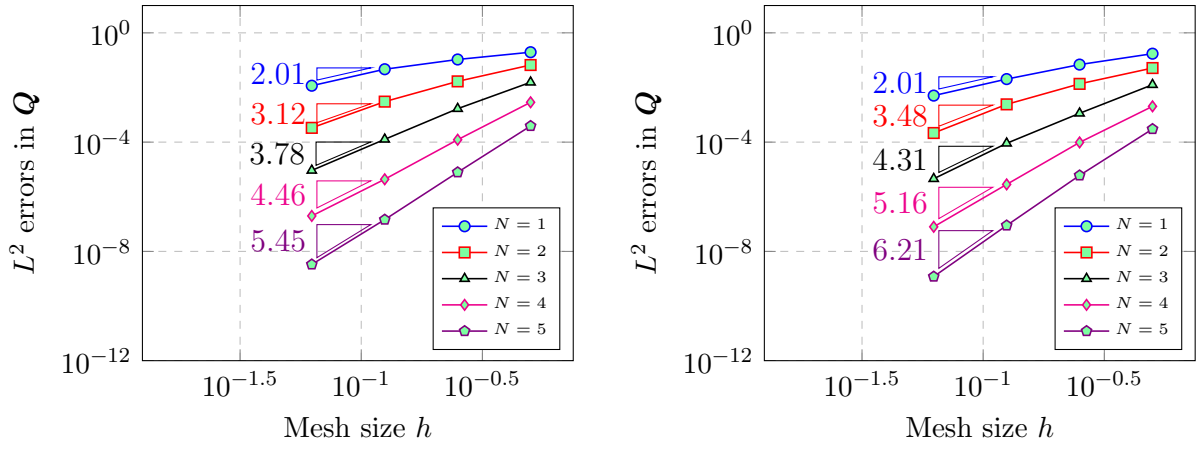

(a) $\tau_v = \tau_\sigma = 0$ (central flux)

(b) $\tau_v = \tau_\sigma = 1$ (penalty flux)

Figure 5.3: Convergence of L^2 error for plane wave in poroelastic media for viscid case ($\eta \neq 0$) with unified DG scheme

5.5.4 Application example

We next demonstrate the accuracy and flexibility of the proposed DG for an application-based problem in linear poroelasticity defined by broad-band Biot's equation. The computation is done using penalty parameters $\alpha_{\boldsymbol{v}} = \alpha_{\boldsymbol{\tau}} = 0.5$. In the following section, the field $\boldsymbol{b}$ represents the center of mass particle velocity vector [87], which is expressed as

$$\boldsymbol{b} = \boldsymbol{v} + \left(\frac{\rho_f}{\rho}\right)\boldsymbol{q}. \tag{5.39}$$

In the following section, the forcing is applied to both the $z-$ component of stress τ_{zz} and the fluid pressure p by a Ricker wavelet point source

$$f(\boldsymbol{x}, t) = (1 - 2(\pi f_0(t - t_0))^2)\exp[-(\pi f_0(t - t_0))^2]\delta(\boldsymbol{x} - \boldsymbol{x}_0), \tag{5.40}$$

where $\boldsymbol{x}_0$ is the position of the point source and f_0 is the central frequency.

To illustrate the effect of viscosity and dynamic permeability of slow P wave in a high frequency regime, a computational experiment in an isotropic sandstone with material properties given in Table 5.3 is performed. The size of the computational domain is 20 cm $\times$ 20 cm. The domain is discretized with uniform triangular element with a minimum edge length of 0.5 mm. Figures 5.4(a)-(b) represent the $x-$ and $z-$ components of the center of mass particle velocity of the isotropic sandstone, for a viscid case ($\eta \neq 0$). The central frequency of the forcing function is $f_0 = 10$ kHz, and polynomials of degree $N = 3$ are used. The propagation time is 19.89 μs. Three

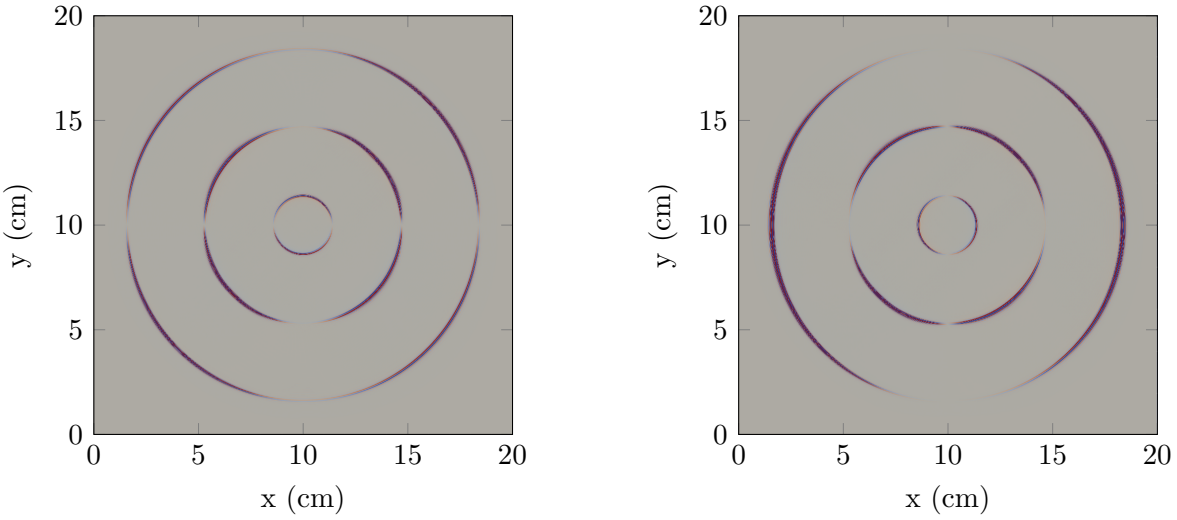

(a) Isotropic Sandstone, b_x with $\eta \neq 0$

(b) Isotropic Sandstone, b_z with $\eta \neq 0$

Figure 5.4: Snapshots of the centre of mass particle velocity in isotropic sandstone, computed at $t = 19.89$ μs, for $\eta \neq 0$. The central frequency of the forcing function is 10 kHz. The solution is computed using polynomials of degree $N = 3$.

events can be observed: the fast P mode, the shear wave, and the slow P mode.This is to be noted that unlike low frequency regime (discussed in Chapter 4), propagation of slow P wave is very well supported by the medium for a viscous pore fluid.

Chapter VI

Effect of capillary pressure on seismic velocities and attenuation

6.1 Abstract

Biot's theory allows incorporation of permeability and viscosity in computing seismic amplitudes for a porous medium that is fully saturated with a single-phase fluid. In its original form, Biot's theory does not explicitly account for capillary effects, e.g., the surface tension between the wetting and non-wetting fluids. This paper uses a model to quantify capillary effects on velocity and attenuation. Studies that have attempted to extend Biot's poroelasticity to include capillary effects found changes in fast P-wave velocity of up to 5 % between the sonic and ultrasonic frequency ranges. Simulations of wave propagation at varying capillary pressure in a rock saturated with multi-phase fluid are also presented. The poroelastic equation for multi-phase fluid is solved by using spectral methods with Fourier grids as collocations points in space and the Runge-Kutta scheme for numerical integration. The numerical simulations show the presence of three compressional (P-) waves, one fast and two *slow* compressional waves corresponding to the wetting and non-wetting phases. The results show that the *slow* P-wave amplitude is significantly affected by capillary pressure variations.

Keywords— Capillary pressure, Seismic velocity, Pseudo-spectral, Biot's model

6.2 Introduction

Wave propagation in porous media (poroelasticity) has been a subject of great interest for geophysicists and engineers alike [71, 32]. The foundation of poroelasticity was laid down through a series of seminal works in [9, 8, 10]. The premise of poroelasticity is that wave propagation sets

both solid and fluid particles in relative motion, and, therefore the energy is propagated through the frame as well as through the pore fluid, with the competing driving forces of inertial and viscous nature depending on the frequency range. Three modes of energy propagation exist in the body, i.e., two compressional (P) (a fast and a slow) and one shear (S) [9, 8]. In contrast, elastic modeling assumes that the propagation media is fully solid and the energy propagates only though P and S modes.

The slow P-wave, which is unique to the poroelastic model, is a diffusive mode of energy propagation that originates from the relative motion between solid and fluid particles. The polarization of the fast P-wave is described by in-phase motion between the solid and fluid particles and the polarization of the slow P-wave is described by the out of phase motion between solid and fluid particles. At frequencies < 100 Hz, the viscous forces generally dominate over the inertial forces attenuating the slow P-wave in the near-field [2]. On the other hand, at frequencies > 1 kHz, inertial forces are dominant over viscous forces and energy contained in the slow P-wave can be significant allowing it to be recorded in the far-field. The first clear documentation of the slow P-wave was at ultrasonic frequencies in a laboratory setting in water saturated sintered glass beads (18.5 % porosity) with velocity of 1040 m/sec [121]. However, before Biot predicted it, [122] reported experimental values of the slow P-wave velocity in snow.

The limitation of Biot's theory in predicting wave attenuation for complex pores and multi-phase fluid has been alluded towards by several researchers [123, 124]. In principle, a complex pore geometry and presence of two or more immiscible fluid phases results in complex relaxation for both fluid and solid phases. In [9, 8] the relaxation term is a visco-dynamic operator which in essence is the frequency-dependent permeability also known as the dynamic permeability term [90]. [125] and [126] extended Biot's theory to multi-phase fluid media by making this visco-dynamic term a capillary pressure [127] dependent, where capillary forces exclusively imply surface tension due to the wetting and non-wetting fluid phases (see also [128], [129] and [130]). Recently, [131] have analyzed the dependence of the phase velocities of the slow P-waves (prevalent in poroelastic media saturated with single to multiphase fluids) on saturation of non-wetting phase (gas) and depth. In brief, the outcome of this study shows that the velocities of the slow wave in the ultrasonic frequency range (P2 and P3 modes) generally decrease as the saturation of non-wetting phase decreases, similar to the present study, wherein the velocity of the slow P-wave modes decreases as capillary pressure increases. In addition to this, those authors have also shown that the velocity of the slow P- wave modes increases as pore pressure increases, where pore pressure is alluded as function of depth.

Other wave propagation theories considering the capillary pressure were developed by [132],

[133], [134], [135] and [136]. [132] use a homogenization theory and a description of the capillary effects at the pore scale, obtaining a generalized Darcy law. [133] derived a model for waves traveling in an elastic porous solid permeated by two immiscible fluids incorporating both inertial and viscous drags in an Eulerian frame of reference, applying their model to a Columbia fine sandy loam saturated by air-water and oil-water. [134] obtained a dynamic model for wave propagation in a porous medium saturated with two immiscible fluids by incorporating three kinds of relaxation mechanisms. These are based on a) A drag force model accounting for attenuation due to global fluid flow, b) A capillary-pressure based mechanism responsible for relaxation of the interface between the wetting and non-wetting fluid phases, and c) A porosity-based relaxation mechanism accounting for local fluid flow. A direct comparison between the present study and capillary-based relaxation model of [134] differs in the method used to compute the capillary pressure. In the limiting case of $p_{ca} = 0$, the non-wetting phase saturation S_n in [134] model is dependent on the irreducible saturation of the wetting phase (S_{rw}), whereas in our model the non-wetting phase saturation S_n is a function of the irreducible saturation of the wetting S_{rw} and non-wetting phase S_{rn}. Thus the capillary pressure model used in the present study defines the concept of relative permeability between the multiphase fluid with saturation more accurately. [134] have shown the variation of velocity and attenuation with respect to the capillary pressure dependent modulus (see their Figs. 2 and 3) unlike in the present study, where the direct dependence on capillary pressure is shown. In general, the attenuation of the P wave increases for certain values of the capillary parameter (see their Fig. 5b). The effect of varying capillary pressures on the numerical solution is not shown in [134]. [135] use a theory similar to that of the present work and find that the capillary pressure greatly affects the displacement of the non-wetting phase (oil or gas in a water saturated background). [136] studied the effect of capillary pressure on the acoustic signature in the framework of the mesoscopic-loss theory. In this study the effect of capillarity was induced through the incorporation of a membrane stiffness in a random medium of patchy saturation. The capillary action leads to an additional stiffening and thereby to higher phase velocities. It also implies a pressure discontinuity at patch interfaces so that wave-induced pressure diffusion process is weakened and attenuation is reduced.

In another experimental modeling study by [137], the P-wave velocity for variable fluid patch sizes is studied, with the patch size being a function of the fluid saturation. In this study, the effect of capillarity is linked to the injection rate, which changes during imbibition due to the redistribution of the viscous and capillary pressure in rock samples. The very idea of this study is based on the redistribution of capillary effects, which in turn changes the stiffness of the fluid-rock system resulting into changes in the rock velocity. According to this concept, [137] has shown that the

overall effect of increasing capillarity causes an increase in static velocity of the P wave (measured experimentally) (see their Figure 6). Unlike our study , they have not mentioned anything about the effects of capillarity on slow P waves and also lacks the representation of the effect of capillarity on numerical simulation of wave propagation.

In another study of wave propagation in rocks saturated with two immiscible fluid, [138] simulated the effect of squirt flow on the P-wave velocity of a rock saturated with water and CO_2. In this study, the authors considered a static dimensionless capillary function bounded above and below by 1 and the ratio of bulk modulus of gas and water, respectively. The modeling approach adopted in the study only models the fast P-wave and lacks the discussions about the slow P-wave modes. The results obtained in this study show that the velocity of the P wave at high frequencies, in general, increases with capillary pressure (see their Figure 4 and 5). In another result (see their Figure 4), the velocity of the P wave with respect to the wetting phase saturation has a similar trend as in Figure 6.1 of the present study. This study also lacks the wave field characteristics with respect to varying capillary pressure.

Extending Biot's theory into the capillary domain led to two key observations. First, a step change in fast P-wave velocity by up to 5 % occurs near the characteristic frequency of the medium [139]. Second, the relative motion between the non-wetting fluid phase and the solid grain gives rise to a second slow P-wave phase [140, 139]. The first finding is of particularly relevant to quantitative interpretation of ultrasonic data, more so when velocity measurements at ultrasonic ranges on undrained core plugs are to be reconciled with the surface seismic velocities. The second finding is relevant in understanding the energy loss mechanism. Although peer studies have laid theoretical and numerical formulations for energy partitioning in presence of more than one fluid phase, the system has not been yet analyzed for varying capillary pressure. Here we analyze the body-wave velocities and their attenuation as a function of capillary pressure. We also present numerical solution for a two-phase fluid system (gas and water) with varying capillary pressure. [139] and [140] have solved the equations developed by [126] using different numerical approaches. Here, we use the first method.

6.3 Theory

Next, we present a summary of wave propagation in partially saturated porous medium developed by [126], [139], [128] and [129] guiding the reader to original references for detail.

6.3.1 Equations of momentum conservation

Let a porous rock saturated by two immiscible fluids denoted with the superscripts s, w and n corresponding to the solid, wetting and non-wetting phases, respectively. Let $\boldsymbol{v_s}, \bar{\boldsymbol{v}}^n$ and $\bar{\boldsymbol{v}}^w$ be particle velocity vectors for solid grain, wetting fluid and non-wetting fluid, respectively and let $\boldsymbol{\tau}, \tau_n$ and τ_w be the total stress tensor for solid, non-wetting phase and wetting phase respectively. Relative particle velocities for non-wetting and wetting phases are defined as $\boldsymbol{v}^n = \phi(\bar{\boldsymbol{v}}^n - \boldsymbol{v_s})$ and $\boldsymbol{v}^w = \phi(\bar{\boldsymbol{v}}^w - \boldsymbol{v_s})$ respectively. The equations of momentum conservation for the solid, wetting and non-wetting phases are

$$\nabla \cdot \tau = \rho \dot{\boldsymbol{v}}_{\boldsymbol{s}} + \rho_n S_n \dot{\boldsymbol{v}}^n + \rho_w S_w \dot{\boldsymbol{v}}^w, \tag{6.1}$$

$$\nabla \tau_n = \rho_n S_n \dot{\boldsymbol{v}}^s + g_1 \dot{\boldsymbol{v}}^n + g_3 \dot{\boldsymbol{v}}^w + S_n^2 \left(\frac{\eta_n}{\kappa_n}\right) \boldsymbol{v^n}, \tag{6.2}$$

$$\nabla \tau_w = \rho_w S_w \dot{\boldsymbol{v}}^s + g_3 \dot{\boldsymbol{v}}^n + g_2 \dot{\boldsymbol{v}}^w + S_w^2 \left(\frac{\eta_w}{\kappa_w}\right) \boldsymbol{v^w}, \tag{6.3}$$

where $S,\ \eta,\ \rho,\ \phi$ and κ are saturation ($S_n + S_w = 1$), viscosity, density, porosity and permeability, respectively. A dot above a variable represents the time derivative. The relative permeability of the non-wetting and wetting phases will be denoted by κ_n and κ_w. [126] define bulk density (ρ) and mass couple coefficients (g_1: solid and non-wetting; g_2: solid and wetting; and g_3: non-wetting and wetting) as

$$\rho = (1-\phi)\rho_s + \phi(S_n\rho_n + S_w\rho_w), \qquad g_1 = \frac{S_n \rho_n F_s}{\phi}\ ,$$
$$g_2 = \frac{S_w \rho_w F_s}{\phi}, \qquad\qquad g_3 = 0.1\sqrt{g_1 g_2}\ ,$$

where F_s is a structural factor as in [141]. The capillary pressure $p_{ca} > 0$ [126] is defined as

$$p_{ca} = A\left[(S_n + S_w - 1)^{-2} - \left(\frac{S_{rn}}{S_n}\right)(1 - S_{rn} - S_{rw})^{-2}\right]\ , \tag{6.4}$$

where, S_{rn} and S_{rw} are residual saturations of the wetting and non-wetting phases. A is constant, constraining $p_{ca} > 0$. The permeabilities κ_n and κ_w are given as

$$\kappa_n = \kappa\left(1 - \frac{1 - S_n}{1 - S_{rn}}\right)^2, \quad \kappa_w = \kappa\left(\frac{1 - S_n - S_{rw}}{1 - S_{rw}}\right)^2\ ,$$

where κ is absolute permeability.

6.3.2 Stress-strain relations

The 2D stress-strain relationship for the multi-phase system in the (x,y)-plane can be expressed as

$$\boldsymbol{S} = \boldsymbol{C} \cdot \boldsymbol{e} \ , \tag{6.5}$$

where $S = [\tau_{xx}, \tau_{yy}, \tau_{xy}, \tau_n, \tau_w]^T$, $\boldsymbol{e} = [\epsilon_{xx}, \epsilon_{yy}, \epsilon_{xy}, \zeta_n, \zeta_w]^T$ and

$$\boldsymbol{C} = \begin{pmatrix} K_c + N & K_c - N & 0 & -B_1 & B_2 \\ K_c - N & K_c + N & 0 & -B_1 & B_2 \\ 0 & 0 & 0 & 2N & 0 \\ B_1 & B_1 & 0 & -M_1 & -M_3 \\ B_2 & B_2 & 0 & -M_3 & -M_2 \end{pmatrix} ,$$

where ϵ's are strain for solid phase and $\zeta_{n,w}$ are variations of fluid content defined as $\dot{\zeta}_{n,w} = -\nabla \cdot \boldsymbol{v}^{n(w)}$. In the stiffness matrix $\boldsymbol{C}$, K_c and N are undrained bulk and dry-rock shear moduli, respectively. Coefficients $B_1,\ B_2,\ M_1,\ M_2$ and M_3 depend on rock and fluid type [129]. To derive the dispersion relation, the stress induced in the non-wetting phase can be rewritten using first principles [126]

$$\tau_n = -(S_n + \beta + \chi)p_n + (\beta + \chi)p_w \ , \tag{6.6}$$

where p_n and p_w are infinitesimal changes in the wetting and non-wetting fluid pressures from the absolute fluid pressure $\bar{p}_n$ and $\bar{p}_w$. β and χ are parameters describing the capillary pressure and defined as $\beta = \dfrac{p_{ca}}{p'_{ca}}$, $\chi = \dfrac{\bar{p}_w}{p'_{ca}}$. p'_{ca} represent the change in capillary pressure with respect to the saturation of the non-wetting phase. Equations (6.2) and (6.6) imply that changes in stress in the non-wetting phase causes changes in the particle velocities (for both solid and relative fluid velocity). Equation (6.6) also implies that the stress in the non-wetting fluid phase is linearly dependent on p_{ca}, which is what in turn creates the dependence of seismic velocities on capillary pressure.

6.3.3 Particle velocity-stress relationship

The particle velocity-stress formulation defines the coupled system of partial differential equations which describes the wave propagation in a porous rock saturated with multi-phase fluids.

Equation (6.1-6.3), can be rewritten as

$$\dot{v_i^s} = \rho(\tau_{ix,x} + \tau_{iy,y}) + \rho_n S_n \left[\tau_{n,i} - S_n^2 \left(\frac{\eta_n}{\kappa_n}\right) v_i^n\right] + \rho_w S_w \left[\tau_{w,i} - S_w^2 \left(\frac{\eta_w}{\kappa_w}\right) v_i^w\right] \ , \tag{6.7}$$

$$\dot{v_i^n} = \rho_n S_n(\tau_{ix,x} + \tau_{iy,y}) + g_1 \left[\tau_{n,i} - S_n^2 \left(\frac{\eta_n}{\kappa_n}\right) v_i^n\right] + g_3 \left[\tau_{w,i} - S_w^2 \left(\frac{\eta_w}{\kappa_w}\right) v_i^w\right] \ , \tag{6.8}$$

$$\dot{v_i^w} = \rho_w S_w(\tau_{ix,x} + \tau_{iy,y}) + g_3 \left[\tau_{n,i} - S_n^2 \left(\frac{\eta_n}{\kappa_n}\right) v_i^n\right] + g_2 \left[\tau_{w,i} - S_w^2 \left(\frac{\eta_w}{\kappa_w}\right) v_i^w\right] \ . \tag{6.9}$$

Equations corresponding to stress components are obtained by differentiating (6.5) with respect to time and can be expressed as

$$\dot{\tau}_{xx} = K_c(\nabla \cdot \boldsymbol{v^s}) + N(v_{x,x} - v_{y,y}) + B_1(\nabla \cdot \boldsymbol{v^n}) + B_2(\nabla \cdot \boldsymbol{v^w}) \ , \tag{6.10}$$

$$\dot{\tau}_{yy} = K_c(\nabla \cdot \boldsymbol{v^s}) - N(v_{x,x} - v_{y,y}) + B_1(\nabla \cdot \boldsymbol{v^n}) + B_2(\nabla \cdot \boldsymbol{v^w}) \ , \tag{6.11}$$

$$\dot{\tau}_{xy} = N(v_{x,y} + v_{y,x}) \ , \tag{6.12}$$

$$\dot{\tau}_n = B_1(\nabla \cdot \boldsymbol{v^s}) - M_1(\nabla \cdot \boldsymbol{v^n}) - M_3(\nabla \cdot \boldsymbol{v^w}) \ , \tag{6.13}$$

$$\dot{\tau}_w = B_2(\nabla \cdot \boldsymbol{v^s}) - M_3(\nabla \cdot \boldsymbol{v^n}) - M_2(\nabla \cdot \boldsymbol{v^w}) \ . \tag{6.14}$$

6.4 Velocity and attenuation

A succinct form of the first-order velocity-stress relation, describing the wave equation for partially saturated porous medium can be recovered by combining equations (6.7-6.9) and (6.10-6.14) and expressed as

$$\frac{d\boldsymbol{w}}{dt} = \boldsymbol{M}\boldsymbol{w} + \boldsymbol{f} \ , \tag{6.15}$$

where $\boldsymbol{w}$ is the wavefield vector $\boldsymbol{w} = [v_x^s, v_x^n, {v_x}^w, v_y^s, v_y^n, v_y^w, \tau_{xx}, \tau_{yy}, \tau_{xy}, \tau_n, \tau_w]$ and $\boldsymbol{f}$ is the forcing function, which is the product of the delta function and the Ricker wavelet in space and time domain, respectively, $\boldsymbol{M}$ is the propagator matrix, containing the material coefficients and spatial

derivatives:

$$\boldsymbol{M} = \begin{pmatrix}
0 & -\rho_n S_n^3\left(\frac{\eta_n}{\kappa_n}\right) & -\rho_w S_w^3\left(\frac{\eta_w}{\kappa_w}\right) & 0 & 0 & 0 & \rho\frac{\partial}{\partial x} & 0 & \rho\frac{\partial}{\partial y} & \rho_n S_n\frac{\partial}{\partial x} & \rho_w S_w\frac{\partial}{\partial x} \\
0 & -g_1 S_n^2\left(\frac{\eta_n}{\kappa_n}\right) & -g_3 S_w^2\left(\frac{\eta_w}{\kappa_w}\right) & 0 & 0 & 0 & \rho_n S_n\frac{\partial}{\partial x} & 0 & \rho_n S_n\frac{\partial}{\partial y} & g_1\frac{\partial}{\partial x} & g_3\frac{\partial}{\partial x} \\
0 & -S_n^2\left(\frac{\eta_n}{\kappa_n}\right) & -S_w^2\left(\frac{\eta_w}{\kappa_w}\right) & 0 & 0 & 0 & \rho_w S_w\frac{\partial}{\partial x} & 0 & \rho_w S_w\frac{\partial}{\partial y} & g_3\frac{\partial}{\partial x} & g_2\frac{\partial}{\partial x} \\
0 & 0 & 0 & 0 & -\rho_n S_n^3\left(\frac{\eta_n}{\kappa_n}\right) & -\rho_w S_w^3\left(\frac{\eta_w}{\kappa_w}\right) & 0 & \rho\frac{\partial}{\partial y} & \rho\frac{\partial}{\partial x} & \rho_n S_n\frac{\partial}{\partial y} & \rho_w S_w\frac{\partial}{\partial y} \\
0 & 0 & 0 & 0 & -g_1 S_n^2\left(\frac{\eta_n}{\kappa_n}\right) & -g_3 S_w^2\left(\frac{\eta_w}{\kappa_w}\right) & 0 & \rho_n S_n\frac{\partial}{\partial y} & \rho_n S_n\frac{\partial}{\partial x} & g_1\frac{\partial}{\partial y} & g_3\frac{\partial}{\partial y} \\
0 & 0 & 0 & 0 & -g_3 S_n^2\left(\frac{\eta_n}{\kappa_n}\right) & -g_2 S_w^2\left(\frac{\eta_w}{\kappa_w}\right) & 0 & \rho_w S_w\frac{\partial}{\partial y} & \rho_w S_w\frac{\partial}{\partial x} & g_3\frac{\partial}{\partial y} & g_2\frac{\partial}{\partial y} \\
(K_c+N)\frac{\partial}{\partial x} & B_1\frac{\partial}{\partial x} & B_2\frac{\partial}{\partial x} & (K_c-N)\frac{\partial}{\partial y} & B_1\frac{\partial}{\partial y} & B_2\frac{\partial}{\partial y} & 0 & 0 & 0 & 0 & 0 \\
(K_c-N)\frac{\partial}{\partial x} & B_1\frac{\partial}{\partial x} & B_2\frac{\partial}{\partial x} & (K_c+N)\frac{\partial}{\partial y} & B_1\frac{\partial}{\partial y} & B_2\frac{\partial}{\partial y} & 0 & 0 & 0 & 0 & 0 \\
N\frac{\partial}{\partial y} & 0 & 0 & N\frac{\partial}{\partial x} & 0 & 0 & 0 & 0 & 0 & 0 & 0 \\
B_1\frac{\partial}{\partial x} & -M_1\frac{\partial}{\partial x} & -M_3\frac{\partial}{\partial x} & B_1\frac{\partial}{\partial y} & -M_1\frac{\partial}{\partial y} & -M_3\frac{\partial}{\partial y} & 0 & 0 & 0 & 0 & 0 \\
B_2\frac{\partial}{\partial x} & -M_3\frac{\partial}{\partial x} & -M_2\frac{\partial}{\partial x} & B_2\frac{\partial}{\partial y} & -M_3\frac{\partial}{\partial y} & -M_2\frac{\partial}{\partial y} & 0 & 0 & 0 & 0 & 0
\end{pmatrix}. \tag{6.16}$$

To analyze the dependence of the phase velocities of each mode present in equation (6.15) requires a dispersion relations for a plane wave. A compressional plane wave propagating in a medium with an attenuation factor $\boldsymbol{\alpha}$, a complex wavevector $\boldsymbol{k} = \boldsymbol{k} - i\boldsymbol{\alpha}$ and an angular frequency of ω, can be expressed as

$$\boldsymbol{q} = \boldsymbol{q_0} \exp\left(\boldsymbol{k}\cdot\boldsymbol{x} - \omega t\right) , \tag{6.17}$$

where $\boldsymbol{q} = [\epsilon,\ \zeta_n,\ \zeta_w]^T$ and $\boldsymbol{q_0}$ is the polarization vector of the compressional modes present in the system. The dispersion relation for a plane wave (Equation (6.17)) governed by Equation (6.15) is expressed as [139]

$$\boldsymbol{\Gamma q_0} = {v_c}^2(\boldsymbol{D} - i\boldsymbol{L})\boldsymbol{q_0} , \tag{6.18}$$

where $\boldsymbol{\Gamma}, \boldsymbol{D}$ and $\boldsymbol{L}$ are stiffness, density and friction matrices.

The three eigenvalues (v_c)s of Equation (6.18) correspond to three P-wave phases with velocities (v_p)s and attenuation (α)s are

$$v_p = \left[\mathrm{Re}\left(\frac{1}{v_c}\right)\right]^{-1}, \quad \alpha = -\omega\left[\mathrm{Im}\left(\frac{1}{v_c}\right)\right] . \tag{6.19}$$

Following [126], the phase velocity of the shear wave is governed by the rotational part of Equations (6.1-6.3). Operating Equation (6.1-6.3) with the curl ($\nabla\times$) operator and using the vector identity $\boldsymbol{a}\cdot(\boldsymbol{a}\times\boldsymbol{b}) = 0$, we get

$$\rho(\nabla\times\dot{\boldsymbol{v}}_{\boldsymbol{s}}) + \rho_n S_n(\nabla\times\dot{\boldsymbol{v}}^n) + \rho_w S_w(\nabla\times\dot{\boldsymbol{v}}^w) = N(\epsilon_{xx,x} + \epsilon_{yy,y}) , \tag{6.20}$$

$$\rho_n S_n(\nabla \times \dot{\boldsymbol{v}}^s) + g_1(\nabla \times \dot{\boldsymbol{v}}^n) + g_3(\nabla \times \dot{\boldsymbol{v}}^w) + S_n^2 \left(\frac{\eta_n}{\kappa_n}\right)(\nabla \times \boldsymbol{v^n}) = 0 \ , \tag{6.21}$$

$$\rho_w S_w(\nabla \times \dot{\boldsymbol{v}}^s) + g_3(\nabla \times \dot{\boldsymbol{v}}^n) + g_2(\nabla \times \dot{\boldsymbol{v}}^w) + S_w^2 \left(\frac{\eta_w}{\kappa_w}\right)(\nabla \times \boldsymbol{v^w}) = 0 \ . \tag{6.22}$$

Analytical expressions of $\bar{\boldsymbol{V}}$ $(\nabla \times (\boldsymbol{v^s}, \boldsymbol{v^n}, \boldsymbol{v^w}))$ can be expressed as,

$$\bar{\boldsymbol{V}} = \bar{\boldsymbol{V}}_{\boldsymbol{0}} e^{i(\boldsymbol{k}\cdot\boldsymbol{x} - \omega t)} \ . \tag{6.23}$$

where $\bar{\boldsymbol{V}}_0$ is the polarization vector of the shear modes present in the system. Substituting Equation (6.23) in Equations (6.20-6.22), we obtain the phase velocity of shear wave, which is

$$v_c = \sqrt{N}\left[\rho - \frac{C_1 + C_2}{g_1^* g_2^* - g_3^2}\right]^{-1/2} \ , \tag{6.24}$$

where $C_1 = \rho_n S_n(g_3^* \rho_n S_n - g_3 \rho_w S_w)$, $C_2 = \rho_w S_w(g_1^* \rho_w S_w - g_3 \rho_n S_n)$, $g_1^* = g_1 - \dfrac{ib_n}{\omega}$ and $g_3^* = g_3 - \dfrac{ib_w}{\omega}$.

6.5 Numerical-simulation method

The next step is to adopt a stable numerical scheme to solve Equation (6.15), which requires a detailed analysis of the eigenvalues of the propagator matrix $\boldsymbol{M}$. As a clarification the largest and the smallest eigenvalues represent velocities of the fast and slow P- modes respectively. Eigenvalues of $\boldsymbol{M}$ are complex conjugates pairs. For non-viscous pore-fluids the eigenvalues are purely imaginary but for a viscous fluid they also have a real part which is negative and which represents attenuation. For the Nivelsteiner sandstone (Table 1), the real part of the largest and smallest eigenvalues are $-145467\ s^{-1}$ and $-1274\ s^{-1}$, respectively. A large difference in magnitude of the eigenvalues makes the system stiff [142] and requires the modeling scheme to have very small time steps for being numerically stable and accurate at the same time.

[140] and [139] solved Equation (6.15) numerically by adopting different approaches. [140] computed the numerical solution in the frequency domain, similar to the form of a Helmholtz equation. At each time step the numerical solution is obtained by solving the system of Helmholtz-like equations across the entire frequency range without any constraint on the choice of the time step (CFL condition). Thus, the problem of stiffness is taken care implicitly at the cost of an added computational complexity. On the other hand, [139] solved Equation (6.15) in the time domain and circumvented the effect of stiffness by adopting the approach of [143]. In this paper, we have followed

[139] to solve Equation (6.15) numerically. This approach firstly separates Equation (6.15) into stiff and non-stiff parts to circumvent the stiffness of the system, secondly it solves them separately and finally merges the solutions obtained from the previous two steps. The spatial derivatives of $\boldsymbol{M}$ are computed by using the Fourier method [32] and the equation is integrated in time with the fourth-order Runge-Kutta method. A brief review of the numerical methods is presented in the following.

The formal solution of Equation (6.15) is given by [144]

$$\boldsymbol{w}(t) = \exp(t\boldsymbol{M})\boldsymbol{w_0} + \int_0^t \exp(\tau\boldsymbol{M}) f(t-\tau) d\tau, \tag{6.25}$$

where $\boldsymbol{w_0}$ is the initial condition and $\exp(t\boldsymbol{M})$ is known as the evolution operator. The splitting algorithm [143] partitions $\boldsymbol{M}$ as $\boldsymbol{M} = \boldsymbol{M_r} + \boldsymbol{M_s}$ with $\boldsymbol{M_r}$ and $\boldsymbol{M_s}$ representing the stiff and non-stiff part of $\boldsymbol{M}$ respectively and expressed as

$$\boldsymbol{M_r} = \left(\begin{array}{c|c} \mathbf{0}_{6\times5} & \boldsymbol{M_{r_1}} \\ \hline \boldsymbol{M_{r_2}} & \mathbf{0}_{5\times5} \end{array} \right) , \tag{6.26}$$

where

$$\boldsymbol{M_{r_1}} = \begin{pmatrix} \rho\dfrac{\partial}{\partial x} & 0 & \rho\dfrac{\partial}{\partial y} & \rho_n S_n \dfrac{\partial}{\partial x} & \rho_w S_w \dfrac{\partial}{\partial x} \\ \rho_n S_n \dfrac{\partial}{\partial x} & 0 & \rho_n S_n \dfrac{\partial}{\partial y} & g_1 \dfrac{\partial}{\partial x} & g_3 \dfrac{\partial}{\partial x} \\ \rho_w S_w \dfrac{\partial}{\partial x} & 0 & \rho_w S_w \dfrac{\partial}{\partial y} & g_3 \dfrac{\partial}{\partial x} & g_2 \dfrac{\partial}{\partial x} \\ 0 & \rho\dfrac{\partial}{\partial y} & \rho\dfrac{\partial}{\partial x} & \rho_n S_n \dfrac{\partial}{\partial y} & \rho_w S_w \dfrac{\partial}{\partial y} \\ 0 & \rho_n S_n \dfrac{\partial}{\partial y} & \rho_n S_n \frac{\partial}{\partial x} & g_1 \dfrac{\partial}{\partial y} & g_3 \dfrac{\partial}{\partial y} \\ 0 & \rho_w S_w \dfrac{\partial}{\partial y} & \rho_w S_w \dfrac{\partial}{\partial x} & g_3 \dfrac{\partial}{\partial y} & g_2 \dfrac{\partial}{\partial y} \end{pmatrix} , \tag{6.27}$$

$$\boldsymbol{M_{r_2}} = \begin{pmatrix} (K_c+N)\frac{\partial}{\partial x} & B_1\frac{\partial}{\partial x} & B_2\frac{\partial}{\partial x} & (K_c-N)\frac{\partial}{\partial y} & B_1\frac{\partial}{\partial y} & B_2\frac{\partial}{\partial y} \\ (K_c-N)\frac{\partial}{\partial x} & B_1\frac{\partial}{\partial x} & B_2\frac{\partial}{\partial x} & (K_c+N)\frac{\partial}{\partial y} & B_1\frac{\partial}{\partial y} & B_2\frac{\partial}{\partial y} \\ N\frac{\partial}{\partial y} & 0 & 0 & N\frac{\partial}{\partial x} & 0 & 0 \\ B_1\frac{\partial}{\partial x} & -M_1\frac{\partial}{\partial x} & -M_3\frac{\partial}{\partial x} & B_1\frac{\partial}{\partial y} & -M_1\frac{\partial}{\partial y} & -M_3\frac{\partial}{\partial y} \\ B_2\frac{\partial}{\partial x} & -M_3\frac{\partial}{\partial x} & -M_2\frac{\partial}{\partial x} & B_2\frac{\partial}{\partial y} & -M_3\frac{\partial}{\partial y} & -M_2\frac{\partial}{\partial y} \end{pmatrix} . \tag{6.28}$$

Matrix $\boldsymbol{M_s}$ can be expressed as

$$\boldsymbol{M_s} = \left(\begin{array}{c|c} \boldsymbol{R_{6\times 6}} & \mathbf{0}_{6\times 5} \\ \hline \mathbf{0}_{5\times 6} & \mathbf{0}_{5\times 5} \end{array}\right) , \tag{6.29}$$

where

$$\boldsymbol{R} = \left(\begin{array}{c|c} \boldsymbol{S_{3\times 3}} & \mathbf{0_{3\times 3}} \\ \hline \mathbf{0}_{3\times 3} & \boldsymbol{S_{3\times 3}} \end{array}\right) , \tag{6.30}$$

where

$$\boldsymbol{S} = \begin{pmatrix} 0 & -\rho_n S_n^3\left(\frac{\eta_n}{\kappa_n}\right) & -\rho_w S_w^3\left(\frac{\eta_w}{\kappa_w}\right) \\ 0 & -g_1 S_n^2\left(\frac{\eta_n}{\kappa_n}\right) & -g_3 S_w^2\left(\frac{\eta_w}{\kappa_w}\right) \\ 0 & -S_n^2\left(\frac{\eta_n}{\kappa_n}\right) & -S_w^2\left(\frac{\eta_w}{\kappa_w}\right) \end{pmatrix} . \tag{6.31}$$

The discretized evolution operator (Equation (6.25)) at time step dt can be expressed as

$$\exp(\boldsymbol{M}dt) = \exp(\frac{1}{2}\boldsymbol{M}_s) exp(\frac{1}{2}\boldsymbol{M}_r) \exp(\frac{1}{2}\boldsymbol{M}_s) \ . \tag{6.32}$$

Equation (6.32) allows to solve the stiff part of the system separately and we can write the differential equation for velocity vector $\boldsymbol{v} = [v_x^s, v_x^n, v_x^w, v_y^s, v_y^n, v_y^w]^T$ as,

$$\dot{\boldsymbol{v}} = \boldsymbol{R}\boldsymbol{v}. \tag{6.33}$$

The solution of Equation (6.33), denoted as $\boldsymbol{w^*}$, is treated as an intermediate corrector term

and can be computed analytically. The evaluation of the non-stiff term is $(\exp(\boldsymbol{M_r}t))$ is perfoemed with the Runge-Kutta scheme and the Fourier method. Thus, the numerical scheme used to solve the system (Equation (6.15)) is

$$\boldsymbol{w}^{n+1} = w^* + \frac{1}{6}(dt)(2\Delta_1 + 2\Delta_2 + 2\Delta_3 + 2\Delta_4) \ , \tag{6.34}$$

where

$\Delta_1 = \boldsymbol{M_r}\boldsymbol{w}^* + \boldsymbol{f}^n, \quad \Delta_2 = \boldsymbol{M_r}(\boldsymbol{w}^* + \frac{1}{2}(dt)\Delta_1) + \boldsymbol{f}^{n+1/2} \ ,$

$\Delta_3 = \boldsymbol{M_r}(\boldsymbol{w}^* + \frac{1}{2}(dt)\Delta_2) + \boldsymbol{f}^{n+1/2}, \quad \Delta_4 = \boldsymbol{M_r}(\boldsymbol{w}^* + dt\Delta_3) + \boldsymbol{f}^{n+1} \ .$

he numerical scheme expressed in Equation (6.34) is "infinitely" accurate in space and achieves second order accuracy in time. We also claim that the numerical scheme (Equation (6.34)) is bounded by accuracy than stability, as the system under the study is stiff. To prove the above claim, a convergence study is performed for a plane wave of which analytical solution is computed using Equation (6.15). Stress and velocity vectors of a plane wave with real wave vector $\boldsymbol{k}$ (no attenuation) and angular frequency ω can be expressed as

$$\boldsymbol{T} = \boldsymbol{T_0} \exp i(\boldsymbol{k} \cdot \boldsymbol{x} - \omega t) \ , \tag{6.35}$$

$$\boldsymbol{V} = \boldsymbol{V_0} \exp i(\boldsymbol{k} \cdot \boldsymbol{x} - \omega t) \ , \tag{6.36}$$

where $\boldsymbol{T} = [\tau_{xx}, \tau_{yy}, \tau_{xy}, \tau_n, \tau_w]^T$ and $\boldsymbol{V} = [v_x^s, v_x^n, v_x{}^w, v_y^s, v_y^n, v_y^w]^T$. $\boldsymbol{T_0}$ and $\boldsymbol{V_0}$ are polarization vectors.

6.6 Results

We illustrate our results using the properties of the Nivelsteiner Sandstone [145] (Table 1), which is a Miocene age quartz dominated formation containing $< 5\%$ clay. We use 3 kPa as the value of A in Equation (6.4) after [129]. In the plots hereon P1 indicates the fast P wave, P2 and P3 the slow waves and S is the shear wave. The characteristic frequency for the Nivelsteiner sandstone is 10 kHz, when fluid flow in the pores changes from laminar to turbulent. For our purpose we change the capillary pressure by changing the water saturation; $S_w = 90\%$ corresponds to a p_{ca} of 3.22 kPa and $S_w = 10\%$ corresponds to a p_{ca} of 1.22 MPa. We perform the basic model validation by predicting the P1 wave with respect to an increasing gas saturation (S_{nw} or S_g; Figure 6.1). As seen in Figure 6.1, v_{P1} drops rapidly when S_g increases initially. As S_g increases further, v_{P1} slightly

Table 6.1: Material properties of the Nivelsteiner sandstone

Medium properties		
Grain	Bulk Modulus, K_s(GPa)	36
	Density, ρ_s (kg/m^3)	2650
Matrix	Bulk Modulus, K_m(GPa)	6.21
	Shear Modulus, N(GPa)	4.55
	Porosity, ϕ	0.33
	Permeability κ (Darcy)	5
Gas (non-wetting phase)	Bulk Modulus, K_n(GPa)	0.022
	Density, ρ_n (kg/m^3)	100
	Viscosity, η_n (cP)	0.015
Water (wetting phase)	Bulk Modulus, K_w(GPa)	2.223
	Density, ρ_w (kg/m^3)	1000
	Viscosity, η_w (cP)	1

increases. This concurs with prevalent understanding about the behavior of gas-brine mixture in porous rocks (e.g, [146, 147], [148]). Our model successfully explains the poromechanical behavior of a gas-brine mixture. For computing Figure 6.1 we have maintained the frequency at 0 Hz. A similar plot (for another sandstone) is given in [126]. Next, we vary the frequency and show the dispersion characteristics of the P1 mode (Figure 6.2a). We present results in Figure 6.2a as percentage change over v_{P1} at the reference frequency of 1 Hz. In line with the other studies [139], Figure 6.2a shows a step change in v_{P1} at 10 KHz. It is notable that the change is more significant for lower S_{nw}. The significance is that well-to-seismic tie can become more erroneous in formations with low gas saturation if capillary effects are not appropriately accounted for. The dispersion characteristics of the P2 and P3 modes (Figure 6.2b and 6.2c respectively) are such that v_{P2} and v_{P3} decrease as capillary pressure increases up to the characteristic frequency beyond which it becomes fairly constant. Further, the shear mode does not have any dispersive properties and thus it is not shown here. We show the attenuation characteristics of the P1, P2 and P3 modes in Figures 6.3a, 6.3b and 6.3c. The attenuation of the P1 mode (Figure 6.3a) is more prominent at frequencies > 3 kHz and, least among all the three modes, increases as capillary pressure increases. This explains that the amplitude of the P1 mode is less affected by fluid viscosity and permeability (absolute and relative). The attenuation characteristics of the P2 mode vary across the entire frequency range and, similar

to P1 mode, the attenuation factor of the P2 mode (most among all the three modes) increases as capillary pressure increases. This clearly shows that the amplitude of the P2 mode is dependent on saturation of the wetting phase (S_w). However, the attenuation of the P3 mode decreases as capillary pressure increases which in turn establishes that the amplitude of the P3 mode is dependent on the saturation of the non-wetting phase S_{nw}. The shear wave is not affected by the fluid phases and thus there is no effect of the varying capillary pressure on its phase velocity and attenuation. [149] presented the theory of wave propagation in a rock saturated with two-phase fluids under variable pressure conditions, especially on $\bar{p_w}$. In this study, they found that the velocity and attenuation of P- (P1, P2 and P3) and shear waves also vary with $\bar{p}_w$. Accordingly, we also computed the simultaneous effect of capillary pressure (p_{ca}) and absolute pressure of the wetting fluid ($\bar{p}_w$) on the velocity of the P-wave modes (see Figure 6.4). Figure 6.4a shows the phase velocity of the P1 mode (computed at 1 MHz) against the capillary pressure p_{ca} at varying $\bar{p}_w$. The phase velocity of this mode decreases as $\bar{p}_w$ increases, which is due to the fact that as $\bar{p_w}$ increases p_{ca} decreases. This further corroborates the dispersion analysis of the P1 mode shown in Figure 6.2a. Figure 6.4b

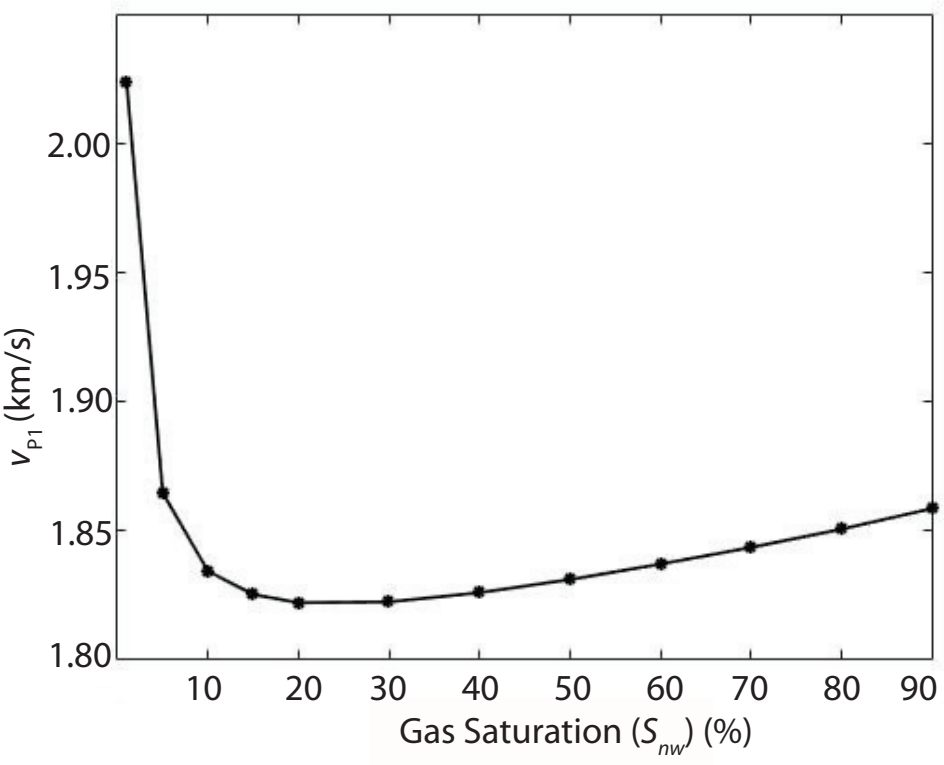

Figure 6.1: Phase velocity of the P1 mode computed at 0 Hz as a function of the saturation of the non-wetting phase.

and 6.4c are plots of the phase velocities of the P2 and P3 modes, computed at variable p_{ca} and $\bar{p}_w$. As $\bar{p}_w$ increases, the first velocity increases at low value of p_{ca} (low gas saturation), whereas at higher values of p_{ca} this velocity decreases. This reconfirms the results of the dispersion analysis for the P2 mode, shown in Figure 6.2b. The phase velocity of the P3 mode against $\bar{p}_w$ is shown in Figure 6.4c. In general, there is a positive correlation with $\bar{p}_w$. This observation is in line with the dispersion analysis of the P3 mode (Figure 6.2c), showing a negative correlation with respect to p_{ca}. Next, we perform numerical simulations but before we test the accuracy of the method. Analytical solutions of Equation (6.15) for the plane waves ((6.35) and (6.36)) are computed by solving a linear system of equations obtained after substituting Equations (6.35) and (6.36) into Equation (6.15). A plot showing the error between the numerical and analytical solutions of the solid particle velocity (v_x^s) versus the number of terms used in Fourier expansion (N_g), computed for values of CFL = 0.8 and 0.6, is shown in Figure 6.4. It is worth to note that as N_g increases the rate of convergence

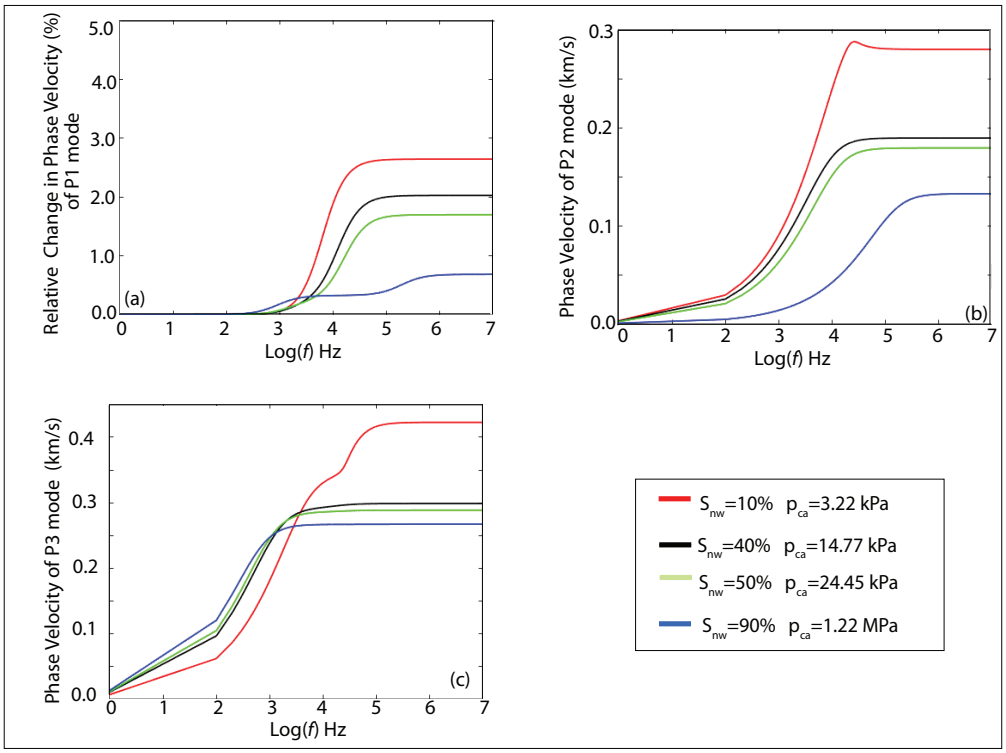

Figure 6.2: Effect of the capillary pressure on (a) the velocity of the fast P1- mode, (b) the velocity of the slow P2-mode and (c) the velocity of the slow P3 mode. Note that different capillary pressures correspond to different saturations of the non-wetting (gas) phase (S_{nw}).

decreases to 4th-order but as time steps is increased (CFL=0.6) the convergence is improved. This proves our claim that the numerical scheme (Equation (6.34)) is of very high order and bounded by convergence not by stability. In addition to this, Figure 6.5 also proves that as the degree of freedom increases in space, the numerical scheme is gradually dominated by the order of the time accuracy. We show the numerical simulation based on Equation (6.15) using a 400 $\times$ 400 grid domain at ultrasonic (300 kHz) and seismic (25 Hz) frequencies. The system of Equations (6.15) is solved numerically for a capillary pressure of 3.22 kPa (S_{nw} = 10 %) and 24.45 kPa (S_{nw} = 50%). Snapshots of the particle velocity of the rock frame in the ultrasonic frequency range captured at p_{ca} = 3.22 kPa and 24.45 kPa, are shown in Figure 6.6a and 6.6b, respectively. Four wave modes P1, P2, P3 and S are marked on all the illustrations shown in Figures 6.6, 6.7 and 6.8. The P2 mode, generated due to the relative motion between the solid and the non-wetting phase, is the classical Biot *slow* P mode with polarity opposite to that of the fast compressional mode P1. The polarity of the P3 mode, generated due to relative motion between the solid and the wetting phase, shows a sync in polarity with the main compressional wave P1. The attenuation characteristics shown in

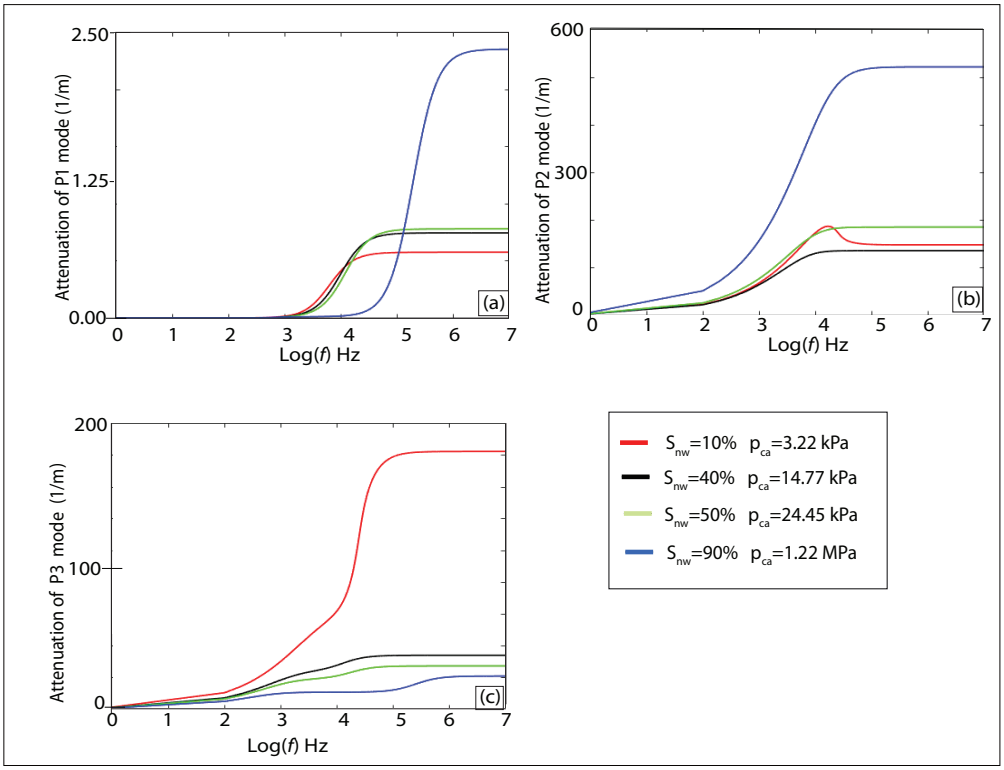

Figure 6.3: Effect of the capillary pressure on (a) the attenuation of the fast P1- mode, (b) the attenuation of the slow P2-mode and (c) the attenuation of the slow P3 mode. Note that different capillary pressures correspond to different saturations of the non-wetting (gas) phase (S_{nw}).

Figure 6.3 indicate that in the high-frequency range the amplitude of the P1 mode decreases as capillary pressure increases, which is validated from Figures 6.6a and 6.6b. Computed maximum absolute particle velocities of the P1 mode at $p_{ca} = 3.22$ kPa and $p_{ca} = 24.45$ kPa are 2×10^{-10} and 8×10^{-11} respectively. This proves the attenuation characteristic of the P1 mode with capillary pressure, obtained from the dispersion analysis. In the high-frequency range the phase velocity of the P2 and P3 modes (Figure 6.2b and 6.2c) decreases as capillary pressure increases, which can be verified from numerical simulation as well. Apparently the distance traversed by P2 and P3 modes in Figure 6.5a is more than in Figure 6.6b, thus proving slow phase velocity for P2 and P3 modes as capillary pressure increases. In the high-frequency range, the attenuation of the P2 mode (Figure 6.3b) increases as capillary pressure increases, which can be validated from numerical

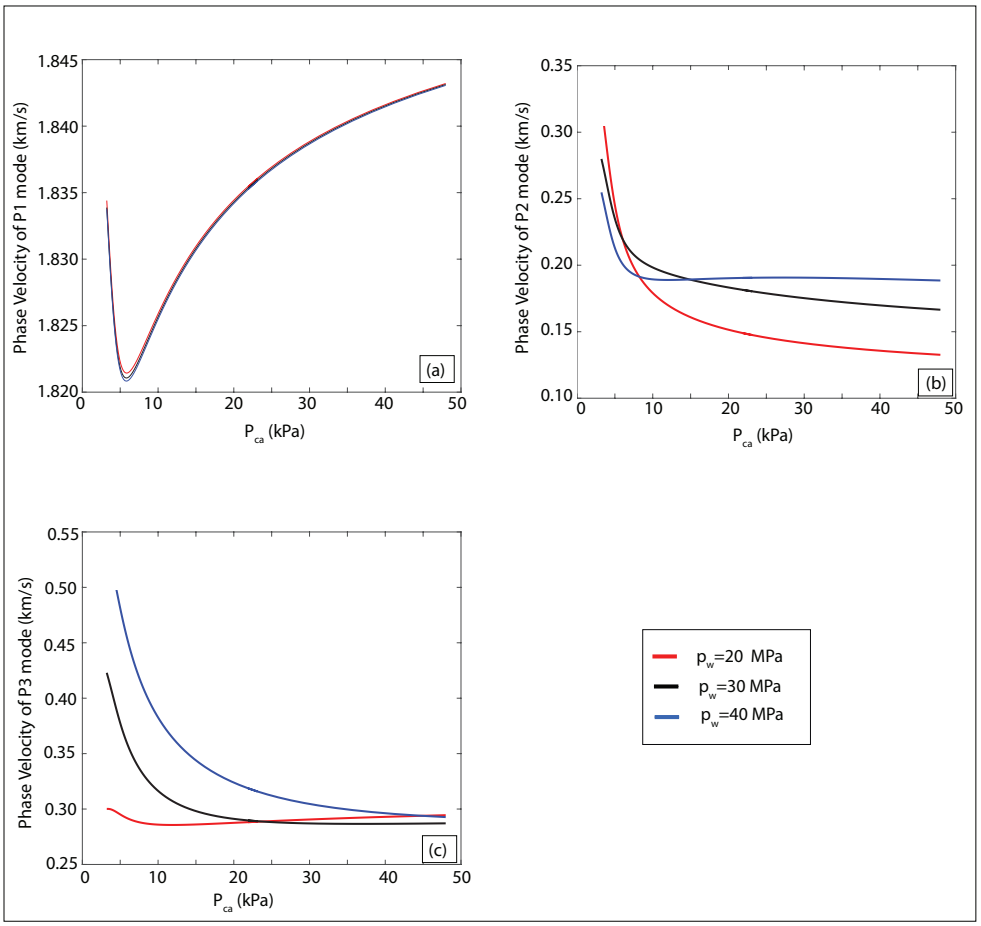

Figure 6.4: Simultaneous effect of capillary pressure and absolute wetting fluid pressure (p_w) on (a) the velocity of the fast P1- mode, (b) the velocity of the slow P2-mode and (c) the velocity of the slow P3 mode. Velocity is computed at frequency of 1 MHz. Note that different absolute wetting fluid pressure (p_w) correspond to different depths of the reservoir rocks.

simulation by extracting the maximum absolute particle velocity in Figure 6.6a and 6.6b. The absolute particle velocity of the P2 mode at $p_{ca} = 3.22$ kPa (Figure 6.6a) and 24.45 kPa (Figure 6.6b) is 7×10^{-10} and 3×10^{-10} respectively, which corroborates the observation from Figure 6.3b. In the high-frequency range the attenuation of the P3 mode (Figure 6.3c) decreases as capillary pressure increases, opposite to the trend observed for the P2 mode. This phenomena correlates very well with the theory, stating that as saturation of non-wetting phase increases (capillary pressure increases) the existence of the P3 mode becomes more prominent due to the fact that P3 mode is the upshot of the relative motion among the particles of the non-wetting phases and the rock frame. The same concept is also applicable for the P2 mode. To corroborate the attenuation characteristics of the P3 mode with numerical simulations, we extracted the absolute particle velocities of the P3 mode from Figures 6.6a and Figure 6.6b. The absolute particle velocities of the P3 mode for $p_{ca} = 3.22$ kPa and 24.45 are 2×10^{-10} and 3×10^{-10} respectively, which justifies the dispersion results for the P3 mode.

Figures 6.6c and 6d shows snapshot (at 1 s) of the horizontal component of the particle

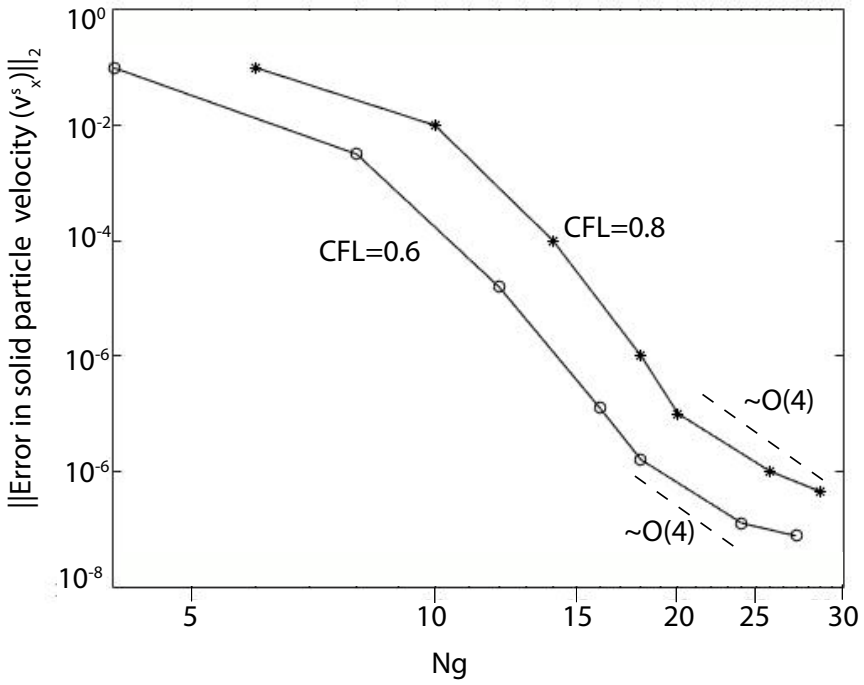

Figure 6.5: Convergence plot between the norm of error of solid velocity and number of term used in Fourier expansion (N_g). Convergence is computed for CFL = 0.8 and CFL = 0.6. (CFL: Courant-Friedrich-Lewy number).

velocity (v_x^s) of the rock frame at 25Hz simulated for $p_{ca} = 3.22$ kPa and 24.45 kPa respectively. The phase velocity of the P1 mode (Figure 6.2a) at 25 Hz varies from 1780 m/s to 1805 m/s with p_{ca} varying from 3.22 kPa to 24.45 kPa. A subtle difference of 25 m/s of velocity between $p_{ca} = 3.22$ kPa and 24.45 kPa is reflected as 1.5 spatial grids in the domain of numerical simulation, which is very hard to visualize in image but a careful examination of Figure 6.6d shows that the P1 mode traversed more distance than the P1 mode in Figure 6.6c. The phase velocity of the P2 (Figure 6.2b) and P3 (Figure 6.2c) modes at 25 Hz is ≈ 0, thus the medium does not support the propagation of slow P modes in the low-frequency range. The attenuation factor of the P2 mode is 40 at $p_{ca} = 3.22$ kPa and 24.45 kPa, which is more than the attenuation factor (≈ 0) of the

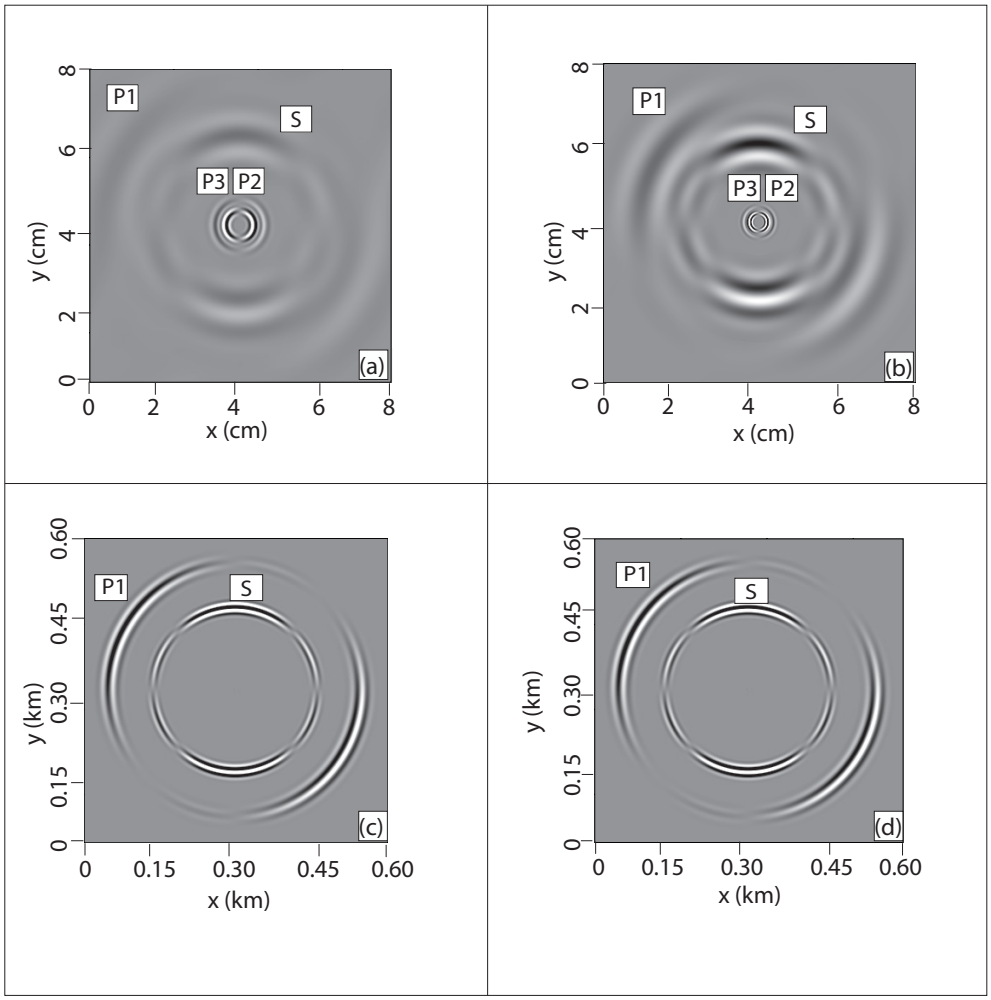

Figure 6.6: Horizontal component of the particle velocity v_x. (a) and (b) are snapshots at 18 μs for a 300 kHz Ricker source wavelet. (c) and (d) are snapshots at 1 s for a 25 Hz Ricker source wavelet. In (a) and (b) the mesh size is 0.18 mm and the size of the time step is 12.5 ns. In (c) and (d) the mesh size is 15 m and the size of the time step (dt) is 1 ms. In (a) and (c) $S_{nw} = 10\%$ and in (b) and (d) $S_{nw} = 50\%$.

P1 mode. This is the effect of capillary pressure on the existence of the P2 mode, which does not appear in the numerical simulation shown in Figures 6.6c and 6.6d. The attenuation characteristic of the P3 mode with varying capillary pressure shows the same pattern as the P2 mode and also does not appear in the numerical simulation shown in Figure 6.6(c) and 6.6(d). Figure 6.7 shows snapshots of the horizontal particle velocity (v_x^n) for the non-wetting phase. Figures 6.7a and 6.7b show that, at high frequencies, the P2 and P3 modes are much stronger in the fluid phases. As capillary pressure increases, the energy contained in the P2 and P3 modes increase, which can be verified by an analysis of the relative amplitudes between the slow (P2 and P3) modes and the fast (P1) mode. The relative amplitude between Figures 6.6a and 6.7a is 1179, whereas the

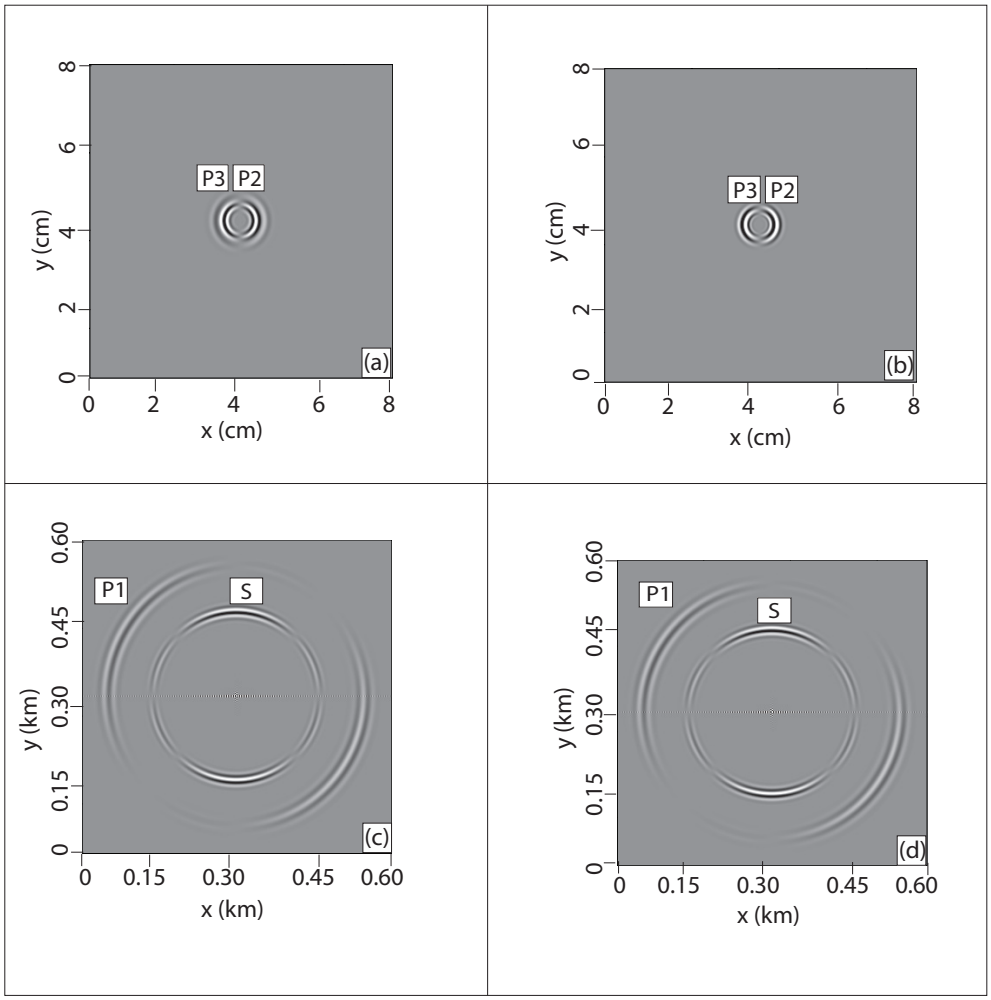

Figure 6.7: Horizontal component of the particle velocity v_x^n. (a) and (b) are snapshots at 18 μs for a 300 kHz Ricker source wavelet. (c) and (d) are snapshots at 1 s for a 25 Hz Ricker source wavelet. In (a) and (b) the mesh size is 0.18 mm and the size of time step is 12.5 ns. In (c) and (d) the mesh size is 15 m and the size of time step (dt) is 1 ms. In (a) and (c) $S_{nw} = 10\%$ and in (b) and (d) $S_{nw} = 50\%$.

relative amplitude between Figures 6.6b and 6.7b is 1200. This justifies our observation of the effect of capillary pressure on the energy contained in the P2 and P3 modes present in the fluid phases. In the low-frequency range (Figures 6.7c and 6.7d), the P2 and P3 modes do not propagate, remaining static and diffusing gradually. The maximum energy is concentrated in the solid phase and is invariable with the capillary pressure.

Figure 6.8 shows snapshots of the horizontal particle velocity (v_x^w) for the wetting phase. Like in the non-wetting phase at high frequencies, the energy is concentrated mainly in the P2 and P3 modes (Figure 6.7a and Figure 6.7b). The relative amplitude between Figures 6.6a and 6.8a is 64, which decreases to 52 between Figures 6.6b and 6.8b. Thus, as capillary pressure increases,

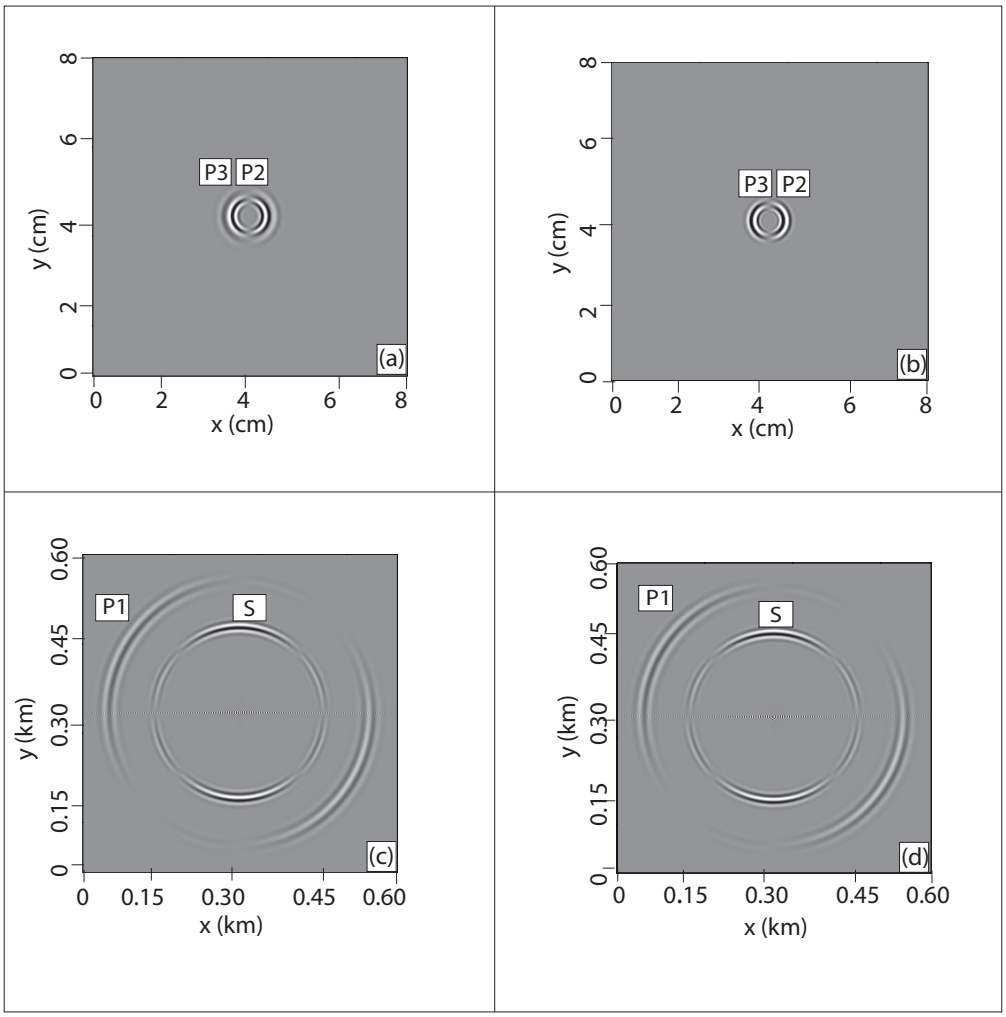

Figure 6.8: Horizontal component of the particle velocity v_x^w. (a) and (b) are snapshots at 18 μs for a 300 kHz Ricker source wavelet. (c) and (d) are snapshots at 1 s for a 25 Hz Ricker source wavelet. In (a) and (b) the mesh size is 0.18 mm and the size of time step is 12.5 ns. In (c) and (d) the mesh size is 15 m and the size of time step (dt) is 1 ms. In (a) and (c) $S_{nw} = 10\%$ and in (b) and (d) $S_{nw} = 50\%$.

the energy contained in the P2 and P3 modes decreases. In the low-frequency range (Figure 6.8c and 6.8d), the physics of the P2 and P3 mode remains same as in the non-wetting phase. Though the gradual increase of the non-wetting saturation S_{nw} increases the concentration of energy in the non-wetting phases, it will never be zero due to the presence of irreducible saturation. Thus, the numerical simulation will not reduce to the classical Biot's case.

Shot gathers representing the horizontal particle motion of the rock frame are shown in Figure 6.9 and 6.10 for the high and low-frequency cases, respectively. These shot gathers, in general, show a stronger shear mode as they represent the horizontal component of the rock frame velocity (v_x^s). The polarity of the wave modes on either side of the origin (offset = 0 m) is phased out by 180^o due to the fact that the polarization vector on either side of the origin is in the opposite direction. The shot gathers shown in Figures 6.9 and 6.10 are simulated for homogeneous medium and modes recorded P1, P2, P3 and S modes are direct arrivals from the source. As expected from previous results (Figures 6.6-6.8) the P1, P2 and P3 modes are well identified in the high-frequency case

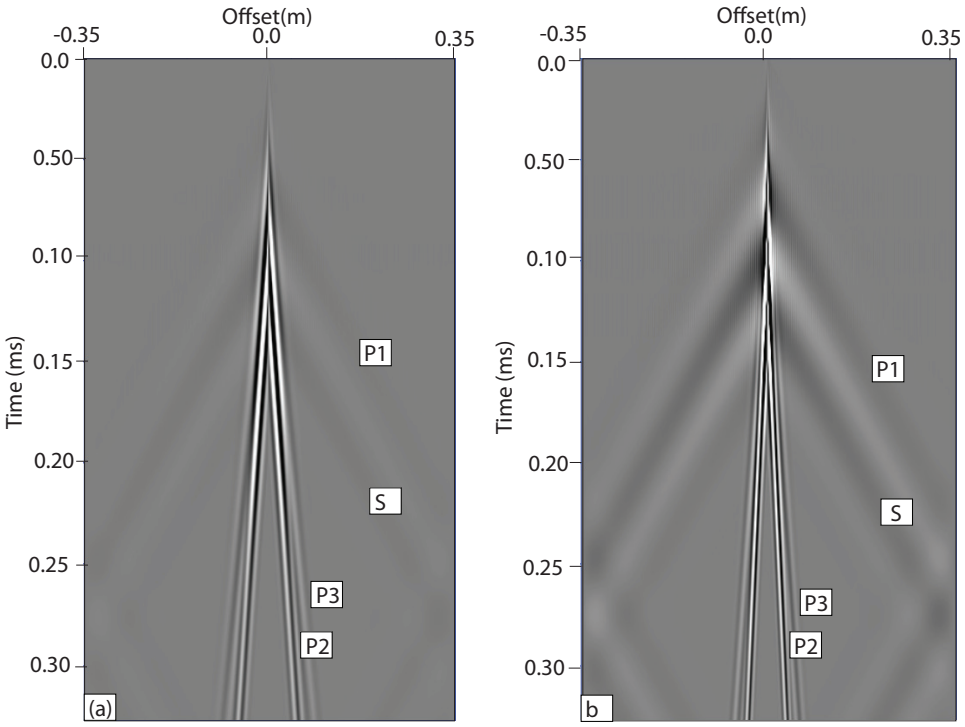

Figure 6.9: Shot gather of the particle velocity at ultrasonic frequencies, v_x^s. In (a) and (b) $S_{nw} = 10\%$ and in (b) and (d) $S_{nw} = 50\%$.

(Figure 6.9), whereas the P and S modes are more dominant in the low-frequency case. In Figure 6.9 and 6.10, the variation of amplitude agrees with the results shown in Figure 6.2 and 6.3.

6.7 Discussion

The effects of multiphase fluids in a porous rock, e.g., wettability, capillary pressure and inter-facial tension has been shown in various physical process, e.g. transport of electric current through porous media [150], capillary imbibition in porous media [151] and spontaneous co-current imbibition [152]. In this study, we have shown the dependence of the phase velocities on capillary pressure for reservoir rocks saturated with multi-phase fluids. Capillary pressure arises due to the pressure difference across the contact interface between the wetting and non-wetting phases and thus it is a monotonically increasing function of the saturation of the non-wetting phase [140]. Figure 6.1 shows plots of the rock frame velocity v_{P1}, known as P-wave velocity in various acoustic and elastic seismic modeling, versus increasing saturation of the non-wetting phase (S_{nw}), which is directly proportional to capillary pressure. Figure 6.1 is in concordance with the fluid substitution model of Gassmann's [153]. The velocity (v_{P1}) in the present study is obtained from the model developed by [126] which assumes a poromechanical approach for deriving the constitutive equations. An effect of

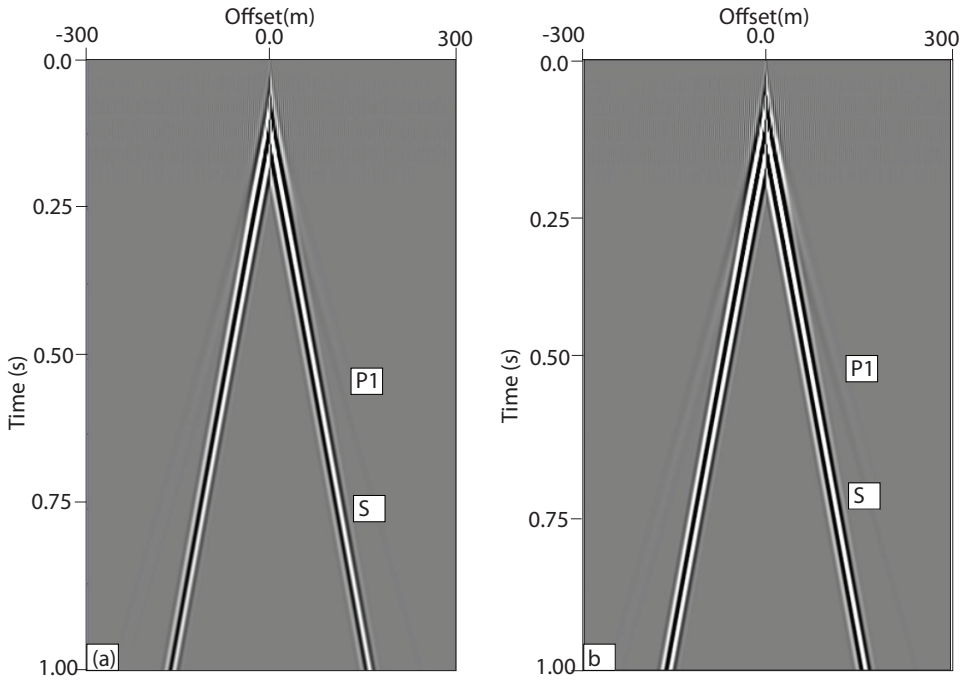

Figure 6.10: Shot gather of the particle velocity at seismic frequencies, v_x^s. In (a) and (b) $S_{nw} = 10\%$ and in (b) and (d) $S_{nw} = 50\%$.

the pore topology on v_{P1} with increasing gas saturation or capillary pressure is not yet explained.

To incorporate the effect of pore topology, we computed the velocity of the reservoir sandstone (Table 1) using the Hashin-Strickman (HS) model [154]. A plot comparing the wet-rock velocity v_{P1} obtained from Equation (6.18) and the velocity obtained from the HS model is shown in Figure 6.11. The velocity obtained from this model over predicts the velocity as it does not incorporate the effect of capillary pressure on the particle motion. Thus the velocity model with respect to capillary pressure shown in Figure 6.1 is more accurate over any static or quasi-static model such than that of the HS model.

The model used in the present study is based on the assumption that pores are completely connected and any isolated pores are part of the matrix mineral. Thus, the velocity model presented in Figure 6.1 may not be able to correctly predict the velocity in low permeability reservoir rocks such as shale, tight carbonates and sands, unless the mineral properties are accurately obtained. In addition to that, the model also assumes that the saturation of the non-wetting phase (S_{nw}) does not account for the effect of interstitial micro gas bubbles present in the wetting phase. As [155] proved, the velocity of sound notably depends on the concentration of micro gas bubbles present in

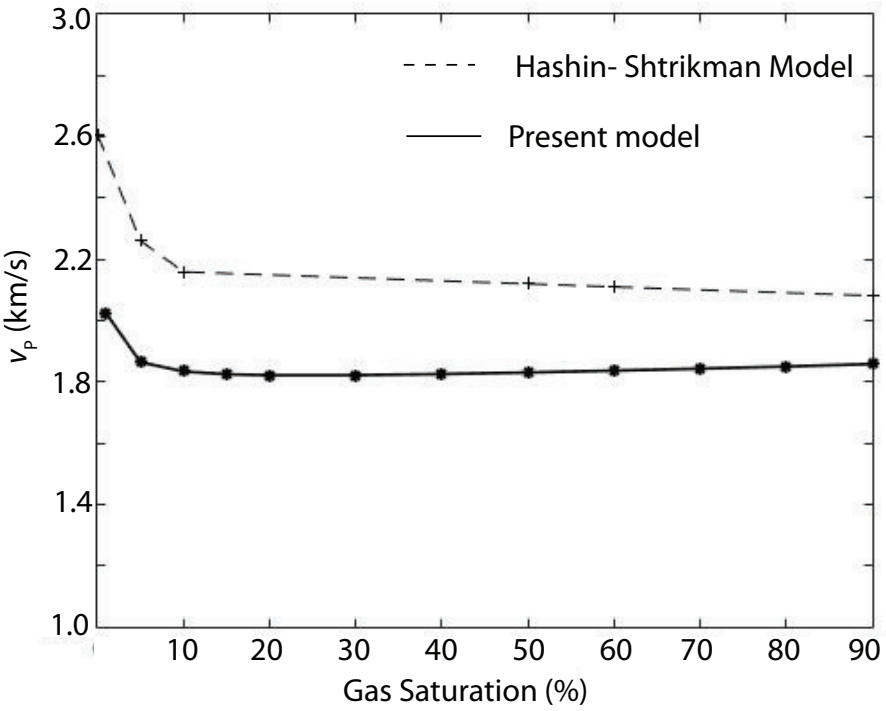

Figure 6.11: Plot comparing the phase velocity of the P1 mode of the wet rock and that of the Hashin-Shtrickman (HS) model.

the wetting phase along with the total gas volume. Thus, the results of velocity model obtained in this study may not be able to explain the effect of micro gas bubble, unless a suitable model to obtain the wetting phase properties is used.

The applicability of the velocity model presented here spans from hydrocarbon exploration to near-surface exploration. Well to seismic tie, an important part of seismic interpretation, is carried out by correlating the sonic log with surface seismic. The mapping of velocity between the sonic range, recorded from sources at ultrasonic frequencies, and surface seismic (obtained from low-frequency sources) does not account for the effect of capillary pressure on velocity obtained from the sonic log. The correct practice to tie the well and seismic data will require an upscaling of the velocity with a-priori information of the saturations in the reservoir zone. The other application comes from near-surface exploration wherein we are interested in the top few meters (0 -10 m) of the subsurface. Seismic data recorded in the near surface setting presumable contains frequencies more than deep seismic data. Thus, wave propagation in the near surface medium may fall in the high-frequency regime. A capillary pressure dependent velocity model may be applicable under two conditions. First, in the presence of a fine grained soil as soil is saturated above the water table due to capillary rise and is under negative pore pressure. Second, in the presence of a coarse grain soil wherein the water will drain from the pores above the water table and thus air will fill the pores of the soil above the water table. These two conditions could be approximated by the presented model. In this work we consider the effect of capillary pressure at a macroscopic scale. Another, indirect but possibly stronger effect is the influence of capillary pressure on fluid flow [156]. In this case partial saturation is affected by the capillary forces inducing mesoscale heterogeneities and fluid patches. Seismic velocity is affected by partial saturation and anelasticity.

In another line of application, the velocity and attenuation model presented here can be used to study the spontaneous imbibition, responsible for the main mechanism of oil production from fractures. [157] has shown that capillary pressure is one of the primary factors responsible for spontaneous imbibition, which, as shown in the present study, varies with the saturation of the wetting and non-wetting fluids. Thus, in events of enhanced oil recovery processes (4D time-lapse seismic study) the aided volume of hydrocarbon due to spontaneous imbibition, can be estimated by considering the effect of capillary pressure in seismic velocity (Figure 6.2 and 6.3).

Chapter VII

Conclusions and future work

7.1 Summary of results

This thesis encircles the development of physics of wave propagation in the porous media, deriving the numerical algorithms and code implementing those algorithms, for high-order discontinuous Galerkin finite element and pseudo spectral modeling of viscoelastic and poroelastic systems of single and two-phase fluids. These models and numerical methods could be applies for quantitative estimation of porosity, permeabilities, viscosity and saturation of fluids present in porous media,

The main objective of the poroelastic model is to understand the attenuation of energy due to relative motion between the solid and fluid particles. Thus, this thesis work starts from understanding the seismic attenuation due to anelasticity of materials; described in chapter 2. In chapter 1, an efficient and accurate simulation of wave equation in attenuative media is performed by implementing the rapid expansion method (REM) and pseudo-spectral method to compute the time and fractional spatial derivatives respectively. Various computational experiments reflect the fact that the proposed efficient numerical scheme accurately incorporates the velocity dispersion, which is caused by Q. A comparison between the analytical and the numerical solutions shows a very good agreement. Numerical simulation for a large scale reservoir model, shows a substantial efficiency of REM over a second-order finite-difference scheme. A study is also carried out, showing the efficiency of our code by comparing the theoretical and actual run times, which shows a very good agreement.

Studies in chapter 3, starts with the development of the mathematical formulation of the poroelastic wave equation in two-dimensional anisotropic porous medium. Chapter 3 shows a rigorous proof of well-posedness of the poroelastic system by showing that the energy rate in the system

is bounded. A numerical scheme is also derived in strong form based on the nodal discontinuous Galerkin finite-element method, paired with a first-order operator splitting approach to handle the stiffness present in the system. A Lax-Friedrich flux, stabilized by the maximum speed of the wave present in the system, is used to implement the natural or interface boundary conditions.The accuracy of the proposed scheme is proved by comparing the numerical solution with an analytical solution. A convergence study shows $O(h^{N+1})$ accuracy. Two dimensional simulations of the wave fields for various real-case scenarios comprising homogeneous and heterogeneous materials with anisotropy are also performed. The simulation correctly produces the fast and slow compressional waves along with the shear waves.

The computation of maximum speed for a poroelastic medium is a computational bottle-neck and it becomes more serious issue for a 3D arbitrary heterogeneous medium. Additionally, usage of the Lax-Friedrich flux for a low order approximation results into a highly dissipative solution. To circumvent these issues, we have a carried out detailed studies in chapter 4 of the thesis starting from formulating the symmetric form of the poroelastic system in three dimensions. Chapter 4, presents a weight-adjusted discontinuous Galerkin (WADG) method for the linear poroelastic wave equations with arbitrary heterogeneous media. The method is energy stable and high order accurate for arbitrary stiffness tensors. The penalty numerical fluxes for this formulation are simple to derive and implement, and their lack of dependence on the stiffness tensors allows for a unified treatment of isotropic and anisotropic media with micro-heterogeneities. Chapter 4 confirms the high-order accuracy of the numerical method using an analytic plane wave solution in a poroelastic media. Results obtained using this method also show good agreement with existing results in the literature for both problems involving both homogeneous and heterogeneous media. Finally, we provide computational results for a large 3D model including the surface topography. This is to be noted that the implementation of this method reduces to the application of the weight-adjusted mass matrix inverse and the evaluation of constant-coefficient terms in the DG formulation. The cost of the latter step can be reduced (especially at high orders of approximation) by using fast methods based on Bernstein-Bezier polynomials for the application of derivative and lift matrices for constant-coefficient terms [104].

The poroelastic models studied in chapter 3 and chapter 4 deals with frequencies less than Biot's characteristic frequency [9], which is only valid for the cases where viscous force is dominant of over the inertial forces. In chapter 5, we formulated a system of equations valid across entire frequency range and named it as "broad-band Biot" system, which is obtained by substituting the static permeability with a frequency dependent permeability. Chapter 5 presents a weight-adjusted

discontinuous Galerkin (WADG) method for the broad-band Biot equations describing poroelastic wave propagation. The method is energy stable and high order accurate for arbitrary stiffness tensors and heterogeneous media. The penalty numerical fluxes for this formulation are simple to derive and implement, and their lack of dependence on the stiffness tensors allows for a unified treatment of isotropic and anisotropic media with micro-heterogeneities. We confirm the high-order accuracy of the numerical method using an analytic plane wave solution in a poroelastic media. A computational experiment for an isotropic sandstone is also performed for an inviscid case.

The poroelastic model described in the chapter 3, 4 and 5 are only valid for the porous medium saturated with single phase fluid. To approximate a more realistic situation and to quantify the effect of capillary pressure on the wavefield, a system of poroelastic wave equation for two-phase fluid is studied in chapter 6. Studies presented in chapter 6 analyzed the dependence of the phase velocity and attenuation in rocks saturated with multi-phase fluids. Numerical simulations of wave propagation at varying capillary pressures are also presented. In the high-frequency range, as capillary pressure increases, the phase velocity of the P1 mode (fast P wave) increases and the velocities of the slow P modes (P2 and P3) decrease substantially. In the high-frequency range, the attenuation of the P1 and P3 modes decreases with capillary pressure, whereas the attenuation of the P2 modes increases. In the low-frequency range, the velocity of the P1 mode increases but remain constant up to the characteristic frequency. The velocity of the P2 mode decreases with increasing capillary pressure but increases gradually with frequency, whereas the velocity of the P3 mode has opposite characteristic than that of the P2 mode. The attenuation of the P1, P2 and P3 modes have little effect. Chapter 6 also validates the dispersion and attenuation relation with numerical solutions of the wave equations at varying capillary pressures. Moreover, velocity of the P1 mode of the wet-rock with respect to the gas saturation is compared with topology-based models such as the Hashin-Shtrickman one. The velocity obtained from the HS model over predicts the actual velocity due to the non-inclusion of the capillary pressure.

7.2 Scope for future work

There are various opportunity for future work based on the current research here.

7.2.1 Extension of rapid expansion method to pure viscoelastic media

The rapid expansion method presented in chapter 1 is applied for pure viscoacoustic media which does not model the shear wave effects. To enhance the accuracy of the physics of the modeling

a viscoelastic approximation of medium defined by a constant Q approach could be considered. Zhu and Carcione [45] presented a model which defines a model to incorporate the shear wave effects for a constant Q medium, defined by a time dependent relaxation function. The same model could be consider to solve it numerically by using REM and pseudo-spectral approaches to compute the time and spatial operator. Solving the viscoelastic model with REM is a prime opportunity for future work.

7.2.2 Extension of the study in chapter 5 for acousto-poroelastic media

The study carried out in chapters 3, 4 and 5 approximate the medium as poroelastic completely and solved it with highly accurate nodal DG method. This setup will not be valid to simulate the marine environment at local scale and the core-mantle boundary (CMB) at global scale, as one of the layers are fluid and approximated correctly by acoustic model. A novel opportunity of future would be an extension of the proposed formulation for the broad-band Biot's model and coupled acousto-poroelastic media.

7.2.3 Implementation of nodal discontinuous Galerkin finite element method for a poroelastic medium saturated with two phase fluids

The numerical solution of the poroelastic wave equation for a two-phase fluid system presented in chapter 6 is solved by using the a low order numerical scheme which is second order accurate. It will be highly desirable to solve this system using the nodal DG method presented in chapter 3 to achieve high accuracy. It will be also worthwhile to analyze the effect of stiffness present in the system in purview of DG implementation.

Bibliography

[1] E. Blanc, G. Chiavassa, and B. Lombard. Biot-JKD model: simulation of 1d transient poroelastic waves with fractional derivatives. *Journal of Computational Physics*, 237:1–20, 2013.

[2] J. Carcione and G. Quiroga-Goode. Some aspects of the physics and numerical modeling of biot compressional waves. *Journal of Computational Acoustics*, 3(04):261–280, 1995.

[3] J. Carcione. Wave propagation in anisotropic, saturated porous media: Plane-wave theory and numerical simulation. *The Journal of the Acoustical Society of America*, 99(5):2655–2666, 1996.

[4] J. de la Puente, M. Dumbser, M. Käser, and H. Igel. Discontinuous galerkin methods for wave propagation in poroelastic media. *Geophysics*, 73(5):T77–T97, 2008.

[5] C. Morency and J. Tromp. Spectral-element simulations of wave propagation in porous media. *Geophysical Journal International*, 175(1):301–345, 2008.

[6] J. Hesthaven and T. Warburton. *Nodal discontinuous Galerkin methods: algorithms, analysis, and applications*. Springer Science & Business Media, 2007.

[7] L.C. Wilcox, G. Stadler, C. Burstedde, and O. Ghattas. A high-order discontinuous Galerkin method for wave propagation through coupled elastic–acoustic media. *Journal of Computational Physics*, 229(24):9373–9396, 2010.

[8] M. Biot. Theory of propagation of elastic waves in a fluid-saturated porous solid. i. low frequency range. *The Journal of the acoustical Society of america*, 28(2):168–178, 1956.

[9] M. Biot. Theory of propagation of elastic waves in a fluid-saturated porous solid. ii. higher frequency range. *The Journal of the acoustical Society of america*, 28(2):179–191, 1956.

[10] M. Biot. Mechanics of deformation and acoustic propagation in porous media. *Journal of applied physics*, 33(4):1482–1498, 1962.

[11] J. Buchanan, R. Gilbert, A. Wirgin, and Y. Xu. *Marine acoustics: direct and inverse problems*, volume 84. Siam, 2004.

[12] R. Gilbert and Z. Lin. Acoustic field in a shallow, stratified ocean with a poro-elastic seabed. *ZAMM-Journal of Applied Mathematics and Mechanics/Zeitschrift für Angewandte Mathematik und Mechanik*, 77(9):677–688, 1997.

[13] S. Cowin. Bone poroelasticity. *Journal of biomechanics*, 32(3):217–238, 1999.

[14] H. Darcy. *Les Fontaines publiques de la ville de Dijon. Exposition et application des principes à suivre et des formules à employer dans les questions de distribution d'eau, etc.* V. Dalamont, 1856.

[15] K. von Terzaghi. Die berechnug der durchlassigkeit des tones aus dem verlauf der hydromechanischen spannungserscheinungen. *Sitzungsber. Akad. Wiss.(Wien). Math.-Naturwiss. Kl., Abt. Iia*, 132:125–138, 1923.

[16] M. Biot. General theory of three-dimensional consolidation. *Journal of applied physics*, 12(2):155–164, 1941.

[17] J. Carcione, C. Morency, and J. Santos. Computational poroelasticity A Review. *Geophysics*, 75(5):75A229–75A243, 2010.

[18] S. Garg, A Nayfeh, and A. Good. Compressional waves in fluid-saturated elastic porous media. *Journal of Applied Physics*, 45(5):1968–1974, 1974.

[19] B. Mikhailenko. Numerical experiment in seismic investigations. *JOURNAL OF GEOPHYSICS-ZEITSCHRIFT FUR GEOPHYSIK*, 58(1-3):101–124, 1985.

[20] S. Hassanzadeh. Acoustic modeling in fluid-saturated porous media. *Geophysics*, 56(4):424–435, 1991.

[21] N. Dai, A. Vafidis, and E. Kanasewich. Wave propagation in heterogeneous, porous media: A velocity-stress, finite-difference method. *Geophysics*, 60(2):327–340, 1995.

[22] G. Chiavassa and B. Lombard. Time domain numerical modeling of wave propagation in 2d heterogeneous porous media. *Journal of Computational Physics*, 230(13):5288–5309, 2011.

[23] J. Santos and E. Oreña. Elastic wave propagation in fluid-saturated porous media. part ii. the galerkin procedures. *ESAIM: Mathematical Modelling and Numerical Analysis*, 20(1):129–139, 1986.

[24] K. Attenborough, D. Berry, and Y. Chen. Acoustic scattering by near-surface inhomogeneities in porous media. Technical report, OPEN UNIV MILTON KEYNES (UNITED KINGDOM) FACULTY OF TECHNOLOGY, 1990.

[25] G. Degrande and G. De Roeck. Fft-based spectral analysis methodology for one-dimensional wave propagation in poroelastic media. *Transport in Porous Media*, 9(1-2):85–97, 1992.

[26] A. Naumovich. On finite volume discretization of the three-dimensional biot poroelasticity system in multilayer domains. *Computational Methods in Applied Mathematics Comput. Methods Appl. Math.*, 6(3):306–325, 2006.

[27] G. Lemoine, M. Ou, and R. LeVeque. High-resolution finite volume modeling of wave propagation in orthotropic poroelastic media. *SIAM Journal on Scientific Computing*, 35(1):B176–B206, 2013.

[28] G. Lemoine. Three-dimensional mapped-grid finite volume modeling of poroelastic-fluid wave propagation. *SIAM Journal on Scientific Computing*, 38(5):B808–B836, 2016.

[29] B. Dupuy, L. De Barros, S. Garambois, and J. Virieux. Wave propagation in heterogeneous porous media formulated in the frequency-space domain using a discontinuous galerkin method. *Geophysics*, 76(4):N13–N28, 2011.

[30] J. Buchanan and R. Gilbert. Determination of the parameters of cancellous bone using high frequency acoustic measurements ii: inverse problems. *Journal of Computational Acoustics*, 15(02):199–220, 2007.

[31] E. Kjartansson. Constant Q-wave propagation and attenuation. *Journal of Geophysical Research: Solid Earth*, 84(B9):4737–4748, 1979.

[32] J. Carcione. *Wave Fields in Real Media: Wave Propagation in Anisotropic, Anelastic, Porous and Electromagnetic Media*. Elsevier Science, 2014.

[33] M. Dablain. The application of high-order differencing to the scalar wave equation. *Geophysics*, 51(1):54–66, 1986.

[34] J. Etgen and J. Dellinger. Accurate wave-equation modeling. In *SEG Technical Program Expanded Abstracts 1989*, pages 494–497. Society of Exploration Geophysicists, 1989.

[35] K. Kelly, R. Ward, S. Treitel, and R. Alford. Synthetic seismograms: A finite-difference approach. *Geophysics*, 41(1):2–27, 1976.

[36] R. Alford, K. Kelly, and D. Boore. Accuracy of finite-difference modeling of the acoustic wave equation. *Geophysics*, 39(6):834–842, 1974.

[37] R. Pratt and M. Worthington. Inverse theory applied to multi-source cross-hole tomography. part 1: Acoustic wave-equation method. *Geophysical prospecting*, 38(3):287–310, 1990.

[38] J. Carcione, D. Kosloff, and R. Kosloff. Wave propagation simulation in a linear viscoacoustic medium. *Geophysical Journal International*, 93(2):393–401, 1988.

[39] J. Carcione, D. Kosloff, and R. Kosloff. Wave propagation simulation in a linear viscoelastic medium. *Geophysical Journal International*, 95(3):597–611, 1988.

[40] I. Štekl and R. Pratt. Accurate viscoelastic modeling by frequency-domain finite differences using rotated operators. *Geophysics*, 63(5):1779–1794, 1998.

[41] J. Carcione, F. Cavallini, F. Mainardi, and A. Hanyga. Time-domain modeling of constant-Q seismic waves using fractional derivatives. *Pure and Applied Geophysics*, 159(7-8):1719–1736, 2002.

[42] M. Caputo. *Elasticita e dissipazione*. Zanichelli, 1969.

[43] F. Mainardi. *Fractional calculus and waves in linear viscoelasticity: an introduction to mathematical models*. World Scientific, 2010.

[44] J. Carcione. A generalization of the Fourier pseudospectral method. *Geophysics*, 75(6):A53–A56, 2010.

[45] T. Zhu and J. Carcione. Theory and modelling of constant-Q P-and S-waves using fractional spatial derivatives. *Geophysical Journal International*, 196(3):1787–1795, 2013.

[46] J. Carcione, T. Zhu, S. Picotti, and D. Gei. Imaging septaria geobody in the boom clay using a Q-compensated reverse-time migration. *Netherlands Journal of Geosciences*, 95(3):283–291, 2016.

[47] R. Pestana and P. Stoffa. Time evolution of the wave equation using rapid expansion method. *Geophysics*, 75(4):T121–T131, 2010.

[48] J. Carcione, D. Kosloff, and R. Kosloff. Wave-propagation simulation in an elastic anisotropic (transversely isotropic) solid. *The Quarterly Journal of Mechanics and Applied Mathematics*, 41(3):319–346, 1988.

[49] I. Podlubny. *Fractional differential equations: an introduction to fractional derivatives, fractional differential equations, to methods of their solution and some of their applications*, volume 198. Elsevier, 1998.

[50] Michele Caputo, José M Carcione, and Fabio Cavallini. Wave simulation in biologic media based on the kelvin-voigt fractional-derivative stress-strain relation. *Ultrasound in medicine & biology*, 37(6):996–1004, 2011.

[51] J. Carcione. *Wave fields in real media: Wave propagation in anisotropic, anelastic, porous and electromagnetic media*, volume 38. Elsevier, 2007.

[52] R. LeVeque. *Finite volume methods for hyperbolic problems*, volume 31. Cambridge university press, 2002.

[53] T. Özdenvar and G. McMechan. Causes and reduction of numerical artefacts in pseudo-spectral wavefield extrapolation. *Geophysical Journal International*, 126(3):819–828, 1996.

[54] D. Kosloff and E. Baysal. Forward modeling by a Fourier method. *Geophysics*, 47(10):1402–1412, 1982.

[55] B. Fornberg. The pseudospectral method: Comparisons with finite differences for the elastic wave equation. *Geophysics*, 52(4):483–501, 1987.

[56] Y. Zhang, H. Zhang, and G. Zhang. A stable TTI reverse time migration and its implementation. *Geophysics*, 76(3):WA3–WA11, 2011.

[57] R. Soubaras and Y. Zhang. Two-step explicit marching method for reverse time migration. In *70th EAGE Conference and Exhibition incorporating SPE EUROPEC*, 2008.

[58] Y. Zhang and G. Zhang. One-step extrapolation method for reverse time migration. *Geophysics*, 74(4):A29–A33, 2009.

[59] D. Kosloff, A. Queiroz Filho, E. Tessmer, and A. Behle. Numerical solution of the acoustic and elastic wave equations by a new rapid expansion method. *Geophysical Prospecting*, 37(4):383–394, 1989.

[60] H. Tal-Ezer, D. Kosloff, and Z. Koren. An accurate scheme for seismic forward modelling. *Geophysical Prospecting*, 35(5):479–490, 1987.

[61] G. Zhan, R. Pestana, and P. Stoffa. Decoupled equations for reverse time migration in tilted transversely isotropic media. *Geophysics*, 77(2):T37–T45, 2012.

[62] H. Tal-Ezer. Spectral methods in time for hyperbolic equations. *SIAM Journal on Numerical Analysis*, 23(1):11–26, 1986.

[63] T. Zhu, J. Harris, and B. Biondi. Q-compensated reverse-time migration. *Geophysics*, 79(3):S77–S87, 2014.

[64] J. Sun, T. Zhu, and S. Fomel. Viscoacoustic modeling and imaging using low-rank approximation. *Geophysics*, 80(5):A103–A108, 2015.

[65] S. Fomel, L. Ying, and X. Song. Seismic wave extrapolation using lowrank symbol approximation. *Geophysical Prospecting*, 61(3):526–536, 2013.

[66] T. Zhu and J. Harris. Modeling acoustic wave propagation in heterogeneous attenuating media using decoupled fractional laplacians. *Geophysics*, 79(3):T105–T116, 2014.

[67] E. Stein. Harmonic analysis real-variable methods, orthogonality, and oscillatory integrals. *Bull. Amer. Math. Soc*, 36:505–521, 1999.

[68] T. Cormen, C. Leiserson, R. Rivest, and C. Stein. *Introduction to algorithms*. MIT press, 2009.

[69] M. Pippig. Pfft: An extension of fftw to massively parallel architectures. *SIAM Journal on Scientific Computing*, 35(3):C213–C236, 2013.

[70] O. Coussy. *Acoustics of porous media*. Editions Technip, 1987.

[71] J. Allard and N. Atalla. *Propagation of sound in porous media: modelling sound absorbing materials 2e*. John Wiley & Sons, 2009.

[72] A. Levander. Fourth-order finite-difference p-sv seismograms. *Geophysics*, 53(11):1425–1436, 1988.

[73] J. Virieux. P-Sv wave propagation in heterogeneous media: Velocity-stress finite-difference method. *Geophysics*, 51(4):889–901, 1986.

[74] T. Özdenvar and G. McMechan. Algorithms for staggered-grid computations for poroelastic, elastic, acoustic, and scalar wave equations. *Geophysical Prospecting*, 45(3):403–420, 1997.

[75] J. Grote, A. Schneebeli, and D. Schötzau. Discontinuous galerkin finite element method for the wave equation. *SIAM Journal on Numerical Analysis*, 44(6):2408–2431, 2006.

[76] D. Komatitsch and J. Vilotte. The spectral element method: an efficient tool to simulate the seismic response of 2d and 3d geological structures. *Bulletin of the seismological society of America*, 88(2):368–392, 1998.

[77] M. Käser, M. Dumbser, J. De La Puente, and H. Igel. An arbitrary high-order discontinuous galerkin method for elastic waves on unstructured meshes—iii. viscoelastic attenuation. *Geophysical Journal International*, 168(1):224–242, 2007.

[78] J. de la Puente, M. Käser, M. Dumbser, and H. Igel. An arbitrary high-order discontinuous galerkin method for elastic waves on unstructured meshes-iv. anisotropy. *Geophysical Journal International*, 169(3):1210–1228, 2007.

[79] R. Ye, M. de Hoop, C. Petrovitch, L. Pyrak-Nolte, and L. Wilcox. A discontinuous galerkin method with a modified penalty flux for the propagation and scattering of acousto-elastic waves. *Geophysical Journal International*, 205(2):1267–1289, 2016.

[80] M. Dumbser, C. Enaux, and E. Toro. Finite volume schemes of very high order of accuracy for stiff hyperbolic balance laws. *Journal of Computational Physics*, 227(8):3971–4001, 2008.

[81] S. Pride. Relationships between seismic and hydrological properties. In *Hydrogeophysics*, pages 253–290. Springer, 2005.

[82] N. Ward, T. Lähivaara, and S. Eveson. A discontinuous galerkin method for poroelastic wave propagation: The two-dimensional case. *Journal of Computational Physics*, 350:690–727, 2017.

[83] B. Cockburn and C. Shu. Runge–kutta discontinuous galerkin methods for convection-dominated problems. *Journal of scientific computing*, 16(3):173–261, 2001.

[84] M. Badiey, I. Jaya, and A. Cheng. Propagator matrix for plane wave reflection from inhomogeneous anisotropic poroelastic seafloor. *Journal of Computational Acoustics*, 2(01):11–27, 1994.

[85] Y. Zeng, J. He, and Q. Liu. The application of the perfectly matched layer in numerical modeling of wave propagation in poroelastic media. *Geophysics*, 66(4):1258–1266, 2001.

[86] R. Hunter. *Foundations of colloid science*. Oxford university press, 2001.

[87] P. Sahay. Natural field variables in dynamic poroelasticity. In *1994 SEG Annual Meeting*. Society of Exploration Geophysicists, 1994.

[88] V. Wheatley, H. Kumar, and P. Huguenot. On the role of riemann solvers in discontinuous galerkin methods for magnetohydrodynamics. *Journal of Computational Physics*, 229(3):660–680, 2010.

[89] J. Chan. Weight-adjusted discontinuous Galerkin methods: Matrix-valued weights and elastic wave propagation in heterogeneous media. *International Journal for Numerical Methods in Engineering*, 113(12):1779–1809, 2018.

[90] D.L. Johnson, J. Koplik, and R. Dashen. Theory of dynamic permeability and tortuosity in fluid-saturated porous media. *Journal of fluid mechanics*, 176:379–402, 1987.

[91] M. Stern, A. Bedford, and H. Millwater. Wave reflection from a sediment layer with depth-dependent properties. *The Journal of the Acoustical Society of America*, 77(5):1781–1788, 1985.

[92] T. Yamamoto and A. Turgut. Acoustic wave propagation through porous media with arbitrary pore size distributions. *The Journal of the Acoustical Society of America*, 83(5):1744–1751, 1988.

[93] J. Rosenbaum. Synthetic microseismograms: logging in porous formations. *Geophysics*, 39(1):14–32, 1974.

[94] A. Klöckner, T. Warburton, J. Bridge, and J. Hesthaven. Nodal discontinuous Galerkin methods on graphics processors. *Journal of Computational Physics*, 228(21):7863–7882, 2009.

[95] M. Ainsworth. Dispersive and dissipative behaviour of high order discontinuous Galerkin finite element methods. *Journal of Computational Physics*, 198(1):106–130, 2004.

[96] Q. Zhan, M. Zhuang, Y. Fang, Y. Hu, Y. Mao, W. Huang, R. Zhang, D. Wang, and Q. Liu. Full-anisotropic poroelastic wave modeling: a discontinuous Galerkin algorithm with a generalized wave impedance. *Computer Methods in Applied Mechanics and Engineering*, 346:288–311, 2019.

[97] J. Chan, R. Hewett, and T. Warburton. Weight-adjusted discontinuous Galerkin methods: curvilinear meshes. *SIAM Journal on Scientific Computing*, 39(6):A2395–A2421, 2017.

[98] E.D. Mercerat and N. Glinsky. A nodal high-order discontinuous Galerkin method for elastic wave propagation in arbitrary heterogeneous media. *Geophysical Journal International*, 201(2):1101–1118, 2015.

[99] J. Chan and T. Warburton. On the penalty stabilization mechanism for upwind discontinuous Galerkin formulations of first order hyperbolic systems. *Computers & Mathematics with Applications*, 74(12):3099–3110, 2017.

[100] H. Deresiewicz and R. Skalak. On uniqueness in dynamic poroelasticity. *Bulletin of the Seismological Society of America*, 53(4):783–788, 1963.

[101] B. Gurevich and M. Schoenberg. Interface conditions for Biot's equations of poroelasticity. *The Journal of the Acoustical Society of America*, 105(5):2585–2589, 1999.

[102] T. Hagstrom and T. Warburton. A new auxiliary variable formulation of high-order local radiation boundary conditions: corner compatibility conditions and extensions to first-order systems. *Wave motion*, 39(4):327–338, 2004.

[103] A. Modave, A. Atle, J. Chan, and T. Warburton. A GPU-accelerated nodal discontinuous Galerkin method with high-order absorbing boundary conditions and corner/edge compatibility. *International Journal for Numerical Methods in Engineering*, 112(11):1659–1686, 2017.

[104] J. Chan and T. Warburton. GPU-accelerated Bernstein–Bézier discontinuous Galerkin methods for wave problems. *SIAM Journal on Scientific Computing*, 39(2):A628–A654, 2017.

[105] K. Guo and J. Chan. Bernstein-Bézier weight-adjusted discontinuous Galerkin methods for wave propagation in heterogeneous media. *arXiv preprint arXiv:1808.08645*, 2018.

[106] H. Xiao and Z. Gimbutas. A numerical algorithm for the construction of efficient quadrature rules in two and higher dimensions. *Computers and Mathematics with Applications*, 59(2):663–676, 2010.

[107] J. Chan, R.J. Hewett, and T. Warburton. Weight-adjusted discontinuous Galerkin methods: wave propagation in heterogeneous media. *SIAM Journal on Scientific Computing*, 39(6):A2935–A2961, 2017.

[108] M Carpenter and C. Kennedy. Fourth-order $2n$-storage Runge-Kutta schemes. Technical Report NASA-TM-109112, NAS 1.15:109112, NASA Langley Research Center, 1994.

[109] J. Chan, Z. Wang, A. Modave, J.F. Remacle, and T. Warburton. GPU-accelerated discontinuous Galerkin methods on hybrid meshes. *Journal of Computational Physics*, 318:142–168, 2016.

[110] E. Toro. The HLL and HLLC Riemann solvers. In *Riemann Solvers and Numerical Methods for Fluid Dynamics*, pages 315–339. Springer, 1999.

[111] G. Strang. On the construction and comparison of difference schemes. *SIAM Journal of Numerical Analysis*, 5:506–517, 1968.

[112] K. Shukla, J. Chan, M. de Hoop, and P. Jaiswal. A weight-adjusted discontinuous galerkin method for the poroelastic wave equation: penalty fluxes and micro-heterogeneities. *arXiv preprint arXiv:1904.02578*, 2019.

[113] X. Zhu and G. McMechan. Numerical simulation of seismic responses of poroelastic reservoirs using Biot theory. *Geophysics*, 56(3):328–339, 1991.

[114] J. Carcione. Viscoelastic effective rheologies for modelling wave propagation in porous media. *Geophysical prospecting*, 46(3):249–270, 1998.

[115] J. Carcione and H. Helle. Numerical solution of the poroviscoelastic wave equation on a staggered mesh. *Journal of Computational Physics*, 154(2):520–527, 1999.

[116] M. Caputo. Linear models of dissipation whose Q is almost frequency independent—II. *Geophysical Journal International*, 13(5):529–539, 1967.

[117] T. Warburton. A low-storage curvilinear discontinuous Galerkin method for wave problems. *SIAM Journal on Scientific Computing*, 35(4):A1987–A2012, 2013.

[118] K. Terzaghi. The shearing resistance of saturated soils and the angle between the planes of shear. In *Proceedings of the 1st international conference on soil mechanics and foundation engineering*, volume 1, pages 54–56. Harvard University Press Cambridge, MA, 1936.

[119] J. Lu and A. Hanyga. Wave field simulation for heterogeneous porous media with singular memory drag force. *Journal of Computational Physics*, 208(2):651–674, 2005.

[120] J. Chan and T. Warburton. GPU-accelerated Bernstein–Bézier discontinuous Galerkin methods for wave problems. *SIAM Journal on Scientific Computing*, 39(2):A628–A654, 2017.

[121] T. Plona. Observation of a second bulk compressional wave in a porous medium at ultrasonic frequencies. *Applied Physics Letters*, 36(4):259–261, 1980.

[122] H Oura. Sound velocity in the snow cover. *Low Temperature Science. Series A, Physical Sciences*, 9:171–178, 1952.

[123] R. Stoll and G. Bryan. Wave attenuation in saturated sediments. *The Journal of the Acoustical Society of America*, 47(5B):1440–1447, 1970.

[124] S. Mochizuki. Attenuation in partially saturated rocks. *Journal of Geophysical Research: Solid Earth*, 87(B10):8598–8604, 1982.

[125] J. Santos, J. Corberó, and J. Douglas Jr. Static and dynamic behavior of a porous solid saturated by a two-phase fluid. *The Journal of the Acoustical Society of America*, 87(4):1428–1438, 1990.

[126] J. Santos, J. Douglas Jr, J. Corberó, and O. Lovera. A model for wave propagation in a porous medium saturated by a two-phase fluid. *The Journal of the Acoustical Society of America*, 87(4):1439–1448, 1990.

[127] M. Dejam, H. Hassanzadeh, and Z. Chen. Capillary forces between two parallel plates connected by a liquid bridge. *Journal of Porous Media*, 18(3):179–188, 2015.

[128] C. Ravazzoli, J. Santos, and J. Carcione. Acoustic and mechanical response of reservoir rocks under variable saturation and effective pressure. *The Journal of the Acoustical Society of America*, 113(4):1801–1811, 2003.

[129] J. Santos, P. Gauzellino, G. Savioli, and R. Martínez Corredor. Numerical simulation in applied geophysics. *Journal of Computer Science & Technology*, 13:137–142, 2013.

[130] J. Santos, P. Gauzellino, G. Savioli, and R. Martínez Corredor. *Numerical Simulation in Applied Geophysics*. Springer, 2016.

[131] J. Santos, G. Savioli, and R. Martínez Corredor. *Slow Waves in a Poroelastic Solid Saturated by Multiphase Fluids*. ASCE Library, 2017.

[132] J. Auriault, O. Lebaigue, and G. Bonnet. Dynamics of two immiscible fluids flowing through deformable porous media. *Transport in Porous Media*, 4(2):105–128, 1989.

[133] W. Lo, G. Sposito, and E. Majer. Wave propagation through elastic porous media containing two immiscible fluids. *Water Resources Research*, 41, W02025(2):W02025, 2005.

[134] J. Lu, A. Hanyga, and D. Jeng. A mixture-theory-based dynamic model for a porous medium saturated by two immiscible fluids. *Journal of Applied Geophysics*, 62(2):89–106, 2007.

[135] Y. Tian, J. Ma, and H. Yang. Wavefield simulation in porous media saturated with two immiscible fluids. *Applied Geophysics*, 7(1):57–65, 2010.

[136] Q. Qi, T. Müller, B. Gurevich, S. Lopes, M. Lebedev, and E. Caspari. Quantifying the effect of capillarity on attenuation and dispersion in patchy-saturated rocks. *Geophysics*, 79(5):WB35–WB50, 2014.

[137] J. Liu, T. Müller, Q. Qi, M. Lebedev, and W. Sun. Velocity-saturation relation in partially saturated rocks: Modelling the effect of injection rate changes. *Geophysical Prospecting*, 64(4):1054–1066, 2016.

[138] G. Papageorgiou and M. Chapman. Wave-propagation in rocks saturated by two immiscible fluids. *Geophysical Journal International*, 209(3):1761–1767, 2017.

[139] J. Carcione, F. Cavallini, J. Santos, C. Ravazzoli, and P. Gauzellino. Wave propagation in partially saturated porous media: simulation of a second slow wave. *Wave Motion*, 39(3):227–240, 2004.

[140] J. Santos, C. Ravazzoli, P. Gauzellino, J. Carcione, and F. Cavallini. Simulation of waves in poro-viscoelastic rocks saturated by immiscible fluids: numerical evidence of a second slow wave. *Journal of Computational Acoustics*, 12(01):1–21, 2004.

[141] J. Berryman. Confirmation of biot's theory. *Applied Physics Letters*, 37(4):382–384, 1980.

[142] M. Jain. *Numerical solution of differential equations*. Wiley Eastern Ltd., 1979.

[143] J. Carcione and G. Seriani. Wave simulation in frozen porous media. *Journal of Computational Physics*, 170(2):676–695, 2001.

[144] J. Carcione, G. Herman, and A. Ten Kroode. Seismic modeling. *Geophysics*, 67(4):1304–1325, 2002.

[145] O. Kelder and D. Smeulders. Observation of the biot slow wave in water-saturated nivelsteiner sandstone. *Geophysics*, 62(6):1794–1796, 1997.

[146] S. Domenico. Effect of brine-gas mixture on velocity in an unconsolidated sand reservoir. *Geophysics*, 41(5):882–894, 1976.

[147] S. Domenico. Elastic properties of unconsolidated porous sand reservoirs. *Geophysics*, 42(7):1339–1368, 1977.

[148] C. Gomez, J. Dvorkin, and T. Vanorio. Laboratory measurements of porosity, permeability, resistivity, and velocity on fontainebleau sandstones. *Geophysics*, 75:E191–E204, 2010.

[149] C. Ravazzoli and J. Santos. A theory for wave propagation in porous rocks saturated by two-phase fluids under variable pressure conditions. *Bolletino di Geofisica Teorica ed Applicata*, 46:261–285, 2005.

[150] J. Cai, W. Wei, X. Hu, and D. Wood. Electrical conductivity models in saturated porous media: a review. *Earth-Science Reviews*, 171:419–433, 2017.

[151] J. Cai and B. Yu. A discussion of the effect of tortuosity on the capillary imbibition in porous media. *Transport in Porous Media*, 89:251–263, 09 2011.

[152] J. Cai, B. Yu, M. Zou, and L. Luo. Fractal characterization of spontaneous co-current imbibition in porous media. *Energy & Fuels*, 24(3):1860–1867, 2010.

[153] F. Gassmann. Uber die elastizitat poroser medien. *Vierteljahrsschrift der Naturforschenden Geselschaft in Zürich*, 96:1–23, 1951.

[154] Z. Hashin and S. Shtrikman. A variational approach to the theory of the elastic behaviour of multiphase materials. *Journal of the Mechanics and Physics of Solids*, 11(2):127–140, 1963.

[155] P. Kepkay and R. Cooke. Velocity of sound as a function of bubble distribution in gas-bearing sediments. *Geophysical Research Letters*, 5(12):1071–1073, 1978.

[156] L. Macias, G. Savioli, J. Santos, J. Carcione, and D. Gei. Analysis of capillary pressure effect on the seismic response of a co 2-storage site applying multiphase flow and wave propagation simulators. *International Journal of Greenhouse Gas Control*, 39:335–348, 2015.

[157] Q. Meng, H. Liu, and J. Wang. A critical review on fundamental mechanisms of spontaneous imbibition and the impact of boundary condition, fluid viscosity and wettability. *Advances in Geo-energy Research*, 1:1–17, 2017.

[158] M. Abramowitz and I. Stegun. Handbook of mathematical functions. dover, new york, 1972.

[159] Michele Caputo, José M Carcione, and Fabio Cavallini. Wave simulation in biologic media based on the kelvin-voigt fractional-derivative stress-strain relation. *Ultrasound in medicine & biology*, 37(6):996–1004, 2011.

[160] D. Bland. *The theory of linear viscoelasticity*. Pergamon Press, 1960.

[161] P. Houston, C. Schwab, and E. Süli. Discontinuous *hp*-finite element methods for advection-diffusion-reaction problems. *SIAM Journal on Numerical Analysis*, 39(6):2133–2163, 2002.

[162] T. Warburton and J.S. Hesthaven. On the constants in $hp-$finite element trace inverse inequalities. *Computer methods in applied mechanics and engineering*, 192:2765–2773, 2003.

[163] V. Dolejší and M. Feistauer. Discontinuous Galerkin methods. *Analysis and Applications to Compressible Flow. Springer Series in Computational Mathematics*, 48, 2015.

[164] E. Süli and D. Mayers. *An introduction to numerical analysis*. Cambridge university press, 2003.

Appendix A

Analytical solution, phase velocity and attenuation of viscoacoustic wave equation

A.1 Convergence and stability of scheme

We prove the convergence criteria of $M > \Delta t R$ for series in equation 2.13. We rewrite 2.13 as

$$H_M(\phi\Delta t) = \sum_{k=0}^{M} C_{2k} J_{2k}(R\Delta t) L_{2k}\left(\frac{i\phi}{R}\right) \ . \tag{1.1}$$

The accuracy of $H_M(\phi\Delta t)$, a polynomial approximation, is defined by its asymptotic rate of convergence as $M \to \infty$. Consider the interval $[m_0, \infty)$, where the asymptotic behavior of equation (4.5) is defined. Thus to a prescribed accuracy, the minimal $M \in [m_0, \infty)$, should be $> m_0$ to resolve all the Fourier modes. This is a necessary and sufficient condition as proven by [62]. Now we can derive the value of m_0 for equation (4.5). It is a well known fact thet the Bessel's function of order k, defined for a variable x as $J_k(x)$, converges to zero exponentially fast if $k > x$ [158]. Thus to resolve all the Fourier modes the interval of asymptotic behavior would be $[z, \infty]$, with $m_0 = x$. Thus, it proves that $H_M(\phi\Delta t)$ will converge exponentially if $k > \Delta t R$.

A.2 Green's function and analytical solution

Equation of motion for wave propagation in anelastic media is expressed as [32, p. 101]

$$\partial_t^2 \epsilon = \frac{1}{\rho}\Delta\sigma. \tag{1.2}$$

Stress-strain relation in anelastic medium is expressed as

$$\sigma = \rho b \partial_t^{2-\beta} \epsilon + f \ , \tag{1.3}$$

where $b = \left(\frac{M_0}{\rho}\right) \omega_0^{-2\gamma}$.
Substituting equation (1.3) in equation (1.2) we get

$$\partial_t^2 \epsilon = b \partial_t^{2-\beta} \Delta\epsilon + \frac{\Delta f}{\rho} \ . \tag{1.4}$$

=Taking Fourier transform of equation (1.4)

$$(i\omega)^2 \epsilon = b(i\omega)^{2-\beta} \Delta\epsilon + \Delta f. \tag{1.5}$$

Using equation (3.8), $b(i\omega)^{2-\beta} = M(\omega)$, we rewrite equation (1.4) as

$$\Delta\epsilon + p^2 \epsilon = -\frac{\Delta f}{M(\omega)}, \tag{1.6}$$

where $p = \frac{\omega}{v_c}$ is wave number and $v_c = \sqrt{\frac{M(\omega)}{\rho}}$ is complex phase velocity.
If v_c is real the medium is lossless. Solution to lossless acoustic equation $(\Delta + p^2)G = -8\delta(r)$ is the Green function G [51] and can be expressed as

$$G(x, y, x_0, y_0, \omega, c_0) = -2iH_0^{(2)}\left(\frac{\omega r}{c_0}\right) \ , \tag{1.7}$$

where c_0 is real velocity in lossless media, H_0^2 is zero order Henkel function of second kind. Coordinate pair (x_0, y_0) is location of source and $r = \sqrt{(x - x_0)^2 + (y - y_0)^2}$. [159] computed anelastic solution by invoking the correspondence principle [160]. According to the correspondence principle, solution in lossy media can be obtained by by substituting c_0 in equation (1.7) with v_c. Thus Green function for strain is

$$G_\epsilon = \frac{\Delta G}{M(\omega)}. \tag{1.8}$$

Since $\Delta G = -p^2 G$ away from the source and $\sigma = M(\omega)\epsilon$, then Green's function for the stress can be expressed as

$$G_\sigma = M(\omega) G_\epsilon = -p^2 G. \tag{1.9}$$

To ensure the inverse Fourier Transform of Green's function to be real, we will set $G(-\omega) = G^*(\omega)$, where $*$ is complex conjugate. Thus the frequency domain solution for stress is given by $\sigma(x, y, x_0, y_0, \omega) = \frac{1}{8} G_\sigma(\omega) f(\omega)$, where $f(\omega)$ is frequency domain representation of $f(t)$. As Henkel function has singularity at $\omega = 0$, we will assume $G(\omega = 0) = 0$.

A.3 Phase velocity and attenuation

The analysis of he propagation characteristic of the medium, defined by equation (3.8), is performed. The phase velocity (v_p) and attenuation factor (α), in a medium of constant properties, for a plane wave, defined by $\sigma = \exp\left[\mathrm{I}\left(\omega t - k_x x - k_z z\right)\right]$, are

$$v_p = \left[\cos\left(\frac{\pi\gamma}{2}\right)\right]^{-1} \left(\frac{\omega}{\omega_0}\right) c \tag{1.10}$$

$$\alpha = \frac{\omega}{c} \left(\frac{\omega_0}{\omega}\right)^{\gamma} \sin\left(\frac{\pi\gamma}{2}\right) \ . \tag{1.11}$$

Appendix B

Operator splitting, max wave speed of poroelastic waves and system of poroacoustic wave equation

B.1 Solution of the stiff part

The system of equations represented by (3.47) is expressed as

$$\partial_t v_x = -\frac{\eta}{\kappa_1}\beta_{12}^{(1)} q_x, \tag{2.1}$$

$$\partial_t v_z = -\frac{\eta}{\kappa_3}\beta_{12}^{(3)} q_z, \tag{2.2}$$

$$\partial_t q_x = -\frac{\eta}{\kappa_1}\beta_{22}^{(1)} q_x, \tag{2.3}$$

$$\partial_t q_z = -\frac{\eta}{\kappa_3}\beta_{22}^{(3)} q_z. \tag{2.4}$$

The solution of equations (2.1)-(2.4) is given as

$$v_x = v_x^n + \frac{\beta_{12}^{(1)}}{\beta_{22}^{(1)}}[\exp\left(-\frac{\eta}{\kappa_1}\beta_{22}^{(1)} dt\right) - 1]q_x^n, \tag{2.5}$$

$$v_z = v_z^n + \frac{\beta_{12}^{(3)}}{\beta_{22}^{(3)}}[\exp\left(-\frac{\eta}{\kappa_3}\beta_{22}^{(3)} dt\right) - 1]q_z^n, \tag{2.6}$$

$$q_x = \exp\left(-\frac{\eta}{\kappa_1}\beta_{22}^{(1)} dt\right) q_x^n, \tag{2.7}$$

$$q_z = \exp\left(-\frac{\eta}{\kappa_3}\beta_{22}^{(3)} dt\right) q_z^n. \tag{2.8}$$

B.2 Computation of λ in (3.57)

A plane-wave solution for the particle velocity vector $V = [v_x, v_z, q_z, q_z]^T$ is

$$\mathbf{V} = \mathbf{V_0} \exp[\mathrm{i}(\mathbf{k}.\mathbf{x} - \omega t)], \tag{2.9}$$

where $\mathbf{V_0}$ is a constant complex vector and $\mathbf{k}$ is wave vector. Substituting (2.9) in (3.1)-(3.4) and (3.20)-(3.23) , we recover

$$\left(\mathbf{\Gamma}^{-1} \cdot \mathbf{L} \cdot \mathbf{C} - V\mathbf{I_4}\right).\mathbf{V} = 0, \tag{2.10}$$

where

$$\mathbf{\Gamma} = \begin{bmatrix} \rho & 0 & \rho_f & 0 \\ 0 & \rho & 0 & \rho_f \\ \rho_f & 0 & \mathrm{i}Y_1(-\omega)/\omega & 0 \\ 0 & \rho_f & 0 & \mathrm{i}Y_3(-\omega)/\omega \end{bmatrix}, \quad \mathbf{L} = \begin{bmatrix} l_x & 0 & l_z & 0 \\ 0 & l_z & l_x & 0 \\ 0 & 0 & 0 & l_x \\ 0 & 0 & 0 & l_z \end{bmatrix}$$

$$\mathbf{C} = \begin{bmatrix} l_x c^u_{11} & l_z c^u_{13} & \alpha_1 M l_x & \alpha_1 M l_z \\ l_x c^u_{13} & l_z c^u_{33} & \alpha_3 M l_x & \alpha_3 M l_z \\ l_z c^u_{55} & l_x c^u_{55} & 0 & 0 \\ \alpha_1 M l_x & \alpha_3 M l_z & M l_x & M l_z \end{bmatrix},$$

with $Y_i(\omega) = \mathrm{i}\omega m_i + \eta/\kappa_i$ and l_x and l_z being direction cosines and $V = \dfrac{\omega^2}{k^2}$.

Term $\mathbf{V}$ in (2.10) represents the phase velocity of waves and can be computed by adopting the approach for eigenvalue computation. Thus

$$\lambda_i = (\mathrm{Re}(1/V_i)) \quad \text{for} \quad i = 1...4,$$
$$\text{and} \quad \lambda = \max(\lambda_i)$$

Energy velocity $\mathbf{V_e}$ can be computed from

$$\mathbf{k^T} \cdot \mathbf{V_e} = \mathbf{V}. \tag{2.11}$$

B.3 System of poroacoustic wave equation

This system is

$$\partial_t \mathbf{q_p} + \mathbf{A_{1p}}\partial_x \mathbf{q_p} + \mathbf{B_{1p}}\partial_x \mathbf{q_p} = \mathbf{D_{1p}}\mathbf{q_p} + \mathbf{f_p}, \tag{2.12}$$

where

$$\mathbf{q_p} = [v_x \; v_z \; q_x \; q_z \; p \; p_f]^T,$$

with p being the bulk pressure, p_f is fluid pressure, v'^s and q'^s are solid and fluid particle velocity (relative to solid). $\mathbf{A_{1p}}$, $\mathbf{B_{1p}}$ and $\mathbf{D_{1p}}$ are defined as

$$\mathbf{A_{1p}} = -\begin{bmatrix} 0 & 0 & 0 & 0 & \beta_{11} & \beta_{12} \\ 0 & 0 & 0 & 0 & 0 & 0 \\ 0 & 0 & 0 & 0 & -\beta_{21} & -\beta_{22} \\ 0 & 0 & 0 & 0 & 0 & 0 \\ -H & 0 & -C & 0 & 0 & 0 \\ -C & 0 & -M & 0 & 0 & 0 \end{bmatrix},$$

$$\mathbf{B_{1p}} = -\begin{bmatrix} 0 & 0 & 0 & 0 & 0 & 0 \\ 0 & 0 & 0 & 0 & \beta_{11} & \beta_{12} \\ 0 & 0 & 0 & 0 & 0 & 0 \\ 0 & 0 & 0 & 0 & -\beta_{21} & -\beta_{22} \\ 0 & -H & 0 & -C & 0 & 0 \\ 0 & -C & 0 & -M & 0 & 0 \end{bmatrix},$$

$$\mathbf{D_{1p}} = -\begin{bmatrix} 0 & 0 & \frac{\eta}{\kappa}\beta_{12} & 0 & 0 & 0 \\ 0 & 0 & 0 & \frac{\eta}{\kappa}\beta_{12} & 0 & 0 \\ 0 & 0 & -\frac{\eta}{\kappa}\beta_{22} & 0 & 0 & 0 \\ 0 & 0 & 0 & -\frac{\eta}{\kappa}\beta_{22} & 0 & 0 \\ 0 & 0 & 0 & 0 & 0 & 0 \\ 0 & 0 & 0 & 0 & 0 & 0 \end{bmatrix},$$

where β's, H, C and M are dependent on the solid bulk modulus (K_s), the fluid bulk modulus (K_f), the solid density (ρ_s), the porosity (ϕ), the permeability (κ), the fluid density (ρ_f) and the

viscosity (η) of the medium, elaborately expressed in [2].

Appendix C

Weight-adjusted discontinuous Galerkin method

C.1 Matrix weight-adjusted inner products

Let $D^{\alpha}\boldsymbol{v}$ denote the component-wise differentiation of $\boldsymbol{v}$ with respect to a $d-$dimensional multi-index α. Then, vector L^p Soblev norms for $\boldsymbol{v}(\boldsymbol{x}) \in \mathbb{R}^d$ can be defined as [89]

$$|\boldsymbol{v}|^p_{W^{k,p}} = \sum_{i=1}^{m} |\boldsymbol{v}_i|^p_{W^{k,p}}, \qquad ||\boldsymbol{v}||^p_{W^{k,p}} = \sum_{i=1}^{m} ||\boldsymbol{v}_i||^p_{W^{k,p}} \qquad 1 \leq p \leq \infty,$$

$$|\boldsymbol{v}|_{W^{k,\infty}} = \max_i |\boldsymbol{v}_i|_{W^{k,\infty}}, \qquad ||\boldsymbol{v}||_{W^{k,\infty}} = \max_i ||\boldsymbol{v}_i||_{W^{k,\infty}},$$

where $W^{k,p}$ and $W^{k,\infty}$ are the Sobolev spaces [104].

Let $\boldsymbol{W}(\boldsymbol{x})$ be a matrix-valued weight function which is pointwise symmetric positive definite

$$0 < w_{min} \leq ||\boldsymbol{W}(\boldsymbol{x})||_2 \leq w_{max} < \infty, \quad 0 < \tilde{w}_{min} \leq ||\boldsymbol{W}^{-1}(\boldsymbol{x})||_2 \leq \tilde{w}_{max} < \infty, \qquad \forall \boldsymbol{x} \in \Omega,$$

where $||\boldsymbol{W}(\boldsymbol{x})||_2$ is matrix 2-norm.

The k^{th} order Sobolev norm for $\boldsymbol{W}(\boldsymbol{x})$ is defined as [89]

$$||\boldsymbol{W}(\boldsymbol{x})||^p_{k,p,\infty} = \sum_{|\alpha| \leq k} \sup_x ||D^{\alpha}\boldsymbol{W}(\boldsymbol{x})||^p_p,$$

where $||D^{\alpha}\boldsymbol{W}(\boldsymbol{x})||^p_p$ is matrix $p-$norm.

C.2 Weight-adjusted approximations with matrix weights

Let $\Pi_N \boldsymbol{u}$ defined as L^2 projection applied to each component of the vector-valued function $\boldsymbol{u}$. We then define the operator $T_{\boldsymbol{W}}$ as [89]

$$T_{\boldsymbol{W}} \boldsymbol{v} = \Pi_N(\boldsymbol{W}\boldsymbol{v}).$$

T_W^{-1} is defined implicitly via [89]

$$\left(\boldsymbol{W} T_{\boldsymbol{W}}^{-1}\boldsymbol{v}, \boldsymbol{\delta v}\right)_{L^2(D^k)} = (\boldsymbol{v}, \boldsymbol{\delta v})_{L^2(D^k)}, \qquad \forall \boldsymbol{\delta v} \in (P^N(D^k))^m.$$

Lemma 1. *Let Π_N denote the component-wise L^2 projection and $\boldsymbol{W} \in (L^\infty)^{m\times m}$. Then $T_{\boldsymbol{W}}$ satisfies the following properties:*

1. $T_{\boldsymbol{W}}^{-1} T_{\boldsymbol{W}} = \Pi_N$
2. $\Pi_N T_{\boldsymbol{W}}^{-1} = \boldsymbol{T}_{\boldsymbol{W}}^{-1} = T_{\boldsymbol{W}}^{-1}$
3. $||T_{\boldsymbol{W}}^{-1}||_{L^2(D^k)} \leq \tilde{w}_{\max}$.
4. $(T_W^{-1}\boldsymbol{v}, \boldsymbol{w})_{L^2(D^k)}$ *forms an inner product on $(P^N)^m \times (P^N)^m$, which is equivalent to the L^2 inner product with equivalence constants $C_1 = \tilde{w}_{\min},\ C_2 = \tilde{w}_{\max}$.*

The proof of Lemma 1 is given in detail in [89].

C.3 Convergence analysis of WADG scheme for poroelastic wave equations

Using the results in Section 4.2, we can extend the semi-discrete convergence analysis in [89, 117, 161] in to linear poroelastic wave propagation on meshes of affine elements. Let $\boldsymbol{U}$ and $\boldsymbol{U}_h$ represent the exact and discrete WADG solutions, respectively. We assume that $\boldsymbol{U}$ and $\dfrac{\partial \boldsymbol{U}}{\partial t}$ are sufficiently regular such that

$$\|\boldsymbol{U}\|_{W^{N+1,2}(\Omega_h)} < \infty, \qquad \left\|\frac{\partial \boldsymbol{U}}{\partial t}\right\|_{W^{N+1,2}(\Omega_h)} < \infty,$$

with $\|\boldsymbol{U}\|^2_{W^{N+1,2}(\Omega_h)} = \sum_k \|\boldsymbol{U}\|^2_{W^{N+1,2}(D^k)}$.

The WADG formulation can be written as

$$\left(T^{-1}_{\boldsymbol{A}_0^{-1}} \frac{\partial \boldsymbol{U}}{\partial t}, \boldsymbol{V}\right)_{L^2(\Omega)} + a(\boldsymbol{U}, \boldsymbol{V}) + b(\boldsymbol{U}, \boldsymbol{V}) = (\boldsymbol{f}, \boldsymbol{V}),$$

$$a(\boldsymbol{U},\boldsymbol{V}) = \sum_{D^k\in\Omega_h}\left(-\left(\sum_{i=1}^{d}\boldsymbol{\tau},\boldsymbol{A}_i\frac{\partial \boldsymbol{g}}{\partial \boldsymbol{x}_i}\right)_{L^2(D^k)} + \left(\sum_{i=1}^{d}\boldsymbol{A}_i\frac{\partial \boldsymbol{v}}{\partial \boldsymbol{x}_i},\boldsymbol{g}\right)_{L^2(D^k)}\right),$$

$$b(\boldsymbol{U},\boldsymbol{V}) = \sum_{D^k\in\Omega_h}\left(\left\langle \boldsymbol{A}_n^T\{\{\boldsymbol{\tau}\}\} + \frac{\alpha_{\boldsymbol{v}}}{2}\boldsymbol{A}_n^T\boldsymbol{A}_n[\![\boldsymbol{v}]\!],\boldsymbol{g}\right\rangle_{L^2(D^k)} + \left\langle \frac{1}{2}\boldsymbol{A}_n[\![\boldsymbol{v}]\!] + \frac{\alpha_{\boldsymbol{\tau}}}{2}\boldsymbol{A}_n\boldsymbol{A}_n^T[\![\boldsymbol{\tau}]\!],\boldsymbol{h}\right\rangle_{L^2(D^k)} - (\boldsymbol{D}\boldsymbol{v},\boldsymbol{g})_{L^2(D^k)}\right)$$

where $\boldsymbol{A}_0(\boldsymbol{x}) = \mathrm{diag}(\boldsymbol{Q}_s,\boldsymbol{Q}_v)$, $\boldsymbol{U}$ and $\boldsymbol{V}$ are group variables, defined as $\boldsymbol{U} = (\boldsymbol{\tau},\boldsymbol{v})$ and $\boldsymbol{V} = (\boldsymbol{h},\boldsymbol{g}) \in (V_h(\Omega_h))^d \times (V_h(\Omega_h))^{N_d}$.

The DG formulation in (4.14) is consistent and thus

$$\left(\boldsymbol{A}_0^{-1}\frac{\partial \boldsymbol{U}}{\partial t},\boldsymbol{V}\right)_{L^2(\Omega)} + a(\boldsymbol{U},\boldsymbol{V}) + b(\boldsymbol{U},\boldsymbol{V}) = (\boldsymbol{f},\boldsymbol{V}), \tag{3.1}$$

$$\left(T^{-1}_{\boldsymbol{A}_0^{-1}}\frac{\partial \boldsymbol{U}_h}{\partial t},\boldsymbol{V}\right)_{L^2(\Omega)} + a(\boldsymbol{U}_h,\boldsymbol{V}) + b(\boldsymbol{U}_h,\boldsymbol{V}) = (\boldsymbol{f},\boldsymbol{V}), \tag{3.2}$$

$\forall\ \boldsymbol{V} \in (V_h(\Omega_h))^d \times (V_h(\Omega_h))^{N_d}$. We decompose the error $\boldsymbol{U}-\boldsymbol{U}_h$ into a projection error $\boldsymbol{\epsilon}$ and a discretization error $\boldsymbol{\eta}$.

$$\boldsymbol{U}-\boldsymbol{U}_h = (\Pi_N\boldsymbol{U}-\boldsymbol{U}_h) - (\Pi_N\boldsymbol{U}-\boldsymbol{U}) = \boldsymbol{\eta}-\boldsymbol{\epsilon}.$$

We assume that $\boldsymbol{U}_h(\boldsymbol{x},0)$ is the L^2 projection of the exact initial condition, such that $\boldsymbol{\eta}|_{t=0} = 0$. We also introduce a consistency error $\delta = \boldsymbol{A}_0\boldsymbol{U} - T^{-1}_{\boldsymbol{A}_0^{-1}}\boldsymbol{U}$ resulting from the approximation of $\boldsymbol{A}_0\boldsymbol{U}$ by a weight-adjusted inner product

$$\boldsymbol{A}_0{}^{-1}\frac{\partial \boldsymbol{U}}{\partial t} - T^{-1}_{\boldsymbol{A}_0^{-1}}\frac{\partial \boldsymbol{U}_h}{\partial t} = \frac{\partial}{\partial t}\left(\boldsymbol{A}_0\boldsymbol{U} - T^{-1}_{\boldsymbol{A}_0^{-1}}\boldsymbol{U}\right) + \frac{\partial}{\partial t}T^{-1}_{\boldsymbol{A}_0^{-1}}(\Pi_N\boldsymbol{U}-\boldsymbol{U}_h) = \frac{\partial \delta}{\partial t} + \frac{\partial}{\partial t}\left(T^{-1}_{\boldsymbol{A}_0^{-1}}\boldsymbol{\eta}\right),$$

where we have used that $T^{-1}_{\boldsymbol{A}_0^{-1}}\Pi_N$. Subtracting the DG and WADG formulations in (3.1) and (3.2) and setting $\boldsymbol{V} = \boldsymbol{\eta}$ yields

$$\frac{1}{2}\frac{\partial}{\partial t}\left(T^{-1}_{\boldsymbol{A}_0^{-1}}\boldsymbol{\eta},\boldsymbol{\eta}\right)_{L^2(\Omega)} + b(\boldsymbol{\eta},\boldsymbol{\eta}) = \left(-\frac{\partial \boldsymbol{\delta}}{\partial t},\boldsymbol{\eta}\right)_{L^2(\Omega)} + a(\boldsymbol{\epsilon},\boldsymbol{\eta}) + b(\boldsymbol{\epsilon},\boldsymbol{\eta}), \tag{3.3}$$

where we have used that $a(\boldsymbol{\eta},\boldsymbol{\eta}) = 0$ from skew-symmetry. We bound $a(\boldsymbol{\epsilon},\boldsymbol{\eta}) + b(\boldsymbol{\epsilon},\boldsymbol{\eta})$ in (3.3) by integrating by parts the stress equation and using the component-wise L^2 orthogonality of $\boldsymbol{\epsilon}$ to

derivatives of $\boldsymbol{\eta}$. This reduces to

$$
\begin{aligned}
&\Bigg| \sum_{D^k \in \Omega_h} \Bigg(\Big\langle \boldsymbol{A}_n^T \{\{ \boldsymbol{\epsilon}_\tau \}\} + \frac{\alpha_{\boldsymbol{v}}}{2} \boldsymbol{A}_n^T \boldsymbol{A}_n [\![\boldsymbol{\epsilon}_v]\!], \boldsymbol{\eta}_v \Big\rangle_{L^2(\partial D^k)} + \Big\langle \boldsymbol{A}_n \{\{ \boldsymbol{\epsilon}_v \}\} + \frac{\alpha_{\boldsymbol{\tau}}}{2} \boldsymbol{A}_n \boldsymbol{A}_n^T [\![\boldsymbol{\epsilon}_{\boldsymbol{\tau}}]\!], \boldsymbol{\eta}_\tau \Big\rangle_{L^2(\partial D^k)} \\
&\qquad - (\boldsymbol{D} \boldsymbol{\epsilon}_v, \boldsymbol{\epsilon}_v)_{L^2(D^k)} \Bigg) \Bigg| \\
&\qquad = \frac{1}{2} \sum_{D^k \in \Omega_h} \Bigg(\Big\langle \{\{ \boldsymbol{\epsilon}_\tau \}\} - \frac{\alpha_{\boldsymbol{v}}}{2} \boldsymbol{A}_n [\![\boldsymbol{\epsilon}_v]\!], \boldsymbol{A}_n [\![\boldsymbol{\eta}_v]\!] \Big\rangle_{L^2(\partial D^k)} + \Big\langle \{\{ \boldsymbol{\epsilon}_v \}\} - \frac{\alpha_{\boldsymbol{\tau}}}{2} \boldsymbol{A}_n^T [\![\boldsymbol{\epsilon}_\tau]\!], \boldsymbol{A}_n^T [\![\boldsymbol{\eta}_\tau]\!] \Big\rangle_{L^2(\partial D^k)} \\
&\qquad - (\boldsymbol{D} \boldsymbol{\epsilon}_v, \boldsymbol{\epsilon}_v)_{L^2(D^k)} \Bigg) \\
&\qquad \leq \frac{1}{2} \sum_{D^k \in \Omega_h} \Big\| \{\{ \boldsymbol{\epsilon}_\tau \}\} - \frac{\alpha_{\boldsymbol{v}}}{2} \boldsymbol{A}_n [\![\boldsymbol{\epsilon}_v]\!] \Big\|_{L^2(\partial D^k)} \| \boldsymbol{A}_n [\![\boldsymbol{\eta}_v]\!] \|_{L^2(\partial D^k)} \\
&\qquad + \Big\| \{\{ \boldsymbol{\epsilon}_v \}\} - \frac{\alpha_{\boldsymbol{\tau}}}{2} \boldsymbol{A}_n^T [\![\boldsymbol{\epsilon}_\tau]\!] \Big\|_{L^2(\partial D^k)} \Big\| \boldsymbol{A}_n^T [\![\boldsymbol{\eta}_\tau]\!] \Big\|_{L^2(\partial D^k)} + \| \boldsymbol{D} \|_{L^\infty(D^k)} \| \boldsymbol{\epsilon}_v \|_{L^2(D^k)} \\
&\qquad \leq C_\tau \sum_{D^k \in \Omega_h} \Bigg(\| \boldsymbol{\epsilon} \|_{L^2(\partial D^k)} \Big(\frac{\alpha_{\boldsymbol{v}}}{2} \| \boldsymbol{A}_n [\![\boldsymbol{\eta}_v]\!] \|^2_{L^2(\partial D^k)} + \frac{\alpha_{\boldsymbol{\tau}}}{2} \Big\| \boldsymbol{A}_n^T [\![\boldsymbol{\eta}_\tau]\!] \Big\|^2_{L^2(\partial D^k)} \Big)^{1/2} + \| \boldsymbol{D} \|_{L^\infty(D^k)} \| \boldsymbol{\epsilon} \|_{L^2(D^k)} \Bigg)
\end{aligned}
$$

where C_τ is maximum of $(\alpha_{\boldsymbol{\tau}}, \alpha_{\boldsymbol{v}})$ and we have also used the property of negative semi-definite matrix $\boldsymbol{D}$. Using the Young's inequality with $\alpha = C_\tau / 2$ yields the following bound

$$
|a(\boldsymbol{\epsilon}, \boldsymbol{\eta}) + b(\boldsymbol{\epsilon}, \boldsymbol{\eta})| \leq b(\boldsymbol{\eta}, \boldsymbol{\eta}) + \frac{C_\tau^2}{4} \sum_{D^k \in \Omega_h} \| \boldsymbol{\epsilon} \|^2_{L^2(\partial D^k)} + \| \boldsymbol{D} \|^2_{L^\infty(D^k)} \| \boldsymbol{\epsilon} \|^2_{L^2(D^k)}.
$$

Applying this to (3.3) and using Cauchy-Schwarz on $\left(\dfrac{\partial \delta}{\partial t}, \boldsymbol{\eta} \right)_{L^2(\partial D^k)}$ yields

$$
\begin{aligned}
\frac{1}{2} \frac{\partial}{\partial t} \left(T^{-1}_{\boldsymbol{A}_0^{-1}} \boldsymbol{\eta}, \boldsymbol{\eta} \right)_{L^2(\Omega)} + b(\boldsymbol{\eta}, \boldsymbol{\eta}) \leq & \left\| \frac{\partial \delta}{\partial t} \right\|_{L^2(\partial D^k)} \| \boldsymbol{\eta} \|_{L^2(\partial D^k)} \\
& + b(\boldsymbol{\eta}, \boldsymbol{\eta}) + \sum_{D^k \in \Omega_h} \frac{C_\tau^2}{4} \left(\| \boldsymbol{\epsilon} \|^2_{L^2(\partial D^k)} + \| \boldsymbol{D} \|^2_{L^\infty(D^k)} \| \boldsymbol{\epsilon} \|^2_{L^2(D^k)} \right)
\end{aligned}
\tag{3.4}
$$

Using a *hp* trace inequality [162]

$$
\sum_{D^k \in \Omega_h} \| \boldsymbol{\epsilon} \|^2_{L^2(\partial D^k)} + \| \boldsymbol{D} \|^2_{L^\infty(D^k)} \| \boldsymbol{\epsilon} \|^2_{L^2(D^k)} \leq \sum_{D^k \in \Omega_h} \left(C_N h^{-1} + \| \boldsymbol{D} \|^2_{L^\infty(D^k)} \right) \| \boldsymbol{\epsilon} \|^2_{L^2(D^k)} \tag{3.5}
$$

$\left(C_N + h \| \boldsymbol{D} \|^2_{L^\infty(D^k)} \right) h^{-1} \leq \widetilde{C}_N h^{-1}$, since $\| \boldsymbol{D} \| = O(1)$ and $\widetilde{C}_N = \left(C_N + h \| \boldsymbol{D} \|^2_{L^\infty(D^k)} \right) h^{-1}$.

Therefore,

$$\sum_{D^k\in\Omega_h} \|\boldsymbol{\epsilon}\|^2_{L^2(\partial D^k)} + \|\boldsymbol{D}\|^2_{L^\infty(D^k)} \|\boldsymbol{\epsilon}\|^2_{L^2(D^k)} \leq \sum_{D^k\in\Omega_h} \widetilde{C}_N h^{-1} \|\boldsymbol{\epsilon}\|^2_{L^2(D^k)}\,, \tag{3.6}$$

$$= \widetilde{C}_N h^{-1} \|\boldsymbol{\epsilon}\|^2_{L^2(\Omega)} \leq \widetilde{C}_N h^{2N+1} \|\boldsymbol{U}\|_{W^{N+1,2}}\,. \tag{3.7}$$

We now use that that $\boldsymbol{Q}_s$ and $\boldsymbol{Q}_v$ are positive definite such that

$$0 < s_{\min} \leq \boldsymbol{u}^T \boldsymbol{Q}_s(\boldsymbol{x})\boldsymbol{u} \leq s_{\max} < \infty$$

$$0 < \tilde{s}_{\min} \leq \boldsymbol{u}^T \boldsymbol{Q}_s(\boldsymbol{x})\boldsymbol{u} \leq \tilde{s}_{\max} < \infty$$

$$0 < v_{\min} \leq \boldsymbol{u}^T \boldsymbol{Q}_v(\boldsymbol{x})\boldsymbol{u} \leq v_{\max} < \infty$$

$$0 < \tilde{v}_{\min} \leq \boldsymbol{u}^T \boldsymbol{Q}_v(\boldsymbol{x})\boldsymbol{u} \leq \tilde{v}_{\max} < \infty$$

We define $A_{\max} = \max\left(s_{\max}\tilde{s}_{\max}, v_{\max}\tilde{v}_{\max}\right),\ A_{\min} = \min\left(\tilde{s}_{\min}, \tilde{v}_{\min}\right)$ and substitute the result of (3.5) in (3.3) performing time integration from $[0, T]$ and using modified Gronwall's inequality (Lemma 1.10 in [163]), (3.5) reduces to

$$\|\boldsymbol{\eta}\|_{L^2(\Omega)} \leq \frac{\widetilde{C}_N T h^{N+1/2}}{A_{\min}} \sup_{t\in[0,T]} \left(h^{1/2} A_{\max} \|\boldsymbol{A}_0\|_{W^{N+1,\infty}(\Omega_h)} \left\| \frac{\partial \boldsymbol{U}}{\partial t} \right\|_{L^2(\Omega)} + \|\boldsymbol{U}\|_{W^{N+1,2}(\Omega_h)} \right).$$

Using the triangle inequality yields

$$\|\boldsymbol{U} - \boldsymbol{U}_h\| \leq (C_1 + C_2 T) h^{N+1/2} \sup_{t\in[0,T]} \left(h^{1/2} A_{\max} \|\boldsymbol{A}_0\|_{W^{N+1,\infty}(\Omega_h)} \left\| \frac{\partial \boldsymbol{U}}{\partial t} \right\|_{L^2(\Omega)} + \|\boldsymbol{U}\|_{W^{N+1,2}(\Omega_h)} \right).$$

where C_1 and C_2 depends on $A_{\min}$ and $A_{\max}$. These estimates show that L^2 errors decrease proportionally to $h^{N+1/2}$. In practice we often observe the rate of convergence to be $O(h^{N+1})$.

C.4 Analytical solution of diffusive part of the poroelastic system

From (3.9), the diffusive part of the system is expressed as

$$\boldsymbol{Q}_v \frac{\partial \boldsymbol{v}}{\partial t} = \boldsymbol{D}\boldsymbol{v}. \tag{3.8}$$

The component wise expression for intermediate velocity vector is

$$\frac{\partial v_1}{\partial t} = -\frac{\eta}{\kappa 1}\beta_v^{(1)} q_1, \tag{3.9}$$

$$\frac{\partial v_2}{\partial t} = -\frac{\eta}{\kappa 2}\beta_v^{(2)} q_2, \tag{3.10}$$

$$\frac{\partial v_2}{\partial t} = -\frac{\eta}{\kappa 3}\beta_v^{(3)} q_3, \tag{3.11}$$

$$\frac{\partial q_1}{\partial t} = -\frac{\eta}{\kappa 1}\beta_q^{(1)} q_1, \tag{3.12}$$

$$\frac{\partial q_2}{\partial t} = -\frac{\eta}{\kappa 2}\beta_q^{(2)} q_2, \tag{3.13}$$

$$\frac{\partial q_2}{\partial t} = -\frac{\eta}{\kappa 3}\beta_q^{(3)} q_3, \tag{3.14}$$

where $\beta_v^{(i)} = \dfrac{\rho_f}{\rho_f^2 - \rho m_i}$ and $\beta_q^{(i)} = \dfrac{\rho}{\rho_f^2 - \rho m_i}$. The above system can be solved analytically, giving

$$v_1^* = v_1^n + \frac{\beta_v^{(1)}}{\beta_q^{(1)}}\left[\exp(\lambda_s^{(1)} dt) - 1\right] q_1^n, \tag{3.15}$$

$$v_2^* = v_2^n + \frac{\beta_v^{(2)}}{\beta_q^{(2)}}\left[\exp(\lambda_s^{(2)} dt) - 1\right] q_2^n, \tag{3.16}$$

$$v_3^* = v_3^n + \frac{\beta_v^{(3)}}{\beta_q^{(3)}}\left[\exp(\lambda_s^{(3)} dt) - 1\right] q_3^n, \tag{3.17}$$

$$q_1^* = \exp(\lambda_s^{(1)} dt) q_1^n, \tag{3.18}$$

$$q_2^* = \exp(\lambda_s^{(2)} dt) q_2^n, \tag{3.19}$$

$$q_3^* = \exp(\lambda_s^{(3)} dt) q_3^n, \tag{3.20}$$

where $\lambda_s^{(i)} = -(\eta/\kappa_i)\beta_q^{(i)}$. The state of intermediate vector $[v_1^*,\ v_2^*,\ v_3^*,\ q_1^*,\ q_2^*,\ q_3^*]$ is the input for the non-stiff being solved with DG scheme.

Appendix D

Weight-adjusted discontinuous Galerkin method for broad-band Biot's equation

D.1 Time domain representation of (5.12)

The shifted fractional derivative operator $(D+\lambda)^\alpha$ for a continuous function $f(t)$ is defined by [49]

$$(D+\lambda)^\alpha f(t) = e^{-\lambda t} D^\alpha [e^{\lambda t} f(t)], \tag{4.1}$$

where $\lambda \geq 0$ and $0 \leq \alpha < 1$, and D^α is the Caputo fractional derivative [116].

The Laplace transformation in variable s for function $f(t)$ with initial condition of $f(0) = 0$ is defined as

$$\mathcal{L}[f(t)](s) = \int_0^\infty f(t) e^{-st} dt. \tag{4.2}$$

Applying the Laplace transform to (4.1) yields [119]

$$\begin{aligned} \mathcal{L}[(D+\lambda)^\alpha f(t)](s) &= \mathcal{L}[e^{-\lambda t} D^\alpha (e^{\lambda t} f(t))](s), \\ &= \mathcal{L}[D^\alpha (e^{\lambda t} f(t))](s+\lambda), \\ &= (s+\lambda)^\alpha L[e^{\lambda t} f(t)](s+\lambda), \\ &= (s+\lambda)^\alpha \hat{f}(s). \end{aligned} \tag{4.3}$$

The inverse Laplace transform of (4.3) is

$$\mathcal{L}^{-1}[(s+\lambda)^\alpha \hat{f}(s)] = (D+\lambda)^\alpha f(t). \tag{4.4}$$

D.2 Computation of weights (a_l) and quadratures in (ϕ_l) in (5.24) [1]

In this work, we have used modified Gauss-Jacobi approach to compute the weights and quadratures. A brief overview modified Gauss-Jacobi approach is presented here. The Gauss-Jacobi approximation of the integral in $[-1, 1]$ is defined as [1, 164]

$$\int_{-1}^{1}(1-x)^{\gamma}(1+x)^{\beta}g(x)dx = \sum_{l=1}^{N} w_l g(x_l). \tag{4.5}$$

Substituting $z = \dfrac{1-x}{1+x}$ in (4.5) will result in mapping $]-1, 1[$ to $]0,\ \infty[$. (4.5) is written as

$$\int_{0}^{\infty} g(z)dz = \int_{-1}^{1} \frac{2}{(1+x)^2} g\left(\frac{1-x}{1+x}\right) dx \tag{4.6}$$

$$= \sum_{l=1}^{N} \frac{2w_l}{(1+x)^2} g\left(\frac{1-x_l}{1+x_l}\right) \tag{4.7}$$

Now RHS of (5.18) is expressed as

$$\int_{0}^{\infty} \frac{1}{\pi}\frac{1}{\sqrt{\alpha}}\phi(\alpha, t) = \sum_{l=1}^{N} a_l \phi(\alpha_l, t) \tag{4.8}$$

, with $\alpha_l = \dfrac{1-x_l}{1+x_l}$ and $a_l = \dfrac{1}{\pi}\left(\dfrac{1-x_l}{1+x_l}\right)^{1/2} \dfrac{2w_l}{(1+x_l)^2}$

In modified Gauss-Jacobi approach the $z = \dfrac{1-x}{1+x}$ is used for mapping $]-1, 1[$ to $]0,\ \infty[$ and thus, $\alpha_l = \left(\dfrac{1-x_l}{1+x_l}\right)^2$ and $a_l = \dfrac{1}{\pi}\left(\dfrac{1-x_l}{1+x_l}\right)\dfrac{4w_l}{(1+x_l)^4}$.

VITA

Khemraj Shukla

Candidate for the Degree of:

Doctor of Philosophy

Dissertation: Seismic wave propagation, attenuation and scattering in porous media across various scales

Major Field: Geology

Biographical:

Education:

Completed the requirements for Doctor of Philosophy in Geology at Oklahoma State University, Stillwater Oklahoma in December, 2019.

Completed the requirements for Master of Science in Physics at Banaras Hindu University, Varansi India in 2005.

Experience:

Employed by Oklahoma State Univeristy in the position of Research/Teaching Assistant in Stillwater, Oklahoma from August 2012 to December 2016.

Professional Memberships:

Student member of SIAM

Student member of SEG